Quantitative Prediction of Effective Material Parameters of Heterogeneous Materials

Der Fakultät Bauingenieur- und Vermessungswesen
der Universität Stuttgart vorgelegte Abhandlung
zur Erlangung der Würde
eines Doktor-Ingenieurs (Dr.-Ing.)

von

Dipl.-Ing. Jack Widjajakusuma

aus

Medan, Indonesien

Hauptberichter:	Prof. Dr.-Ing. Wolfgang Ehlers
Mitberichter:	Prof. Dr. rer. nat. Hans Herrmann
	Prof. Dr.-Ing. Stefan Diebels

Institut für Mechanik (Bauwesen) der Universität Stuttgart
Lehrstuhl II, Prof. Dr.-Ing. W. Ehlers

Contents

1 Introduction **11**

1.1 Statement of the problem 11

1.2 Scope of this thesis 14

2 Stochastic foundations and characterization of random media **17**

2.1 Elements of stochastic methods 18

2.1.1 Random process and probability density functions 18

2.1.2 Statistical homogeneity and ergodicity 21

2.2 Geometrical properties of heterogeneous media 22

2.2.1 Correlation functions, porosity and specific internal surfaces 22

2.2.2 Probability density functions of local geometric observables 24

2.3 Digital images and their geometrical characterization 27

2.3.1 ***Hoshen-Kopelman*** algorithm 30

2.4 Digitized samples 33

3 Basic equations of continuous media **39**

3.1 Kinematics of continua 39

3.1.1 The gradient of deformation, displacement and velocity 41

3.1.2 Kinematics of line, surface and volume elements 42

3.1.3 Strain 43

3.2 Balance relations of continuum physics 44

3.2.1 Global balance laws 44

3.2.2 Local balance laws and jump conditions 45

3.2.3 Balance of mass 49

3.2.4 Balance of linear momentum 49

3.2.5 Balance of moment of momentum 50

3.2.6 Energy balance 50

3.2.7 Entropy inequality 51

3.2.8 Balance equations of electrodynamics 51

3.3 Constitutive Relations 53

3.3.1 Heat conduction 54

3.3.2 Linear elasticity 54

3.3.3 Linear electromagnetic rigid continua 55

3.4 Concept of representative elementary volume 56

3.5 Boundary conditions associated with REV 59

3.5.1 Heat conduction problem 59

3.5.2 Elastostatic case 61

3.6 Instances of the ***Hill***'s condition 61

3.7 Definition of effective material parameters 63

3.7.1 Effective thermal conductivity 63

3.7.2 Effective elastic moduli 64

4 Numerical solution techniques **67**

4.1 ***Laplace*** equation 68

4.2 Frequency-dependent permittivity problems 73

4.3 ***Rayleigh-Ritz*** variational method for the elastic case 74

4.4 Iterative solution methods 76

4.4.1 SOR iterative method 76

4.4.2 CG method 79

4.4.3 Complex-valued symmetric coefficient matrix 81

5 Effective medium theory **83**

5.1 Thermal conductivity 88

5.1.1 Average heat flux through a coated sphere 88

5.1.2 ***Bruggeman*** effective medium approximation 90

5.1.3 ***Maxwell-Garnett*** theory 92

5.1.4 Differential effective medium 94

5.1.5 Mixing law based on the local porosity theory 96

5.2 Complex-valued permittivity 101

5.3 Linear elastic case 103

5.3.1 Average stress in a coated sphere 104

5.3.2 ***Bruggeman*** effective medium approximation 108

5.3.3 ***Maxwell-Garnett*** theory 109

5.3.4 Differential effective medium 110

5.3.5 Generalized self-consistent method 111

6 Rigorous bounds and cross properties 113

6.1 Duality concept 115

6.1.1 Classical variational principles 115

6.1.2 ***Hashin-Shtrikman*** variational principles 117

6.2 Bounds on the thermal conductivity 118

6.3 Bounds on the complex-valued permittivity 123

6.4 Bounds on the elastic constants 126

6.5 Cross-properties relationship 129

7 Examples 133

7.1 Thermal conductivity 133

7.2 Complex-Valued permittivity 142

7.3 Elastic moduli 147

8 Summary and conclusions 151

8.1 Summary 151

8.2 Directions for future work 153

A Some useful formulae of vector and tensor calculus i

B Spherical basis system iii

B.1 Transformation laws iii

B.2 Tensor analysis in spherical coordinates vi

B.3 Some applications viii

B.3.1 ***Laplace*** equation viii

B.3.2 Linear isotropic elasticity viii

Deutsche Zusammenfassung

Die vorliegende Arbeit befaßt sich mit der theoretischen und numerischen Bestimmung von effektiven Materialkonstanten von Stoffen mit heterogener Mikrostruktur. Die betrachtete Problematik ist für viele technische und naturwissenschaftliche Fragestellungen von Bedeutung, genannt seien exemplarisch die Erkundung von Öllagerstätten, Ultraschallbehandlungen von menschlichem Gewebe, die Festigkeit von Verbundwerkstoffen oder die Ausbreitung von Schadstoffen im Boden.

Auf der Mikroskala variieren die Materialeigenschaften derartiger Medien, während sie auf der Makroskala als homogen betrachtet werden können. Die homogenen Feldgrößen, die auf der Makroskala auftreten, sind die Mittelwerte der fluktuierenden Felder auf der Mikroskala. Die effektiven Materialparameter beschreiben die Zusammenhänge zwischen den makroskopischen Feldgrößen. Beispiele dafür sind die effektiven elastischen Konstanten $\overset{4}{\overline{\mathbf{C}}}$, die im Rahmen der geometrischen linearen Elastizitätstheorie den Zusammenhang zwischen dem makroskopischen Dehnungsfeld $\overline{\boldsymbol{\varepsilon}}$ und dem makroskopischen Spannungsfeld $\overline{\mathbf{T}}$ beschreiben. Dabei sind $\overline{\boldsymbol{\varepsilon}}$ bzw. $\overline{\mathbf{T}}$ die Mittelwerte des fluktuierenden mikroskopischen Verzerrungsfeldes $\boldsymbol{\varepsilon}$ bzw. der fluktuierenden mikroskopischen Spannung $\mathbf{T} = \overset{4}{\mathbf{C}}\,\boldsymbol{\varepsilon}$. Die effektiven Materialparameter geben daher an, wie sich der Körper im Mittel verhält.

In dieser Arbeit werden drei ganz unterschiedliche Arten von effektiven makroskopischen Materialkonstanten behandelt, die man aus den mikroskopischen Daten bestimmt. Die erste Gruppe von Materialkonstanten verknüpft ein divergenzfreies mit einem rotationsfreien Vektorfeld (Laplace-Gleichung). Beispiele dafür sind die Wärmeleitfähigkeit, die reellwertige dielektrische Konstante, die elektrische Leitfähigkeit, die Diffusionskonstante und die magnetische Suszeptibilität. Als zweite Gruppe wird die komplexwertige dielektrische Konstante berechnet, die ein dissipatives Medium kennzeichnet (Laplace-Gleichung im Komplexen). Im dritten Fall werden die elastischen Konstanten ermittelt, z. B. der Kompressionsmodul K und der Schubmodul G (Gleichgewichtsbeziehung plus *Hooke*sches Gesetz).

Das zentrale Problem im Rahmen der Theorie der heterogenen Medien ist die Bestimmung dieser effektiven Materialparameter. In der Literatur gibt es zu deren Berechnung eine Vielzahl verschiedener Verfahren oder Modelle zur Berechnung dieser, welche auf theoretischen oder phänomenologischen Grundlagen basieren. Diese Verfahren können im wesentlichen in „exakte“ Berechnungsmethoden und Näherungsmethoden eingeteilt werden.

In dieser Arbeit wird auf beide Wege eingegangen, um verschiedene effektive Materialparameter zu ermitteln und die verschiedenen Methoden miteinander zu vergleichen und zu bewerten. Als beste Methode wird diejenige bezeichnet, die bei minimalem Rechenaufwand die beste Übereinstimmung mit experimentellen Daten bzw. numerischen Simulationen liefert. Die Abhängigkeit von der Mikrogeometrie und von den mikroskopischen Materialparametern der jeweiligen Komponenten erschwert eine allgemeingültige Definition der besten Methode für die eingangs erwähnten drei Materialgruppen. Das **Ziel der vorliegenden Arbeit** ist es, für die verschiedenen Klassen von effektiven Materialparametern die jeweils beste Methode herauszufinden, allgemeine Bewertungskriterien zu

erarbeiten und den Einfluß der Mikrogeometrie auf die Bestimmung der Materialparameter zu analysieren.

Die Unkenntnis detaillierter Informationen über die Mikrogeometrie heterogener Medien wird kompensiert durch statistischen Konzepte, die im Kapitel 2 erläutert werden. Nach einer kurzen Einführung der grundlegenden statistischen Begriffe und Konzepte werden diese auf die Charakterisierung der heterogenen Medien angewandt. Die quantitative Charakterisierung kann entweder durch eine Zahl oder eine Funktion erfolgen. Der Volumenanteil oder die spezifische innere Oberfläche sind Zahlen, Funktionen dagegen sind die n-Punkt-Korrelationsfunktionen, die Verteilungsfunktion von Volumenanteilen oder die Wahrscheinlichkeitsdichte von zusammenhängenden Komponenten. Aufgrund der modernen digitalen Bildverarbeitung (z. B. Röntgenbild, Elektronenmikroskopie oder Kernspin-Tomographie) wird heutzutage die Mikrogeometrie realer heterogenen Medien exakt bis an die Grenze der Auflösung erfaßt. Die beschriebenen Charakterisierungsmethoden werden zu diesem Zweck entsprechend erläutert und auf diskrete heterogene Medien angewandt.

In Kapitel 3 werden im Rahmen einer kontinuumsmechanischen Betrachtungsweise die Grundgleichungen zur Bestimmung der effektiven Materialparameter aufgestellt. In Abschnitt 3.1 wird die Kinematik des Kontinuums kurz beschrieben. Im Anschluß daran werden die Bilanzgleichungen der Kontinuumsmechanik und der Elektrodynamik diskutiert. Die Bilanzen für Masse, Impuls, Drall, Energie, elektrische Ladung und die Entropieungleichung können in sogenannten allgemeinen Bilanzrelationen zusammengefaßt werden, die im Volumen eines Köpers gültig sind. Die Bilanzen für die Normale des magnetischen Flusses (*Faraday*sches Gesetz) und der elektrischen Verschiebung (*Ampère*sches Gesetz) stellt man in sogenannten allgemeinen Bilanzrelationen der Oberflächen zusammen. Zur Lösung eines konkreten Randwertproblems müssen die kinematischen Beziehungen und die Bilanzrelationen durch stoffabhängige Konstitutivbeziehungen ergänzt werden. In dieser Arbeit werden drei Konstitutivgleichungen aufgestellt, nämlich das Wärmeleitungsgesetz (*Fourier*sches Gesetz), das lineare Materialgesetz für elektromagnetische Medien und das lineare Elastizitätsgesetz (*Hooke*sches Gesetz).

In den Abschnitten 3.4–3.7 werden die Beziehungen zwischen den Feldgrößen auf der Mikroskala und der Makroskala angegeben, und es wird die Definition effektiver Materialparameter eingeführt. Mit Hilfe der Durchschnittsbildung können die makroskopischen Größen als Mittelwerte von den entsprechenden mikroskopischen Größen ausgedrückt werden. In Verbindung mit der Mittelung wird der Begriff des Repräsentativen Elementarvolumens (REV) vorgestellt. Das REV spielt die Rolle des Materialpunkts in der klassischen Kontinuumsmechanik. Deswegen muß das REV klein genug sein, um als Materialpunkt betrachtet werden zu können. Auf der anderen Seite muß es groß genug sein, um die wesentlichen Eigenschaften der Mikroinhomogenität erfassen zu können, damit (statistisch gesehen) die lokalen Eigenschaften des Mediums wiedergegeben werden. Durch Ausnutzung der statistischen Homogenität genügt es, repräsentativ ein REV zu betrachten, weil das effektive Materialverhalten innerhalb des REV genau dasselbe ist wie das des gesamten Körpers. Konsequenterweise reicht es aus, das homogene Randwertproblem nur bezüglich des REV und nicht bezüglich des gesamten Körpers zu betrachten.

Ein effektiver Materialparameter kann auf zweierlei Arten definiert werden. Einmal,

indem man die gemittelten Feldgrößen (z. B. gemittelte Spannung $\overline{\mathbf{T}}$, gemittelte Verzerrung $\overline{\epsilon}$, gemittelter Wärmefluß $\overline{\mathbf{q}}$ etc.) des *Fourier*schen Wärmeleitungsgesetzes, der elektromagnetischen Konstitutivgleichung, des Elastizitätsgesetzes etc. mit dem jeweiligen effektiven Materialparameter (z. B. dem effektiven Kompressionsmodul $\overline{K}$, der effektiven Wärmeleitfähigkeit $\overline{k}$ etc.) verknüpft. Die effektiven Materialgrößen sind im allgemeinen verschieden von den lokalen. Diese erste Art von Definition wird in der Literatur als direkte Definition bezeichnet (*Aboudi* [1], *Hashin* [79]). Die zweite Definition basiert auf dem Energieprinzip (*Aboudi* [1], *Hashin* [79]), mit dessen Hilfe obere und untere Schranken hergeleitet werden können. Die *Hill*sche Bedingung, d. h. die Annahme der Erfüllung der Ergodizität für die Energiemittlung, ist notwendige Voraussetzung dafür, daß beide Definitionen überstimmen. Andernfalls läßt sich das heterogene Material nicht durch einen effektiven Materialparameter beschreiben.

Zur Bestimmung der effektiven Materialparameter kennt man wie eingangs erwähnt „exakte“ Berechnungsmethoden und verschiedene Näherungsmethoden. In Kapitel 4 wird die exakte Methode beschrieben. „Exakt“ bedeutet, daß die Mikrostruktur des heterogenen Materials bekannt ist. Die detaillierte Information der Mikrostruktur erhält man entweder mittels Modellbildung (*Garboczi* & *Bentz* [68], *Yeong* & *Torquato* [195], *Biswal et al.* [32]) oder mittels Computertomographie (*Garboczi* & *Bentz* [69], *van Genabeek* & *Rothman* [178], *Widjajakusuma et al.* [185], *Michel et al.* [123]). In der Regel wird diese Information in diskreter Form gespeichert, daher werden entsprechende Computeralgorithmen benötigt, um die Randwertprobleme der diskreten, digitalisierten Medien zu lösen. Diese Algorithmen werden ausführlich behandelt.

Als erstes wird die Wärmeleitungsgleichung mit der Methode der finiten Volumen (*Patankar* [141]) diskretisiert, die ein Spezialfall der Methode der gewichteten Residuen (*Gresho* & *Sani* [77]) ist. Dieses Verfahren wird wegen seiner Kompatibilität mit der Definition von „Zusammenhang“ für ein diskretes Medium gewählt. Unter dieser Definition versteht man, daß die Wärme (Fluid) nur durch die Oberflächen der Elemente (Pixels) und nicht durch die Ecken der Elemente fließt (vgl. die Diskussion in Abschnitt 4.1 und Abbildung 4.2). Durch Lösen des diskretisierten Gleichungssystems können der lokale Wärmefluß und die lokale Temperatur bestimmt werden. Danach werden die Felder gemittelt und aus diesen Mittelwerten kann die effektive Wärmeleitfähigkeit $\overline{k}$ bestimmt werden. Die effektive komplexwertige dielektrische Konstante erhält man folgendermaßen: zuerst wird die komplexwertige Potentialgleichung mit der Methode der finiten Volumen diskretisiert, anschließend wird das resultierende komplexwertige Gleichungssystem für das unbekannte elektrische Potential gelöst. Danach werden das lokale elektrische Feld und die lokale elektrische Verschiebung berechnet und gemittelt. Mit diesen gemittelten Feldgrößen berechnet man die effektive komplexwertige dielektrische Konstante. Im Fall des elastischen Problems wird die elastische Verzerrungsenergiefunktion, d. h. die im Körper gespeicherte elastische Energie, mittels der Finite-Elemente-Methode diskretisiert. Daraus erhält man die Verschiebungen bzw. die Verzerrungen und über das lokale *Hooke*sches Gesetz (die lokalen Materialparameter sind bekannt) die lokale Spannung. Im nächsten Schritt werden die lokale Spannung und die lokale Verzerrung gemittelt, um für die gemittelte konstitutive Spannungs-Verzerrungsbeziehung den effektiven Elastizitätsmodul zu berechnen. Die Ergebnisse der „exakten“ Methode können als experimentelle Resultate angesehen wer-

den. Grundsätzlich geht man in allen drei Fällen davon aus, daß das lokale mikroskopische Verhalten und das makroskopische Verhalten durch die gleichen Konstitutivgleichungen beschrieben werden.

Die Näherungsmethoden können als „direkte“ Methoden (Kapitel 5) und „Schranken“-Methoden (Kapitel 6) klassifiziert werden. In der Regel fehlt die detaillierte Information über die Geometrie der Mikrostruktur, deshalb ist man auf charakteristische Größen wie Volumenanteile der Konstituierenden, 2-Punkt-Korrelationsfuntionen oder spezifische innere Oberflächen zur Kennzeichnung der Mikrogeometrie angewiesen. Diese reichen zur Berechnung der effektiven Materialparameter mittels der beiden Näherungsmethoden für die meisten technischen Probleme vollkommen aus. Desweiteren sind diese Methoden recht einfach zu handhaben.

Die „direkten“ Methoden, die in Kapitel 5 beschrieben werden, modellieren das heterogene Medium und basieren auf einigen heuristischen Annahmen über die Mikrostruktur des heterogenen Mediums. Da in vielen technischen Bereichen und im Ingenieurwesen (wie in der technischen Physik, in der Verfahrenstechnik, im Maschinenbau, im Bauingenieurswesen oder in der Werkstoffkunde) die Bestimmung der effektiven Materialparameter eine wichtige Rolle spielt, sind zahlreiche Modelle basierend auf theoretischen und phänomenologischen Grundlagen entwickelt worden (siehe *Aboudi* [1], *Markov* [115], *Nemat-Nasser & Hori* [135], *Priou* [146], *Sihvola* [164]). Deshalb ist es wichtig, einige von den am weitesten verbreiteten Modellen zu untersuchen, miteinander zu vergleichen und so weit wie möglich Beziehungen zwischen den verschiedenen Modellen herzustellen. Diese Modelle werden auch Mischungsgesetze genannt.

Es ist wünschenswert, die Mischungsgesetze so einfach wie möglich zu formulieren. Im einfachsten Fall enthält, das Mischungsgesetz nur die mikroskopischen Materialparameter und die Volumenanteile der Konstituierenden. Im allgemeinen müssen jedoch zusätzliche Informationen über die Mikrostruktur des heterogenen Mediums bekannt sein, falls eine genauere Vorhersage gewünscht wird. Diese zusätzlichen Informationen könnten die Geometrie des Korns (des Einschlusses), die Isotropie des Mediums oder die Korrelationen zwischen den Komponenten betreffen.

Zur Veranschaulichung betrachtet man ein heterogenes Medium, das aus den Komponenten φ^F und φ^S bestehen möge. Der gesamte Volumenanteil und die Wärmeleitfähigkeit von φ^F bzw. φ^S seien $\overline{n}^F$ und k^F bzw. $\overline{n}^S$ und k^S. Man beschränkt sich auf den Fall der Wärmeleitfähigkeit, andere Materialparameter können analog behandelt werden.

Wiener [188] nahm für das Problem der Wärmeleitung in einem heterogenen Medium ein Mehrschichtenmodell an. Dabei können zwei Fälle auftreten. Im ersten Fall, wenn die Schichten senkrecht zur Richtung des aufgebrachten Temperaturgefälles verlaufen, entspricht das System einer Serienschaltung. Die effektive Wärmeleitfähigkeit $\overline{k}$ dieses System ist durch

$$\overline{k} = \left(\frac{\overline{n}^F}{k^F} + \frac{\overline{n}^S}{k^S} \right)^{-1} \tag{0.1}$$

gegeben. Im zweiten Fall, wenn die Schichten parallel zur Richtung des aufgebrachten Temperaturgefälles angeordnet sind, entspricht das System einer Parallelschaltung. In

diesem Fall ergibt sich die effektive Wärmeleitfähigkeit $\overline{k}$ zu

$$\overline{k} = \overline{n}^F k^F + \overline{n}^S k^S. \tag{0.2}$$

Im Kontext des elastischen Problems entsprechen diese Fälle den Modellen von *Reuss* [150] bzw. *Voigt* [182]. Diese empirische Modelle können verallgemeinert werden:

$$(\overline{k})^i = \overline{n}^F (k^F)^i + \overline{n}^S (k^S)^i, \qquad -1 \leq i \leq 1. \tag{0.3}$$

Für $i = -1$ und $i = 1$ erhält man die beiden *Wiener*schen Modelle. Weiterhin kann man für $i \to 0$ das Modell von *Lichtenecker* [109, 110] wiederfinden:

$$\ln(\overline{k}) = n^F \ln(k^F) + \overline{n}^S \ln(k^S). \tag{0.4}$$

Für $i = 1/3$ ergibt sich aus (0.3) das *Looyenga*sche Mischungsgesetz

$$(\overline{k})^{1/3} = n^F (k^F)^{1/3} + \overline{n}^S (k^S)^{1/3}. \tag{0.5}$$

Die entsprechenden Herleitungen von (0.1) and (0.2) findet man in Kapitel (5).

Es ist offensichtlich, daß der einzige Eingabeparameter des obigen Modells bezüglich der Mikrostruktur der Volumenanteil ist. Der Volumenanteil ist sicherlich der einflußreichste geometrische Parameter zur Berechnung der effektiven Materialparameter. Jedoch ist er in vielen Fällen nicht ausreichend, um genaue effektive Materialparameter vorherzusagen, weil die Mikrostruktur im allgemeinen komplex ist und nicht ausreichend mit einem einzigen Parameter beschrieben werden kann.

Als Beispiel betrachten wir ein Zwei-Komponenten-Medium, das jeweils aus 50% φ^F (wärmeisolierendem Material) und φ^S (wärmeleitfähigem Material) besteht, wobei zwei Fälle diskutiert werden: (i) Die Einschlüsse von φ^F sind stochastisch in der Matrix von φ^S verteilt. (ii) Die Einschlüsse von φ^S sind stochastisch in der Matrix von φ^F verteilt. Es ist offensichtlich, daß das heterogene Material im ersten Fall leitfähig ist, im zweiten Fall dagegen nicht. Mischungsgesetze, die nur Volumenanteile und die Wärmeleitfähigkeit als Eingabeparameter benutzen, würden in den Fällen (i) und (ii) dieselbe effektive Wärmeleitfähigkeit liefern und sind daher zur Beschreibung des skizzierten Problems nicht geeignet. Aus diesen Beispielen sieht man sofort, daß die Kenntnis der Matrixphase eine wesentliche Rolle spielt. Deswegen möchte man solche zusätzlichen Informationen in die Modelle einzubauen.

Verbesserte Näherungsmethoden basieren auf der Theorie des effektiven Mediums. Die Hauptidee dieser Theorie kann folgendermaßen erkärt werden: dem heterogenen Material wird virtuell ein Einschluß (Korn) mit bekannten Materialparametern entnommen und in ein homogenes Medium mit unbekannten effektiven Materialparametern eingelagert. Man löst nun für das Korn und seine homogene Umgebung, d. h. für das isolierte Einkörperproblem mit dem Korn als Störung, das Randwertproblem des heterogenen Körpers. Die Lösung besteht aus der effektiven Feldgröße plus einem Störungsanteil infolge des Einschlusses. Der isolierte Einkörper mit Korn ist im heterogenen Ausgangsvolumen

n-mal enthalten. Nun werden die ermittelten Feldgrößen plus Störungen gleich den Feldgrößen des effektiven Mediums (ohne Einschluß) gesetzt. Das bedeutet aber, daß die gemittelten Störungen verschwinden müssen. Diese selbstkonsistente Bedingung ermöglicht es schließlich, die unbekannten effektiven Materialparameter zu bestimmen (siehe *Kröner* [103, 104], *Budiansky* [38] und *Nemat-Nasser & Hori* [135]).

Viele bekannte Modelle können mittels der Theorien des effektiven Mediums hergeleitet werden. Diese verschiedenen Modelle können auf verschiedene Annahmen über die Mikrostruktur zurückgeführt werden. Im Fall der Wärmeleitfähigkeit werden in dieser Arbeit folgende Modelle diskutiert: die Theorie des effektiven Mediums nach *Bruggeman* (BEMA) [37], die *Maxwell-Garnett*-Approximation (MGT) [122], die Theorie des differentialen effektiven Mediums (DEM) [37]) und das Näherungsverfahren basierend auf der lokalen Porositätstheorie (MLLPT) (*Hilfer* [88], *Widjajakusuma et al.* [186]). Im Fall der komplexwertigen dielektrischen Konstanten werden dieselbe Modelle benutzt, aber sie müssen entsprechend modifiziert werden. Für den Fall der elastischen Konstanten werden die BEMA, die MGT, die DEM und das Drei-Phasen-Modell von *Christensen-Lo* (GSCM) [46] benutzt. In diesem Fall sind die BEMA bzw. die MGT als *Krönersche* selbstkonsistente Methode [103] bzw. *Mori-Tanaka*-Modelle [133] bekannt. In dieser Arbeit werden jedoch aus historischen Gründen die Bezeichnungen BEMA bzw. MGT verwendet. Weiterhin werden zur Vereinheitlichung in diesem Abschnitt die englischen Abkürzungen benutzt.

In Kapitel 6 wird die zweite Klasse der Näherungsmethoden, nämlich die „Schranken"-Methode (vgl. *Beran* [17], *Bergman* [19, 21] *Kröner* [106], *Milton* [126, 128] *Ponte Castañeda & Suquet* [39], *Willis* [191, 192]) in kompakter Form hergeleitet. In der „Schranken"-Methode werden untere und obere Schranken berechnet, um die effektiven Materialparameter einzugrenzen. Der Vorteil dieser Methode ist, daß die Schranken mathematisch streng abgeleitet und bei Hinzufügen von zusätzlicher Information über die Mikrostruktur systematisch verbessert werden können. Weiterhin können die Schranken benutzt werden, um die Genauigkeit der „direkten" Methode zu testen.

Optimale Schranken sind Schranken, die mit der verfügbaren Information nicht verbessert werden können. Beispiele sind *Reuss-* und *Voigt*-Schranken [182, 150] und untere und obere *Hashin-Shtrikman-* Schranken [83]. Die *Voigt-* und *Reuss-* Schranken sind die besten Schranken, wenn man nur die Materialparameter und die Volumenanteile der Komponenten kennt. Wenn man dazu noch Isotropie des Mediums annimmt, erhält man die *Hashin-Shtrikman-* Schranken, die enger als *Voigt-* und *Reuss-* Schranken sind. Anhand dieser Beispiele sieht man sofort, daß die Schranken umso enger sind, je mehr Informationen zur Verfügung steht.

Es gibt viele Zugänge, um die Schranken herzuleiten. Am häufigsten benutzt man Variationsprinzipien, die man in das klassische Variationsprinzip (Prinzip vom Minimum der potentiellen Energie W bzw. Prinzip vom Minimum der komplementären Energie) und in das *Hashin-Shtrikman* [83] Variationsprinzip unterteilen kann. Durch Einsetzen der zulässigen Ansatzfunktionen in das klassische Variationsprinzip erhält man die Schranken. Dabei bedeutet zulässige Ansatzfunktion, daß sie bestimmte physikalische Bedingungen und Randbedingungen erfüllen muß. Zulässige Ansatzfunktionen für das Prinzip von Minimum der potentiellen Energie bzw. für das Prinzip von Minimum der komplementären Energie, die enge Schranken liefern, sind in der Regel schwierig zu finden. Deswegen führt

man das Variationsprinzip von *Hashin-Shtrikman* [83] ein, mit dem man bei gleichem Aufwand sogar noch bessere Schranken erhält. In diesem Fall wird die potentielle Energie W auf die des Referenzmediums W_0 bezogen, indem man die Differenz beider bildet $(W - W_0)$.

In der vorliegenden Arbeit werden die klassischen und die *Hashin-Shtrikman* Variationsprinzip zur Herleitung der oberen und unteren Schranken für die effektive Wärmeleitfähigkeit $\overline{k}$, den effektiven Kompressionsmodul $\overline{K}$ und den effektiven Schubmodul $\overline{G}$ benutzt. Die resultierenden Schranken hängen von den Ansatzfunktionen ab, wobei diese die Information über die Mikrostruktur widerspiegeln. Je mehr Information die Ansatzfunktionen enthalten, desto besserere Schranken liefern sie. Die klassischen Variationsprinzipien geben Schranken der Ordnung $2n-1$ an, das *Hashin-Shtrikman* Variationsprinzip dagegen liefert Schranken der Ordnung $2n$. Die Schranken n-ter Ordnung berechnet man mittels n-Punkt-Korrelationsfunktionen. In dieser Arbeit werden die Schranken bis zur dritten Ordnung angegeben. Für den Fall der Wärmeleitfähigkeit werden die Schranken wie folgt bezeichnet: die *Wiener*-Schranken (von erster Ordnung) [188], die *Hashin-Shtrikman*-Schranken (von zweiter Ordnung) [83] und die *Beran*-Schranken (von dritter Ordnung) [15]. Im Fall der elastischen Konstanten kennt man die untere *Reuss*- und die obere *Voigt*-Schranke (von erster Ordnung) [150, 182] die *Hashin-Shtrikman*-Schranken (von zweiter Ordnung) [83], die *Beran-Molyneux*-Schranken für den Kompressionsmodul (von dritter Ordnung) [16] und die *McCoy*-Schranken für den Schubmodul (von dritter Ordnung) [62].

Für ein dissipatives Medium, für das die Felder und die Materialparameter durch komplexwertige Variablen ausgedrückt werden (siehe Abschnitte 3.3.3, 4.2 und 5.2), können die Variationsprinzipien nicht mehr angewendet werden. Der Grund dafür ist der Verlust der Anordnung bei komplexen Zahlen, was dazu führt, daß kein Minimum oder Maximum existiert. Um diese Schwierigkeiten zu vermeiden, werden die Schranken für die komplexwertige dielektrische Konstanten mittels der sogenannten analytischen Methode hergeleitet (siehe *Bergmann* [19, 21] *Milton* [127, 128]). Der Schlüssel für die analytische Methode ist, daß die komplexwertige dielektrische Konstante in ihrer Spektralzerlegung dargestellt wird. Das zulässige Gebiet der effektiven dielektrischen Konstante in der komplexer Ebene, das von den Schranken eingegrenzt wird, ist linsenförmig. Mit zunehmender Genauigkeit, d. h. mit zunehmender Information über die Mikrostruktur des Mediums, zieht sich das linsenförmige Gebiet auf den Lösungspunkt (die effektive komplexwertige dielektrische Konstante) zusammen (vgl. Abbildung 6.1). Für ein nicht-dissipatives Medium (reellwertige dielektrische Konstante) gehen diese Schranken in die bekannten reellwertigen Schranken für die effektive Wärmeleitfähigkeit über.

Leider ist in den meisten praktischen Situationen die erforderliche Information, um optimale Schranken zu erlangen, nicht verfügbar. Häufig kennt man beispielsweise nur die Volumenanteile sowie einen geometrischen Parameter, obwohl zwei benötigt werden. In anderen Fällen kennt man zwar gewisse effektive Materialparameter, allerdings sind diese die nicht von Interesse. Ein Beispiel: es ist die effektive Wärmeleitfähigkeit bekannt, aber gesucht wird der effektive Schubmodul. Deshalb ist es wichtig, eine Methode zu finden, die die verfügbaren Informationen optimal auszunutzt. In der Literatur ist diese Methode als „Kreuzrelationen“ bekannt. Die Idee hierzu wurde von *Prager* [144] und

Berryman & Milton [26] vorgeschlagen, eine detaillierte kritische Anwendung auf reale heterogene Medien wurde jedoch, soweit dies dem Autor bekannt ist, erstmalig in dieser Arbeit durchgeführt.

In Kapitel 7 werden die beschriebenen Näherungsmethoden anhand von realen heterogenen Sandsteinproben, für die die computertomographisch ermittelte Mikrostruktur bekannt ist, validiert. Die ersten beiden Proben sind gering verfestigte Sandsteine und werden als Probe A bzw. B bezeichnet. Die dritte Probe ist *Berea*-Sandstein und wird im folgenden Probe C genannt. Die vierte (D1), fünfte (D2) und sechste (D3) Probe sind die *Fountainebleau*-Sandsteine. Zwei weitere Datensätze (R1 und R2) erhält man durch Rekonstruktion der Probe C mit Hilfe des sogenannten *Gauss*schen Rekonstruktionsalgorithmus (siehe *Adler* [2]). Grundidee solcher Rekonstruktionen ist es, die Übereinstimmung der 2-Punkt-Korrelationsfunktion und der Volumenanteile von Modell und Originalprobe zu erreichen. Der einzige Unterschied zwischen den beiden Modellen R1 und R2 ist, daß die Auflösung von R2 doppelt so groß ist wie die von R1. Die charakteristischen Daten dieser Datensätze werden in Tabelle 2.1 angegeben.

Zur Bestimmung der effektiven Wärmeleitfähigkeit $\overline{k}$ werden alle acht Datensätze herangezogen, wobei jeweils sechs verschiedene Kontrastverhältnisse der Wärmeleitfähigkeit ($2 \leq k^F/k^S \leq \infty$) der beiden Komponenten untersucht werden. Zuerst werden Temperaturgradient und Wärmefluß mittels der Methode der finiten Volumen berechnet. Aus den Mittelungen des Temperaturgradienten und des Wärmeflusses folgt die effektive Wärmeleitfähigkeit $\overline{k}$. Diese Simulationsergebnisse werden im folgenden als Bezugsdaten zur Überprüfung der Genauigkeit verschiedener Näherungsverfahren verwendet.

Am Beispiel von C, R1 und R2 (sie haben fast identische Volumenanteile und 2-Punkt-Korrelationsfunktionen aber sehr unterschiedliche Morphologien) kann sehr deutlich beobachtet werden, daß die Morphologie im Fall geringer Kontrastverhältnisse nur eine geringe Auswirkung hat, aber eine größere Auswirkung im Fall höherer Kontrastverhältnisse. Für geringe Kontrastverhältnisse sind die effektiven Leitfähigkeiten aller drei Datensätze gleich, während sie für höhere Kontrastverhältnisse sehr unterschiedlich sind (vgl. Tabelle 7.1). Für den Grenzfall von $k^F/k^S = \infty$ ist die effektive Leitfähigkeit $\overline{k}$ von C dreimal bzw. viermal so groß wie diejenige von R1 bzw. von R2.

Die Resultate aller Näherungsmethoden stimmen quantitativ mit den Simulationsergebnisse im Fall niedriger Kontrastverhältnisse überein. Man kann daraus schließen, daß in diesem Fall die Kenntnis der Volumenanteile und der Wärmeleitfähigkeit der Konstituierenden völlig für die Berechnung der effektiven Wärmeleitfähigkeit ausreicht.

Für höhere Kontrastverhältnisse stimmen die Resultate derjenigen Näherungsverfahren, die mehr Information über die Mikrostruktur verwenden, quantitativ besser mit den Simulationsergebnissen überein. Deswegen liefert das Modell, das auf der lokalen Porositätstheorie basiert, die besten Ergebnisse, weil es die Verteilungsfunktionen der Volumenanteile $p(n^F, L)$ und der Konnektivität der Komponenten $p_{\mathcal{L}}(n^F, L)$ enthält. Weiterhin ergeben sich bei diesem Modell unterschiedliche Werte $\overline{k}$ für C, R1 und R2, wohingegen sich bei allen anderen Modellen dieselbe effektive Wärmeleitfähigkeit für diese drei Datensätze ergibt. Allerdings hängen die Resultate sehr stark von der charakteristischen Längenskala L ab. Die Hauptschwierigkeit bei Verwendung solcher Modelle besteht in der quantitati-

ven Berechnung dieser Längenskala. Die vorhandenen Kriterien (siehe *Boger et al.* [34], *Hilfer et al.* [91], *Widjajakusuma et al.* [186]) zur Bestimmung dieser Längenskala L sind nicht allgemein gültig, weil sie vom Kontrastverhältnis abhängen (vgl. Abbildung 7.3). Die weitere Schwierigkeit bei Verwendung des MLLPT-Modells ist die Bestimmung der beiden Verteilungsfunktionen $p(n^F, L)$ und $p_{\mathcal{L}}(n^F, L)$, weil hierfür die detaillierte Mikrostruktur bekannt sein muß. Der Vorteil gegenüber der „exakten" Methode ist, daß man $\overline{k}$ relativ schnell und einfach abschätzen kann, sobald man diese Verteilungsfunktionen kennt. Das Modell von *Looyenga* [111] liefert gute Ergebnisse für höhere Kontrastverhältnisse für alle Datensätze, wobei die Approximationswerte immer kleiner sind als die Simulationresultate. Allerdings kann es auch keine unterschiedlichen Resultate für die Datensätze C, R1, R2 liefern, weil der einzige Eingabeparameter für das *Looyenga*-Modell der Volumenanteil der Komponenten ist.

Die Schranken von *Prager*, die man aus der effektiven Leitfähigkeit für ein Kontrastverhältnis für jedes andere Verhältnis herleiten kann, sind wesentlich schärfer als diejenigen von *Hashin-Shtrikman*. Für den Grenzfall von $k^F/k^S = \infty$ ist zwar die untere Schranke gleich null, aber die obere Schranke kann zur Bestimmung der effektiven Leitfähigkeit $\overline{k}$ verwendet werden. Die obere Schranke, die den Wert von $\overline{k}$ für das Kontrastverhältnis $k^F/k^S = 10000$ als Information benutzt, ergibt ein $\overline{k}$, das sehr gut mit dem Simulationsergebnis übereinstimmt. Da die „exakte" Methode für den Fall von $k^F/k^S = \infty$ nur sehr langsam konvergiert, kann man diese obere Schranke in guter Näherung als effektive Leitfähigkeit $\overline{k}$ für $k^F/k^S = \infty$ benutzen. Im Gegensatz zu dem Verfahren von *Hashin-Shtrikman* liefert die Methode von Prager unterschiedliche Schranken für C, R1 und R2.

Zur Bestimmung der dielektrischen Konstanten wird, wie im Fall der Wärmeleitung, die komplexwertige Potentialgleichung mittels der Methode der finiten Volumen diskretisiert, und man erhält das elektrische Feld und die elektrische Verschiebung. Aus diesen gemittelten Feldgrößen wird die effektive, komplexwertige, dielektrische Konstante $\tilde{\varepsilon}^c$ berechnet. Es werden nur vier Datensätze (A, B, C, D1) benutzt und für jeden Datensatz sechs verschiedene Frequenzen ($\omega = 10^{-4}$/s bis $\omega = 10^{2}$/s) behandelt.

Die BEMA und die MGT liefern zwar qualitativ richtige Ergebnisse, allerdings gibt es keine gute quantitative Übereinstimmung mit den Simulationsresultaten (siehe *Ma et al.* [114]). Für einzelne Frequenzen liefert die MLLPT gute Ergebnisse, falls man die charakteristische Längenskala kennt. Im allgemeinen gibt es jedoch entweder im Realteil oder im Imaginärteil von $\overline{\tilde{\varepsilon}}^c$ Abweichungen von den Simulationsergebnissen. Wie im Fall der Wärmeleitung läßt sich auch hier eine geeignete Längenskala nur schwer bestimmen.

In diesem Fall empfiehlt es sich, die Schranken von dritter Ordnung zu verwenden, da sie einen engeren Bereich um die effektive, komplexwertige, dielektrische Konstante $\overline{\tilde{\varepsilon}}^c$ eingrenzen als die Schranken erster und zweiter Ordnung. Den hierfür benötigten geometrischen Parameter ζ (*Milton-Torquato* Parameter) kann man aus der „Kreuzrelation" gewinnen, und zwar aus der effektiven Wärmeleitfähigkeit mit Hilfe der Schranken von *Beran* [15].

Im linear elastischen Fall läßt sich das Randwertproblem mittels der Methode der Finiten Elemente diskretisieren. Die Finite-Elemente-Gleichungen können z. B. mit Hilfe des *Ritz*schen Verfahrens hergeleitet werden. Aus der Lösung des Gleichungsystems werden

die lokalen Verzerrungen und die lokalen Spannungen ermittelt. Die effektiven elastischen Moduli können aus den gemittelten Verzerrungen und den gemittelten Spannungen berechnet werden. Als Datensatz wird ein Teil des *Fontainebleau*-Sandsteins (D1) mit der Größe $64 \times 64 \times 64$ Pixel verwendet. Zwei Fälle von niedrigem und hohem Kontrastverhältnis werden untersucht: (i) Kompressionsmodul $K^F = 1.0 \cdot 10^5 \mathrm{N/mm^2}$ und Schubmodul $G^F = 2.0 \cdot 10^5 \mathrm{N/mm^2}$ bzw. $K^S = 20.0 \cdot 10^5 \mathrm{N/mm^2}$ und $G^F = 50.0 \cdot 10^5 \mathrm{N/mm^2}$. (ii) Kompressionsmodul $K^F = 17.5 \cdot 10^5 \mathrm{N/mm^2}$ und Schubmodul $G^F = 8.0 \cdot 10^5 \mathrm{N/mm^2}$ bzw. Kompressionsmodul $K^S = 1750 \cdot 10^5 \mathrm{N/mm^2}$ und Schubmodul $G^F = 800 \cdot 10^5 \mathrm{N/mm^2}$. Hierbei bezeichnen sich die hochgestellten Indizes F und S jeweils auf die Phasen φ^F and φ^S.

Wie im Fall der Wärmeleitung liefern alle „direkten“ Näherungsmethoden für geringes Kontrastverhältnis Resultate, die mit den Ergebnissen der Finite-Elemente-Methode sehr gut übereinstimmen. Für höhere Kontrastverhältnisse sind die Resultat allerdings sehr unterschiedlich in ihrer Genauigkeit, wobei die BEMA noch die besten Ergebnisse liefert.

Die geometrischen Parameter, die für die Schranken dritter Ordnung von *Beran-Molyneux* und von *McCoy* benötigt werden, können aus der effektiven Wärmeleitfähigkeit gewonnen werden. Diese Schranken sind schärfer als die Schranken von *Hashin-Shtrikman*. Weiterhin kann die obere Schranke von *Beran-Molyneux* bzw. von *McCoy* benutzt werden, um den effektiven Kompressionsmodul $\overline{K}$ bzw. den effektiven Schubmodul $\overline{G}$ zu approximieren. Zwar liegen alle Resultate der „direkten“ Näherungsmethoden innerhalb der Schranken von *Hashin-Shtrikman*, aber nur die BEMA und die DEM liegen auch innerhalb der Schranken von dritter Ordnung. Da jedoch der effektive Kompressionsmodul $\overline{K}$, der mittels der DEM berechnet wird, zu niedrig ist, empfiehlt sich hier die Verwendung der BEMA.

Ist keine detaillierte Kenntnis über die Mikrogeometrie heterogener Medien vorhanden, kann folgendes Fazit gezogen werden: (i) Im Fall niedriger Kontrastverhältnisse kann man „direkte“ Näherungsmethoden zur Bestimmung der effektiven Wärmeleitfähigkeit (darunter auch die effektive reellwertige dielektrische Konstante, die effektive elektrische Leitfähigkeit, die effektive Diffusionskonstante und die effektiven magnetische Suszeptibilität) und der elastischen Konstanten benutzen. (ii) Im Fall höherer Kontrastverhältnisse müssen die „direkten“ Methoden mit äußerster Vorsicht benutzt werden. (iii) Ist ein effektiver Materialparameter, z. B. die effektive Wärmeleitfähigkeit, für ein bestimmtes Kontrastverhältnis bekannt, kann dieser effektive Materialparameter zusammen mit der „Kreuzrelationen“ ausgenutzt werden, um schärfere Schranken für andere Materialparameter (die elastischen Konstanten, die komplexwertige dielektrische Konstante) zu ermitteln. Diese Methode erweist sich in Fälle höherer Kontrastverhältnisse und der komplexwertigen dielektrischen Konstanten als sehr nützlich. (iv) Im Fall komplexwertiger dielektrischer Konstanten sind zur Bestimmung der effektiven komplexwertigen dielektrischen Konstanten die „Schranken“-Methoden von *Bergman* und *Milton* die geeignetesten Methode.

Chapter 1

Introduction

1.1 Statement of the problem

Heterogeneous materials can often be considered as mixtures of homogeneous constituents. Examples for such materials are natural materials like wood, soil, rock, lake and sea ice, snow, parts of human bodies (liver, various biological tissues, blood, bones, etc.), agricultural products, and human-made materials like bricks, concrete, ceramics, fibre reinforced materials, metal matrix composites, contact lenses, woven-clothes and so on. The material properties of the heterogeneous material vary from grain (small region) to grain. Within the grain, the material properties are uniform and equal to the material properties of one of the constituents. The size scale of the grains is called the micro-length-scale and it defines the domain of microscopic properties. On larger scales (the macro-length-scale), the heterogeneous material often behaves like a homogeneous material with effective material properties which generally differ from those of the constituents. *Material properties* are defined as the abilities of materials to respond to the imposed stimuli. Three representative examples are investigated. Namely, the problem of heat conduction, of electromagnetism and of linear elasticity. The effective material parameters governing the different models on the macroscopic scale are the effective thermal conductivity, the effective electric permittivity, and the effective elastic moduli.

Thermal conductivity is defined as the ability of a conducting material to transport heat due to an imposed temperature gradient field. Thermal conductivity plays a central role in various engineering applications. For example, the knowledge of thermal conductivities of soils and rocks can be used to determine the loss of heat from buried pipes such as steam and hot water distribution lines, electrical power transmission lines, and oil and gas lines. This knowledge is also helpful in designing thermally insulating materials such as enhanced heat insulation for porous building materials, enhanced safety in fires for high performance concrete and enhanced heat transfer for fiber-ceramic composites in the automobile.

The electric permittivity is defined as the ability of a material to resist the formation of an electric field within the material due to an imposed electric field. The knowledge of the electric permittivity and electric conductivity of heterogeneous media is useful in

theoretical and applied science. Examples for this case are ranging from the detection of water or oil content in soils and rocks using electrical measurements in finding water or oil resources, the microwave heating of agricultural products, the bioimpedance analysis for gathering information regarding the internal state of human bodies, and the design of the marine and aircraft systems in radar visibility.

The elastic moduli can be defined as the ability of an elastic material to respond to the stress caused by an imposed stress field. The knowledge of elastic moduli of heterogeneous materials are required to study the strength and failure of composite, foam and ceramic materials, which are extensively used in the aerospace, automobile or construction industries. This knowledge is also helpful in designing an enhanced strength and toughness of high performance composite, foam and ceramic materials.

The central problem in the theory of heterogeneous media is the determination of the effective material parameters. In the literature, several theoretical approaches have been proposed to determine the effective material properties (*Aboudi* [1], *Beran* [17], *Bergman & Stroud* [22], *Christensen* [44], *Hashin* [79, 80], *Jeulin & Ostoja-Starzewski* [98], *Markov* [115], *Nemat-Nasser & Hori* [135], *Sihvola* [164], *Suquet* [168], *Quintanilla* [147], *Torquato* [170], *Willis* [191]). These approaches can be divided into exact numerical calculation methods and approximation methods. In this thesis, all of these methods will be used to predict the various effective material parameters. This includes thermal conductivity (by mathematical analogy also the magnetic permeability, the diffusion constant, the electric conductivity and the real-valued electric permittivity), complex-valued electric permittivity, and elastic moduli. All of these methods which are applied to determine the effective properties of heterogeneous materials will be examined and compared to each other. The best method will be the one which has the optimal balance of the accuracy of the predictions, the required analysis and the computational effort. The purpose of the thesis is to have the proper methods and guidelines for predicting various effective material properties. This can be done by comparing various approaches explained above which will produce general guideline for predicting the effective material properties.

For an exact numerical calculation, one needs a full information of the microgeometry of the heterogeneous medium either by terms of special microstructures or obtained by image processing techniques. Upon obtaining the detailed microstructure of heterogeneous media, one can solve a boundary-value problem of the microscale. Then, the obtained field quantities can be averaged, and from these averaging quantities, the effective material parameters can be computed. In general, the microgeometrical data are stored in discrete digital image form. Therefore, appropriate numerical algorithms should be developed. For this purpose, in this thesis, numerical algorithms based on the finite volume method (*Patankar* [141]) and based on the finite element method (*Hughes* [95]) will be implemented. Other works and methods related to this subject are the finite difference method (*Adler* [2]), the fast *Fourier* transformation (*Moulinec et al.* [134]) and the lattice-*Boltzmann* method (*van Genabeek & Rothman* [178]).

The approximation methods can be classified into direct methods and bounds methods. In most engineering and science problems, these methods are the sole methods to estimate the effective material parameters, because in most cases, only a partial information of the microgeometry such as volume fractions of the constituents, two-point correlation

functions and/or specific internal surfaces are known. These methods are also used, if one needs an easy way to predict the effective material properties.

The direct methods use some assumptions and postulations based on some physical intuition about the microstructure of the system to model the heterogeneous medium. From this model, one can obtain so-called mixing laws, which give the prediction of the effective properties of the materials. Since in many technical and engineering disciplines (physics, electromagnetics, material science, applied mechanics, thermal engineering or bio-engineering) the prediction of the effective material parameters plays a central role, a vast number of mixing laws has evolved based on the theoretical and empirical framework (*Aboudi* [1], *Markov* [115], *Nemat-Nasser & Hori* [135], *Priou* [146], *Sihvola* [164]). Therefore, it is important to investigate some of commonly used mixing laws and whenever possible, to find their relationships. Many of the widely used mixing laws can be derived from one principle, namely from the effective medium theory also called the self-consistent method (*Choy* [43], *Landauer* [108], *Kröner* [105], *Nemat-Nasser & Hori* [135]). These mixing laws are obtained in heuristic manners, therefore, the only way to justify their accuracy is by comparing their predicted effective value with the computer simulation data. This thesis is also intended to study the widely used mixing laws based on the effective medium approximation, and whenever possible, the predictions using these mixing laws will be compared to the computer simulation data.

The second class of the approximation methods is the bounds method (*Beran* [17], *Bergman* [19, 21], *Kröner* [106], *Milton* [126, 127, 129], *Ponte Castañeda & Suquet* [39], *Willis* [191, 192]). In bounds methods, lower and upper bounds are established and applied to confine the effective material parameters of a heterogeneous medium. The advantage of the bounds method is that the bounds can be derived rigorously and be made narrower by systematically incorporating more microstructural information.

Bounds which can be attained for all values of constituents material parameters, volume fractions, and correlation functions are called the optimal bounds. The optimal bounds are the tightest bounds in their class, which means that one cannot obtain tighter bounds with the same microstructure information as the input data. Prominent examples are *Voigt* [182], *Reuss* [150], and *Hashin-Shtrikman* [83] bounds. The *Voigt* and *Reuss* bounds are the narrowest bounds that can be obtained if only the constituents material parameters and the constituents volume fractions are known. If in addition to constituents material parameters and constituents volume fractions, the medium is known to be isotropic, then the best attained bounds are the *Hashin-Shtrikman* bounds which are narrower than the *Voigt* and *Reuss* bounds. Thus, it is clear that the more information is incorporated into the bounds, the narrower they will be.

Unfortunately, in most practical situation, the required information to attain optimal bounds is not available. This inappropriate information can be (i) the volume fractions and only one microgeometry parameter are known, whereas it needs the volume fractions and two known microgeometry parameter. (ii) the volume fractions and the value of some effective material parameters are known, whereas the value of some effective material parameter indeed are not needed, (iii) only the value of some effective material parameters are known, whereas it is not needed. Therefore, it is important to find a method to use the available information optimally. This idea has been proposed by *Prager* [144] and

Berryman & Milton [26]; however, a critical evaluation using real heterogeneous media is provided nowhere. The last part of this thesis deals with the quantitative prediction of effective material parameters using bounds methods. Furthermore, the comparison with the computational data and with the predictions using direct methods will also be presented.

1.2 Scope of this thesis

The structure of this thesis is outlined as follows.

Chapter 2 is devoted to stochastic methods and to the characterization of random media. First, in Section 2.1, a brief introduction to the probability theory is given, followed by the discussion of the statistical homogeneity and ergodicity. Then, the probability tool is used to characterize random media quantitatively. These quantities can be solely numbers such as porosity or specific internal surfaces, or functions such as correlation functions, local porosity distribution functions or local percolation distribution functions. Then, these characterization methods will be modified and applied to digital images, which can be seen as discrete media (Section 2.3). In Subsection 2.3.1, the *Hoshen-Kopelman* algorithm is introduced, which is used to assess the connectivity property of the phases of the discrete medium. Finally, the characterization methods are applied to the digitized real materials, which are obtained from the computer tomography (Section 2.4).

Chapter 3 deals with some concepts and basic laws of continuum physics and with the relationship between the macro-properties (effective properties) and the microstructure of the micro-constituents. In Section 3.1, a brief discussion of the kinematics (motion and deformation) of continua regardless of their forces will be presented. Then, in Section 3.2, attention will be focused on balance equations which are independent of the material properties and the geometry. Kinematical relationships and balance equations alone are still insufficient to solve boundary-value problems. In order to solve these problems, constitutive equations are needed. This topic will be discussed in Section 3.3. Since this thesis will treat three basic physical problems namely heat transfer, electrostatics and elastomechanics, the discussion of the corresponding constitutive equations for conductive, electromagnetic non-deformable, and linear elastic solid materials will be presented. The second part of Chapter 3 will be focused on the transition of field quantities from the microscale to those of the macroscale. The volume averaging procedure may be used as a vehicle for this transition. The volume averaging procedure is tied to the concept of a representative volume element as discussed in Section 3.4. Then the associated boundary-value problems and the associated averaging theorems will be given in Section 3.5. By assuming that the random media behaviour is governed by the same constitutive laws both on the micro- and macrolevel, the effective material parameters of the random media which provide the relation between the field quantities on the micro- and macrolevel, will be defined in Section 3.7. In general, these effective material parameters are different from those of the components of random media. Section 3.6 discusses the condition under which these effective constitutive laws are valid. The overall material properties provide the relation between the field quantities on the micro- and macrolevel, in which

the macrofield quantities can be seen as the average of the corresponding microfields.

Chapter 4 provides the numerical techniques to solve the boundary-value problems of the digitized inhomogeneous media. Section 4.1 deals with the discretization of the heat conduction (*Laplace*) equation for inhomogeneous media using the finite volume method. Section 4.2 presents the discretization of the complex-valued *Laplace* equation using the finite volume method. This complex-valued *Laplace*an governs the quasi-static electric field in a dissipative medium. Section 4.3 discusses the discretization of the potential energy equation for an elastic medium using the finite element method based on the *Rayleigh-Ritz* variational formulation. Section 4.4 focuses on the solving of these discretization equations. In the real-valued case, depending on the size of the linear system of the discretization equations, two solvers will be presented, namely, the successive over-relaxation (SOR) and the conjugate-gradient (cg) methods. In the complex-valued case, the cg method has to be modified appropriately and this method will be presented in Subsection 4.4.3.

In Chapter 5, a number of widely used approximation methods based on the effective medium theory are studied in a systematic manner. These approximation methods will be used to predict the effective material parameters of three different physical cases (linear thermal conductive, linear electric and linear elastic cases). The effective medium approximations make use of the solution of the so-called single inclusion problem, which is a boundary-value problem for an inclusion embedded in an infinite homogeneous medium with different material properties. The first part of this chapter deals with the linear thermal conductive material. It starts with the boundary-value problem for a single inclusion. Using the solution of this boundary-value problem, the *Bruggeman* effective medium approximation (BEMA), the *Maxwell-Garnett* theory (MGT), the differential effective medium (DEM), and the recently developed mixing law based on the local porosity theory can be derived. Since the effective thermal conductivity can only be obtained using a numerical method, the corresponding numerical method will be presented in Subsection 5.1.5. All of these mixing laws can be also applied to compute the effective complex-valued permittivity of a dissipative linear electric material. Therefore, in Section 5.2, all of these mixing laws will be collected and rewritten in the corresponding forms. The numerical method which is used to solve the complex-valued equation of the mixing law based on the local porosity theory will be given in Section 5.2. The last part of this chapter is devoted to predicting the effective elastic moduli using the mixing laws which are similar to those of the linear thermal conductivity case. This includes the BEMA, the MGT, the DEM and the generalized self-consistent method (GSCM). The derivation of these mixing laws is established using the solutions of the single inclusion problem, which can be divided into the dilatation and the shear state.

Chapter 6 presents the so-called bounds method for estimating effective material parameters. The bounds method confines the actual value of the effective material parameter using lower and upper bounds. These bounds can be made successively tighter by taking into account more geometrical and physical information of the heterogeneous medium. The bounds on the real-valued material parameters will be derived using the classical variational principles as well as the *Hashin-Shtrikman* variational principles. Applying these variational principles to the linear conductive case, the bounds on the effective

thermal conductivity can be attained. This includes the *Wiener*, *Hashin-Shtrikman*, and *Beran* bounds (Section 6.2). Then the bounds on the complex-valued permittivity will be derived using *Bergman*'s representation theorem in Section 6.3. Section 6.4 deals with the bounds on the elastic moduli such as the *Reuss* and the *Voigt*, the *Hashin-Shtrikman*, the *Beran-Molyneux* and the *McCoy* bounds. Finally, attention is focused on the cross property relations between the effective material parameters of the same heterogeneous medium. These relations link different material parameters to each other. They can be relations between effective thermal and effective electric conductivities or between effective thermal conductivity and effective elastic moduli or between effective shear and effective bulk moduli (Section 6.5).

Chapter 7 presents the numerical computation of the effective material parameters of the digitized samples given in Subsection 2.4. In order to verify the accuracies of the various mixing laws given in Chapter 5, the predicted effective values will be compared to the effective values obtained numerically. The bounds method is also employed to justify the accuracies of these mixing laws. The cross property relationship will also be studied numerically in this chapter.

Chapter 8 gives the summary of this thesis and some proposals for improving and extending the present work.

Chapter 2

Stochastic foundations and characterization of random media

The stochastic nature of the microstructure of a heterogeneous medium causes fluctuations in its physical properties such as material parameters, internal electric fields, internal stresses or internal strains (*Axell & Helsing*, [8] *Beran* [20], *Bobeth & Diener* [33], *Widjajakusuma et al.* [187]), and in geometrical properties such as volume fractions, internal surfaces or microstructure connectivity (*Biswal et al.* [31], *Cheng & Torquato* [41]). In Section 2.1.1 some of the stochastic methods which effectively capture these random fluctuations in heterogeneous media are briefly described.

In most real situations, only the average (macroscopic) physical and geometrical quantities are known or are of interest. Thus, statistical methods are needed for characterizing the underlying fluctuations in the microstructure properties quantitatively and relating them to the macroscopic parameters. The macroscopic physical and geometrical quantities can be interpreted as the average values of the corresponding local quantities. As an example, consider the flow of fluid through a permeable rock. For most cases, it is not possible to know the detailed velocity distribution of the fluid within a single pore and the average velocity of the water within a single pore, more over it is not desirable. On the other hand, the variation of the average velocity of the fluid as it moves through the rock over distances which are large compared to the average diameter of a pore is known. This average velocity can be interpreted as the volume average of the velocity of the fluid at each point in the structure.

Two types of averages are considered in the theory of heterogeneous media: the ensemble average and the volume average. The ensemble average involves an addition of observed values from many independent realizations and a division of the sum of the observed values by the number of observations (samples), whereas the volume average involves an integration of the observed values over the entire or the partial region of the medium and dividing it by the volume of the region. The ensemble average is more general than the volume average. Consider a beam loaded by a single force in the middle and supported at the ends. The ensemble, in this case, could be a set of samples with small variations in the point where the force is applied. If the observer can control the variability precisely, the ensemble may even consist of only one realization. Here, the ensemble

averaging leads to the correct shear force with the jump from negative to positive, which is the exact solution. The volume averaging, on the other hand, leads to the vanishing shear force.

Although the ensemble average is more general than the volume average, it requires a large number of realizations (samples). Therefore, in practice, the volume average which requires only one sample is more widely used. However, the requirement that the heterogeneous sample must have a large (infinite) volume is hard to fulfill in most practical cases. Two assumptions are made to overcome this: (i) the sample is assumed statistically homogeneous, i. e., the volume of the given sample or any large enough subvolume of the given sample can be used for volume averaging, and (ii) ergodicity, i. e., the ensemble average is equivalent to the volume average. This leads to the concept of the representative volume element, which will be briefly discussed in the next chapter (*Nemat-Nasser* & *Hori* [135], *Krajcinovic* [102]).

In practice, a detailed description of the microgeometry of a random heterogeneous medium is not available and also impractical. Therefore, it is important to characterize a random heterogeneous medium without knowing the microgeometry in all its detail. Moreover, these characterization must be useful in estimating the effective material parameters. By applying the stochastic tools described in Section 2.1, a random heterogeneous medium can be characterized using some partial geometrical information. This can be volume fractions, specific internal surfaces, n-point correlation function or distribution functions of the constituents' volume fractions or of the constituents' connectivity properties. Section 2.2 will be devoted to discussing some of these characterization quantities.

These characterization methods will be applied to real heterogeneous samples. Through recent advances in digital image processing techniques such as X-ray imaging, scanning and transmission electron microscopy, nuclear magnetic resonance (*Wong* [142] and the references therein), high resolution microgeometrical information of heterogeneous samples can now be obtained. These valuable techniques are nondestructive, which means that the same samples can be reused in complementary studies either by any of the above techniques or by doing direct experimental measurements. In Section 2.3, the statistical methods discussed in Section 2.1 and the geometrical characterization methods discussed in Section 2.2 are reformulated to be compatible with these discrete media. Then, in Section 2.4, these methods will be applied to the digitized samples.

2.1 Elements of stochastic methods

2.1.1 Random process and probability density functions

Consider a collection of N samples of a fluid-saturated porous aluminium foam endowed with a Cartesian coordinate frame $\{\mathcal{O}, \mathbf{e}_i\}$ with the origin $\mathcal{O}$ at the same material point for each specimen. Considering the saturated foam as a biphasic material, the indicator function $\mathcal{I}^\alpha(\omega_i, \mathbf{x})$ can be used for describing the solid and the fluid phases φ^S and φ^F

(the saturated aluminium foam):

$$\mathcal{I}^{\alpha}(\omega_i, \mathbf{x}) = \begin{cases} 1 & : \quad \text{for} \quad \mathbf{x} \in \varphi^{\alpha}(\omega_i), \\ 0 & : \quad \text{for} \quad \mathbf{x} \notin \varphi^{\alpha}(\omega_i). \end{cases} \tag{2.1}$$

Therein, ω_i represents the i-th specimen, $\mathbf{x}$ is the position vector and $\varphi^{\alpha}(\omega_i)$ indicates the phase φ^{α} of the i-th specimen. The collection of such specimens is called an ensemble. ω_i is one of the realizations and the set ω of all possible realizations forms the sample space. The function $\mathcal{I}^{\alpha}(\omega, \mathbf{x})$ is called a (discrete) random field or a random process, which is a multidimensional function of the sample space ω and the position $\mathbf{x}$.

Consider a point P_1 at $\mathbf{x}_1$ of each porous medium of the ensemble. It is impossible to say exactly whether this point belongs to the fluid phase φ^F or to the solid phase φ^S. The probability of P_1 belonging to the phase φ^{α} is assigned by introducing one-point probability density functions

$$p^{\alpha}(\mathbf{x}_1) = p(\mathcal{I}^{\alpha}(\mathbf{x}_1) = 1) = \lim_{N^{\alpha} \to \infty} \frac{N^{\alpha}}{N} = \left\langle \mathcal{I}^{\alpha}(\mathbf{x}_1) \right\rangle = S_1^{\alpha}(\mathbf{x}_1), \tag{2.2}$$

where N^{α} denotes the number of specimens in which P_1 is located in the phase φ^{α}. The angular brackets in (2.2) denote the ensemble average taken over all possible realizations. The function $\mathcal{I}^{\alpha}(\mathbf{x}_1)$ is a representation of a random variable and, for simplicity, the variable ω has been dropped henceforth. $S_1^{\alpha}(\mathbf{x}_1)$ denotes the one-point correlation function, which is the averaging of the indicator function $\mathcal{I}^{\alpha}(\mathbf{x}_1)$. For $\mathcal{I}^{\alpha}(\mathbf{x}_1)$, its averaging is exactly the same as the probability $p(\mathcal{I}^{\alpha}(\mathbf{x}_1) = 1)$, therefore, the correlation function will be referred as the probability function of the phase φ^{α}.

The probability density function $p^{\alpha}(\mathbf{x}_1)$ provides very limited information. Additional information, such as whether two points of the specimen at distance r belong to the same phase, or the shapes of the phases, or the connectivity of the phases etc., can be obtained through higher point correlation functions. The two-point probability density function $p^{\alpha,\alpha}(\mathbf{x}_1, \mathbf{x}_2)$ gives the probability of finding two points in the phase φ^{α}. It is defined as

$$\begin{aligned} p^{\alpha,\alpha}(\mathbf{x}_1, \mathbf{x}_2) &= p(\mathcal{I}^{\alpha}(\mathbf{x}_1) = 1, \mathcal{I}^{\alpha}(\mathbf{x}_2) = 1) = \lim_{N \to \infty} \frac{N^{\alpha,\alpha}}{N} \\ &= \left\langle \mathcal{I}^{\alpha}(\mathbf{x}_1)\, \mathcal{I}^{\alpha}(\mathbf{x}_2) \right\rangle = S_2^{\alpha}(\mathbf{x}_1, \mathbf{x}_2), \end{aligned} \tag{2.3}$$

where $N^{\alpha,\alpha}$ is the number of specimens where both points fall simultaneously into the phase φ^{α}. Particular and analogous interpretations can be applied for $p^{F,F}(\mathbf{x}_1, \mathbf{x}_2)$, $p^{F,S}(\mathbf{x}_1, \mathbf{x}_2)$, $p^{S,F}(\mathbf{x}_1, \mathbf{x}_2)$ and $p^{S,S}(\mathbf{x}_1, \mathbf{x}_2)$. Consequently, the n-point probability density function for phase φ^{α} is defined as

$$p^{\alpha,\cdots,\alpha}(\mathbf{x}_1, \cdots, \mathbf{x}_n) = \left\langle \mathcal{I}^{\alpha}(\mathbf{x}_1) \ \cdots \mathcal{I}^{\alpha}(\mathbf{x}_n) \right\rangle = S_n^{\alpha}(\mathbf{x}_1, \cdots, \mathbf{x}_n). \tag{2.4}$$

In general, there are 2^n numbers of n-point probability density functions. These n-point correlation functions can be expressed as a set of correlation functions for a phase φ^{α} (*Torquato & Stell* [172]). Thus, one can simply consider the correlation functions for phase

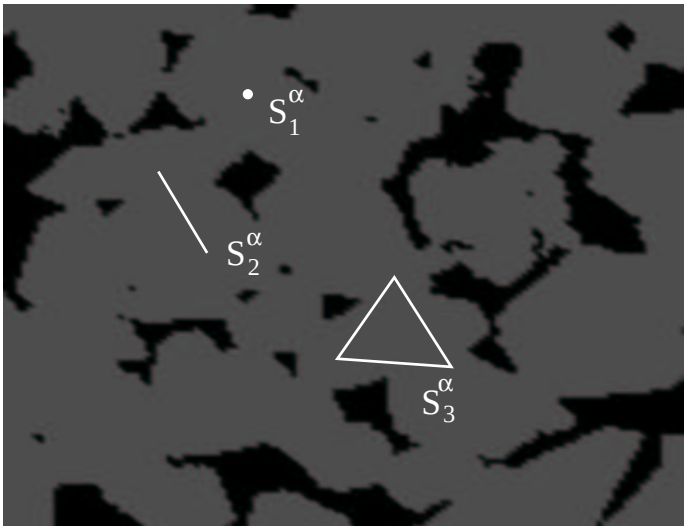

Figure 2.1: Lower-order correlation functions. Shown are the one-point correlation function S_1^α, two-point correlation function S_2^α and the three-point correlation function S_3^α for phase φ^α (grey region).

φ^α denoted by S_n. If the points $\mathbf{x}_1 \cdots \mathbf{x}_n$ become more and more dense, the microstructure information contained in the n-point probability density functions also increases. In the limit of $n \to \infty$, the probability functional $\lim_{n\to\infty} S_n(\mathbf{x}_1, \cdots, \mathbf{x}_n) = p(\mathbf{x})$ completely describes the whole random medium. Here, the probability density functions instead of the cumulative distribution functions are used to describe the random quantities. Hence, the probability density function of a random variable E will be used interchangeably with the terms *probability distribution of* E or *distribution of* E or just *probability of* E.

If the random variables $E(\mathbf{x}_1), \cdots, E(\mathbf{x}_n)$ are assumed to take any value on the real line, the joint probability density function $p\,(E(\mathbf{x}_1), \cdots, E(\mathbf{x}_n))\ \mathrm{d}E(\mathbf{x}_1) \cdots \mathrm{d}E(\mathbf{x}_n)$ gives the probability that $E(\mathbf{x}_1)$ lies between $E(\mathbf{x}_1) - 1/2\,\mathrm{d}E(\mathbf{x}_1)$ and $E(\mathbf{x}_1) + 1/2\,\mathrm{d}E(\mathbf{x}_1)$ and $E(\mathbf{x}_2)$ lies between $E(\mathbf{x}_2) - 1/2\,\mathrm{d}E(\mathbf{x}_2)$ and $E(\mathbf{x}_2) + 1/2/, \mathrm{d}E(\mathbf{x}_2)$ and so forth. Then, a *marginal probability density function* can be obtained from n-point probability density function by

$$p(E(\mathbf{x}_i)) = \overbrace{\int_{-\infty}^{\infty} \cdots \int_{-\infty}^{\infty}}^{(n-1)-\text{fold}} p(E(\mathbf{x}_1), E(\mathbf{x}_2), \cdots, E(\mathbf{x}_n)) \\ \mathrm{d}E(\mathbf{x}_1) \cdots \mathrm{d}E(\mathbf{x}_{i-1})\, \mathrm{d}E(\mathbf{x}_{i+1}) \cdots \mathrm{d}E(\mathbf{x}_n). \tag{2.5}$$

This relates the values of $E(\mathbf{x})$ at point $\mathbf{x}_i$ to the values at other points $\mathbf{x}_1, \cdots, \mathbf{x}_{i-1}, \mathbf{x}_{i+1}$ $\cdots, \mathbf{x}_n$. The expectation value or ensemble average of any function $\langle\, f(E(\mathbf{x}_1), \cdots, E(\mathbf{x}_n))\,\rangle$ is defined as

$$\langle\, f(E(\mathbf{x}_1), \cdots, E(\mathbf{x}_n))\,\rangle \;=\; \int_{-\infty}^{\infty} \cdots \int_{-\infty}^{\infty} f(E(\mathbf{x}_1), \cdots, E(\mathbf{x}_n)) \\ p(E(\mathbf{x}_1), \cdots, E(\mathbf{x}_n))\ \mathrm{d}E(\mathbf{x}_1) \cdots \mathrm{d}E(\mathbf{x}_n). \tag{2.6}$$

A more thorough and rigorous treatment of stochastic methods can be found elsewhere (*Beran* [17], *Papoulis* [140]).

2.1.2 Statistical homogeneity and ergodicity

As discussed above, the random variable is assumed to be stationary or homogeneous, i. e., its probability density function $p(E(\mathbf{x}_1), E(\mathbf{x}_2), \cdots, E(\mathbf{x}_n))$ is invariant under any translation $\mathbf{q} \in V^3$

$$p(E(\mathbf{x}_1), E(\mathbf{x}_2), \cdots, E(\mathbf{x}_n)) = p(E(\mathbf{x}_1 + \mathbf{q}), E(\mathbf{x}_2 + \mathbf{q}), \cdots, E(\mathbf{x}_n + \mathbf{q})). \tag{2.7}$$

The property of statistical homogeneity implies that the probability density function $p(E(\mathbf{x}_1), E(\mathbf{x}_2), \cdots, E(\mathbf{x}_n))$ does not depend on the chosen origin but depends solely on $(n-1)$ position vectors, i. e., $p(E(\mathbf{0}), E(\mathbf{x}_2 - \mathbf{x}_1), \cdots, E(\mathbf{x}_n - \mathbf{x}_1))$. Note that the term *homogeneous* refers to the probability density functions and not to the sample itself. Particularly, the expectation value of the random variable $\langle\, E(\mathbf{x}) \,\rangle$ does not depend on the position at all

$$\langle\, E(\mathbf{x}) \,\rangle = \int_{-\infty}^{\infty} E\, p(E)\, \mathrm{d}E = \langle\, E \,\rangle\,. \tag{2.8}$$

The definition of statistical stationarity or homogeneity introduced above is termed as *strict-sense stationary*. This definition of statistical homogeneity can be weakened by requiring that only one-point and two-point probability density functions are invariant under the translation $\mathbf{q}$. This less restrictive definition is called *wide-sense stationary*. (*Auñón & Chandrasekar* [7]).

Due to statistical homogeneity, the statistical properties of the whole space are similar. Thus, one can substitute the ensemble averages (2.6) by the volume averages of any single sample, i. e., each single realization completely represents the whole ensemble. This property is known as *ergodicity*. In this case, one has

$$\langle\, f(E(\mathbf{x}_1), \cdots, E(\mathbf{x}_n)) \,\rangle = \overline{f(E(\mathbf{x}_1), \cdots, E(\mathbf{x}_n))} \tag{2.9}$$

with

$$\overline{f(E(\mathbf{x}_1), \cdots, E(\mathbf{x}_n))} = \lim_{V \to \infty} \frac{1}{V} \int_{\mathcal{B}} f(E(\mathbf{x}_1 + \mathbf{q}), \cdots, E(\mathbf{x}_n + \mathbf{q}))\, \mathrm{d}v, \tag{2.10}$$

where the integral is evaluated with respect to the variable $\mathbf{q}$. The integral is taken over the body $\mathcal{B}$ of the heterogeneous medium, and V represents its volume. Consequently, under the assumption of ergodicity, the average of the random variable $E(\mathbf{x})$ can be expressed as

$$\overline{E} = \int_{-\infty}^{\infty} E(\mathbf{x})\, p(E(\mathbf{x}))\, \mathrm{d}E(\mathbf{x}) = \lim_{V \to \infty} \frac{1}{V} \int_{\mathcal{B}} E(\mathbf{x})\, \mathrm{d}v. \tag{2.11}$$

From (2.11), it is seen that ergodicity, on the one hand, requires the ensemble to be independent of the spatial position and, on the other hand, the volume average to be independent of the realization, i. e., an ergodic ensemble must be stationary, but a stationary ensemble needs not to be ergodic.

The basic underlying assumption of statistical homogeneity is never exactly satisfied in actual problems. To be exactly homogeneous, an infinite volume is needed. Therefore, it is important to ensure that homogeneity can be assumed approximately in space intervals. These intervals are much larger than the characteristic lengths of the microscopic inhomogeneity. The assumption of statistical homogeneity in the theory of heterogeneous media plays the same role as the assumption of homogeneity in the theory of the continuum physics.

2.2 Geometrical properties of heterogeneous media

The overall physical properties of heterogenous media depend strongly on their microstructures. Unfortunately, in most physical situations, only partial information of the microstructure is known. Therefore, it is necessary to develop some geometrical quantities which, based on this partial information, can be used as input parameters for predicting the effective physical properties. These geometrical quantities can take different forms, such as simple numbers like volume fractions or specific internal surfaces, or functions, such as correlation functions or fluctuations of the volume fractions. They should be measurable and independent of the experimental method. Furthermore, it is desirable to develop geometrical quantities which are sensitive enough to the topological and geometrical properties and which can be used to distinguish one heterogeneous medium from another. For example, the porosities or the two-point correlation functions from two different media can be nearly identical, even though their microstructures may be very different.

2.2.1 Correlation functions, porosity and specific internal surfaces

The porosity or the one-point correlation function has significant influence on the effective transport properties of a porous material. It is defined as the ratio of the volume of the pore space V^F to the total sample volume V:

$$\overline{n}^F = \overline{\mathcal{I}^F(\mathbf{x}_1)} = V^F/V. \tag{2.12}$$

Note that in this work it has to be differentiated between the local volume fraction n^F (of a subregion) and the total volume fraction $\overline{n}^F$ (of the whole medium). In addition to the porosity, a second type of one-point correlation functions known as the one-point surface correlation function $\overline{\mathcal{M}(\mathbf{x})}$, also plays a prominent role in various transport phenomena of porous media. Examples can be found in porous catalysts (*Dullien* [53], *Sahimi* [153, 154]) or in fluid transport and fluid trapping in porous media (*Scheidegger* [155], *Torquato* [170]). Here, the interface indicator function $\mathcal{M}(\mathbf{x}) = |\operatorname{grad}\mathcal{I}^F(\mathbf{x})|$ is a generalized function, which is non zero when $\mathbf{x}$ is located on the interface ∂F and zero elsewhere:

$$\mathcal{M}(\mathbf{x}) = \begin{cases} 1 & : \quad \text{for} \quad \mathbf{x} \in \partial\varphi^F, \\ 0 & : \quad \text{for} \quad \mathbf{x} \notin \partial\varphi^F. \end{cases} \tag{2.13}$$

The function $\overline{s}$ defined as the ratio of the internal surface area $A^{\partial\varphi^F}$ and the total sample volume V can be used to define the specific internal surface area s:

$$\overline{s} = \overline{\mathcal{M}(\mathbf{x})} = A^{\partial\varphi^F}/V\,[\mathrm{m}^{-1}]. \tag{2.14}$$

The porosity and the specific internal surface, are insufficient for a complete statistical characterization of a porous medium, since they do not provide any information about how the components of the porous medium vary from point to point. As discussed in the previous section, a full characterization of a porous medium requires the complete n-point correlation functions (*Torquato* [170], *Torquato* & *Stell* [172, 173]). In practice, however, mostly the two-point correlation function and rarely three-point correlation functions are used. Correlations beyond five-point correlation functions are never really computed, except in some special cases, where they can be determined analytically (*Markov* [116, 117], *Quintanilla* [147]).

For any statistically homogeneous and isotropic porous medium, the two-point correlation function $S_2(\mathbf{x}_1, \mathbf{x}_2)$ depends only on the distance $|\mathbf{x}_2 - \mathbf{x}_1| = r$, i. e., $S_2(\mathbf{x}_1, \mathbf{x}_2) = S_2(r)$. In this case, the slope of the two-point correlation function at the origin $|\mathbf{x}_2 - \mathbf{x}_1| = r = 0$ can be linked to the specific internal surface $\overline{s}$ (*Debye et al.* [51], *Berryman* [27]):

$$\left.\frac{\partial S_2(r)}{\partial r}\right|_{r=0} = \begin{cases} -\frac{\overline{s}}{2} & : \text{ one-dimensional space,} \\ -\frac{\overline{s}}{\pi} & : \text{ two-dimensional space,} \\ -\frac{\overline{s}}{4} & : \text{ three-dimensional space.} \end{cases} \tag{2.15}$$

The porosity and its square are related to the two-point correlation function via

$$\lim_{r\to 0} S_2(r) = \overline{n}^F, \qquad \lim_{r\to\infty} S_2(r) = (\overline{n}^F)^2. \tag{2.16}$$

Sometimes, it is convenient to work with the normalized two-point correlation function $\overline{S}(r)$,

$$\overline{S}_2(r) = \frac{\overline{\mathcal{I}^F(0)\,\mathcal{I}^F(r)} - \left(\overline{n}^F\right)^2}{\overline{n}^F(1-\overline{n}^F)}. \tag{2.17}$$

Obviously, $\overline{S}_2(0) = 1$ when $r = 0$ and decays to zero as $|r| \to \infty$, i. e., $\overline{S}(\infty) = 0$.

The distance r at which $\overline{S}_2(r)$ becomes *effectively zero* will be denoted as *characteristic correlation length* L_c. There are several possibilities to obtain L_c. The common way is to use the value of r at which $\overline{S}_2(r)$ is equal to $\exp(-1)$ or to use the value of r at which $|\overline{S}_2(r)| \leq \delta$ for a small δ. At this length scale, one can assume that the different parts of the microstructure cannot interact with each other. This assumption plays an important role in the effective medium theory (Chapter 5). Therefore, the correlation length may be used as a measure of the inhomogeneity scale of the random medium. For anisotropic mixtures, the correlation length can be different for different space directions. The relationship between the specific internal surface and the two-point correlation length can also be obtained in the anisotropic case (*Berryman* [23]).

2.2.2 Probability density functions of local geometric observables

This section deals with the fluctuations of microgeometrical quantities such as porosity, specific internal surface or connectivity of heterogeneous media. These fluctuations have been studied by different authors who deal with different problems such as fracture of composite materials (*Botsis* & *Beldica* [35]), scattering by heterogeneous media (*Debye et al.* [51], *Sheng* [162]), characterization of porous media (*Biswal et al.* [31, 32]) and transport in porous media (*Boger et al.* [34], *Hilfer* [88, 89], *Sahimi* [154], *Widjajakusuma et al.* [185, 186]). Even in periodic heterogeneous random media, there exist local volume fraction fluctuations (*Quintanilla* & *Torquato* [148]). The fluctuation described by the standard deviation of the corresponding geometrical quantities is only a number that does not provide much useful structural information about the heterogeneous medium. The fluctuations are better captured by corresponding probability density functions. In order to obtain these, the porous sample can be subdivided into m non-overlapping windows $\mathbb{K}^1, \cdots, \mathbb{K}^m$. For simplicity, the windows are chosen to be cubical of side lengths L. Thus, one can denote the window as $\mathbb{K}^i(\mathbf{x}_i, L)$, where $\mathbf{x}_i$ is the position vector of the center of the window $\mathbb{K}^i(\mathbf{x}_i, L)$. Measured geometrical quantities from these windows can then be collected into various histograms. From these, the probability density function of the corresponding geometrical properties can be obtained. These probability density functions depend on the size and shape of the chosen windows. This kind of microstructure geometry characterization was proposed in the local porosity theory by *Hilfer* [88, 89] and in term of coarseness by *Lu* & *Torquato* [113].

Local porosity distribution function

The local porosity within the region $\mathbb{K}^i(\mathbf{x}_i, L)$ is defined as

$$n^F(\mathbf{x}_i, L) = \frac{V(\varphi^F \cap \mathbb{K}^i(\mathbf{x}_i, L))}{V(\mathbb{K}^i(\mathbf{x}_i, L))}, \tag{2.18}$$

where $\mathcal{B}^F$ represents the region of the phase φ^F. The local porosity distribution function $p(n^F, L)$ is given by

$$p(n^F, L) = \frac{1}{m} \sum_{i=1}^{m} \delta(n^F - n^F(\mathbf{x}_i, L)), \tag{2.19}$$

where $\delta(n^F - n^F(\mathbf{x}, L))$ is the *Dirac* delta function. The function $p(n^F, L)$ gives the probability to find a local porosity n^F in the range of $n^F - 1/2\,\mathrm{d}n^F$ to $n^F + 1/2\,\mathrm{d}n^F$. Clearly, the local porosity and its distribution function rely on how the sample is divided. For $L = \infty$, the observed window is equal to the whole porous medium and the local porosity distribution function reduces to

$$p(n^F, L = \infty) = \delta(n^F - \overline{n}^F). \tag{2.20}$$

For $L = 0$, the observed window is equal to a point of the porous medium and the local porosity distribution function can be expressed in terms of the total porosity $\overline{n}^F$:

$$p(n^F, L = 0) = \overline{n}^F\, \delta(n^F - 1) + (1 - \overline{n}^F)\, \delta(n^F). \tag{2.21}$$

The expectation value of the local porosity is equal to

$$\overline{n}^F(L) = \int_0^1 n^F \, p(n^F, L) \, \mathrm{d}n^F. \tag{2.22}$$

Local specific internal surface distribution function

Similarly to (2.18) and (2.19), the local specific internal surface s within the region $\mathbb{K}^i(\mathbf{x}_i, L)$ and the local specific internal surface distribution function $p(s, L)$ are defined as

$$s(\mathbf{x}_i, L) = \frac{A(\partial\varphi^F \cap \mathbb{K}^i(\mathbf{x}_i, L))}{V(\mathbb{K}^i(\mathbf{x}_i, L))} \tag{2.23}$$

and

$$p(s, L) = \frac{1}{m} \sum_{i=1}^{m} \delta(s - s(\mathbf{x}_i, L)), \tag{2.24}$$

respectively. Moreover, one can define a joint probability density $p(n^F, s, L)$ of finding a local porosity n^F and a local specific internal surface s in the range of $[n^F - 1/2\,\mathrm{d}n^F, n^F + 1/2\,\mathrm{d}n^F]$ and $[s - 1/2\,\mathrm{d}s, s + 1/2\,\mathrm{d}s]$ as

$$p(n^F, s, L) = \frac{1}{m} \sum_{i=1}^{m} \delta(n^F - n^F(\mathbf{x}_i, L)) \, \delta(s - s(\mathbf{x}_i, L)). \tag{2.25}$$

Local percolation distribution function

The phase connectivity of a heterogeneous medium plays a decisive role in transport phenomena of the heterogeneous medium. For example, the values of conductivity and permeability of a porous medium depend significantly on how good or how bad is the interconnectivity between the pores. The strength of the porous material is determined by the connection of its matrix phase. These connectivity properties of a heterogeneous medium can be captured through the percolation theory.

Originally, *Flory* [66] and *Stockmayer* [166] introduced percolation processes in dealing with the problems of polymerization and gelation. Many years later, *Broadbent* & *Hammersley* [36] reintroduced the percolation concept in the context of the spreading of fluid particles through a porous medium. The terms of percolation can be seen as the flow of fluid through heterogeneous media; similar to the flow of coffee in a percolator. The connectivity varies randomly within the medium meaning that through some subregions (windows) the fluid can flow easier than through others; however, at some subregions it cannot flow at all. The term fluid-flow can be interpreted in a general sense meaning that it could be a flow of liquid, a flow of electric current, a spread of disease, a passing of information, and so on. Similarly, the heterogeneous medium can be interpreted as an alloy, population in a city, computer network and so on. A comprehensive treatment and the application of the percolation theory in various disciplines of sciences and engineering can be found in, e. g., *Stauffer* & *Aharony* [165] and *Sahimi* [153].

Consider a percolation parameter $p_{\mathcal{L}}$ which gives the average degree of connectivity between various subregions of a random medium. When $p_{\mathcal{L}} = 0$, all subregions are totally isolated from every other subregion. When $p_{\mathcal{L}} = 1$, all subregions are connected to neighbouring subregions. When the random medium is connected from one side to the other through paths which span completely across the system, a so-called spanning cluster exists. The term percolation threshold $p_{\mathcal{L}c}$ can be defined in the following way. Starting from $p_{\mathcal{L}} = 0$ if one creates connections among the subregions, at $p_{\mathcal{L}} = p_{\mathcal{L}c}$, a spanning cluster exists for the first time. When $p_{\mathcal{L}} \geq p_{\mathcal{L}c}$, there always exists a spanning cluster, although some isolated clusters can still be present. Applying the concept of percolation to the flow problems of (heterogeneous) porous media means that, whenever the porosity of a porous medium is above this critical value, fluid particles can always flow from one side of the random medium to its opposite side and, whenever porosity is below this value, the fluid particles can not flow from one side to the opposite side.

Similar to the definitions of the local porosity and of the local specific internal surface, the indicator function for the connectivity of the pore space within a subregion $\mathbb{K}^i(\mathbf{x}_i, L)$ can be defined. This connectivity indicator function $\mathcal{L}(\mathbf{x}_i, L)$ takes the value 1 if fluid can flow from one side to the opposite side and takes the value 0 otherwise:

$$\mathcal{L}(\mathbf{x}_i, L) = \begin{cases} 1 & : \text{ if } \mathbb{K}^i(\mathbf{x}_i, L) \text{ allows isotropic percolation,} \\ 0 & : \text{ otherwise.} \end{cases} \tag{2.26}$$

The local percolation probability $p_{\mathcal{L}}(n^F, L)$ is the probability of finding a percolating geometry in all three directions in the observed window $\mathbb{K}^i$ of length L in which the local porosity and the local specific internal surface area are n^F and s, respectively.

$$p_{\mathcal{L}}(n^F, s, L) = \sum_{i=1}^{m} \frac{\mathcal{L}(\mathbf{x}_i, L)\, \delta(n^F - n^F(\mathbf{x}_i, L))\, \delta(s - s(\mathbf{x}_i, L))}{\delta(n^F - n^F(\mathbf{x}_i, L))\, \delta(s - s(\mathbf{x}_i, L))}. \tag{2.27}$$

Total fraction of percolating regions

The local percolation probability $p_{\mathcal{L}}(n^F, s, L)$ gives the local connectivity property (connectivity property of windows $\mathbb{K}^i$). To obtain the global overall connectivity, one has to take the average of the local percolation probability over all windows:

$$p(L) = \int_0^\infty \int_0^1 p(n^F, s, L)\, p_{\mathcal{L}}(n^F, s, L)\, \mathrm{d}n^F\, \mathrm{d}s. \tag{2.28}$$

The function $p(L)$ gives the total fraction of percolating cells. If the value of $p(L)$ of a given porous sample is above (under) some critical value p_c, then fluid can (not) flow through this porous sample. Obviously, $\lim_{L\to\infty} p(L) = 0$ if the pore space of a given porous sample is disconnected and $\lim_{L\to\infty} p(L) = 1$ if its pore space is connected.

2.3 Digital images and their geometrical characterization

In practice, microgeometric information of a heterogeneous medium is stored in discrete digital image form. Therefore, the characterization methods for continuum heterogeneous media, which are introduced in the previous sections, must be appropriately modified for this purpose.

To obtain a digital image that can be used for a computational purpose, a digital image has to pass through following steps: Through image formation, the sample is irradiated with energy, e. g. x-rays, and it absorbs an amount of energy, which can be converted into an electric energy and can be measured by a sensor. The sensor, which can be considered to be moving at particular locations in the image, measures a certain amount of energy at these particular locations. This can be seen as subdividing the sample into picture elements and laying the measure point in the middle of the picture element. This process is known as sampling, and the picture element and its size are called pixel and spatial resolution, respectively. The second step is to assign (quantize) the continuous measurement values of the sensor into integer numbers. In general, the integer numbers range from 0 (black) to 255 (white) corresponding to a grey-level scale. For a biphasic material composed of φ^S and φ^F only two integer numbers 0 and 1 are needed, which can be assigned to φ^S and φ^F, respectively. The third step is to store the location of each pixel and the corresponding grey-scale value, on the output data storage device as an array. Hence, the digital image is just an array of positive integers. A detailed description of digital image processing can be found in, e. g., *Castleman* [40].

Certainly, the quality of the digital image approximation is determined by its resolution, the higher the resolution is, the better the real image approximation produced by digital imaging will be. This can be clearly seen in Figure 2.2. By decreasing the resolution size, the surface value of the digitized circle approximates better the surface value of the actual circle; by simply counting the pixels, one can show that the approximation error decreases from 27.32 % (at the resolution size r) to 0.53 % (at the resolution size $r/8$). However, the approximation of the circle circumference by the digitized circle remains the same, i. e., $8r$, independent of the resolution size. This discrepancy has to be always taken into account when dealing with internal surfaces of digitized heterogeneous samples. Similar to the two-dimensional case, in the three-dimensional case, when a sphere is approximated by a digitized image of cubic voxels, the sphere and its volume can be well approximated at high resolutions, but the sphere's surface is approximated by $6\pi r^2$ at any resolution size.

Now, the statistical methods and the characterization methods presented in the previous section are reformulated to be applied to the digital image. Let us consider the three-dimensional digitized biphasic sample (composed of phases φ^S and φ^F) with the dimension $M_1 \times M_2 \times M_3$ and the resolution size a. The indicator function $\mathcal{I}^F(\mathbf{x}_i)$ indicating

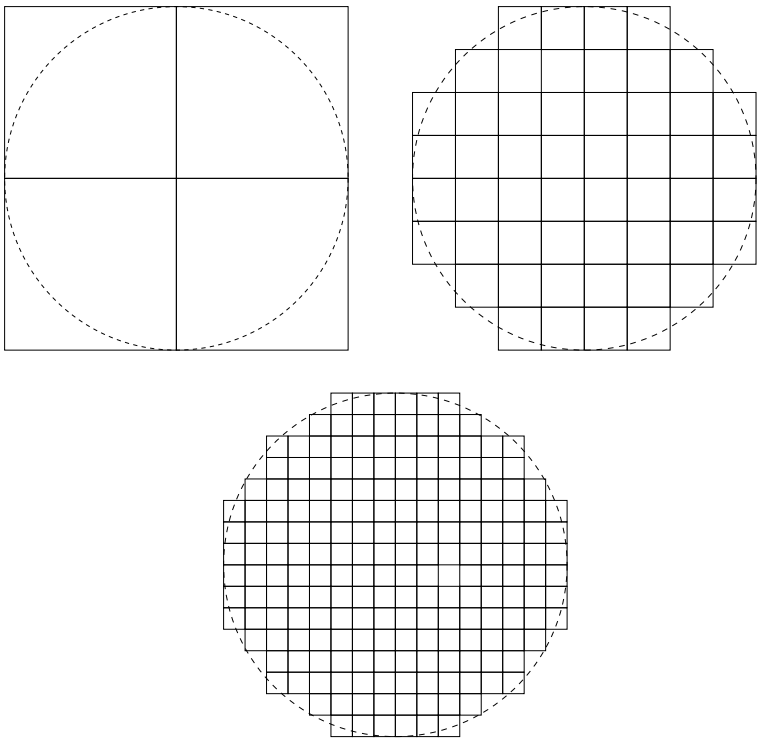

Figure 2.2: Digital images of a circle of radius r at different resolution sizes. Top left showing the digitalization circle at the resolution size r, top right showing it at $r/4$, and below showing it at $r/8$.

the phase φ^F can be written as

$$\mathcal{I}^F(\mathbf{x}_i) = \begin{cases} 1 & : \quad \text{for } \varphi^F - \text{voxel}, \\ 0 & : \quad \text{for } \varphi^S - \text{voxel}, \end{cases} \tag{2.29}$$

where $\mathbf{x}_i$ is the location of the ith voxel. Then the total porosity (the volume fraction of the pore space) of the digital image can be obtained by simply counting the φ^F-voxels and dividing with the total number of voxels $M = M_1\, M_2\, M_3$:

$$\overline{n}^F = \frac{1}{M} \sum_{i=1}^{M} \mathcal{I}^F(\mathbf{x}_i). \tag{2.30}$$

The standard deviation of the volume fraction can be written as

$$\operatorname{dev} \overline{n}^F = \Big[\frac{1}{M} \sum_{i=1}^{M} (\mathcal{I}^F(\mathbf{x}_i) - \overline{n}^F)^2 \Big]^{1/2}. \tag{2.31}$$

The standard deviation $\operatorname{dev} n^F$, which describes the fluctuation of geometrical quantities, may be used to examine the fluctuation of computed $\overline{n}^F$ in several cross sections or several sections of the same heterogeneous sample in predicting the porosity $\overline{n}^F$ of the

whole sample from its cross section. In the same manner, the specific internal surface can be obtained by counting the interface elements between φ^F- and φ^S-voxels:

$$\overline{s} = \frac{1}{M} \sum_{j=1}^{M} \mathcal{M}(\mathbf{x}_j). \tag{2.32}$$

Therein, the interface indicator function $\mathcal{M}(\mathbf{x}_j)$ is defined via

$$\mathcal{M}(\mathbf{x}_j) = \begin{cases} 1 & : \text{ for interface between } \varphi^F\text{- and } \varphi^S\text{-voxels,} \\ 0 & : \text{ otherwise,} \end{cases} \tag{2.33}$$

where $\mathbf{x}_j$ is the position of the interface of φ^F- and φ^S-voxels. Since digital images have a finite size $M_1 \times M_2 \times M_3$, the actual evaluation of the two-point correlation function for the phase φ^F is given by

$$S_2(\mathbf{y}) = \frac{1}{N} \sum_{i=1}^{N} \mathcal{I}^F(\mathbf{x}_i)\, \mathcal{I}^F(\mathbf{x}_i + \mathbf{y}), \tag{2.34}$$

where $\mathbf{y}$ is the distance between the points $\mathbf{x}_i$ and $\mathbf{x}_i + \mathbf{y}$, $N = (M_1 - y_1) \times (M_2 - y_2) \times (M_3 - y_3)$, and y_1, y_2 and y_3 are the components of the vector $\mathbf{y} = y_1\mathbf{e}_1 + y_2\mathbf{e}_2 + y_3\mathbf{e}_3$. $S_2(\mathbf{y})$ can be normalized as

$$\overline{S}_2(\mathbf{y}) = \frac{S_2(\mathbf{y}) - (\overline{n}^F)^2}{\overline{n}^F(1 - \overline{n}^F)}. \tag{2.35}$$

For a statistically homogeneous medium, it is useful to convert $\overline{S}_2(\mathbf{y})$ according to (2.35) to the form $\overline{S}_2(r)$ (for details, see *Berryman* [23]). The three-point correlation function for the phase φ^F can be given as

$$S_3 = \frac{1}{K} \sum_{i=1}^{K} \mathcal{I}^F(\mathbf{x})\, \mathcal{I}^F(\mathbf{x} + \mathbf{y})\, \mathcal{I}^F(\mathbf{x} + \mathbf{z}). \tag{2.36}$$

where $K = [M_1 - \max(y_1, z_1)]\,[M_2 - \max(y_2, z_2)]\,[M_3 - \max(y_3, z_3)]$, y_i and z_i are the vector components of the distance vectors $\mathbf{y}$ and $\mathbf{z}$, respectively. These vector components satisfy following relationships $0 \leq y_1, z_1 \leq (M_1 - 1)$, $0 \leq y_2, z_2 \leq (M_2 - 1)$ and $0 \leq y_3, z_3 \leq (M_3 - 1)$. One can measure the correlation functions from a two-dimensional cross section of the sample. After converting the two-point correlation function $S_2(\mathbf{y})$ of the cross section into its polar form $S_2(r)$, the corresponding porosity and the specific internal surface can also be calculated according to (2.15).

Similarly, the local geometrical characterization quantities within an observed cubical region $\mathbb{K}^i(\mathbf{x}_i, L)$ with side length L (in the units of pixel) and centered at $\mathbf{x}_i$ can be computed. The local porosity of an observed window can be found by counting the φ^F-voxels within it. Thus,

$$n^F(L) = \frac{1}{J} \sum_{i=1}^{J} \mathcal{I}^F(\mathbf{x}_i), \tag{2.37}$$

where $J = L^3$. The local porosity distribution $p(n^F, L)$ is given by

$$p(n^F, L) = \frac{1}{m} \sum_{i=1}^{m} \delta(n^F - n^F(\mathbf{x}_i, L)), \tag{2.38}$$

where m is the number of placements of the observed window $\mathbb{K}^i(\mathbf{x}_i, L)$ and the function $\delta(n^F - n^F(\mathbf{x}, L))$ is the Dirac delta function. Thereby, $\mathbb{K}^i(\mathbf{x}_i, L)$ is placed on all lattice sites $\mathbf{x}_j$ which are at least in a distance $L/2$ from the boundary sample, hence, $m = \prod_{i=1}^{3}(M_i - L+1)$. The reason to use the overlapping windows instead of the non-overlapping windows (which are theoretically required) is to ensure better statistics.

The connectivity property of the observed windows can be examined using the *Hoshen-Kopelman* algorithm, which is discussed in the next subsection. With the aid of the indicator function for the connectivity of a region,

$$\mathcal{L}(\mathbf{x}_i, L) = \begin{cases} 1 & : \text{ if } \mathbb{K}^i(\mathbf{x}_i, L) \text{ percolating in all 3 direction,} \\ 0 & : \text{ otherwise,} \end{cases} \tag{2.39}$$

the *local percolation probability* $p_{\mathcal{L}}(n^F, L)$ can be computed via

$$p_{\mathcal{L}}(n^F, L) = \frac{\sum_{i=1}^{m} \mathcal{L}(\mathbf{x}_i, L)\delta(n^F - n^F(\mathbf{x}_i, L))}{\sum_{i=1}^{m} \delta(n^F - n^F(\mathbf{x}_i, L))}. \tag{2.40}$$

The total fraction of percolating regions of size L is given by integration over all local porosities:

$$p(L) = \int_0^1 p(n^F, L) p_{\mathcal{L}}(n^F, L)\, \mathrm{d}n^F. \tag{2.41}$$

It is important to note that, although the porosity or the two-point correlation function of a three-dimensional sample can be estimated from its two-dimensional cross sections, the percolation property of a three-dimensional sample cannot be similarly mapped from its two-dimensional cross-section (*Stauffer & Aharony* [165]). The percolation threshold is higher for a two-dimensional cross-section. Moreover, real sandstone is corresponding to the correlated disordered medium and usually has a lower percolation threshold than the uncorrelated disordered medium.

2.3.1 *Hoshen-Kopelman* algorithm

The connectivity property in digitized heterogeneous media can be investigated using *Hoshen-Kopelman* algorithm (HKA). Consider a two-dimensional lattice with dimension of 7×7 pixels (squares), in which the grey (1) and white (0) pixels represent the phases φ^F and φ^S, respectively, as shown in Figure 2.3. Two pixels are called as neighbouring pixels if and only if they have a common side length, thus a two-dimensional pixel has 4 (north, east, west and south) neighbours. The neighbouring pixels are defined as connected if they have the same colour; a cluster is defined as a group of connected neighbour pixels. Note that by this definition, two pixels belonging to the same class and touching at one corner are disconnected. For example, the pixel which occupies the first row (from the

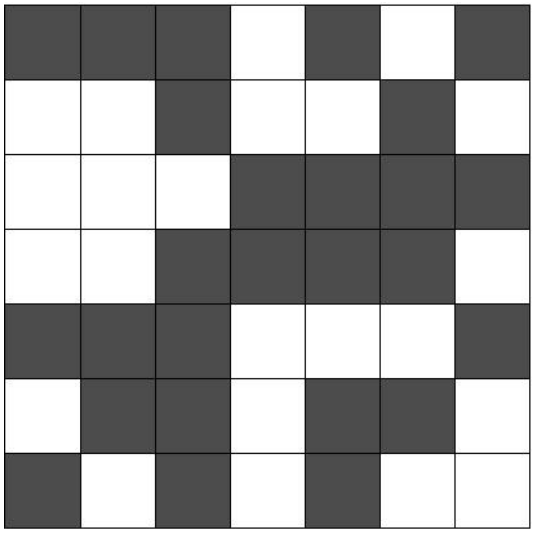

Figure 2.3: Illustration for the *Hoshen-Kopelman* algorithm.

top) and the fifth column (from the left) and the pixel which occupies the second row and the sixth column are not connected according to this definition (see Figure 2.3). Therefore, a membership of a pixel in a cluster depends on the used neighborhood rule. However, the results of this connectivity definition are in good agreement with their continuum counterparts, if the resolution of the digital images are high enough (*Garboczi et al.* [70, 71]).

The HKA requires two arrays, one for labels $L(i,j)$ assigned to the cluster number and another one assigned to the indices of labels $N(i)$, which will be used to reduce the redundant labels. One can start from the top left corner, go from left to the right in each line and go down from the top line to the bottom line. To determine the clusters for the grey pixels, the labels and the indices of the labels are assigned as follows: all of the white pixels are always set to zero, the grey pixel is assigned to a new integer $L(i,j)$ and the index of the label is assigned to $N(L(i,j)) = L(i,j)$, if it does not have both western and northern grey neighbours, else it is assigned to the number of its neighbours label. Through this assigning rule, the first both lines look like:

$$\begin{array}{cccccccc} 1 & 1 & 1 & 0 & 2 & 0 & 3 & N(1)=1 \quad N(2)=2 \quad N(3)=3 \\ 0 & 0 & 1 & 0 & 0 & 4 & 0 & N(4)=4 \end{array}$$

In the third line, there is a problem to assign the grey pixel which is at sixth from the left, because this grey pixel has western and northern grey neighbours, which have two different labels. In this case, the smaller number of these two labels, i. e., 4, is chosen for this pixel and simultaneously the index of the larger label is set to the value of smaller label, i. e., $N(5) = 4$. This implies that label 5 is redundant label, which can be seen easily from Figure 2.3. The index of the label will solve this redundant problem, because of going back to renumber all labels 5 into 4 would be inefficient for a lattice with large dimension. Now, the third line reads

0 0 0 5 5 4 4 N(5) = 4

Analogically, the reminder of the following lines can be written as

0	0	6	5	5	4	0	$N(6) = 5$
7	7	6	0	0	0	8	$N(7) = 6$ $\quad N(8) = 8$
0	7	6	0	9	9	0	$N(9) = 9$
10	0	6	0	9	0	0	$N(10) = 10$

The final labels and their indices can be given as

Label L	1	2	3	4	5	6	7	8	9	10
Index of Label $N(L)$	1	2	3	4	4	5	6	8	9	10

The last step is to check whether a label is redundant or not, because a redundant label should be renumbered and reassigned to its *home* cluster. It can be done as follows:

- Check if $N(L) = L$, if yes, check the next label.
- Else set $L = N(L) = L'$, and check if the new label $N(L') = L'$, if yes, check the next label.
- Otherwise repeat the above step until the label is equal to its index.

After renumbering, each cluster will have a unique label; the clusters for the above problem can be renumbered and classified into 7 clusters (cf. Figure 2.4).

1	1	1	0	2	0	3
0	0	1	0	0	4	0
0	0	0	4	4	4	4
0	0	4	4	4	4	0
4	4	4	0	0	0	8
0	4	4	0	9	9	0
10	0	4	0	9	0	0

Figure 2.4: The label of the clusters after renumbering.

A spanning cluster exists if the same label occurs on two different opposite edges; in this case it is the cluster with label 4. The HKA given here can be extended to the

three-dimensional case. A comprehensive review and an efficient computer program for the two-dimensional case can be found in the appendix of the monograph by *Stauffer & Aharony* [165].

2.4 Digitized samples

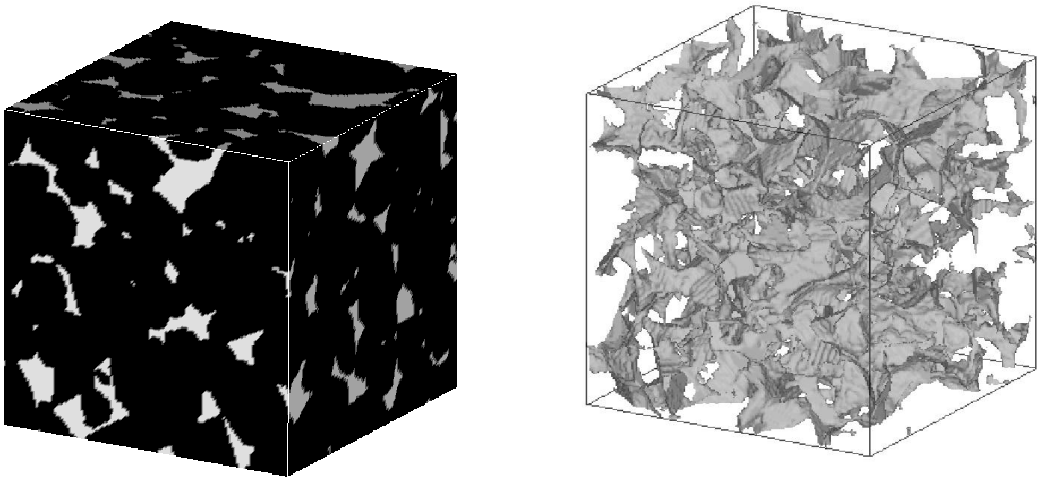

Figure 2.5: Left: Three-dimensional perspective of surface cuts of a $128 \times 128 \times 128$ voxel of a *Fontainebleau* sandstone D1 obtained via microtomography (each voxel has dimension $7.5 \times 7.5 \times 7.5 \mu\,\mathrm{m}^3$). The pore space is grey and the solid phase is black. Right: The pore space of the same sample. The pore space is grey and opaque and the solid phase is transparent.

In this section, the methods discussed in the previous section are applied to analyzing real digitized heterogeneous media. The obtained characterization quantities will be used later in connection with estimating the effective material parameters. The sample presented here uses data of eight natural sandstones produced by computer assisted tomography [Source: R. Hilfer [32, 31]]. The first and second samples are weakly consolidated sandstones (*Sst6d* and *Sst20d*) and are abbreviated as samples A and B, respectively. The third sample is a digitized microstructure of *Berea* sandstone and is denoted as sample C. The forth, fifth and sixth samples are digitized *Fontainebleau* sandstone (D1, D2 and D3, respectively). Indeed, all of these *Fontainebleau* samples are obtained by slicing from the larger *Fontainebleau* sandstone with dimension $300 \times 300 \times 299$ (in units of pixel). From Table 2.1, it is obvious that the porosity fluctuates in this larger *Fontainebleau* sample.

The last two samples (R1 and R2) are obtained by the *Gauss*ian field reconstruction method (*Adler* [2] and the references therein). Both samples are numerically reconstructed [Source: B. Biswal [32, 30]] from the same given real sample C, but with different length scales. R2 is two times coarser than R1. Thus, R2 has twicely the actual size of R1. The basic idea of this method is to reconstruct a medium which should have the same two-point correlation function and volume fractions as the reference (real) medium. The

main procedure can be described as follows. Firstly, from a reference medium (here *Berea* sandstone is selected as a reference medium), the two-point correlation function and the volume fractions can be measured experimentally. Secondly, a discrete standard *Gauss*ian field which consists of statistically independent (uncorrelated) *Gauss*ian random variables is generated. Then, this random fields are successively passed through a linear and a nonlinear filter. The linear filter changes the uncorrelated random fields to correlated ones, whose mean value is equal to 0 and whose variance is equal to 1. The given correlation function and volume fractions are taken into account by constructing this linear filter. The nonlinear filter produces the reconstructed sample with this correlated random field as input parameter.

Through the digitization process, the samples are represented by a cubic lattice of voxels with a resolution (lattice constant) a. The dimension of the samples is denoted as $M_1 \times M_2 \times M_3$ (in unit of a^3), the total bulk porosity is $\overline{n}^F$ and the specific internal surface s (in units of $1/a$). The bulk porosity and the specific internal surface are found by counting the pixels of phase φ^F and their interfaces, respectively. Because of the fact that a digitized sphere has a surface area of approximately $6\pi r^2$ as opposed to $4\pi r^2$ (see also discussion in Section 2.3 and Figure 2.2), the values of s should be corrected by multiplying them with the value 4/6.

Sample	a	$M_1 \times M_2 \times M_3$	$\overline{n}^F$	s
fine *Sst6d* (A)	10μm	$95 \times 128 \times 128$	0.3200	0.3325
coarse *Sst20d* (B)	30μm	$73 \times 128 \times 128$	0.2470	0.2698
Berea (C)	10μm	$128 \times 128 \times 128$	0.1775	0.2188
Fontainebleau (D1)	7.5μm	$128 \times 128 \times 128$	0.1208	0.1151
Fontainebleau (D2)	7.5μm	$128 \times 128 \times 128$	0.1476	0.1133
Fontainebleau (D3)	7.5μm	$128 \times 128 \times 128$	0.1171	0.1137
R1	10μm	$128 \times 128 \times 128$	0.1783	0.2837
R2	20μm	$128 \times 128 \times 128$	0.1776	0.4095

Table 2.1: Resolution a, dimension $M_1 \times M_2 \times M_3$ (in units of a^3), total porosity $\overline{n}^F$ and specific internal surface s (in units of $1/a$).

Since all of the *Fontainebleau* samples were obtained from the same but larger real *Fontainebleau* sandstone, one can conclude that the porosity strongly fluctuates from one region to another, while the specific internal surface fluctuates only slightly. In the case of the reconstructed samples, all of the samples' porosities more or less are similar with the reference porosity (the porosity of sample C) as it should be, however, the internal surfaces are a little bit different. The significant discrepancy of the specific internal surface of R2 with those of C and R1 is due to the fact that the resolution of R2 is twice than those of C and R1. All of these data are summarized in Table 2.1.

In the literature, there are different ways to define the correlation length L_c. Recall that the correlation length is the length, where $\overline{S}(r)$ becomes effectively zero. To define L_c, one can take the length at which $\overline{S}(r) = 0.01$ (for other definitions see, e. g., *Gardiner* [72]). These correlation length values can be found from the Figures 2.6 and 2.7. They

are tabulated in Table 2.2. The left side of Figure 2.6 shows the correlation functions of

Sample	$L_c[a]$	s estimated from $\overline{S}(r)$	corrected s
A	8.0	0.2355	0.2217
B	8.4	0.1973	0.1799
C	18.4	0.1499	0.1459
D1	13.8	0.0802	0.0767
D2	21.8	0.0791	0.0755
D3	13.9	0.0791	0.0758
R1	18.2	0.1905	0.1891
R2	6.7	0.2753	0.2730

Table 2.2: Correlation length L_c (in units of a), the estimation of internal surface s (in units of a) using correlation values and the values s by direct counting (after the correction by multiplying with 6/8).

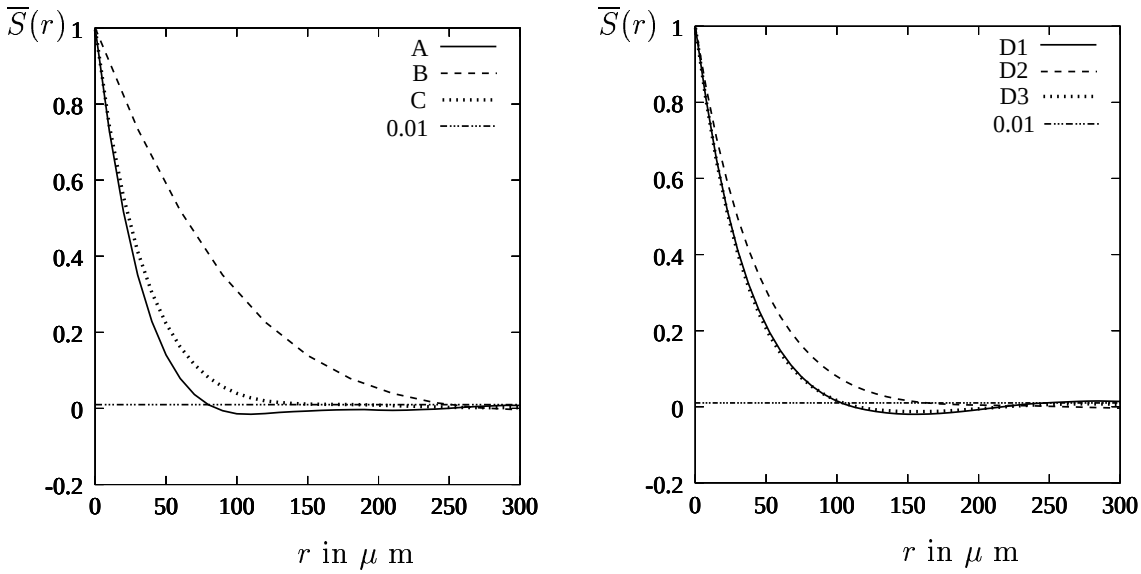

Figure 2.6: The normalized two-point correlation functions $\overline{S}(r)$ of different samples.

the first three samples, while the right side of Figure 2.6 shows the correlation functions of the different parts of the *Fontainebleau* sandstone. The correlation function of D1 more or less is the same as that of D3, while the correlation function of D2 is quite different. The correlation functions of the reconstructed media R1 and R2 as displayed in Figure 2.7 are seen to be in excellent agreement with the reference values of sample C. The specific internal surface s can be estimated from these correlation functions using (2.15) and (2.17). The estimated values are displayed in Table 2.2 together with the correction values of s (from Table 2.1). Obviously, the correlation function provides a reasonable estimation of the specific internal surface s.

Using the equations of Section 2.2.2, $p(n^F, L)$, $p_{\mathcal{L}}(n^F, L)$, the function of percolating regions $p(L)$ can be computed for these eight digitized sandstone samples. In Figure 2.8,

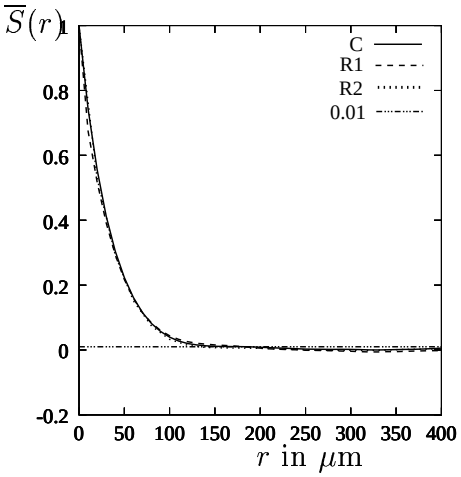

Figure 2.7: The normalized two-point correlation functions $\overline{S}(r)$ of *Berea* sandstone and its reconstruction models.

$p(L)$ is plotted versus L (in units of a) for the eight samples. For all samples, $p(L)$ is

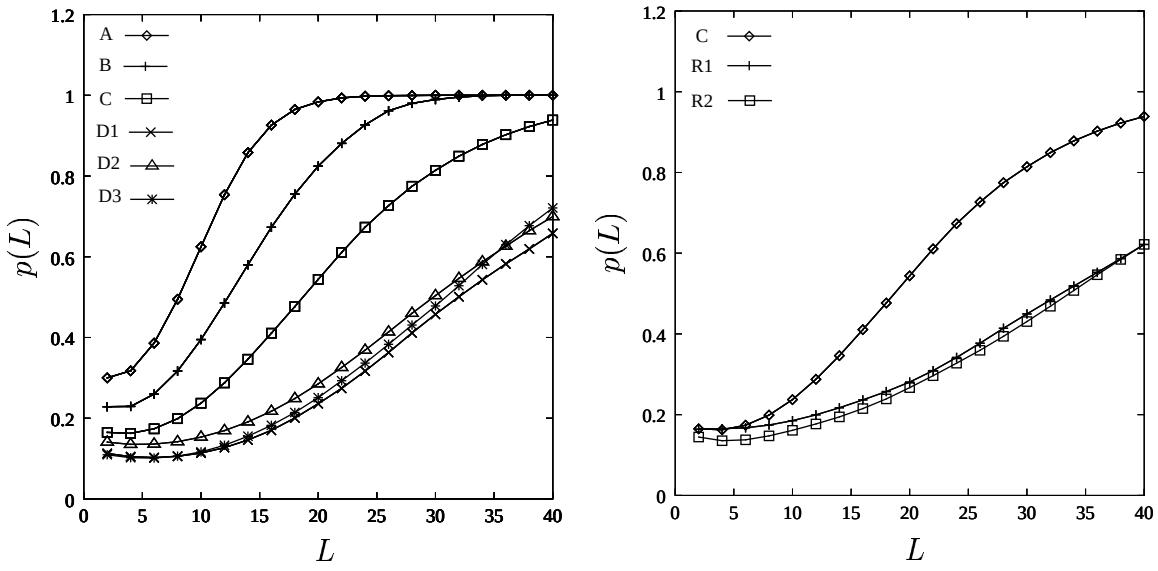

Figure 2.8: Total fraction of percolating regions $p(L)$ of the eight samples at different windows' length L (in the units of a).

sigmoidal in shape. The porosity plays an important role in determining the connectivity of a porous medium (cf. Table 2.1 and the left side of Figure 2.8). However, the right side of Figure 2.8 implies that the connectivity depends on the morphology of the microstructure because all of the three samples (C, R1 and R2) have almost the same average porosities but very different connectivity properties. The connectivity of sample C is better than those of both reconstructed samples. Therefore, in predicting the effective material parameters, one has to include more microstructure information in addition to the porosity. Indeed, in Chapter 7.1, one can see the effective conductivity of sample

C will be of order 10 larger than the effective conductivities of samples R1 and R2 in the case of infinite contrast ratio $k^F/k^S = \infty$. Here, k^F and k^S are the conductivities of the fluid phase and the solid phase, respectively. This results from the fact that the reconstructed porous samples R1 and R2 have more isolated pore spaces than the real sample C (cf. Chapter 7). This can immediately be seen from the pictures of the cross sections of these three samples as depicted in Figure 2.9.

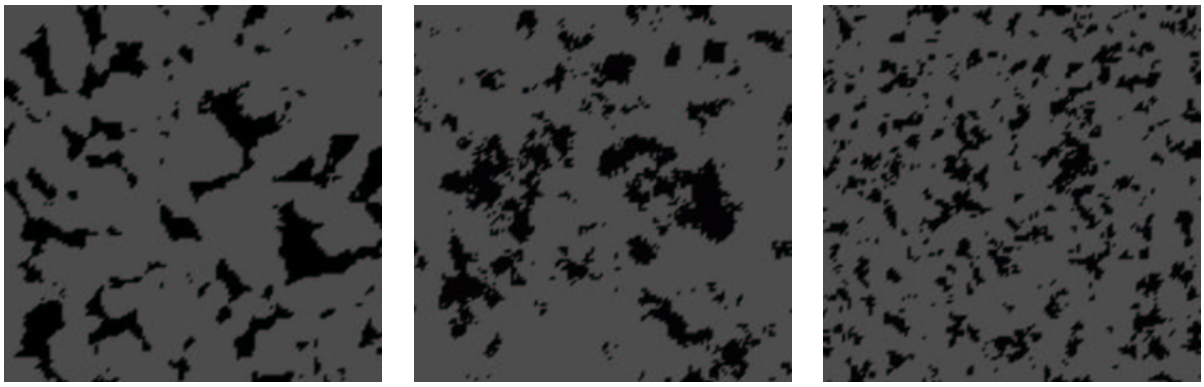

Figure 2.9: The cross sections of the sample C (left) and its reconstructions R1 (middle) and R2 (right).

Chapter 3

Basic equations of continuous media

In Chapter 2 some concepts of stochastics and geometric characterization of random media have been discussed; however, the discussion excludes any physical laws. Every physical process, regardless deterministic or random, is governed by physical laws. Heterogeneous media, both at micro-level and at the macro-level, are governed by the same basic physical laws, namely, the classical continuum physics. The reason is that the typical micro length-scale (the size scale of grains) is still much larger than the atomic or molecular length scale. Therefore, the first part of this chapter is devoted to review some basic ideas and concepts of the continuum physics. This includes the kinematics of continua (Section 3.1), the balance principles of continua (Section 3.2) and the constitutive relations (Section 3.3). The detailed description of the continuum physics are given elsewhere (*Ehlers* [58, 59], *Eringen & Maugin* [63], *Haupt* [84], *Holzapfel* [94], *Truesdell & Toupin* [176]).

The second part of this chapter discusses the relationship between the effective macro-properties and the micro-properties. The effective macro-properties can be deduced using the volume averaging procedure. To this end, the concept of a representative volume element is introduced (Section 3.4). Then in Section 3.5, the associated boundary-value problems are formulated and the necessary averaging theorems are presented. By considering the same constitutive laws governing at both levels, the effective material parameters (the effective thermal conductivity and elastic moduli) can be defined (Section 3.7). Finally, the validity of the effective constitutive laws (at the macro-level) is examined in Section 3.6.

3.1 Kinematics of continua

Consider a set of material points occupying a region $\mathcal{B}_0$ of *Euclid*ian space $\mathbb{E}^3$ at time t_0, which has a volume V_0 and a surface $\partial\mathcal{B}_0$. The material points are endowed with physical properties like mass density, charge density, energy density and entropy density, which are needed to sustain mechanical forces, electromagnetic forces and heat fluxes. After choosing a particular basic system, every material point X can be put into bijective correspondence with a particular point in $\mathbb{E}^3$, whose position vector is $\mathbf{X}$. This can be

expressed mathematically by

$$\begin{gathered} \boldsymbol{\chi}_0(\mathcal{B}_0, t_0) \in \mathbb{E}^3, \\ \mathbf{X} = \boldsymbol{\chi}_0(X, t_0), \qquad X = \chi_0^{-1}(\mathbf{X}). \end{gathered} \tag{3.1}$$

The function $\boldsymbol{\chi}_0$ is called configuration. Furthermore, this configuration can be designated as reference configuration.

A motion is defined as a family of configurations parameterized by the time t

$$\begin{gathered} \boldsymbol{\chi}_t(\mathcal{B}, t) \in \mathbb{E}^3, \\ \mathbf{x} = \boldsymbol{\chi}_t(X, t) = \boldsymbol{\chi}_t(\chi_0^{-1}(\mathbf{X}), t) = \boldsymbol{\chi}(\mathbf{X}, t). \end{gathered} \tag{3.2}$$

The configuration $\boldsymbol{\chi}(\mathbf{X}, t)$ at the current time t is called current configuration, and $\mathbf{x}$ is the position vector of the material point X at time t. If it is assumed that continuum discontinuities such as coalescence or breakup of the continuum do not occur, then the motion $\boldsymbol{\chi}_t(X, t)$ is a continuously differentiable bijective mapping (*Truesdell & Toupin* [176]). This assumption is known as the *axiom of continuity*. Thus, $(3.2)_2$ is invertible:

$$\mathbf{X} = \boldsymbol{\chi}^{-1}(\mathbf{x}, t). \tag{3.3}$$

Equation $(3.2)_2$ states that a motion transforms the material point X with the spatial position $\mathbf{X}$ at time t_0 to the position $\mathbf{x}$ at time t. Equation (3.3) states that the position vector $\mathbf{x}$ at time t can be traced back to the starting position $\mathbf{X}$ of X at time t_0. It is noteworthy to say that the choice of the reference configuration is arbitrary and the reference configuration needs not even be a configuration ever occupied by the body during its motion.

The displacement $\mathbf{u}$ of the material point X can be defined as relative of its actual position to its reference position via

$$\mathbf{u} = \mathbf{x} - \mathbf{X}. \tag{3.4}$$

The velocity $\dot{\mathbf{x}}\,(\mathbf{X}, t)$ and acceleration $\ddot{\mathbf{x}}\,(\mathbf{X}, t)$ of the material point X are defined as

$$\dot{\mathbf{x}}\,(\mathbf{X}, t) = \frac{\partial \boldsymbol{\chi}(\mathbf{X}, t)}{\partial t}, \tag{3.5}$$

$$\ddot{\mathbf{x}}\,(\mathbf{X}, t) = \frac{\partial^2 \boldsymbol{\chi}(\mathbf{X}, t)}{\partial t^2} = \frac{\partial\, \dot{\mathbf{x}}\,(\mathbf{X}, t)}{\partial t}, \tag{3.6}$$

respectively.

Any vectorial function $\boldsymbol{\alpha}$ given as $\boldsymbol{\alpha}(\mathbf{X}, t)$ is called *Lagrange*an or material description, whereas given as $\boldsymbol{\alpha}(\mathbf{x}, t)$ is called *Euler*ian or spatial description (*Haupt* [84], *Holzapfel* [94]). The material time derivatives are defined as

$$\begin{aligned} \dot{\boldsymbol{\alpha}}\,(\mathbf{X}, t) &= \frac{\mathrm{d}}{\mathrm{d}t}\,\boldsymbol{\alpha}(\mathbf{X}, t) = \frac{\partial}{\partial t}\,\boldsymbol{\alpha}(\mathbf{X}, t), \\ \dot{\boldsymbol{\alpha}}\,(\mathbf{x}, t) &= \frac{\mathrm{d}}{\mathrm{d}t}\,\boldsymbol{\alpha}(\mathbf{x}, t) = \frac{\partial}{\partial t}\,\boldsymbol{\alpha}(\mathbf{x}, t) + \operatorname{grad}\boldsymbol{\alpha}(\mathbf{x}, t)\;\dot{\mathbf{x}}\,(\mathbf{x}, t) \end{aligned} \tag{3.7}$$

for a function in *Lagrange*an description and a function in *Euler*ian description, respectively. Here, $\dot{\mathbf{x}}\,(\mathbf{x},t)$ is the spatial (*Euler*ian) representation of the velocity. The material time derivatives express the time rate change of a function $\boldsymbol{\alpha}$ of a material point X. Mathematically, $\mathrm{d}/\mathrm{d}t$ represents the total derivative with respect to time taking into account the motion of the material point X. Note that the first term and the second term on the right of $(3.7)_2$ are called the local and convective derivative, respectively. The local term describes the rate of change of $\boldsymbol{\alpha}$ at the particular location $\mathbf{x}$, while the convective term gives the contribution due to the motion of the material point X. Thus, from $(3.7)_2$, the acceleration in *Euler*ian description can be given in the form

$$\ddot{\mathbf{x}}\,(\mathbf{x},t) = \frac{\mathrm{d}}{\mathrm{d}t}\,\dot{\mathbf{x}}\,(\mathbf{x},t) = \frac{\partial\,\dot{\mathbf{x}}\,(\mathbf{x},t)}{\partial t} + [\operatorname{grad}\dot{\mathbf{x}}\,(\mathbf{x},t)]\,\dot{\mathbf{x}}\,(\mathbf{x},t). \tag{3.8}$$

3.1.1 The gradient of deformation, displacement and velocity

The deformation gradient $\mathbf{F}$ is given by

$$\mathbf{F} = \frac{\partial \mathbf{x}}{\partial \mathbf{X}} = \operatorname{Grad}\mathbf{x}, \tag{3.9}$$

where $\operatorname{Grad}(\cdot)$ is the gradient operator with respect to $\mathbf{X}$. The material displacement gradient $\operatorname{Grad}\mathbf{u}$ can be obtained by taking the gradient of (3.4), thus

$$\operatorname{Grad}\mathbf{u} = \mathbf{F} - \mathbf{I}. \tag{3.10}$$

According to the axiom of continuity, $\mathbf{F}$ is not singular, i. e., $\det\mathbf{F} \neq 0$. The material velocity gradient is defined as

$$\dot{\mathbf{F}} = \frac{\partial\,\dot{\mathbf{x}}}{\partial \mathbf{X}} = \operatorname{Grad}\dot{\mathbf{x}}, \tag{3.11}$$

and the spatial velocity gradient is given by

$$\mathbf{L} = \frac{\partial\,\dot{\mathbf{x}}}{\partial \mathbf{x}} = \operatorname{grad}\dot{\mathbf{x}}\,. \tag{3.12}$$

The relationship between the two descriptions of the velocity gradients can be easily found from the chain rule of differentiation as

$$\mathbf{L} = \frac{\partial\,\dot{\mathbf{x}}}{\partial \mathbf{x}} = \frac{\partial\,\dot{\mathbf{x}}}{\partial \mathbf{X}}\frac{\partial \mathbf{X}}{\partial \mathbf{x}} = \dot{\mathbf{F}}\,\mathbf{F}^{-1} \tag{3.13}$$

or, vice verse,

$$\dot{\mathbf{F}} = \mathbf{L}\,\mathbf{F}. \tag{3.14}$$

The spatial velocity gradient $\mathbf{L}$ can be additively and uniquely decomposed into a symmetric and a skewsymmetric part. The symmetric part $\mathbf{D}$ is called the stretching or strain rate tensor

$$\mathbf{D} = \tfrac{1}{2}\left(\mathbf{L} + \mathbf{L}^T\right), \tag{3.15}$$

whereas the skewsymmetric part $\mathbf{W}$ is called the spin or vorticity tensor

$$\mathbf{W} = \tfrac{1}{2}\left(\mathbf{L} - \mathbf{L}^T\right). \tag{3.16}$$

3.1.2 Kinematics of line, surface and volume elements

By (3.9), a relationship between a material line element $\mathrm{d}\mathbf{X}$ in the reference configuration and a material line $\mathrm{d}\mathbf{x}$ in the actual configuration can be established as

$$\mathrm{d}\mathbf{x} = \mathbf{F}\,\mathrm{d}\mathbf{X}. \tag{3.17}$$

By defining $\mathrm{d}\mathbf{A} = \mathrm{d}\mathbf{X}_1 \times \mathrm{d}\mathbf{X}_2$ as the surface element in the reference configuration and $\mathrm{d}\mathbf{a} = \mathrm{d}\mathbf{x}_1 \times \mathrm{d}\mathbf{x}_2$ as the surface element in the actual configuration and using (3.17), (A.1) and (A.2) the corresponding relation for a surface element can be established as

$$\mathrm{d}\mathbf{a} = \overset{+}{\mathbf{F}}\,\mathrm{d}\mathbf{A} = \det\mathbf{F}\,\mathbf{F}^{T-1}\,\mathrm{d}\mathbf{A}. \tag{3.18}$$

Let $\mathrm{d}V = (\mathrm{d}\mathbf{X}_1 \times \mathrm{d}\mathbf{X}_2)\cdot\mathrm{d}\mathbf{X}_3$ and $\mathrm{d}v = (\mathrm{d}\mathbf{x}_1 \times \mathrm{d}\mathbf{x}_2)\cdot\mathrm{d}\mathbf{x}_3$ be the volume elements in the reference and in the actual configurations, respectively. Using (3.17) again and some simple algebraic manipulations, the following relation can be obtained:

$$\mathrm{d}v = \det\mathbf{F}\,\mathrm{d}V. \tag{3.19}$$

The detailed discussion of the relationships (3.17)-(3.18) can be found elsewhere, e. g. *Haupt* [84] and *Holzapfel* [94]. Using (3.17) and (3.13), a relationship between a material line element $\mathrm{d}\mathbf{x}$ and its material derivative can be obtained:

$$(\mathrm{d}\mathbf{x})^{\bullet} = \dot{\mathbf{F}}\,\mathrm{d}\mathbf{X} = \dot{\mathbf{F}}\,\mathbf{F}^{-1}\,\mathrm{d}\mathbf{x} = \mathbf{L}\,\mathrm{d}\mathbf{x}. \tag{3.20}$$

Using (3.18) and the relation

$$(\overset{+}{\mathbf{F}})^{\bullet} = [\,\underbrace{(\mathbf{L}\cdot\mathbf{I})}_{\operatorname{div}\dot{\mathbf{x}}}\mathbf{I} - \mathbf{L}^T\,]\,\overset{+}{\mathbf{F}}, \tag{3.21}$$

the material time derivative of a surface element $(\mathrm{d}\mathbf{a})^{\bullet}$ can be obtained:

$$(\mathrm{d}\mathbf{a})^{\bullet} = [\,(\operatorname{div}\dot{\mathbf{x}})\,\mathbf{I} - \mathbf{L}^T\,]\,\mathrm{d}\mathbf{a}. \tag{3.22}$$

Furthermore, with

$$(\det\mathbf{F})^{\bullet} = \det\mathbf{F}\ \operatorname{div}\dot{\mathbf{x}} \tag{3.23}$$

and (3.19), the material derivative $(\mathrm{d}v)^{\bullet}$ of volume elements can be calculated as

$$(\mathrm{d}v)^{\bullet} = (\operatorname{div}\dot{\mathbf{x}})\,\mathrm{d}v. \tag{3.24}$$

These relations are applied to compute the derivatives of volume and surface integrals as required in the balance equations.

The material time derivative of a volume integral of any vector field $\boldsymbol{\psi}$ over a material volume $\mathcal{B}$ with boundary $\partial\mathcal{B}$ is given by

$$\frac{\mathrm{d}}{\mathrm{d}t}\int_{\mathcal{B}}\boldsymbol{\psi}\,\mathrm{d}v = \int_{\mathcal{B}}(\dot{\boldsymbol{\psi}} + \boldsymbol{\psi}\operatorname{div}\dot{\mathbf{x}})\,\mathrm{d}v = \int_{\mathcal{B}}\frac{\partial\boldsymbol{\psi}}{\partial t}\,\mathrm{d}v + \int_{\partial\mathcal{B}}\boldsymbol{\psi}\,(\dot{\mathbf{x}}\cdot\mathrm{d}\mathbf{a}). \tag{3.25}$$

This identity is known as the *Reynolds'* transport theorem. It can be proven by carrying material time derivative inside the integral and using $(3.7)_2$, (3.24) and the divergence theorem (A.9). The result (3.25) can be extended to an observed volume $\mathcal{B}_o$ with a boundary $\partial\mathcal{B}_o$, which is moving with a non-material velocity $\mathbf{w}$, i. e.,

$$\frac{\mathrm{d}}{\mathrm{d}t}\bigg|_{\mathbf{w}} \int_{\mathcal{B}_o} \boldsymbol{\psi}\, \mathrm{d}v = \int_{\mathcal{B}_o} \frac{\partial \boldsymbol{\psi}}{\partial t}\, \mathrm{d}v + \int_{\partial\mathcal{B}_o} \boldsymbol{\psi}\, (\mathbf{w}\cdot \mathrm{d}\mathbf{a}). \tag{3.26}$$

This may be seen by imagining that $\mathcal{B}_o \cup \partial\mathcal{B}_o$ consists of some fictituous material particles which have velocity $\mathbf{w}$. If the volume $\mathcal{B}_o$ is assumed to coincide with the material volume $\mathcal{B}$ at time t, the local derivative in (3.25) can be eliminated using (3.26). This leads to

$$\frac{\mathrm{d}}{\mathrm{d}t}\int_{\mathcal{B}} \boldsymbol{\psi}\, \mathrm{d}v = \frac{\mathrm{d}}{\mathrm{d}t}\bigg|_{\mathbf{w}} \int_{\mathcal{B}} \boldsymbol{\psi}\, \mathrm{d}v + \int_{\partial\mathcal{B}} \boldsymbol{\psi}\, [(\dot{\mathbf{x}} - \mathbf{w})\cdot \mathrm{d}\mathbf{a}]. \tag{3.27}$$

The material time derivative of a surface integral of any vector field $\boldsymbol{\varsigma}$ over a material surface $\mathcal{S}$ is given by

$$\frac{\mathrm{d}}{\mathrm{d}t}\int_{\mathcal{S}} \boldsymbol{\varsigma}\cdot \mathrm{d}\mathbf{a} = \int_{\mathcal{S}} \Big[\frac{\partial \boldsymbol{\varsigma}}{\partial t} + (\mathrm{div}\,\boldsymbol{\varsigma})\ \dot{\mathbf{x}} + \mathrm{rot}\,(\boldsymbol{\varsigma}\times \dot{\mathbf{x}})\Big]\cdot \mathrm{d}\mathbf{a}. \tag{3.28}$$

The proof of (3.28) follows upon carrying out the material derivative $(3.7)_2$ inside the integral and using (3.22). By making use of *Stokes'* theorem (A.11), (3.28) can be rewritten as

$$\frac{\mathrm{d}}{\mathrm{d}t}\int_{\mathcal{S}} \boldsymbol{\varsigma}\cdot \mathrm{d}\mathbf{a} = \int_{\mathcal{S}} \Big[\frac{\partial \boldsymbol{\varsigma}}{\partial t} + (\mathrm{div}\,\boldsymbol{\varsigma})\ \dot{\mathbf{x}}\ \Big]\cdot \mathrm{d}\mathbf{a} + \oint_{\partial\mathcal{S}} (\boldsymbol{\varsigma}\times \dot{\mathbf{x}})\cdot \mathrm{d}\mathbf{x}, \tag{3.29}$$

where $\partial\mathcal{S}$ is the boundary of the curve $\mathcal{S}$. Similar to (3.26), (3.29) can be extended to an observed surface $\mathcal{S}_o$ bounded by a curve $\partial\mathcal{S}_o$, which is moving with a non-material velocity $\mathbf{w}$. Thus,

$$\frac{\mathrm{d}}{\mathrm{d}t}\bigg|_{\mathbf{w}} \int_{\mathcal{S}_o} \boldsymbol{\varsigma}\cdot \mathrm{d}\mathbf{a} = \int_{\mathcal{S}_o} \Big[\frac{\partial \boldsymbol{\varsigma}}{\partial t} + (\mathrm{div}\,\boldsymbol{\varsigma})\,\mathbf{w}\Big]\cdot \mathrm{d}\mathbf{a} + \oint_{\partial\mathcal{S}_o} (\boldsymbol{\varsigma}\times \mathbf{w})\cdot \mathrm{d}\mathbf{x}. \tag{3.30}$$

If the surfeace $\mathcal{S}_o$ is assumed to coincide with the material surface $\mathcal{S}$ at time t, the local time derivative in (3.28) can be substituted using (3.30). This leads to

$$\frac{\mathrm{d}}{\mathrm{d}t}\int_{\mathcal{S}} \boldsymbol{\varsigma}\cdot \mathrm{d}\mathbf{a} = \frac{\mathrm{d}}{\mathrm{d}t}\bigg|_{\mathbf{w}} \int_{\mathcal{S}} \boldsymbol{\varsigma}\cdot \mathrm{d}\mathbf{a} + \int_{\mathcal{S}} \mathrm{div}\,\boldsymbol{\varsigma}\,(\dot{\mathbf{x}} - \mathbf{w})\cdot \mathrm{d}\mathbf{a} + \oint_{\partial\mathcal{S}} [\boldsymbol{\varsigma}\times (\dot{\mathbf{x}} - \mathbf{w})]\cdot \mathrm{d}\mathbf{x}. \tag{3.31}$$

3.1.3 Strain

The deformation gradient $\mathbf{F}$ can be uniquely decomposed into an orthogonal tensor $\mathbf{R}$, which describes the rotation of line elements, and a symmetric positive-definite tensor, which describes the deformation of line elements:

$$\mathbf{F} = \mathbf{R}\,\mathbf{U} = \mathbf{V}\,\mathbf{R}. \tag{3.32}$$

The second-rank tensors $\mathbf{U}$ and $\mathbf{V}$ are called the right and left stretch tensors, respectively.

The difference between the square of the line element in the current configuration and the square of the line element in the reference configuration is given by

$$\begin{aligned} \mathrm{d}\mathbf{x}\cdot\mathrm{d}\mathbf{x} - \mathrm{d}\mathbf{X}\cdot\mathrm{d}\mathbf{X} &= 2\mathbf{E}\cdot(\mathrm{d}\mathbf{X}\otimes\mathrm{d}\mathbf{X}) \\ &= 2\mathbf{A}\cdot(\mathrm{d}\mathbf{x}\otimes\mathrm{d}\mathbf{x}), \end{aligned} \tag{3.33}$$

where

$$\mathbf{E} = \tfrac{1}{2}(\mathbf{F}^T\,\mathbf{F} - \mathbf{I}) \tag{3.34}$$

and

$$\mathbf{A} = \tfrac{1}{2}(\mathbf{I} - \mathbf{F}^{T^{-1}}\mathbf{F}^{-1}) \tag{3.35}$$

are known as the *Green-Lagrange* $\mathbf{E}$ and *Euler-Almansi* $\mathbf{A}$ strain tensors, respectively.

In many cases, it is useful to express the tensor $\mathbf{E}$ by means of the displacement gradient $\operatorname{Grad}\mathbf{u}$, which can be gained by inserting (3.10) into (3.33). Thus

$$\mathbf{E} = \tfrac{1}{2}\left[\operatorname{Grad}\mathbf{u} + (\operatorname{Grad}\mathbf{u})^T + (\operatorname{Grad}\mathbf{u})^T\operatorname{Grad}\mathbf{u}\right]. \tag{3.36}$$

If the displacement gradient is small, the non-linear terms of the finite stress tensor (3.36) can be neglected and the strain tensor reduces to

$$\boldsymbol{\varepsilon} = \tfrac{1}{2}\left[\operatorname{Grad}\mathbf{u} + (\operatorname{Grad}\mathbf{u})^T\right], \tag{3.37}$$

where $\boldsymbol{\varepsilon}$ denotes the *Lagrange*an infinitesimal strain tensor.

3.2 Balance relations of continuum physics

3.2.1 Global balance laws

The balance relations of continuum physics can be formulated axiomatically and can be classified into volume and surface balance relations (*Eringen* & *Maugin* [63]).

The master volume balance relation of a vectorial physical field quantity $\boldsymbol{\psi}$ can be written as

$$\frac{\mathrm{d}}{\mathrm{d}t}\int_{\mathcal{B}}\boldsymbol{\psi}\,\mathrm{d}v = \int_{\partial\mathcal{B}}\boldsymbol{\Phi}\,\mathrm{d}\mathbf{a} + \int_{\mathcal{B}}\boldsymbol{\sigma}\,\mathrm{d}v. \tag{3.38}$$

(3.38) postulates that the rate of change of $\boldsymbol{\psi}$ in a body $\mathcal{B}$ is equal to the total efflux $\boldsymbol{\Phi}\,\mathbf{n}$ across the surface $\partial\mathcal{B}$ and the external supply $\boldsymbol{\sigma}$ within $\mathcal{B}$. Here, $\boldsymbol{\psi}$ and $\boldsymbol{\sigma}$ are the n-rank tensor fields, $\boldsymbol{\Phi}$ is the $(n+1)$-rank tensor field and $\mathbf{n}$ is the outwards oriented unit surface normal of $\partial\mathcal{B}$. For a scalar field ψ, the terms $\boldsymbol{\Phi}\,\mathbf{n}$ and $\boldsymbol{\sigma}$ have to be replaced by $\boldsymbol{\phi}\cdot\mathbf{n}$ and σ, respectively. Hence,

$$\frac{\mathrm{d}}{\mathrm{d}t}\int_{\mathcal{B}}\psi\,\mathrm{d}v = \int_{\partial\mathcal{B}}\boldsymbol{\phi}\cdot\mathrm{d}\mathbf{a} + \int_{\mathcal{B}}\sigma\,\mathrm{d}v. \tag{3.39}$$

For electromagnetic continua, (3.38) should be supplemented by the master surface balance relation which can be formulated as

$$\frac{\mathrm{d}}{\mathrm{d}t}\int_{\mathcal{S}}\boldsymbol{\varsigma}\cdot\mathrm{d}\mathbf{a} = \oint_{\partial\mathcal{S}}\boldsymbol{\tau}\cdot\mathrm{d}\mathbf{x} + \int_{\mathcal{S}}\boldsymbol{\varpi}\cdot\mathrm{d}\mathbf{a}. \tag{3.40}$$

(3.40) expresses that the rate of change of the physical field quantity ς at the two-sided material surface $\mathcal{S}$ is balanced by the total efflux $\boldsymbol{\tau}$ through the closed boundary curve $\partial\mathcal{S}$ and the external supply $\boldsymbol{\varpi}$ within $\mathcal{S}$.

For open systems, the production terms $\hat{\boldsymbol{\psi}}$ and $\hat{\varsigma}$ have to be added to the balance equations (3.38) and (3.40), respectively. The production terms are caused by the exchange of the material points with the environment. Prominent examples of this case are concrete (*Neville* [136]) and, in general, multiphase continua (*de Boer* [49], *de Boer & Ehlers* [50], *Ehlers* [56, 60], *Truesdell* [175]).

3.2.2 Local balance laws and jump conditions

The local form of the balance laws, which are partial differential equations, can be derived from the global balance laws (3.38) and (3.40). The fields governed by these partial differential equations must be smooth within the continuum. However, eventhough the fields are piecewise continuous functions, they still satisfy the global balance equations (3.38) and (3.40), because the integral of piecewise continuous functions exists. In this case, the local form of the balance equations can still be used but they must be supplemented with the jump conditions, whenever the derivatives of the fields do not exist. In this subsection, the boundary conditions for the piecewise continuous fields, which are known as jump conditions, will be derived.

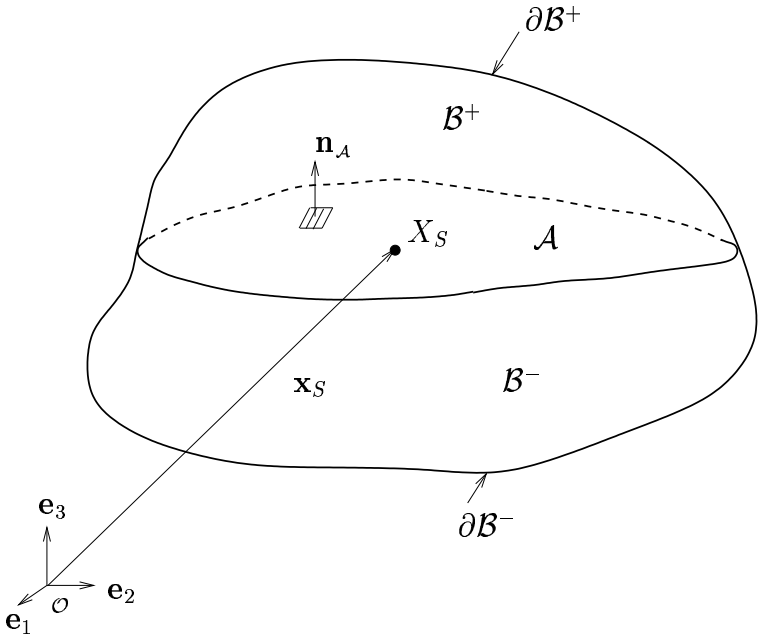

Figure 3.1: Discontinuity surface $\mathcal{A}$.

The vector field $\boldsymbol{\psi}$ is considered to be a continuous function in $\mathcal{B}$ except on the discontinuity surface $\mathcal{A}$ which moves with the velocity $\mathbf{w}$ through the material body $\mathcal{B}$. The region on the side of the positive direction normal vector $\mathbf{n}_\mathcal{A}$ is denoted by $\mathcal{B}^+$ and on

the other side is denoted by $\mathcal{B}^-$ as shown in Figure 3.1. The limit values of $\boldsymbol{\psi}(\mathbf{x},t)$ are defined as

$$\boldsymbol{\psi}^+ = \lim_{\mathbf{x}\to\mathbf{x}_{\mathcal{A}}^+} \boldsymbol{\psi}(\mathbf{x},t), \qquad \boldsymbol{\psi}^- = \lim_{\mathbf{x}\to\mathbf{x}_{\mathcal{A}}^-} \boldsymbol{\psi}(\mathbf{x},t) \tag{3.41}$$

as $\mathbf{x}$ approaches the position $\mathbf{x}_{\mathcal{A}}$ on the surface $\mathcal{A}$ from the $+$ and $-$ sides, respectively. Then, the jump of $\boldsymbol{\psi}(\mathbf{x},t)$ across the surface is defined by

$$[\![\boldsymbol{\psi}]\!] = \boldsymbol{\psi}^+ - \boldsymbol{\psi}^-. \tag{3.42}$$

Because the material body $\mathcal{B}$ contains a discontinuity surface $\mathcal{A}$, the transport theorem (3.25) cannot be used to calculate the right side of (3.38). This transport theorem has to be modified to accomodate the presence of $\mathcal{A}$. To this end, the volume $\mathcal{B}$ is splitted into two subvolumes $\mathcal{B}^+$ and $\mathcal{B}^-$ bounded by $\partial\mathcal{B}^+ \cup \mathcal{A}$ and $\partial\mathcal{B}^- \cup \mathcal{A}$, respectively. Hence,

$$\frac{\mathrm{d}}{\mathrm{d}t}\int_{\mathcal{B}} \boldsymbol{\psi}\,\mathrm{d}v = \frac{\mathrm{d}}{\mathrm{d}t}\int_{\mathcal{B}^+} \boldsymbol{\psi}\,\mathrm{d}v + \frac{\mathrm{d}}{\mathrm{d}t}\int_{\mathcal{B}^-} \boldsymbol{\psi}\,\mathrm{d}v. \tag{3.43}$$

The volumes $\mathcal{B}^+$ and $\mathcal{B}^-$ are not material volumes, since the velocity $\mathbf{w}$ of the discontinuity surface $\mathcal{A}$ differs from the material velocity $\dot{\mathbf{x}}$. This means that (3.25) still cannot be used; however, one can apply (3.27) to the right side of (3.43):

$$\begin{aligned}\frac{\mathrm{d}}{\mathrm{d}t}\int_{\mathcal{B}} \boldsymbol{\psi}\,\mathrm{d}v \;=\; & \frac{\mathrm{d}}{\mathrm{d}t}\bigg|_{\mathbf{w}}\int_{\mathcal{B}^+} \boldsymbol{\psi}\,\mathrm{d}v + \int_{\partial\mathcal{B}^+} \boldsymbol{\psi}\,[(\dot{\mathbf{x}}-\mathbf{w})\cdot\mathrm{d}\mathbf{a}] - \int_{\mathcal{A}} \boldsymbol{\psi}^+\,[(\dot{\mathbf{x}}^+-\mathbf{w})\cdot\mathbf{n}_{\mathcal{A}}]\,\mathrm{d}a + \\ & + \frac{\mathrm{d}}{\mathrm{d}t}\bigg|_{\mathbf{w}}\int_{\mathcal{B}^-} \boldsymbol{\psi}\,\mathrm{d}v + \int_{\partial\mathcal{B}^-} \boldsymbol{\psi}\,[(\dot{\mathbf{x}}-\mathbf{w})\cdot\mathrm{d}\mathbf{a}] + \int_{\mathcal{A}} \boldsymbol{\psi}^-\,[(\dot{\mathbf{x}}^--\mathbf{w})\cdot\mathbf{n}_{\mathcal{A}}]\,\mathrm{d}a.\end{aligned} \tag{3.44}$$

By considering (3.26), (3.44) can be rewritten as

$$\frac{\mathrm{d}}{\mathrm{d}t}\int_{\mathcal{B}} \boldsymbol{\psi}\,\mathrm{d}v = \int_{\mathcal{B}} \frac{\partial\boldsymbol{\psi}}{\partial t}\,\mathrm{d}v + \int_{\partial\mathcal{B}} \boldsymbol{\psi}(\dot{\mathbf{x}}\cdot\mathrm{d}\mathbf{a}) - \int_{\mathcal{A}} [\![\boldsymbol{\psi}\otimes(\dot{\mathbf{x}}-\mathbf{w})]\!]\,\mathbf{n}_{\mathcal{A}}\,\mathrm{d}a. \tag{3.45}$$

Similarly, the surface integral of the right side of the balance equation (3.38) is splitted into two parts:

$$\int_{\partial\mathcal{B}} \boldsymbol{\Phi}\,\mathrm{d}\mathbf{a} = \int_{\partial\mathcal{B}^+\cup\mathcal{A}} \boldsymbol{\Phi}\,\mathrm{d}\mathbf{a} + \int_{\partial\mathcal{B}^-\cup\mathcal{A}} \boldsymbol{\Phi}\,\mathrm{d}\mathbf{a} = \int_{\partial\mathcal{B}^+} \boldsymbol{\Phi}\,\mathrm{d}\mathbf{a} + \int_{\partial\mathcal{B}^-} \boldsymbol{\Phi}\,\mathrm{d}\mathbf{a} - \int_{\mathcal{A}} [\![\boldsymbol{\Phi}]\!]\,\mathbf{n}_{\mathcal{A}}\,\mathrm{d}a. \tag{3.46}$$

Then, by applying (3.45) to the left side of (3.38), considering (3.46) and using the divergence theorem (A.9), one obtains

$$\int_{\mathcal{B}} [\dot{\boldsymbol{\psi}} + \boldsymbol{\psi}\,\mathrm{div}\,\dot{\mathbf{x}} - \mathrm{div}\,\boldsymbol{\Phi} - \boldsymbol{\sigma}]\,\mathrm{d}v - \int_{\mathcal{A}} [\![\boldsymbol{\psi}\otimes(\dot{\mathbf{x}}-\mathbf{w}) - \boldsymbol{\Phi}]\!]\,\mathbf{n}_{\mathcal{A}}\,\mathrm{d}a = \mathbf{0}. \tag{3.47}$$

A similar argument can be applied to evaluate the rate of change of $\int_{\mathcal{S}} \boldsymbol{\varsigma}\cdot\mathrm{d}\mathbf{a}$ in a surface $\mathcal{S}$ that contains a discontinuity line $\mathcal{C}$. If $\mathcal{S}$ is decomposed into $\mathcal{S}^+ \cup \mathcal{C}$ and $\mathcal{S}^- \cup \mathcal{C}$, the left side of (3.40) can be written as

$$\frac{\mathrm{d}}{\mathrm{d}t}\int_{\mathcal{S}} \boldsymbol{\varsigma}\cdot\mathrm{d}\mathbf{a} = \frac{\mathrm{d}}{\mathrm{d}t}\int_{\mathcal{S}^+\cup\mathcal{C}} \boldsymbol{\varsigma}\cdot\mathrm{d}\mathbf{a} + \frac{\mathrm{d}}{\mathrm{d}t}\int_{\mathcal{S}^-\cup\mathcal{C}} \boldsymbol{\varsigma}\cdot\mathrm{d}\mathbf{a}. \tag{3.48}$$

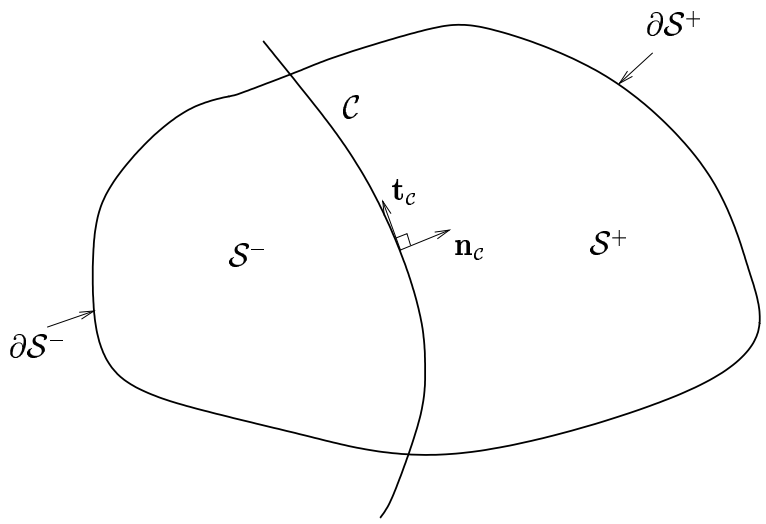

Figure 3.2: Discontinuity line $\mathcal{C}$.

Using (3.31) to evaluate the right side of (3.48) and by considering (3.30), (3.48) can be rewritten as

$$\frac{\mathrm{d}}{\mathrm{d}t}\int_{\mathcal{S}} \boldsymbol{\varsigma}\cdot\mathrm{d}\mathbf{a} = \int_{\mathcal{S}} \left[\frac{\partial \boldsymbol{\varsigma}}{\partial t} + \operatorname{div}\boldsymbol{\varsigma}\ \dot{\mathbf{x}}\right]\cdot\mathrm{d}\mathbf{a} + \oint_{\partial\mathcal{S}} (\boldsymbol{\varsigma}\times\dot{\mathbf{x}})\cdot\mathrm{d}\mathbf{x} - \oint_{\mathcal{C}} [\![\boldsymbol{\varsigma}\times(\dot{\mathbf{x}}-\mathbf{w})]\!]\cdot\mathbf{t}_{\mathcal{C}}\,\mathrm{d}x, \quad (3.49)$$

where $\mathbf{t}_c$ designates the tangent vector of $\mathcal{C}$. It is necessary to split the line integral of the right side of (3.40) into two parts. Hence,

$$\oint_{\partial\mathcal{S}} \boldsymbol{\tau}\cdot\mathrm{d}\mathbf{x} = \oint_{\partial\mathcal{S}^+\cup\mathcal{C}} \boldsymbol{\tau}\cdot\mathrm{d}\mathbf{x} + \oint_{\partial\mathcal{S}^-\cup\mathcal{C}} \boldsymbol{\tau}\cdot\mathrm{d}\mathbf{x} = \oint_{\partial\mathcal{S}^+} \boldsymbol{\tau}\cdot\mathrm{d}\mathbf{x} + \oint_{\partial\mathcal{S}^-} \boldsymbol{\tau}\cdot\mathrm{d}\mathbf{x} - \oint_{\mathcal{C}} [\![\boldsymbol{\tau}]\!]\cdot\mathbf{t}_{\mathcal{C}}\,\mathrm{d}x. \quad (3.50)$$

Using (3.49) and (3.50), the surface balance law (3.40) can be modified in the case of a surface $\mathcal{S}$ which contains a discontinuity line $\mathcal{C}$ to

$$\int_{\mathcal{S}} \left[\frac{\partial \boldsymbol{\varsigma}}{\partial t} + \operatorname{div}\boldsymbol{\varsigma}\ \dot{\mathbf{x}} + \operatorname{rot}(\boldsymbol{\varsigma}\times\dot{\mathbf{x}} - \boldsymbol{\tau}) - \boldsymbol{\varpi}\right]\cdot\mathrm{d}\mathbf{a} - \oint_{\mathcal{C}} \mathbf{k}\cdot([\![\boldsymbol{\varsigma}\times(\dot{\mathbf{x}}-\mathbf{w}) - \boldsymbol{\tau}]\!]\times\mathbf{n}_c)\,\mathrm{d}x = 0. \quad (3.51)$$

The second term of the left side of (3.51) is obtained by introducing the binormal vector $\mathbf{k}$ with the property $\mathbf{t}_c = -\mathbf{k}\times\mathbf{n}_c$ and the tripel scalar product rule $\mathbf{a}\cdot(\mathbf{b}\times\mathbf{c}) = \mathbf{b}\cdot(\mathbf{c}\times\mathbf{a})$.

The global balance laws (3.47) and (3.51) are assumed to be valid for any given volume of integration. This statement is known as *axiom of locality*. Then it is a consequence of a mathematical theorem that the integrands of (3.47) and (3.51) must be zero at any point in $\mathcal{B}$, which leads to the following local balance equations.

The local balance law in the volume reads

$$\dot{\boldsymbol{\psi}} + \boldsymbol{\psi}\operatorname{div}\dot{\mathbf{x}} - \operatorname{div}\boldsymbol{\Phi} - \boldsymbol{\sigma} = \mathbf{0} \quad \text{in} \quad \mathcal{B}, \quad (3.52)$$

$$[\![\boldsymbol{\psi}\otimes(\dot{\mathbf{x}}-\mathbf{w}) - \boldsymbol{\Phi}]\!]\,\mathbf{n}_{\mathcal{A}} = \mathbf{0} \quad \text{on} \quad \mathcal{A}, \quad (3.53)$$

where $\boldsymbol{\psi}\otimes(\dot{\mathbf{x}}-\mathbf{w})$ must be replaced by $\psi\,(\dot{\mathbf{x}}-\mathbf{w})$ for a scalar field ψ.

The local surface balance law reads

$$\overset{*}{\boldsymbol{\varsigma}} - \operatorname{rot} \boldsymbol{\tau} - \boldsymbol{\varpi} = \mathbf{0} \text{ in } \mathcal{S}, \tag{3.54}$$

$$\left[\!\left[\boldsymbol{\varsigma} \times (\dot{\mathbf{x}} - \mathbf{w}) - \boldsymbol{\tau} \right]\!\right] \times \mathbf{n}_c = \mathbf{0} \text{ on } \mathcal{C}, \tag{3.55}$$

where

$$\overset{*}{\boldsymbol{\varsigma}} = \frac{\partial \boldsymbol{\varsigma}}{\partial t} + \operatorname{div} \boldsymbol{\varsigma}\ \dot{\mathbf{x}} + \operatorname{rot} (\boldsymbol{\varsigma} \times \dot{\mathbf{x}}).$$

Balance laws	$\boldsymbol{\psi}$ (ψ)	$\boldsymbol{\Phi}$ $(\boldsymbol{\phi})$	$\boldsymbol{\sigma}$ (σ)
Mass	ρ	0	0
Linear momentum	$\rho\ \dot{\mathbf{x}}$	$\mathbf{T}$	$\rho\,\mathbf{f}$
Moment of momentum	$\mathbf{x} \times \rho\ \dot{\mathbf{x}}$	$\mathbf{x} \times \mathbf{T}$	$\mathbf{x} \times \rho\,\mathbf{f}$
Energy	$\rho\,(\varepsilon + \frac{1}{2}\ \dot{\mathbf{x}} \cdot \dot{\mathbf{x}})$	$\mathbf{T}^T\ \dot{\mathbf{x}} - \mathbf{q}$	$\dot{\mathbf{x}} \cdot \rho\,\mathbf{f} + \rho\, r$
Entropy	$\rho\,\eta$	$-\mathbf{q}/\theta$	$\rho r/\theta$
Electric charge	q_e	$\mathbf{j} - q_e\ \dot{\mathbf{x}}$	0

Table 3.1: Local volume balance laws.

The different fields $\boldsymbol{\psi}$ (ψ), $\boldsymbol{\Phi}$ $(\boldsymbol{\phi})$ and $\boldsymbol{\sigma}$ (σ) of the volume balance are listed in Table 3.1. Here, ρ is the mass density, $\mathbf{T}$ is the *Cauchy* stress tensor, $\mathbf{f}$ is the body force density, ε is the internal energy density, $\mathbf{q}$ is the heat flux vector, r is the heat supply (radiation), θ is the temperature, q_e is the charge density and $\mathbf{j}$ is the electric current density.

The fields $\boldsymbol{\varsigma}$, $\boldsymbol{\tau}$ and $\boldsymbol{\varpi}$ are tabulated in Table 3.2. The magnetic flux vector, the electric displacement vector, the electric field and the magnetic field are represented by $\mathbf{b}$, $\mathbf{d}$, $\mathbf{e}$ and $\mathbf{h}$, respectively.

Laws	$\boldsymbol{\varsigma}$	$\boldsymbol{\tau}$	$\boldsymbol{\varpi}$
Faraday	$\mathbf{b}$	$-\mathbf{e} - \dot{\mathbf{x}} \times \mathbf{b}$	$\mathbf{0}$
Ampère	$-\mathbf{d}$	$-\mathbf{h} + \dot{\mathbf{x}} \times \mathbf{d}$	$\mathbf{j} - q_e\ \dot{\mathbf{x}}$

Table 3.2: Local surface balance laws.

3.2.3 Balance of mass

From Table 3.1 and (3.52) the local form of the balance of mass

$$\dot{\rho} + \rho \operatorname{div} \dot{\mathbf{x}} = 0 \qquad \text{in } \mathcal{B} \tag{3.56}$$

and its corresponding jump condition

$$[\![\rho\,(\dot{\mathbf{x}} - \mathbf{w})]\!] \cdot \mathbf{n}_{\mathcal{A}} = 0 \qquad \text{on } \mathcal{A} \tag{3.57}$$

can be obtained.

3.2.4 Balance of linear momentum

By employing Table 3.1, (3.52) and taking the mass balance (3.2.3) into consideration, then the local balance of momentum can be expressed as

$$\operatorname{div} \mathbf{T} + \rho \mathbf{f} = \rho\, \ddot{\mathbf{x}} \qquad \text{in } \mathcal{B} \tag{3.58}$$

with the jump condition

$$[\![\rho\, \dot{\mathbf{x}} \otimes (\dot{\mathbf{x}} - \mathbf{w}) - \mathbf{T}]\!]\, \mathbf{n}_{\mathcal{A}} = \mathbf{0} \quad \text{on } \mathcal{A}. \tag{3.59}$$

If the discontinuity surface $\mathcal{A}$ is a material surface

$$\mathbf{w} = \dot{\mathbf{x}}, \tag{3.60}$$

(3.59) reduces to

$$[\![\mathbf{T}]\!]\, \mathbf{n}_{\mathcal{A}} = \mathbf{0} \qquad \text{on } \mathcal{A}. \tag{3.61}$$

If the discontinuity surface $\mathcal{A}$ coincides with the surface of the body

$$\rho^{+} = 0, \qquad \dot{\mathbf{x}}^{-} = \mathbf{w}, \tag{3.62}$$

(3.59) reduces to

$$[\![\mathbf{T}]\!]\, \mathbf{n}_{\mathcal{A}} = \mathbf{0} \qquad \text{on } \mathcal{A}. \tag{3.63}$$

When $\mathbf{T}^{+}\mathbf{n}_{\mathcal{A}}$ is interpreted as the traction $\mathbf{t}$ and $\mathbf{T}^{-}\mathbf{n}_{\mathcal{A}}$ is set to $\mathbf{T}\mathbf{n}$, (3.63) gives the boundary condition on tractions:

$$\mathbf{T}\mathbf{n} = \mathbf{t} \qquad \text{on } \partial\mathcal{B}. \tag{3.64}$$

If the discontinuity surface is a fixed surface

$$\mathbf{w} = \mathbf{0}, \tag{3.65}$$

(3.59) reduces to

$$[\![\rho\, \dot{\mathbf{x}} \otimes \dot{\mathbf{x}} - \mathbf{T}]\!]\, \mathbf{n}_{\mathcal{A}} = \mathbf{0} \quad \text{on } \mathcal{A}. \tag{3.66}$$

If the acceleration $\ddot{\mathbf{x}}$ vanishes, (3.58) reduces to the equilibrium condition

$$\operatorname{div} \mathbf{T} + \rho \mathbf{f} = \mathbf{0} \qquad \text{in } \mathcal{B}. \tag{3.67}$$

3.2.5 Balance of moment of momentum

The balance of moment of momentum takes the local form as

$$\mathbf{T} = \mathbf{T}^T \qquad \text{in } \mathcal{B}. \tag{3.68}$$

They can be obtained by using Table 3.1 and combining the result with the local balance of momentum (3.58). The local balance of moment of momentum states that the *Cauchy* stress tensor is symmetric, which is merely valid in classical continuum mechanics. The jump condition for the moment of momentum is satisfied identically according to (3.59) and (3.61).

3.2.6 Energy balance

From the Table 3.1 and (3.52), the local form of the energy balance reads

$$[\rho\,(\varepsilon + \tfrac{1}{2}\,\dot{\mathbf{x}}\cdot\dot{\mathbf{x}})]^{\bullet} + [\rho\,(\varepsilon + \tfrac{1}{2}\,\dot{\mathbf{x}}\cdot\dot{\mathbf{x}})]\,\mathrm{div}\;\dot{\mathbf{x}} - \mathrm{div}\,(\mathbf{T}^T\,\dot{\mathbf{x}} - \mathbf{q}) - \rho(\mathbf{f}\cdot\dot{\mathbf{x}} + r) = 0. \tag{3.69}$$

After considering the balance of linear momentum (3.58) and of moment of momentum (3.68), (3.69) can be written as

$$\rho\;\dot{\varepsilon} - \mathbf{T}\cdot\mathbf{D} + \mathrm{div}\,\mathbf{q} - \rho\, r = 0 \qquad \text{in } \mathcal{B}. \tag{3.70}$$

From (3.53) the corresponding jump condition reads

$$[\![\rho\,(\varepsilon + \tfrac{1}{2}\,\dot{\mathbf{x}}\cdot\dot{\mathbf{x}})\,(\dot{\mathbf{x}} - \mathbf{w}) - \mathbf{T}\,\dot{\mathbf{x}} + \mathbf{q}]\!] \cdot \mathbf{n}_{\mathcal{A}} = 0 \qquad \text{on } \mathcal{A}. \tag{3.71}$$

For the case that the discontinuity surface $\mathcal{A}$ is a material surface ($\mathbf{w} = \dot{\mathbf{x}}$), (3.71) reduces to

$$[\![\mathbf{q} - \mathbf{T}\,\dot{\mathbf{x}}]\!] \cdot \mathbf{n}_{\mathcal{A}} = 0 \qquad \text{on } \mathcal{A}. \tag{3.72}$$

This states that the jump on the energy of tractions across a material interface is balanced with that of the normal component of the heat flux vector. If the material velocity is continuous across $\mathcal{A}$ using (3.63) this further reduces to

$$[\![\mathbf{q}]\!] \cdot \mathbf{n}_{\mathcal{A}} = 0 \qquad \text{on } \mathcal{A}. \tag{3.73}$$

If the discontinuity surface $\mathcal{A}$ coincides with the surface of the body ($\rho^+ = 0$, $\dot{\mathbf{x}}^- = \mathbf{w}$), (3.71) becomes

$$(\mathbf{q} - \mathbf{T}\,\dot{\mathbf{x}}^-) \cdot \mathbf{n} = -\mathbf{q}_0 \cdot \mathbf{n} - \mathbf{t}\cdot\dot{\mathbf{x}}^+ \qquad \text{on } \partial\mathcal{B}, \tag{3.74}$$

where $\mathbf{T}^+\mathbf{n}_{\mathcal{A}} = \mathbf{t}$, $\mathbf{q}^+\cdot\mathbf{n}_{\mathcal{A}} = -\mathbf{q}_0\cdot\mathbf{n}$, $\mathbf{T}^- = \mathbf{T}$, $\mathbf{q}^- = \mathbf{q}$ and $\mathbf{n}_{\mathcal{A}} = \mathbf{n}$ are set. (3.74) gives the boundary conditions on the energy flux across the surface of the body. If the tractions are attached to the surface, then $\dot{\mathbf{x}}^- = \dot{\mathbf{x}}^+$ and by employing (3.63), one obtains

$$\mathbf{q}\cdot\mathbf{n} = \mathbf{q}_0\cdot\mathbf{n} \qquad \text{on } \partial\mathcal{B}. \tag{3.75}$$

If the discontinuity surface is a fixed surface ($\mathbf{w} = \mathbf{0}$), (3.59) reduces to

$$[\![\rho\,(\varepsilon + \tfrac{1}{2}\,\dot{\mathbf{x}}\cdot\dot{\mathbf{x}})\,\dot{\mathbf{x}} - \mathbf{T}\,\dot{\mathbf{x}} + \mathbf{q}]\!] \cdot \mathbf{n}_{\mathcal{A}} = 0 \qquad \text{on } \mathcal{A}. \tag{3.76}$$

3.2.7 Entropy inequality

The second law of thermodynamics states that a non-negative entropy production exists in every thermodynamical processes, i. e. $\hat{\psi} = \hat{\eta} \geq 0$. Considering the second law of thermodynamics in combination with Table 3.1 and (3.52), the local form of the entropy inequality can be formulated as follows:

$$\rho\,\dot{\eta} + \operatorname{div}\left(\frac{\mathbf{q}}{\theta}\right) - \frac{\rho\, r}{\theta} \geq 0. \tag{3.77}$$

The local form of the entropy balance is used as a criterion to check whether or not thermomechanical processes are admissable, a condition that has to be satisfied by every admissable thermomechanical processes.

With introduction of the *Helmholtz free energy* ψ by

$$\psi = \varepsilon - \theta\,\eta \tag{3.78}$$

and eliminating the heat supply r in (3.77) by use of (3.70), the *generalized Clausius-Duhem* inequality can be obtained:

$$-\rho\,(\dot{\psi} + \eta\ \dot{\theta}) + \mathbf{T}\cdot\mathbf{D} - \frac{\mathbf{q}\cdot\operatorname{grad}\theta}{\theta} \geq 0. \tag{3.79}$$

The *Helmholtz* free energy plays an important role in the development of constitutive equations (*Haupt* [84], *Truesdell & Toupin* [176]).

3.2.8 Balance equations of electrodynamics

This subsection presents the balance equations of electrodynamics, which are known as *Maxwell*'s equations. Contrary to the balance laws of thermomechanics which can be derived only from the general volume balance law, the balance laws of the electrodynamics are obtained not only from the general volume balance law, but also from the general surface balance law.

The conservation of magnetic flux $\mathbf{b}$ is given by

$$\int_{\partial\mathcal{B}} \mathbf{b}\cdot\mathrm{d}\mathbf{a} = 0. \tag{3.80}$$

The conservation of electric flux $\mathbf{d}$, which is known as the *Gauß*'s law, is given by

$$\int_{\partial\mathcal{B}} \mathbf{d}\cdot\mathrm{d}\mathbf{a} = \int_{\mathcal{B}} q_e\,\mathrm{d}v. \tag{3.81}$$

(3.81) implies that the net electric flux $\mathbf{d}$ through a surface $\partial\mathcal{B}$ is equal to the total charge q_e enclosed within the volume $\mathcal{B}$. (3.80) and (3.81) are equivalent to the local forms

$$\operatorname{div}\mathbf{b} = 0 \qquad \text{in } \mathcal{B}, \tag{3.82}$$

$$\operatorname{div}\mathbf{d} = q_e \qquad \text{in } \mathcal{B}. \tag{3.83}$$

The corresponding jump conditions are given by

$$[\![\mathbf{b}]\!] \cdot \mathbf{n} = 0 \qquad \text{on } \mathcal{A}, \tag{3.84}$$

$$[\![\mathbf{d}]\!] \cdot \mathbf{n} = 0 \qquad \text{on } \mathcal{A}. \tag{3.85}$$

(3.82), (3.83) and the corresponding jump conditions (3.84), (3.85) follows from the application (3.46) and the divergence theorem (A.9) in (3.80) and (3.81). From Table 3.2 and (3.40), the global form of *Faraday*'s law can be written as

$$\frac{\mathrm{d}}{\mathrm{d}t} \int_{\mathcal{S}} \mathbf{b} \cdot \mathrm{d}\mathbf{a} = \oint_{\partial \mathcal{S}} (-\mathbf{e} - \dot{\mathbf{x}} \times \mathbf{b}) \cdot \mathrm{d}\mathbf{x}, \tag{3.86}$$

where $(-\mathbf{e} - \dot{\mathbf{x}} \times \mathbf{b})$ is the electromotive intensity. The local form of *Faraday*'s law can be obtained by employing (3.54), (3.55) and by considering (3.82). Thus,

$$\operatorname{rot} \mathbf{e} + \frac{\partial \mathbf{b}}{\partial t} = \mathbf{0} \qquad \text{in } \mathcal{S}. \tag{3.87}$$

The corresponding jump condition reads

$$[\![\mathbf{b} \times (\dot{\mathbf{x}} - \mathbf{w}) + \mathbf{e} + \dot{\mathbf{x}} \times \mathbf{b}]\!] \times \mathbf{n}_{\mathcal{C}} = \mathbf{0} \qquad \text{on } \mathcal{C}. \tag{3.88}$$

From Table 3.2 and (3.40), the global form of *Ampère*'s law can be written as

$$\frac{\mathrm{d}}{\mathrm{d}t} \int_{\mathcal{S}} -\mathbf{d} \cdot \mathrm{d}\mathbf{a} = \oint_{\partial \mathcal{S}} (-\mathbf{h} + \dot{\mathbf{x}} \times \mathbf{d}) \cdot \mathrm{d}\mathbf{x} + \int_{\mathcal{S}} (\mathbf{j} - q_e \, \dot{\mathbf{x}}) \cdot \mathrm{d}\mathbf{a}, \tag{3.89}$$

where $(-\mathbf{h} + \dot{\mathbf{x}} \times \mathbf{d})$ is the magnetomotive intensity. By employing (3.54), (3.55) and (3.83), the local form of the *Ampère*'s law

$$\operatorname{rot} \mathbf{h} = \frac{\partial \mathbf{d}}{\partial t} + \mathbf{j} \qquad \text{in } \mathcal{S}, \tag{3.90}$$

and the corresponding jump condition

$$[\![-\mathbf{d} \times (\dot{\mathbf{x}} - \mathbf{w}) + \mathbf{h} - \dot{\mathbf{x}} \times \mathbf{d}]\!] \times \mathbf{n}_{\mathcal{C}} = \mathbf{0} \qquad \text{on } \mathcal{C}. \tag{3.91}$$

can be obtained. For the discontinuity line $\mathcal{C}$ is equal to the material line, the jump conditions (3.88) and (3.90) reduce to

$$[\![\mathbf{e} + \dot{\mathbf{x}} \times \mathbf{b}]\!] \times \mathbf{n}_{\mathcal{C}} = \mathbf{0} \qquad \text{on } \mathcal{C}, \tag{3.92}$$

$$[\![\mathbf{h} - \dot{\mathbf{x}} \times \mathbf{d}]\!] \times \mathbf{n}_{\mathcal{C}} = \mathbf{0} \qquad \text{on } \mathcal{C}. \tag{3.93}$$

By transforming (3.87), (3.90), (3.82) and (3.83) into the *Fourier* space, the differential form of the *Maxwell* equations can be expressed as

$$\operatorname{rot} \mathbf{e}(\mathbf{x}, \omega) = i\,\omega\, \mathbf{b}(\mathbf{x}, \omega), \tag{3.94}$$

$$\operatorname{rot} \mathbf{h}(\mathbf{x}, \omega) = -i\,\omega\, \mathbf{d}(\mathbf{x}, \omega) + \mathbf{j}(\mathbf{x}, \omega), \tag{3.95}$$

$$\operatorname{div} \mathbf{b}(\mathbf{x}, \omega) = 0, \tag{3.96}$$

$$\operatorname{div} \mathbf{d}(\mathbf{x}, \omega) = q_e(\mathbf{x}, \omega), \tag{3.97}$$

where ω represents the frequency and $i = \sqrt{-1}$.

In the quasi-static limit $\omega \to 0$ the electric field $\mathbf{e}(\mathbf{x}, \omega)$ and the magnetic field $\mathbf{h}(\mathbf{x}, \omega)$ can be expanded into power series around $\omega = 0$, which can be written as

$$\begin{aligned} \mathbf{e}(\mathbf{x}, \omega) &= \sum_{k=0}^{\infty} \frac{\omega^k}{k!} \left[\frac{\partial^k}{\partial \omega^k} \mathbf{e}(\mathbf{x}, \omega) \right]_{\omega=0} = \sum_{k=0}^{\infty} \mathbf{e}^k(\mathbf{x}, \omega), \\ \mathbf{b}(\mathbf{x}, \omega) &= \sum_{k=0}^{\infty} \frac{\omega^k}{k!} \left[\frac{\partial^k}{\partial \omega^k} \mathbf{b}(\mathbf{x}, \omega) \right]_{\omega=0} = \sum_{k=0}^{\infty} \mathbf{b}^k(\mathbf{x}, \omega). \end{aligned} \tag{3.98}$$

By substituting the electromagnetic fields according to (3.98) into the *Faraday*'s law (3.94) and equating the same order of ω:

$$\operatorname{rot} \mathbf{e}^0(\mathbf{x}) = \mathbf{0}, \tag{3.99}$$

$$\operatorname{rot} \mathbf{e}^k(\mathbf{x}, \omega) = i\,\omega\, \mathbf{b}^{k-1}(\mathbf{x}, \omega) \qquad m = 1, 2, \ldots \ . \tag{3.100}$$

By applying the same treatment to other field quantities, the electrostatic equations can be obtained from (3.94) and (3.97) for $k = 0$, hence,

$$\operatorname{rot} \mathbf{e}^0(\mathbf{x}) = 0, \tag{3.101}$$

$$\operatorname{div} \mathbf{d}^0(\mathbf{x}) = q_e^0(\mathbf{x}), \tag{3.102}$$

and similarly by (3.95) and (3.96) the magnetostatic equations can be written in the form

$$\operatorname{rot} \mathbf{h}^0(\mathbf{x}) = \mathbf{j}^0(\mathbf{x}), \tag{3.103}$$

$$\operatorname{div} \mathbf{b}^0(\mathbf{x}) = 0. \tag{3.104}$$

It can be seen from (3.101) and (3.103) that in the quasi-static case the field quantities of the *Maxwell* equations can be decoupled into two cases, namely into the electrostatic and the magnetostatic case. It is known from vector analysis (*de Boer* [48]) that a rotation-free vector field can be expressed as a minus of a gradient of a scalar potential $U(\mathbf{x})$. Hence, $\mathbf{e}^0(\mathbf{x})$ may be written as

$$\mathbf{e}^0(\mathbf{x}) = -\operatorname{grad} U(\mathbf{x}). \tag{3.105}$$

A comprehensive discussion about this topic can be found elsewhere (*Eringen* & *Maugin* [63], *Jackson* [97]).

3.3 Constitutive Relations

The balance equations discussed in the last sections are universal laws which are valid in the free space and for every material. They are independent of the material properties and of the geometry of the boundary-value problems. However, balance relations themselves are usually insufficient to determine the physical fields of the bodies and because

of this shortcoming, additional equations are needed. Some of these so-called constitutive equations will be presented briefly in this section. These equations describe how the material distributes momentum and energy internally. By employing the axioms of the constitutive theory such as the *Clausius-Duhem* inequality (3.79), the *determinism*, the *local action*, the *equipresence*, the *material frame indifference*, and the *dissipation*, the dependence of the constitutive relations on the kinematical and physical variables can be determined. Then, upon the choice of the *Helmholtz* free energy ψ the special constitutive equations can be found. This section will focus on the constitutive equations for heat conductive media, linear rigid electromagnetic bodies and linear elastic materials. However, only the end result of these constitutive relations will be summarized here since the complete derivations and thorough discussions of them can be found elsewhere (*Ehlers* [58, 59, 55, 57, 60], *Haupt* [84]).

3.3.1 Heat conduction

In the framework of a linear theory, the relation between the heat flux vector $\mathbf{q}$ and the temperature gradient $\operatorname{grad}\theta$ as the driving force is given by the *Fourier*'s law

$$\mathbf{q} = -k \operatorname{grad}\theta, \tag{3.106}$$

where k is the isotropic thermal conductivity constant.

3.3.2 Linear elasticity

The theory of linear elasticity is valid within the limits of geometric linearization, i. e., in terms of infinitesimal deformation and strain, and hence, there is no difference between the reference and the actual configuration. The constitutive equation for a linear elastic solid relates the stress $\mathbf{T}$ and strain $\boldsymbol{\varepsilon}$ through the expression

$$\mathbf{T} = \overset{4}{\mathbf{C}}\,\boldsymbol{\varepsilon} \tag{3.107}$$

which is known as the generalized *Hooke*'s law. In terms of the Lamé constants λ and μ, the elastic tensor $\overset{4}{\mathbf{C}}$ for an isotropic body can be written as

$$\overset{4}{\mathbf{C}} = 2\mu\,(\mathbf{I}\otimes\mathbf{I})^{\overset{23}{T}} + \lambda\,\mathbf{I}\otimes\mathbf{I}, \tag{3.108}$$

where $\mathbf{I}$ is the second-rank identity tensor. The *Young*'s modulus E, *Poisson*'s ratio ν, bulk modulus K and shear modulus G are related to the Lamé constants in the form

$$\begin{aligned} E &= \mu\,(3\lambda + 2\mu)/(\lambda+\mu), \\ \nu &= \lambda/[2(\lambda+\mu)], \\ K &= \lambda + 2\mu/3, \\ G &= \mu. \end{aligned} \tag{3.109}$$

In the isotropic case, it is often very useful to split the stress and strain into spherical (hydrostatic) and deviatoric components. The spherical components of the stress $\mathbf{T}^K$ and of the strain $\boldsymbol{\varepsilon}^K$ are defined by

$$\mathbf{T}^K = \tfrac{1}{3}(\mathbf{T}\cdot\mathbf{I})\,\mathbf{I}, \tag{3.110}$$

$$\boldsymbol{\varepsilon}^K = \tfrac{1}{3}(\boldsymbol{\varepsilon}\cdot\mathbf{I})\,\mathbf{I}. \tag{3.111}$$

Then, the deviatoric stress $\mathbf{T}^D$ and strain $\boldsymbol{\varepsilon}^D$ take the form

$$\mathbf{T}^D = \mathbf{T} - \mathbf{T}^K, \tag{3.112}$$

$$\boldsymbol{\varepsilon}^D = \boldsymbol{\varepsilon} - \boldsymbol{\varepsilon}^K. \tag{3.113}$$

The exploitation of (3.108)-(3.113) allows to cast the stress-strain relations (3.107) into the form

$$\mathbf{T}^K = 3K\,\boldsymbol{\varepsilon}^K \tag{3.114}$$

and

$$\mathbf{T}^D = 2G\,\boldsymbol{\varepsilon}^D. \tag{3.115}$$

Here, K relates the spherical stress tensor $\mathbf{T}^K$ to the spherical strain tensor $\boldsymbol{\varepsilon}^K$, while G connects the deviatoric stress tensor $\mathbf{T}^D$ with deviatoric strain tensor $\boldsymbol{\varepsilon}^D$.

3.3.3 Linear electromagnetic rigid continua

The general constitutive relations for linear electromagnetic materials in the frequency domain have the form

$$\mathbf{d}(\mathbf{x},\omega) = \tilde{\boldsymbol{\varepsilon}}(\mathbf{x},\omega)\,\mathbf{e}(\mathbf{x},\omega) + \tilde{\boldsymbol{\xi}}(\mathbf{x},\omega)\,\mathbf{h}(\mathbf{x},\omega), \tag{3.116}$$

$$\mathbf{b}(\mathbf{x},\omega) = \tilde{\boldsymbol{\mu}}(\mathbf{x},\omega)\,\mathbf{h}(\mathbf{x},\omega) + \tilde{\boldsymbol{\zeta}}(\mathbf{x},\omega)\,\mathbf{e}(\mathbf{x},\omega), \tag{3.117}$$

where $\tilde{\boldsymbol{\varepsilon}}(\mathbf{x},\omega)$, $\tilde{\boldsymbol{\xi}}(\mathbf{x},\omega)$ $\tilde{\boldsymbol{\mu}}(\mathbf{x},\omega)$ and $\tilde{\boldsymbol{\zeta}}(\mathbf{x},\omega)$ are material parameter tensors of second-rank. The media, which are characterized by (3.116) and (3.117), are called as bianisotropic media (*Kong* [101]). The bianisotropic media become both polarized and magnetized if subjected to an electric or a magnetic field. When the media become only polarized under an electric field and become only magnetic under a magnetic field, the media are called anisotropic media. This can be expressed by the following constitutive equations:

$$\mathbf{d}(\mathbf{x},\omega) = \tilde{\boldsymbol{\varepsilon}}(\mathbf{x},\omega)\,\mathbf{e}(\mathbf{x},\omega), \tag{3.118}$$

$$\mathbf{b}(\mathbf{x},\omega) = \tilde{\boldsymbol{\mu}}(\mathbf{x},\omega)\,\mathbf{h}(\mathbf{x},\omega). \tag{3.119}$$

Isotropic media are media, whose polarization or magnetization are equivalent in all directions under an electric or magnetic field, respectively. Then, the second-rank tensors $\tilde{\boldsymbol{\varepsilon}}$ and $\tilde{\boldsymbol{\mu}}$ reduce to the scalar electric permittivity $\tilde{\varepsilon}$ and magnetic permeability $\tilde{\mu}$. The constitutive relations can simply be written as

$$\mathbf{d}(\mathbf{x},\omega) = \tilde{\varepsilon}(\mathbf{x},\omega)\,\mathbf{e}(\mathbf{x},\omega), \tag{3.120}$$

$$\mathbf{b}(\mathbf{x},\omega) = \tilde{\mu}(\mathbf{x},\omega)\,\mathbf{h}(\mathbf{x},\omega). \tag{3.121}$$

In vacuum the electric permittivity is $\tilde{\varepsilon} = \tilde{\varepsilon}_0 = 8.854 \times 10^{-12}$ farad/m and the magnetic permeability is $\tilde{\mu} = \tilde{\mu}_0 = 4\pi \times 10^{-7}$ henry/m. For the electrostatic or magnetostatic case the constitutive relations are independent of the frequency ω, thus (3.120) and (3.121) become

$$\mathbf{d}(\mathbf{x}) = \tilde{\varepsilon}(\mathbf{x})\,\mathbf{e}(\mathbf{x}), \tag{3.122}$$

$$\mathbf{b}(\mathbf{x}) = \tilde{\mu}(\mathbf{x})\,\mathbf{h}(\mathbf{x}). \tag{3.123}$$

In real media the electric field may also contribute to the electric current, which is expressed in the linear *Ohm*'s law

$$\mathbf{j}(\mathbf{x}) = \tilde{\sigma}(\mathbf{x})\,\mathbf{e}(\mathbf{x}), \tag{3.124}$$

where $\tilde{\sigma}(\mathbf{x})$ is the electrical conductivity. Since the *Maxwell*'s equations (3.94)-(3.97) are written in the complex notation, the material parameters are also given as complex-valued numbers. Using the constitutive relations (3.122) and (3.124), the right-hand-side of (3.95) can be written in terms of the electric field $\mathbf{e}$

$$-\mathrm{i}\,\omega\mathbf{d} + \mathbf{j} = -\mathrm{i}\,\omega \underbrace{(\tilde{\varepsilon} + \frac{\mathrm{i}\tilde{\sigma}}{\omega})}_{\tilde{\varepsilon}^c}\,\mathbf{e}. \tag{3.125}$$

The complex-valued permittivity $\tilde{\varepsilon}^c$ contains the material permittivity $\tilde{\varepsilon}$ as the real part and the ratio of the material conductivity $\tilde{\sigma}$ to the frequency ω, i. e., $\tilde{\sigma}/\omega$, as the imaginary part. These real and imaginary parts are connected to each other through the dispersion relation, which is also known as *Kramers-Kronig* relation (*Sihvola* [164]).

The electric current $\mathbf{j}$ is responsible for the loss of energy of the field, because $\mathbf{j}$ and $\mathbf{e}$ are in the same phases. In general, the imaginary part of $\tilde{\varepsilon}^c$ implies that the medium is dissipative. The propagating electromagnetic waves in such conductive media attenuate to $\exp(-1) \approx 37\%$ of their original value at a propagation distance δ_s (*Sihvola* [164]). This distance is known as the penetration depth or the skin depth and amounts to

$$\delta_s = \sqrt{\frac{2}{\omega\,\tilde{\mu}\,\tilde{\sigma}}}. \tag{3.126}$$

3.4 Concept of representative elementary volume

The concept of representative elementary volume (REV) is introduced to provide a valuable dividing boundary between macroscopic and microscopic theories in treating heterogeneous media. For scales larger than the REV, the macroscopic continuum theories for a homogeneous medium are applicable, while for scales smaller than the REV, the microstructure of the heterogeneous medium must be considered. In order to define the REV, the heterogeneous medium is assumed to be ergodic and to be statistically homogeneous. Recalling that the assumption of ergodicity allows replacing ensemble averages by volume averages. This assumption implies that instead of an observation of an esemble

of samples, an observation of a single sample is enough. The assumption of statistical homogeneity causes the volume average quantities not to depend on the volume. Therefore, it can be assumed that there exists a large enough subvolume of the sample which can be used to obtain essentially the same average quantities. This subvolume is referred to as the REV. The volume of the REV should be small enough to be seen, macroscopically, as a material point of the heterogeneous medium and large enough in the microscopical scale so that it consists of a large number of which statistically represent the local continuum properties. The best choice of the REV is the one that includes the most dominant features which have the largest influence on the overall properties of interest and, at the same time, yields the simplest model. Note that *representative* means that the REV will have the same macro properties as any other of such elements and as the whole medium. Therefore one can use a REV and the whole medium interchangeably. The definition applied here is a loose definition, a rigorous definition of a REV can be found in the work of *Drugan & Willis* [52].

The basic underlying assumption of statistical homogeneity is never exactly satisfied in actual problems, since to be exactly homogeneous, an infinite volume is needed. Thus, it is important to assure oneself that homogeneity can be assumed approximately in space intervals, which are larger compared to the characteristic lengths (the typical size of grains). In this context, one may consider three length scales which are related to the concept of the REV. The first one is called microscale which defines the heterogeneity (associated with the grains) within an REV. The second one is called miniscale which defines the size of an REV. The third one is called macroscale which is associated with the sample. To provide applicable results, these length scales have to satisfy following inequalities:

$$\text{MICRO} \ll \text{MINI} \ll \text{MACRO}. \tag{3.127}$$

This is known as the *Hashin* MMM principle [80]. If the lengths of the microscale, of the miniscale and of the macroscale are denoted by d, D and L, respectively, then, according to the *Hashin* MMM principle, these length scales satisfy

$$\frac{d}{D} \ll 1, \qquad \frac{D}{L} \ll 1. \tag{3.128}$$

Let $\mathbf{x}$ be a position vector to a reference point in the REV (e. g., centroid) defining its location and $\mathbf{y}$ be a local coordinate system being defined inside the REV and originating at $\mathbf{x}$. The macroscopic physical quantity $\overline{\boldsymbol{\phi}}(\mathbf{x})$ (e. g., macro heat flux, macro strain fields) depends on $\mathbf{x}$, while the corresponding micro quantity $\boldsymbol{\phi}(\mathbf{x}, \mathbf{y})$ within the REV is a function of both global and local variables, $\mathbf{x}$ and $\mathbf{y}$. The macroscopic quantity can be obtained from the microscopic one by volume averaging over the REV $\mathcal{B}$:

$$\overline{\boldsymbol{\phi}}(\mathbf{x}) = \frac{1}{V} \int_{\mathcal{B}} \boldsymbol{\phi}(\mathbf{x}, \mathbf{y}) \, \mathrm{d}v. \tag{3.129}$$

Thereby, the integration over $\mathcal{B}$ is taken with respect to the local coordinate $\mathbf{y}$ and V is the volume of the REV. This procedure is known as homogenization.

The inverse procedure is called as localization. In this case, starting with the macroscopic quantity $\overline{\boldsymbol{\phi}}(\mathbf{x})$ the corresponding microscopic quantity $\boldsymbol{\phi}(\mathbf{x}, \mathbf{y})$ can be determined

using the microscopic constitutive laws, the boundary conditions and the equations of microscopic equilibrium:

$$\operatorname{div}_{\mathbf{y}} \boldsymbol{\phi} = 0. \tag{3.130}$$

Here, the operator $\operatorname{div}_{\mathbf{y}}$ means that the divergence operator is taken with respect to $\mathbf{y}$. Of course, the obtained micro quantity $\boldsymbol{\phi}(\mathbf{x}, \mathbf{y})$ must satisfy the corresponding condition (3.129).

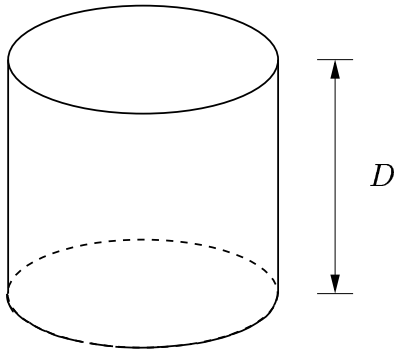

Figure 3.3: Pillbox used in the proof of the scale separation.

Due to the argument of the scale separation, the volume sources and inertia effects can be neglected in (3.130). To prove it, consider that the REV has a shape of a flat cylindrical pill box as shown in Fig. 3.3. If D denotes the height of this pill box, then $V(\mathcal{B}) = D\,A(\partial\mathcal{B})$. Furthermore, in (3.38) the integration of the field ψ and of the external supply σ in (3.38) are assumed to satisfy the axiom of continuity with respect to the volume $V(\mathcal{B})$. This axiom means that for any configuration $\boldsymbol{\chi}_t$ of $\mathcal{B}$ there are positive constants α and β, which depend on $\boldsymbol{\chi}_t$, such that if $V(\mathcal{B})$ is sufficiently small, then

$$\begin{aligned} \left| \int_{\mathcal{B}} \psi \, \mathrm{d}v \right| &\leq \alpha\, V(\mathcal{B}), \\ \left| \int_{\mathcal{B}} \sigma \, \mathrm{d}v \right| &\leq \beta\, V(\mathcal{B}). \end{aligned} \tag{3.131}$$

Similarly, the integration of the efflux term $\boldsymbol{\phi}\,\mathbf{n}$ can be bounded:

$$\left| \int_{\partial\mathcal{B}} \boldsymbol{\phi} \cdot \mathrm{d}\mathbf{a} \right| \leq \gamma\, A(\partial\mathcal{B}). \tag{3.132}$$

Therein, γ is a positive constant, which depends on the configuration $\boldsymbol{\chi}_t$. Applying (3.38) to the REV and taking the limit $D \to 0$, the disk $\partial\mathcal{B}$ being kept fixed, so that its area remains constant. The limit of the integral over the volume is 0, since the parameter D tends to 0. Thus only the limit of the integral over the surface remains to be considered:

$$\lim_{D \to 0} \int_{\partial\mathcal{B}} \boldsymbol{\phi} \cdot \mathrm{d}\mathbf{a} = 0. \tag{3.133}$$

For validity of the same type of constitutive laws on micro and macroscale, the so-called *Hill*'s condition [93], which requires the equality between micro and macro energy, must be satisfied. The *Hill*'s condition implies the ergodicity condition. For an example, a linear elastic heterogeneous material obeys a global (effective) *Hooke*'s law if

$$\overline{\mathbf{T}\,\boldsymbol{\varepsilon}} = \overline{\mathbf{T}}\,\overline{\boldsymbol{\varepsilon}}, \tag{3.134}$$

where $\mathbf{T}$ and $\boldsymbol{\varepsilon}$ are the stress and strain fields, respectively.

To produce a statistical homogeneity field in a heterogeneous medium it is expedient to apply boundary conditions that produce homogeneous fields in an homogeneous body. Such boundary conditions will consequently be called homogeneous and will be discussed in the next subsections.

3.5 Boundary conditions associated with REV

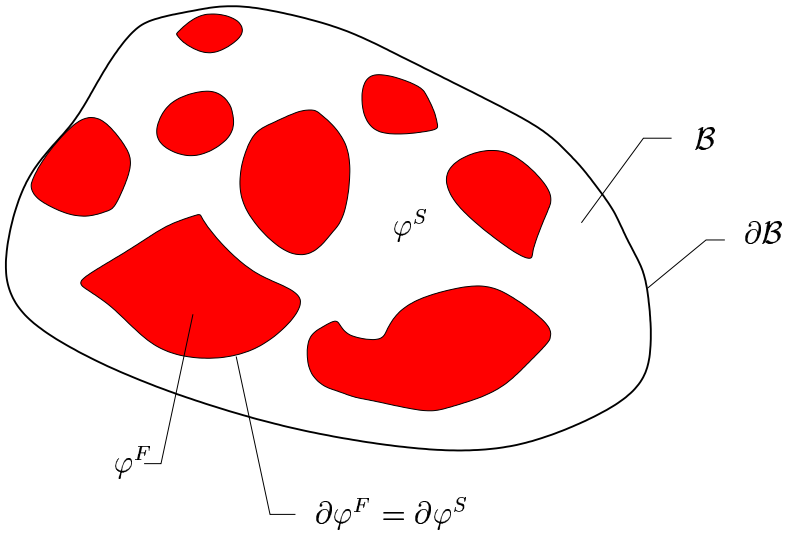

Figure 3.4: Inhomogeneous material $\mathcal{B} = \mathcal{B}^{\mathcal{S}} \cup \mathcal{B}^{\mathcal{F}}$ composed of the phases φ^S and φ^F.

3.5.1 Heat conduction problem

The average gradient theorem.

If a linear boundary temperature is prescribed on the boundary $\partial\mathcal{B}$, then the external boundary condition may take the form of

$$\theta_0 = \mathbf{p}_0 \cdot \mathbf{x} \qquad \text{on } \partial\mathcal{B}, \tag{3.135}$$

where $\mathbf{p}_0$ is a constant vector. Then, the volume average of the temperature gradient $\overline{\operatorname{grad}\theta}$ of the medium can be completely determined in terms of $\mathbf{p}_0$. If the volume average

of an arbitrary integrable field quantity $\mathbf{p}(\mathbf{x})$ is defined by

$$\overline{\mathbf{p}} = \frac{1}{V}\int_{\mathcal{B}} \mathbf{p}(\mathbf{x})\,\mathrm{d}v, \tag{3.136}$$

where V is the volume of the body $\mathcal{B}$, then, the volume average of the temperature gradient can be written as

$$\overline{\operatorname{grad}\theta} = \frac{1}{V}\int_{\mathcal{B}} \operatorname{grad}\theta\,\mathrm{d}v = \frac{1}{V}\left[\int_{\mathcal{B}^F} \operatorname{grad}\theta\,\mathrm{d}v + \int_{\mathcal{B}^S} \operatorname{grad}\theta\,\mathrm{d}v\right]. \tag{3.137}$$

The volume integral can be transformed to the surface integral using theorem (A.13)

$$\overline{\operatorname{grad}\theta} = \frac{1}{V}\left[\int_{\partial\mathcal{B}^F} \theta\,\mathrm{d}\mathbf{a} + \int_{\partial\mathcal{B}^S} \theta\,\mathrm{d}\mathbf{a}\right], \tag{3.138}$$

where $\partial\mathcal{B}^F$ and $\partial\mathcal{B}^S$ are the bounding surfaces of phases φ^F and φ^S, respectively. The interfaces $\partial\mathcal{B}^F \cap \partial\mathcal{B}^S$ and the external surface $\partial\mathcal{B}$ are included in these surfaces. For a perfect bonded material, the temperature θ is continuous across the interfaces $\partial\mathcal{B}^F \cap \partial\mathcal{B}^S$ and it follows that the contributions from $\partial\mathcal{B}^F \cap \partial\mathcal{B}^S$ in the two integrals of (3.137) invalidate each other. By substituting (3.135) into (3.137) and transforming back to the volume integration, one comes up with

$$\overline{\operatorname{grad}\theta} = \frac{1}{V}\int_{\partial\mathcal{B}} \theta\,\mathrm{d}\mathbf{a} = \mathbf{p}_0. \tag{3.139}$$

The average flux theorem

If at the surface boundary $\partial\mathcal{B}$ the normal component of the heat flux is prescribed, then one may write:

$$q_s = -\mathbf{q}_0 \cdot \mathbf{n}. \tag{3.140}$$

Here, q_s can be interpreted as the heat influx and $\mathbf{n}$ denotes the outwards oriented unit surface normal of $\partial\mathcal{B}$. For this boundary condition the average heat flux $\overline{\mathbf{q}}$ is identical to the prescribed heat flux $\mathbf{q}_0$, which can be established as follows. The average heat flux $\overline{\mathbf{q}}$ is given by

$$\overline{\mathbf{q}} = \frac{1}{V}\int_{\mathcal{B}} \mathbf{q}\,\mathrm{d}v = \frac{1}{V}\left[\int_{\mathcal{B}^F} \mathbf{q}\,\mathrm{d}v + \int_{\mathcal{B}^S} \mathbf{q}\,\mathrm{d}v\right]. \tag{3.141}$$

By employing $\operatorname{grad}\mathbf{x} = \mathbf{I}$ and $\operatorname{div}\mathbf{q} = 0$, the heat flux $\mathbf{q}$ can be reformulated as

$$\mathbf{q} = (\operatorname{grad}\mathbf{x})\,\mathbf{q} + (\operatorname{div}\mathbf{q})\,\mathbf{x} = \operatorname{div}(\mathbf{x}\otimes\mathbf{q}). \tag{3.142}$$

Thus, one has

$$\overline{\mathbf{q}} = \frac{1}{V}\left\{\int_{\partial\mathcal{B}^F} (\mathbf{q}\cdot\mathbf{n})\,\mathbf{x}\,\mathrm{d}a + \int_{\partial\mathcal{B}^S} (\mathbf{q}\cdot\mathbf{n})\,\mathbf{x}\,\mathrm{d}a\right\}. \tag{3.143}$$

If the material is perfectly bonded, the integration of two terms at the internal boundaries $\partial\mathcal{B}^F \cap \partial\mathcal{B}^S$ invalidate each other, one needs to evaluate the integration solely at the outer boundary $\partial\mathcal{B}$. With the boundary-value (3.140) one obtains

$$\overline{\mathbf{q}} = -\frac{1}{V}\int_{\partial\mathcal{B}} (\mathbf{q}_0\cdot\mathbf{n})\,\mathbf{x}\,\mathrm{d}a = -\frac{1}{V}\int_{\partial\mathcal{B}} (\mathbf{x}\otimes\mathrm{d}\mathbf{a})\,\mathbf{q}_0 = -\frac{1}{V}\int_{\mathcal{B}} (\operatorname{grad}\mathbf{x})\,\mathbf{q}_0\,dv = -\mathbf{q}_0. \tag{3.144}$$

3.5.2 Elastostatic case

The average strain theorem

If a displacement $\mathbf{u}_0 = \boldsymbol{\varepsilon}_0\mathbf{x}$ is applied on $\partial\mathcal{B}$, the volume average strain can be expressed in terms of the prescribed displacement components which are independent of the microgeometry and the material parameters of the components. The volume average strain tensor $\overline{\boldsymbol{\varepsilon}}$ reads

$$\overline{\boldsymbol{\varepsilon}} = \frac{1}{V}\int_{\mathcal{B}} \boldsymbol{\varepsilon}(\mathbf{x})\,\mathrm{d}v = \frac{1}{V}\left[\int_{\mathcal{B}^F} \boldsymbol{\varepsilon}(\mathbf{x})\,\mathrm{d}v + \int_{\mathcal{B}^S} \boldsymbol{\varepsilon}(\mathbf{x})\,\mathrm{d}v\right]. \tag{3.145}$$

Using the strain-displacement relations (3.37) and the divergence theorem, (3.145) becomes

$$\overline{\boldsymbol{\varepsilon}} = \frac{1}{2V}\left[\int_{\partial\mathcal{B}^F} (\mathbf{u}\otimes\mathrm{d}\mathbf{a} + \mathrm{d}\mathbf{a}\otimes\mathbf{u}) + \int_{\partial\mathcal{B}^S} (\mathbf{u}\otimes\mathrm{d}\mathbf{a} + \mathrm{d}\mathbf{a}\otimes\mathbf{u})\right]. \tag{3.146}$$

The boundaries $\mathcal{B}^F$ and $\mathcal{B}^S$ are the whole boundaries for both phases consisting of the external and internal parts. If the material is perfectly bonded, the contribution of internal boundaries $\partial\varphi^F$ and $\partial\varphi^S$ invalidate each other, which leads to

$$\begin{aligned}\overline{\boldsymbol{\varepsilon}} &= \frac{1}{2V}\int_{\partial\mathcal{B}} (\mathbf{u}\otimes\mathrm{d}\mathbf{a} + \mathrm{d}\mathbf{a}\otimes\mathbf{u}) = \frac{1}{2V}\int_{\partial\mathcal{B}} [(\boldsymbol{\varepsilon}_0\mathbf{x})\otimes\mathrm{d}\mathbf{a} + \mathrm{d}\mathbf{a}\otimes(\boldsymbol{\varepsilon}_0\mathbf{x})] \\ &= \frac{1}{2V}\int_{\mathcal{B}} \{\mathrm{grad}\,(\boldsymbol{\varepsilon}_0\mathbf{x}) + [\mathrm{grad}\,(\boldsymbol{\varepsilon}_0\mathbf{x})]^T\}\,\mathrm{d}v = \boldsymbol{\varepsilon}_0.\end{aligned} \tag{3.147}$$

The average stress theorem

If a uniform traction $\mathbf{t} = \mathbf{T}_0\mathbf{n}$ is prescribed on $\partial\mathcal{B}$, the volume average stresses can be formulated in terms of the boundary traction only. The volume average stresses are independent of the microgeometry and the material parameters of the components. Due to the argument of the scale separation, $\mathrm{div}\,\mathbf{T} = 0$, then

$$\mathrm{div}\,(\mathbf{x}\otimes\mathbf{T}) = (\mathrm{grad}\,\mathbf{x})\,\mathbf{T}^T + \mathbf{x}\otimes\mathrm{div}\,\mathbf{T} = (\mathrm{grad}\,\mathbf{x})\,\mathbf{T} = \mathbf{I}\,\mathbf{T} = \mathbf{T}. \tag{3.148}$$

Using (3.148), the volume average stress tensor $\overline{\mathbf{T}}$ can be evaluated:

$$\begin{aligned}\overline{\mathbf{T}} &= \frac{1}{V}\int_{\mathcal{B}} \mathbf{T}\,\mathrm{d}v = \frac{1}{V}\int_{\mathcal{B}} \mathrm{div}\,(\mathbf{x}\otimes\mathbf{T})\,\mathrm{d}v = \frac{1}{V}\int_{\partial\mathcal{B}} (\mathbf{x}\otimes\mathbf{T})\,\mathrm{d}\mathbf{a} \\ &= \frac{1}{V}\int_{\partial\mathcal{B}} (\mathbf{x}\otimes\mathbf{T}_0)\,\mathrm{d}\mathbf{a} = \frac{1}{V}\int_{\mathcal{B}} \mathrm{div}\,(\mathbf{x}\otimes\mathbf{T}_0)\,\mathrm{d}v = \mathbf{T}_0.\end{aligned}$$

3.6 Instances of the *Hill*'s condition

In this section, the validity of the same type of constitutive laws on micro- and macroscale, the so-called *Hill*'s condition [93] is presented. The *Hill*'s condition requires the equality between micro and macro energy, must be satisfied and it implies the ergodicity condition.

By assuming that the homogeneous medium admits an effective dissipative potential, the average values of the heat flux and the temperature gradient can be related to the average value of the dissipative energy (for a linear conductivity case). The *Hill*'s condition for a linear conductivity case is given by

$$\overline{\mathbf{q} \cdot \operatorname{grad} \theta} = \overline{\mathbf{q}} \cdot \overline{\operatorname{grad} \theta}. \tag{3.149}$$

It can be proven that under the given boundary conditions as described in Section 3.5.1, the *Hill*'s condition holds. Due to the argument of the scale separation, $\operatorname{div} \mathbf{q} = 0$, then the average of the dissipative potential can be formulated as

$$\frac{1}{2}\overline{\mathbf{q} \cdot \operatorname{grad} \theta} = \frac{1}{2V}\int_{\mathcal{B}} \mathbf{q} \cdot \operatorname{grad} \theta \mathrm{d}v = \frac{1}{2V}\int_{\mathcal{B}} \operatorname{div}(\theta\, \mathbf{q}) \mathrm{d}v = \frac{1}{2V}\int_{\partial\mathcal{B}} \theta\, \mathbf{q} \cdot \mathrm{d}\mathbf{a}. \tag{3.150}$$

If $\theta_0 = \mathbf{p}_0 \cdot \mathbf{x}$ at $\partial\mathcal{B}$, then (3.150) becomes

$$\begin{aligned} \frac{1}{2}\overline{\mathbf{q} \cdot \operatorname{grad} \theta} &= \frac{1}{2}\mathbf{p}_0 \cdot \frac{1}{V}\int_{\partial\mathcal{B}} \mathbf{x}\,(\mathbf{q} \cdot \mathrm{d}\mathbf{a}) = \frac{1}{2}\overline{\operatorname{grad} \theta} \cdot \frac{1}{V}\int_{\mathcal{B}} \operatorname{div}(\mathbf{x} \otimes \mathbf{q})\, \mathrm{d}v \\ &= \frac{1}{2}\overline{\operatorname{grad} \theta} \cdot \frac{1}{V}\int_{\mathcal{B}} \mathbf{q}\, \mathrm{d}v = \frac{1}{2}\overline{\operatorname{grad} \theta} \cdot \overline{\mathbf{q}} \end{aligned} \tag{3.151}$$

If $q = -\mathbf{q}_0 \cdot \mathbf{n}$ at $\partial\mathcal{B}$, then (3.150) becomes

$$\frac{1}{2}\overline{\mathbf{q} \cdot \operatorname{grad} \theta} = -\frac{1}{2V}\mathbf{q}_0 \cdot \int_{\partial\mathcal{B}} \theta\, \mathrm{d}\mathbf{a} = \frac{1}{2}\overline{\mathbf{q}} \cdot \frac{1}{V}\int_{\partial\mathcal{B}} \operatorname{grad} \theta\, \mathrm{d}v = \frac{1}{2}\overline{\mathbf{q}} \cdot \overline{\operatorname{grad} \theta} \tag{3.152}$$

In the linear elastic case, the *Hill*'s condition states that the average values of stress and strain can be connected to the average value of the elastic potential energy. In this case the *Hill*'s condition reads

$$\overline{\mathbf{T} \cdot \boldsymbol{\varepsilon}} = \overline{\mathbf{T}} \cdot \overline{\boldsymbol{\varepsilon}}. \tag{3.153}$$

It can be proven that under the given boundary conditions as described in Section 3.5.2, the *Hill*'s condition holds. For $\operatorname{div} \mathbf{T} = 0$ (the argument of the scale separation), the average of the potential energy can be formulated as

$$\frac{1}{2}\overline{\mathbf{T} \cdot \boldsymbol{\varepsilon}} = \frac{1}{2V}\int_{\mathcal{B}} \mathbf{T} \cdot \operatorname{grad} \mathbf{u}\, \mathrm{d}v = \frac{1}{2V}\int_{\mathcal{B}} \operatorname{div}(\mathbf{T}\mathbf{u})\, \mathrm{d}v = \frac{1}{2V}\int_{\partial\mathcal{B}} (\mathbf{T}\,\mathbf{u}) \cdot \mathrm{d}\mathbf{a}. \tag{3.154}$$

If the traction $\mathbf{t} = \mathbf{T}_0\mathbf{n}$ at $\partial\mathcal{B}$ is prescribed, then one has

$$\begin{aligned} \frac{1}{2}\overline{\mathbf{T} \cdot \boldsymbol{\varepsilon}} &= \frac{1}{2V}\int_{\partial\mathcal{B}} (\mathbf{T}\,\mathbf{u}) \cdot \mathrm{d}\mathbf{a} = \frac{1}{2V}\int_{\partial\mathcal{B}} (\mathbf{T}\mathbf{n}) \cdot \mathbf{u}\, \mathrm{d}a = \frac{1}{2V}\mathbf{T}_0 \cdot \int_{\partial\mathcal{B}} \mathbf{u} \otimes \mathrm{d}\mathbf{a} \\ &= \frac{1}{2}\mathbf{T}_0 \cdot \int_{\mathcal{B}} \operatorname{grad} \mathbf{u}\, \mathrm{d}v = \frac{1}{2}\overline{\mathbf{T}} \cdot \frac{1}{V}\int_{\mathcal{B}} \boldsymbol{\varepsilon}\, \mathrm{d}v = \frac{1}{2}\overline{\mathbf{T}} \cdot \overline{\boldsymbol{\varepsilon}}. \end{aligned} \tag{3.155}$$

Thereby, the average stress theorem (3.149) and $\operatorname{div} \mathbf{T} = 0$ are used. If the displacement $\mathbf{u}_0 = \boldsymbol{\varepsilon}_0\mathbf{x}$ at $\partial\mathcal{B}$ is given, then

$$\begin{aligned} \frac{1}{2}\overline{\mathbf{T} \cdot \boldsymbol{\varepsilon}} &= \frac{1}{2V}\int_{\partial\mathcal{B}} (\mathbf{T}\,\mathbf{u}) \cdot \mathrm{d}\mathbf{a} = \frac{1}{2V}\int_{\partial\mathcal{B}} (\boldsymbol{\varepsilon}_0\,\mathbf{x}) \cdot \mathbf{T}\, \mathrm{d}\mathbf{a} = \frac{1}{2V}\int_{\mathcal{B}} \operatorname{div}[\mathbf{T}\,(\boldsymbol{\varepsilon}_0\,\mathbf{x})]\, \mathrm{d}v \\ &= \frac{1}{2V}\int_{\mathcal{B}} [\mathbf{T} \cdot (\boldsymbol{\varepsilon}_0 \operatorname{grad} \mathbf{x})]\, \mathrm{d}v = \frac{1}{2V}\int_{\mathcal{B}} \mathbf{T}\, \mathrm{d}v \cdot \boldsymbol{\varepsilon}_0 = \frac{1}{2}\overline{\mathbf{T}} \cdot \overline{\boldsymbol{\varepsilon}}, \end{aligned} \tag{3.156}$$

where the average strain theorem (3.147) and $\operatorname{div} \mathbf{T} = 0$ are used.

3.7 Definition of effective material parameters

The objective of this section is to define precisely what the *effective material parameters* mean. A precise definition is required if one wishes to make precise mathematical statements about it. The definitions of effective material parameters will be given in the framework of the so-called *direct method* (*Hashin* [80], *Beran* [14], *Aboudi* [1]). In this definition, the effective material parameter provides a relation between the *average field* and the *average flux*. Another definition is based on the energy method (*Hashin* [80], *Beran* [14], *Aboudi* [1]). The average and energy methods were proven by *Hill* [92], to be equivalent if the *Hill* condition is fulfilled (see also *Nemat-Nasser* & *Hori* [135], *Aboudi* [1]). Another way to obtain the effective material properties is using forward amplitude scattering in the wave propagation context (*Sheng* [162], *Sabina* & *Willis* [152], *Stroud* & *Pan* [167]). For simplicity, the medium is assumed to be isotropic on both micro- and macrolevels. In general, the media can be anisotropic, even if they are isotropic on the microscale. This effect arises out of the asymmetry of the microgeometries.

The formulation of the effective material parameter will make use of the concept of the REV. In formulating boundary-value problems associated with an REV, the body forces and other inertia terms can be excluded, because these forces represent the effect of the materials not in contact with the considered continuum (*Nemat-Nasser* & *Hori* [135] p. 19). For example, the effective elastic moduli of the heterogeneous medium are the same on earth as well as on the moon, although the body forces are different for both places. This can be rigorously proven using the asymptotic method of multiple scales (*Bensoussan et al.* [13]). However, in this thesis, the proof will make use of scale separation.

To be more specific, the random medium under study is considered as a biphasic medium composed of phases φ^S and φ^F, which can be any materials. The interface between both phases is denoted by $\partial\varphi^F = \partial\varphi^S$.

3.7.1 Effective thermal conductivity

In this subsection, the precise definition of the effective thermal conductivity is given. This definition, by mathematical analogy, can be used for the magnetic permeability, the electric permittivity, the electric conductivity, and the diffusion coefficient. Furthermore, the definition can be directly applied to the complex-valued electric permittivity (frequency dependent permittivity), if the field quantities are considered to be complex-valued quantities (frequency-dependence).

The local heat conduction reads

$$\operatorname{div} \mathbf{q}(\mathbf{x}) = 0 \qquad \mathbf{x} \in \mathcal{B},\ \mathbf{x} \notin \partial\varphi^F. \tag{3.157}$$

The local *Fourier*'s law (3.106)

$$\mathbf{q}(\mathbf{x}) = -k(\mathbf{x}) \operatorname{grad} \theta(\mathbf{x}), \tag{3.158}$$

where

$$k(\mathbf{x}) = k^F\ \mathcal{I}^F(\mathbf{x}) + k^S\ \mathcal{I}^S(\mathbf{x}) \tag{3.159}$$

is a function of the thermal conductivities of phases φ^F and φ^S, i. e., k^F and k^S, respectively. Here, $\mathcal{I}^F(\mathbf{x})$ and $\mathcal{I}^S(\mathbf{x})$ are the indicator functions given by (2.1). Across the interface $\partial\varphi^F$, the temperature θ and the normal heat flux $q_n = \mathbf{q}\cdot\mathbf{n}$ must be continuous. Here, $\mathbf{n}$ is the normal vector of the interface. The effective thermal conductivity $\overline{k}$ relates the average of the heat flux $\overline{\mathbf{q}}$ to the average of the gradient $\overline{\operatorname{grad}\theta}$ of the temperature field:

$$\overline{\mathbf{q}} = -\overline{k}\,\overline{\operatorname{grad}\theta(\mathbf{x})}. \tag{3.160}$$

The results obtained are valid for the heat conduction problem, however, they are applicable straightforwardly to electrostatics, magnetostatics, electric conduction, diffusion and thermal conduction problems (see Table 3.3). This circumstance is in agreement with the universality of the disordered potential equations, which govern all these kinds of physical problems.

Problem	Potential θ	$\operatorname{grad}\theta$	k	$\mathbf{q}$
electrostatics	electric potential	electric field	permittivity	electric displacement
magnetostatics	magnetic potential	magnetic field	magnetic permeability	magnetic induction
electric conduction	electric potential	electric field	electric conductivity	current density
diffusion	concentration	concentration gradient	diffusion constants	mass flux
heat conduction	temperature	temperature gradient	heat conductivity	heat flux

Table 3.3: Disordered potential problems which are considered here.

3.7.2 Effective elastic moduli

In this subsection, the effective elastic moduli is precisely defined. The local equilibrium equation reads

$$\operatorname{div}\mathbf{T}(\mathbf{x}) = \mathbf{0} \qquad \mathbf{x}\in\mathcal{B} \quad \text{and} \quad \mathbf{x}\notin\partial\varphi^F, \tag{3.161}$$

where $\mathbf{T}(\mathbf{x})$ denotes the stress tensor. The local *Hooke*'s law is given by

$$\mathbf{T} = \overset{4}{\mathbf{C}}\,\boldsymbol{\varepsilon}. \tag{3.162}$$

The effective elastic tensor $\overline{\overset{4}{\mathbf{C}}}$ is defined by the average stress $\overline{\mathbf{T}}$ and the average strain $\overline{\boldsymbol{\varepsilon}}$ tensors via

$$\overline{\mathbf{T}} = \overline{\overset{4}{\mathbf{C}}}\,\overline{\boldsymbol{\varepsilon}}. \tag{3.163}$$

For an isotropic material, the effective elastic tensor is given by

$$\overset{4}{\mathbf{C}} = 2\,\overline{\mu}\,(\mathbf{I}\otimes\mathbf{I})^{23}_{T} + \overline{\lambda}\,\mathbf{I}\otimes\mathbf{I}. \tag{3.164}$$

The average strain and stress tensors can be decomposed into their spherical and deviatoric parts as described in Section 3.3.2:

$$\overline{\mathbf{T}}^K = \tfrac{1}{3}\left(\overline{\mathbf{T}}\cdot\mathbf{I}\right)\mathbf{I}, \tag{3.165}$$

$$\overline{\boldsymbol{\varepsilon}}^K = \tfrac{1}{3}\left(\overline{\boldsymbol{\varepsilon}}\cdot\mathbf{I}\right)\mathbf{I}, \tag{3.166}$$

$$\overline{\mathbf{T}}^D = \overline{\mathbf{T}} - \overline{\mathbf{T}}^K, \tag{3.167}$$

$$\overline{\boldsymbol{\varepsilon}}^D = \overline{\boldsymbol{\varepsilon}} - \overline{\boldsymbol{\varepsilon}}^K. \tag{3.168}$$

$\overline{\mathbf{T}}^K$ and $\overline{\mathbf{T}}^D$ are the average spherical and deviatoric stress tensor, respectively, and $\overline{\boldsymbol{\varepsilon}}^K$ and $\overline{\boldsymbol{\varepsilon}}^D$ are the average spherical and deviatoric strain tensor, respectively. Introduction of (3.165)-(3.168) into (3.163), considering (3.164) and (3.109) leads to

$$\overline{\mathbf{T}}^K = 3\,\overline{K}\,\overline{\boldsymbol{\varepsilon}}^K, \tag{3.169}$$

$$\overline{\mathbf{T}}^D = 2\,\overline{G}\,\overline{\boldsymbol{\varepsilon}}^D. \tag{3.170}$$

Christensen [44] showed that under creeping flow conditions, there is a similarity between the determination of the effective shear modulus of composite materials and the determination of effective viscosity of a suspension of perfectly rigid particles in an incompressible fluid.

Chapter 4

Numerical solution techniques

The objective of this chapter is to give the numerical methods to solve the boundary-value problems that have been discussed in Chapter 3, if the detailed microgeometry of the random media is known. Practically, for real materials, the knowledge of the microgeometry can be obtained by microtomography (*Garboczi* & *Bentz* [69], *van Genabeek* & *Rothman* [178], *Widjajakusuma et al.* [185] and *Michel et al.* [123]), while for idealized materials, the knowledge of the microgeometry can be found by models (*Garboczi* & *Bentz* [68], *Yeong* & *Torquato* [195] and *Biswal et al.* [32]). Usually, microgeometric information is stored in discrete digital image form; thus, to solve boundary-value problems on these digitized heterogeneous media, computer algorithms are needed. Therefore, in this chapter, a discussion regarding computer algorithms will be presented. From the solutions of these boundary-value problems, the effective material parameters can be directly determined by averaging the solutions. Three cases regarding their physical and mathematical nature will be discussed. The first one is the case of the effective thermal conductivity of a heterogeneous medium solved using a finite volume discretization. The second case is the determination of the frequency-dependent effective permittivity of a medium composed of two phases at finite frequency. This problem is also solved using a finite volume program. The finite volume method can be seen as a special case of the weighted residual methods. This method is chosen because of its compatibility with the definition of connectivity for a digitized medium which is introduced in Section 2.3. With respect to the connectivity definition, the heat can flow only through the element's interface, not through the element's nodes (Section 4.1 and Figure 4.2). Both cases mentioned above are very similar; both of them are solved in the same way by discretizing the *Laplace* equation. The difference between them is that the discretized equations of the thermal conductivity problem are given as a system of linear equations of real variables, while the frequency-dependent permittivity case gives a system of linear equations of complex-valued variables. At zero frequency, the effective permittivity problem is governed by the same equation as the effective conductivity problem, because both problems have the same mathematical structure as shown in Table 3.3. Finally, the third case concerns the effective elastic moduli of a medium composed of different materials which is solved using the finite element method. The finite element method will be derived from the *Rayleigh-Ritz* variational principle.

4.1 *Laplace* equation

In the heat conduction case, the governing partial differential equation is the *Laplace* equation

$$\operatorname{div}[k(\mathbf{x}) \operatorname{grad} \theta(\mathbf{x})] = 0, \tag{4.1}$$

where $k(\mathbf{x})$ is the local thermal conductivity and $\theta(\mathbf{x})$ is the local temperature field. The thermal conductivity $k(\mathbf{x})$ is dependent on the thermal conductivities k^F and k^S belonging to the phases φ^F and φ^S, respectively. Thus,

$$k(\mathbf{x}) = k^F \, \mathcal{I}^F(\mathbf{x}) + k^S \, \mathcal{I}^S(\mathbf{x}). \tag{4.2}$$

Since $k^F \neq k^S$, $k(\mathbf{x})$ is a discontinuous function with the discontinuity at the interfaces $\partial\varphi^S$. The solution of (4.1), if existing, cannot be the solution to a partial differential equation (4.1) in the conventional sense, because derivatives are not defined at the discontinuity. Instead, the solution is required to satisfy a family of related integral equations. Integrating (4.1) over the heterogeneous medium's region $\mathcal{B}$, one obtains

$$\int_{\mathcal{B}} \operatorname{div}[k(\mathbf{x}) \operatorname{grad} \theta(\mathbf{x})] \, \mathrm{d}v = 0. \tag{4.3}$$

The solution of (4.3) is known as the weak or distribution solution (*Wladimirow* [193]).

In general, (4.3) cannot be solved analytically, it has to be solved numerically. Looking for an appropriate shape function to approximate $\theta(\mathbf{x})$ for the whole domain $\mathcal{B}$ is a very difficult task. The function $\theta(\mathbf{x})$ is expected to have a large variation over the problem's domain $\mathcal{B}$ due to the material inhomogeneity. Additionally, this function has to fulfill the complicated internal boundary conditions (Section 6). In order to meet those requirements, the approximating function should be described in terms of a family of piecewise continuous functions. Each piecewise continuous function *takes care* of only a part of the solution domain.

Transcribing the above idea means that the solution domain $\mathcal{B}$ is subdivided into a finite number of non-overlapping subdomains that will be called control volumes (CVs), where in each CV, $\theta(\mathbf{x})$ is approximated by a piecewise continuous function. The numerical technique used here is the finite volume method (FVM) and is widely used in the computational fluid dynamics community (*Durran* [54], *Patankar* [141] and *Ferziger & Perić* [65]). The FVM is chosen here because of its compatibility with the definition of connectivity for a digitized medium which is introduced in Section 2.3. With respect to this connectivity definition, the heat can flow only through the element's interface, not through the element's nodes and edges. Another reason is that the FVM, through its formulation, automatically satisfies the conservation equation of the whole region $\mathcal{B}$ as well as of each CV.

In the three-dimensional case, the CV may take a cubic form, as is shown in Figure 4.1. The computational node at which the variable value θ has to be computed is located at the centroid P of the cube. The variable values at the CV surfaces and the surface integrals are expressed approximately through these values at the nodal points. For a digital image, a voxel is taken as a CV and the computational node is placed at the middle of voxel.

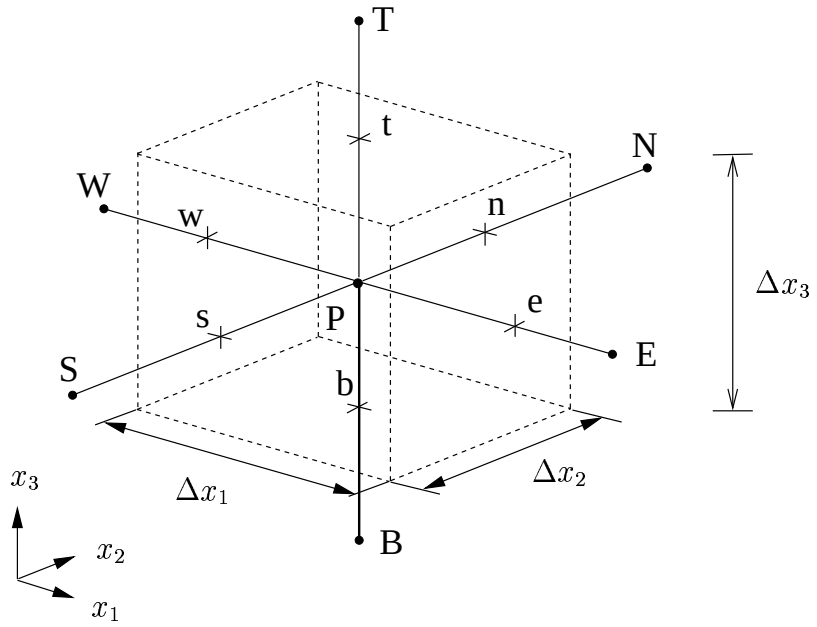

Figure 4.1: A typical three-dimensional control volume $\mathcal{B}^j$ with compass notation. The nodal point P lies in the center of the CV. The neighbouring nodal points are denoted as east E, west W, south S, north N, bottom B and top T. The small letters e, w, s, n, b and t denote to the east, west, south, north, bottom and top control volume interfaces.

By applying (4.3) to each CV $\mathcal{B}^j$ and using *Gauß*' divergence theorem gives

$$\oint_{\partial\mathcal{B}^j} k(\mathbf{x}) \operatorname{grad}\theta(\mathbf{x}) \cdot \mathbf{n} \, \mathrm{d}a = 0. \tag{4.4}$$

If the values of conductivities and the gradients at the CV's interfaces are assumed to be constant, (4.4) can be approximated as

$$\left[k_e \left(\frac{\partial\theta}{\partial x_1}\right)_e - k_w \left(\frac{\partial\theta}{\partial x_1}\right)_w\right] \Delta x_2 \, \Delta x_3 + \left[k_n \left(\frac{\partial\theta}{\partial x_2}\right)_n - k_s \left(\frac{\partial\theta}{\partial x_2}\right)_s\right] \Delta x_1 \, \Delta x_3 +$$

$$\left[k_t \left(\frac{\partial\theta}{\partial x_3}\right)_t - k_b \left(\frac{\partial\theta}{\partial x_3}\right)_b\right] \Delta x_1 \, \Delta x_2 = 0. \tag{4.5}$$

Equation (4.5) represents the balance equation of the heat flux in the CV.

The gradients at the interfaces can be approximated linearly by assuming a linear profile between P and its nearest neighbours. For example, the gradient at the e-face can be approximated linearly as

$$\left(\frac{\partial\theta}{\partial x_1}\right)_e \approx \frac{\theta_E - \theta_P}{\Delta x_1}. \tag{4.6}$$

Here, θ_E is the nodal point of the CV of the east neighbour. The conductivity value at the interface e can be approximated using the harmonic mean value:

$$k_e = \frac{2\, k_P \, k_E}{k_P + k_E}. \tag{4.7}$$

Hence, the heat flux q_e can be written as

$$q_e = k_e \left(\frac{\partial \theta}{\partial x_1}\right)_e \approx \frac{2\,k_P\,k_E}{k_P + k_E}\frac{\theta_E - \theta_P}{\Delta x_1}. \tag{4.8}$$

The reason to choose the harmonic mean value in (4.7) instead of the arithmetic mean value is that the heat flux q_e at the interface e is given correctly in the following two limiting cases. The first is either $k_E = 0$ or $k_P = 0$ leading to $k_e = 0$ and thus $q_e = 0$, which implies that the heat flux at the interface of an insulator vanishes (as it should be). The second is $k_P \gg k_E$, in this case $q_e \approx 2k_E\,(\theta_E - \theta_P)/\Delta x_1$ arises, which implies that the high conductivity material around P would give a negligible resistance if compared to the material around E, which is physically correct. If k_e is taken as the arithmetic formula of k_P and k_E, i. e., $k_e = 1/2\,(k_P + k_E)$, then for the first case ($k_P = 0$ or $k_E = 0$) the heat flux $q_e \approx 1/2\,(k_P + k_E)(\theta_E - \theta_P)/\Delta x_1$ is not equal to zero at the insulator's interface, and it is a wrong result, because $k_e \neq 0$. For the second case, the heat flux q_e depends strongly on k_P through the arithmetic approximation, but in fact, it must approximately depend solely on k_E. In this case, again the arithmetic approximation leads to the wrong result.

Following the same approximation procedure for the other faces of the CV, the discretized form of (4.5) can be obtained and rearranged in the form:

$$k_b\,\theta_B + k_s\,\theta_S + k_w\,\theta_W + A_P\,\theta_P + k_e\,\theta_E + k_n\,\theta_N + k_t\,\theta_T = 0. \tag{4.9}$$

The coefficients k_i and A_P are tabulated:

k_b	k_s	k_w	k_e	k_n	k_t	A_P
$\frac{2\,k_P\,k_B}{k_P + k_B}$	$\frac{2\,k_P\,k_S}{k_P + k_S}$	$\frac{2\,k_P\,k_W}{k_P + k_W}$	$\frac{2\,k_P\,k_E}{k_P + k_E}$	$\frac{2\,k_P\,k_N}{k_P + k_N}$	$\frac{2\,k_P\,k_T}{k_P + k_T}$	$-(k_b + k_s + k_w + k_e + k_n + k_t)$

The spatial location of the computational node of the i-th CV $\theta(\mathbf{x}_i)$ can be referenced using the grid indices $\theta(i, j, k)$. Meanwhile, the computational nodes in (4.9) are written in the compass notation and these nodes are normally stored in computers in one-dimensional arrays. Therefore, it is expedient to set a relationship among them. Table 4.1 shows the conversion between the grid indices, compass notation and storage locations.

Grid indices	Compass notation	Storage location
(i, j, k)	P	$l = (k-1)\,N_j\,N_i + (i-1)\,N_j + j$
$(i, j, k-1)$	B	$l - N_i\,N_j$
$(i-1, j, k)$	W	$l - N_j$
$(i, j-1, k)$	S	$l - 1$
$(i, j+1, k)$	N	$l + 1$
$(i+1, j, k)$	E	$l + N_j$
$(i, j, k+1)$	T	$l + N_i\,N_j$

To gain useful solutions, boundary conditions are needed; thus, they should be supplemented in (4.5). As discussed in Section 3.5.1, there are two types of boundary conditions, namely external boundary conditions which are prescribed from outside and internal boundary conditions which are caused by the inhomogeneity of the material. Since each voxel of the digital image is taken as a CV, the inhomogeneity can solely appear at the interfaces of the CVs. Through the formulation of the FVM, the internal boundary conditions (jump relations) are automatically satisfied, because the temperature θ and the normal component of the heat flux $q = \mathbf{q} \cdot \mathbf{n}$ are continuous at the interfaces. To solve this problem, the mixed boundary conditions are chosen as follows. The first boundary condition is the one with a temperature gradient that is prescribed across the sample. The temperature gradient can be produced by giving different temperature values at opposite surfaces of the sample; for example, west and east surfaces. This condition is called *Dirichlet* boundary condition. The second boundary condition is the one with the heat flux that cannot flow out at the other four faces of the sample. This is a *Neumann* boundary condition, which involves the derivative of the temperature while the temperature itself is unknown. In the FVM formulation, the known heat flux can be directly inserted into (4.5). For example, the corresponding discretized equation for the CV, whose top interfaces represent the top of the sample, can be obtained by substituting

$$q_t = k_t \left(\frac{\partial \theta}{\partial x_3} \right)_t = 0 \tag{4.10}$$

into (4.5). Hence,

$$\left[k_e \left(\frac{\partial \theta}{\partial x_1} \right)_e - k_w \left(\frac{\partial \theta}{\partial x_1} \right)_w \right] \Delta x_2 \, \Delta x_3 + \left[k_n \left(\frac{\partial \theta}{\partial x_2} \right)_n - k_s \left(\frac{\partial \theta}{\partial x_2} \right)_s \right] \Delta x_1 \, \Delta x_3$$
$$- k_b \left(\frac{\partial \theta}{\partial x_3} \right)_b \Delta x_1 \, \Delta x_2 = 0. \tag{4.11}$$

By doing so, the required number of equations for the unknown temperature can be constructed, and the result is a system of linear algebraic equations, which can be written as

$$\boldsymbol{A}\,\boldsymbol{\theta} = \boldsymbol{b}, \tag{4.12}$$

where $\boldsymbol{A}$ is the coefficient matrix and $\boldsymbol{\theta}$ the unknown temperature values. The vector $\boldsymbol{b}$ is called the right-hand side, which has zero elements except those which are known from the *Dirichlet* boundary condition.

It is necessary to discuss the infinite contrast limit case (the ratio of the thermal conductivities of both constituents are either 0 or ∞) using the FVM, because there is a pitfall in connection using the FVM. For simplicity, a two-dimensional case is considered. The insulating $k^S = 0$ and conducting $k^F \neq 0$ materials are represented by white and grey colours, respectively, as displayed in Figure 4.2. Through the harmonic approximation, the correct heat flux can be obtained in this limiting case. The heat fluxes are denoted by the straight lines in Figure 4.2. For example, the heat flux cannot flow from 36th to 37th CVs, but it can flow from 36-th to 29-th CVs (Figure 4.2). However, there is a pitfall by the posed finite volume formulation since the heat flux cannot flow from 30

to 38 even though they are physically connected by corners, because the heat flux can only flow through the CV's interfaces, but not through the CV's corners by definition. To overcome this shortcoming, the definition of *connectivity* between neighbours has to be modified. Substantially, it means that the heat fluxes are allowed to flow through the corner, which can be achieved by finite element or first-passage formulations. In the finite element formulation, again each pixel can be taken as an element, but the computational nodes now lie in the pixel's corner (Section 4.3). The nodes at the corners of a given pixel are connected to 9 different nodes, one with itself, four with the first nearest and four with the second nearest neighbours, which are the nodes in the corners of the four pixels that share a corner. Note that in three-dimensional, each node is mathematically connected to 27 nodes (itself + 26 neighbours).

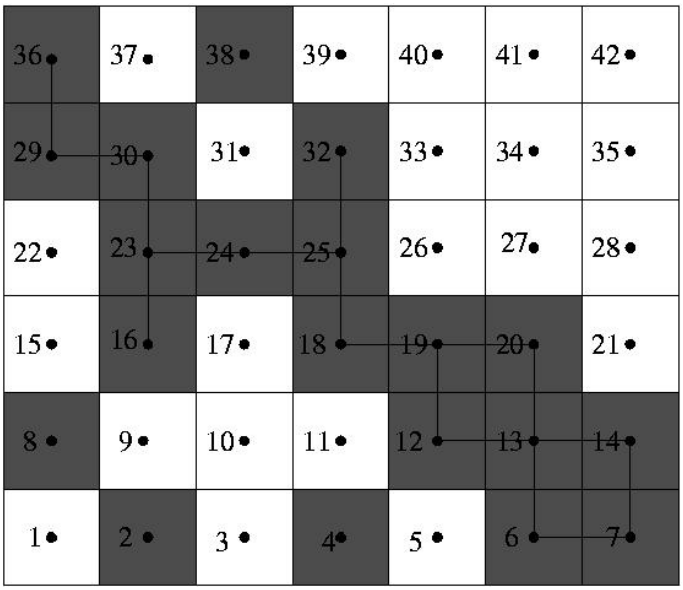

Figure 4.2: Two-dimensional CVs for a part of a digital image. The computational nodes are in the middle of the pixels. The white area is non-conducting and the grey area is conducting. The lines indicate that the fluid can flow from one control volume to another control volume.

If the resolution of the image is high enough, which means that even the smallest feature is composed of many pixels, the use of different methods will give insignificantly different results (*Garboczi et al.* [70]). However, if the resolution of the image is low, different methods may produce different results. Therefore, the definition of how the pixels are connected will determine which method has to be used. Otherwise, the choice is arbitrary. From this explanation it can be concluded that conducting biphasic materials physically composed of pixels connected only by corners would be connected electrically when using finite elements or limit-passage, but disconnected electrically when using finite volume or finite differences of lower order (*Garboczi et al.* [70], *Kim & Torquato* [100]).

4.2 Frequency-dependent permittivity problems

In the quasi-static case, the frequency-dependent permittivity problems are governed by the elliptic linear differential equations which have complex-valued coefficients and solutions. By taking the divergence of (3.95), by considering $\operatorname{div}\operatorname{rot}\mathbf{h} = 0$, and using (3.105) and (3.125), the governing equations for this case can be formulated as

$$\operatorname{div}\left(\tilde{\varepsilon}^c(\omega,\mathbf{x})\operatorname{grad}U(\omega,\mathbf{x})\right) = 0, \qquad \mathbf{d}(\omega,\mathbf{x}) = \tilde{\varepsilon}^c(\omega,\mathbf{x})\,\mathbf{e}(\omega,\mathbf{x}), \tag{4.13}$$

where $\mathbf{d}(\omega,\mathbf{x})$ is the electric displacement, $\mathbf{e}(\omega,\mathbf{x}) = -\operatorname{grad}U(\omega,\mathbf{x})$ is the electric field, and $U(\omega,\mathbf{x})$ is the electric potential. Here, $\tilde{\varepsilon}^c(\omega,\mathbf{x}) = \tilde{\varepsilon}(\omega,\mathbf{x}) + \mathrm{i}\,\sigma(\omega,\mathbf{x})/\omega$ is the complex-valued permittivity. The real part of $\tilde{\varepsilon}_c(\omega,\mathbf{x})$ represents the permittivity of the medium, while the imaginary part represents the conductivity of the medium which is scaled by the frequency ω. It should be emphasized again that the complex-valued permittivity implies that the treated medium is lossy or dissipative.

Similar to the thermal conductive case, (4.13) can be discretized using the FVM yielding

$$\left[\tilde{\varepsilon}_e^c(\omega)\left(\frac{\partial U}{\partial x_1}\right)_e - \tilde{\varepsilon}_w^c(\omega)\left(\frac{\partial U}{\partial x_1}\right)_w\right]\Delta x_2\,\Delta x_3 + \left[\tilde{\varepsilon}_n^c(\omega)\left(\frac{\partial U}{\partial x_2}\right)_n - \tilde{\varepsilon}_s^c(\omega)\left(\frac{\partial U}{\partial x_2}\right)_s\right]\Delta x_1\,\Delta x_3$$
$$+\left[\tilde{\varepsilon}_t^c(\omega)\left(\frac{\partial U}{\partial x_3}\right)_t - \tilde{\varepsilon}_b^c(\omega)\left(\frac{\partial U}{\partial x_3}\right)_b\right]\Delta x_1\,\Delta x_2 = 0, \tag{4.14}$$

where the permittivities $\tilde{\varepsilon}_i^c(\omega)$ are still dependent of the frequency ω. Equation (4.14) gives the balance of the electric displacement $\mathbf{d}(\omega)$ in a CV.

Like in the real case, the gradients at the interfaces are also approximated linearly. For example, the gradient at the e-face can be given approximately by

$$\left(\frac{\partial U}{\partial x_1}\right)_e \approx \frac{U_E - U_P}{\Delta x_1}. \tag{4.15}$$

As the reason given in the thermal conductive case, the permittivity value at the interface is approximated using the harmonic mean. For example, the permittivity at e-face is given by

$$\tilde{\varepsilon}_e^c(\omega) = \frac{2\,\tilde{\varepsilon}_P^c(\omega)\,\tilde{\varepsilon}_E^c(\omega)}{\tilde{\varepsilon}_P^c(\omega) + \tilde{\varepsilon}_E^c(\omega)}. \tag{4.16}$$

Hence, the electric displacement d_e can be written as

$$d_e(\omega) \approx \frac{2\,\tilde{\varepsilon}_P^c(\omega)\,\tilde{\varepsilon}_E^c(\omega)}{\tilde{\varepsilon}_P^c(\omega) + \tilde{\varepsilon}_E^c(\omega)}\frac{U_E - U_P}{\Delta x_1}. \tag{4.17}$$

Following the same approximation procedure for other faces of the CV, the discretized form of (4.14) can be formulated as

$$\tilde{\varepsilon}_b^c(\omega)\,U_B + \tilde{\varepsilon}_s^c(\omega)\,U_S + \tilde{\varepsilon}_w^c(\omega)\,U_W + A_P(\omega)\,U_P + \tilde{\varepsilon}_e^c(\omega)\,U_E + \tilde{\varepsilon}_n^c(\omega)\,U_N + \tilde{\varepsilon}_t^c(\omega)\,U_T = 0, \tag{4.18}$$

where

$$A_P(\omega) = -(\tilde{\varepsilon}_b^c(\omega) + \tilde{\varepsilon}_s^c(\omega) + \tilde{\varepsilon}_w^c(\omega) + \tilde{\varepsilon}_e^c(\omega) + \tilde{\varepsilon}_n^c(\omega) + \tilde{\varepsilon}_t^c(\omega)) \tag{4.19}$$

and

$$\tilde{\varepsilon}_i^c(\omega) = \frac{2\,\tilde{\varepsilon}_P^c(\omega)\,\tilde{\varepsilon}_I^c(\omega)}{\tilde{\varepsilon}_P^c(\omega) + \tilde{\varepsilon}_I^c(\omega)} \tag{4.20}$$

with $I = B, S, W, E, N, T$. Obviously, the linear system of equations (4.18) still contains the frequency ω, thus (4.18) has to be solved for each ω.

4.3 *Rayleigh-Ritz* variational method for the elastic case

In this section, a numerical solution, which is based on the finite element method, is applied to compute the elastic moduli of a digitized heterogeneous medium. The finite element will be formulated using the *Rayleigh-Ritz* variational method (*Hughes* [95]), which starts directly from a variational formulation for the potential energy. To derive the finite element equation, each voxel will be chosen to be an element, where the nodes are placed at the corners of the element (cf. Figure 4.3).

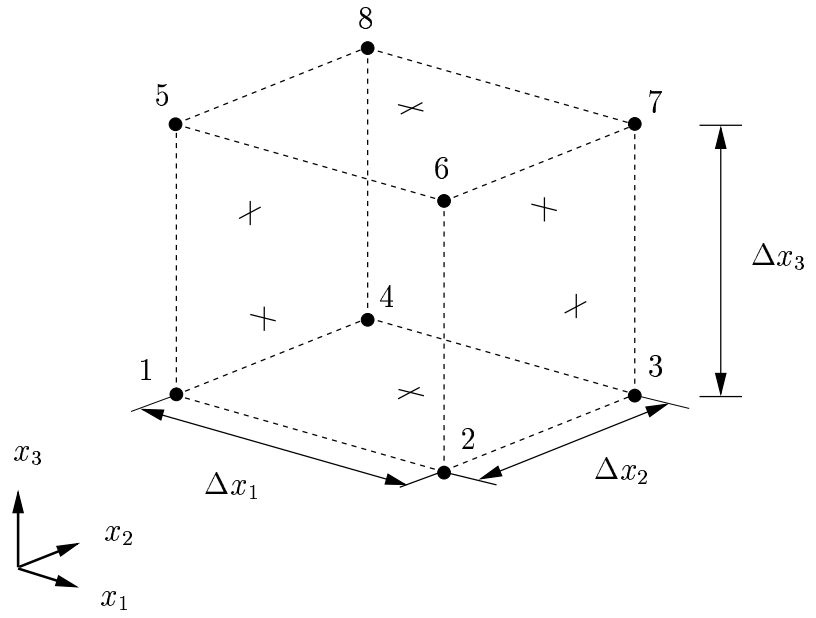

Figure 4.3: A typical 3D tri-linear finite element with local coordinates (x_1, x_2, x_3).

The potential energy for a linear isotropic elastic material in a voxel is given by

$$w = \frac{1}{2} \int_{\mathcal{B}^j} \boldsymbol{\varepsilon} \cdot (\overset{4}{\mathbf{C}}\,\boldsymbol{\varepsilon})\, \mathrm{d}v, \tag{4.21}$$

where

$$\boldsymbol{\varepsilon} = \frac{1}{2}(\operatorname{grad}\mathbf{u} + \operatorname{grad}^T\mathbf{u}), \tag{4.22}$$

$$\overset{4}{\mathbf{C}} = \lambda\,\mathbf{I}\otimes\mathbf{I} + 2G\,\overset{4}{\mathbf{I}}. \tag{4.23}$$

Here, the voxel is assumed to have side lengths $x_1 = x_2 = x_3 = 1$ (in units of resolution). Note that the potential energy of the whole digitized medium can be approximated by summing the voxel's potential energy. As with the method of weighted residuals (see 4.1), the displacement $\mathbf{u}(\mathbf{x})$ is approximated by linear interpolation of the nodal displacements, such that

$$\mathbf{u}(\mathbf{x}) = \sum_i N^i(\mathbf{x})\,\mathbf{u}^i. \tag{4.24}$$

Here $N^i(\mathbf{x})$ are the shape functions, which have the following forms:

$$\begin{aligned}
N^1 &= (1-x_1)(1-x_2)(1-x_3),\\
N^2 &= x_1(1-x_2)(1-x_3),\\
N^3 &= x_1x_2(1-x_3),\\
N^4 &= (1-x_1)x_2(1-x_3),\\
N^5 &= (1-x_1)(1-x_2)x_3,\\
N^6 &= x_1(1-x_2)x_3,\\
N^7 &= x_1x_2x_3,\\
N^8 &= (1-x_1)x_2x_3.
\end{aligned}$$

With the aide of these shape functions, the gradient of the displacement field $\mathbf{u}$ can be expressed as

$$\operatorname{grad}\mathbf{u} = \mathbf{u}_{,l}\otimes\mathbf{e}_l = u_{k,l}\,\mathbf{e}_k\otimes\mathbf{e}_l \tag{4.25}$$

with

$$u_{k,l}(\mathbf{x}) = \sum_i N^i_{,l}(\mathbf{x})\,u^i_k\ . \tag{4.26}$$

The strain field $\boldsymbol{\varepsilon}$ can be found by substituting (4.25) into (4.22). By inserting this expression for $\boldsymbol{\varepsilon}$ and (4.23) into (4.21), the potential energy becomes dependent on the nodal displacements $\mathbf{u}^i$. Now, the principle of minimum potential energy is applied. To find the minimum energy, the derivative of w with respect to the nodal displacements u^i_k (k-th coefficient of displacement at the i-th node) must be set to zero. Thus,

$$\frac{\partial w}{\partial u^i_k} = 0. \tag{4.27}$$

The *Rayleigh-Ritz* variational method can be applied whether the approximation function N^i is defined locally, as described here, or globally, as in the case of applying *Beran*'s method in deriving the bounds (Chapter 6).

4.4 Iterative solution methods

After obtaining the set of discrete equations (4.12), the next step is to solve them. Since the coefficient matrix $\boldsymbol{A}$ in (4.12) is a sparse, large and positive definite matrix, the best way to solve the system is using iterative methods. An iterative method uses a trial and error solution as a start solution and improves it systematically until a proper result is found. Since there are many iterative methods to solve such problems, some criteria have to be taken into account in finding the most suitable method. The first criterion is whether the method works well to solve the problem. A method which works well for one problem may not work as well or even not at all for another problem. The second criterion is the storage capacities of computers, since the unknown variables and the coefficient matrices can be very large for three-dimensional problems. For example, for just 100 unknowns in each direction in a three-dimensional problem, the total number will be 100^3 unknowns and the non-zero components of the coefficient matrix $\boldsymbol{A}$ will be $7 \cdot 100^3$. The third criterion is the convergence rate of the methods, since the results have to be obtained in a proper time.

A method which is a good candidate to solve this problem is the successive over-relaxation (SOR) method, since it needs the lowest storage requirement compared to other iterative methods (*Barrett et al.* [11]). Using the SOR method for the digital image problem, only the voxels' values and the solution vector need to be stored. The coefficient matrix $\boldsymbol{A}$ and the right-hand side $\boldsymbol{b}$ can be computed in every iteration in order to work with a larger system of equations. However, the computational process will be slower since $\boldsymbol{A}$ and $\boldsymbol{b}$ have to be computed in every iteration step. The main disadvantage of the SOR method is that the convergence rate and the accuracy of the result depend on the judicious choice of the so-called *overrelaxation parameter* ω. Moreover, in some cases, especially in the case of complex-valued variables, the SOR method converges very slowly and it may even diverge depending on the choice of ω. To solve the shortcoming of the SOR method in solving such problems, a conjugate-gradient (CG) method should be applied. The CG method needs to store four auxiliary vectors. For the complex-valued case, the CG method has to be properly modified (*van der Vorst & Melissen* [177], *Freund* [67]). Because of its important relation to this work, the SOR and CG methods will be briefly presented in this section. A comprehensive discussion and the mathematical proof can be found in, e. g., *Axelsson* [9] or *Golub & van Loan* [75]. To enable one to work with larger problems and a faster convergence rate, the computer programs must be parallelized.

4.4.1 SOR iterative method

The simplest iterative method can be expressed in the form of

$$\boldsymbol{M}\,\boldsymbol{\theta}^{(r)} = \boldsymbol{N}\,\boldsymbol{\theta}^{(r-1)} + \boldsymbol{b}. \tag{4.28}$$

If $\hat{\boldsymbol{\theta}}$ represents the exact solution of (4.12), then, by definition, the converging case must be $\boldsymbol{\theta}^{(r)} = \boldsymbol{\theta}^{(r-1)} = \hat{\boldsymbol{\theta}}$. Comparing (4.28) to (4.12) gives

$$\boldsymbol{A} = \boldsymbol{M} - \boldsymbol{N}. \tag{4.29}$$

From (4.29), the iteration matrix $\boldsymbol{M}^{-1}\boldsymbol{N}$ is a function of the coefficient matrix $\boldsymbol{A}$. If $\boldsymbol{M}^{-1}\boldsymbol{N}$ does not vary from iteration to iteration, then the iterative method is called *stationary*.

To gain a lower computational cost, the matrices $\boldsymbol{M}$ and $\boldsymbol{N}$ have to be chosen properly. Obviously, to solve (4.28), $\boldsymbol{M}$ must be easily invertible, which means that from the computational point of view $\boldsymbol{M}$ must be diagonal or triangular or perhaps a block triangular or block matrix. The computation of $\boldsymbol{N}\,\boldsymbol{\theta}^{(r-1)}$ is cheap, since $\boldsymbol{A}$ and thus $\boldsymbol{N}$ is sparse. For example, if $\boldsymbol{M} = \boldsymbol{D}$ and $\boldsymbol{N} = -(\boldsymbol{L} + \boldsymbol{U})$ are chosen, then this iteration method is known as the *Jacobi* iterative method:

$$\boldsymbol{\theta}^{(r)} = -\boldsymbol{D}^{-1}\,(\boldsymbol{L} + \boldsymbol{U})\,\boldsymbol{\theta}^{(r-1)} + \boldsymbol{D}^{-1}\,\boldsymbol{b}. \tag{4.30}$$

Therein, $\boldsymbol{D}$, $\boldsymbol{L}$ and $\boldsymbol{U}$ represent the diagonal, lower-triangular and upper triangular parts of $\boldsymbol{A}$, respectively. If $\boldsymbol{M} = \boldsymbol{L} + \boldsymbol{D}$ and $\boldsymbol{N} = -\boldsymbol{U}$ are selected, then it is called the *Gauß-Seidel* method:

$$\boldsymbol{\theta}^{(r)} = (\boldsymbol{L} + \boldsymbol{D})^{-1}\left(-\boldsymbol{U}\,\boldsymbol{\theta}^{(r-1)} + \boldsymbol{b}\right). \tag{4.31}$$

For a positive definite matrix $\boldsymbol{A}$, the *Jacobi* and *Gauß-Seidel* methods converge (*Axelsson* [9], *Varga* [181]). A complex-valued matrix $\boldsymbol{A}$ is called positive definite in the complex plane $\mathbb{C}^n$ if its quadratic form $\boldsymbol{\theta}^T\boldsymbol{A}\,\boldsymbol{\theta}$ is positive for all non-zero vectors $\boldsymbol{\theta}$ in $\mathbb{C}^n$.

Since the *Jacobi* and *Gauß-Seidel* methods converge very slow in the real problems, an *overcorrection* to the value of $\bar{\boldsymbol{\theta}}^{(r)}$ at the r-th iteration of the *Gauß-Seidel* iteration can be made to counter its shortcoming. Thus,

$$\boldsymbol{\theta}^{(r)} = \omega_{SOR}\,\bar{\boldsymbol{\theta}}^{(r)} + (1 - \omega_{SOR})\,\boldsymbol{\theta}^{(r-1)}, \tag{4.32}$$

where ω_{SOR} is the overcorrection factor or overrelaxation parameter. This method is called SOR. By introducing the residual vector

$$\boldsymbol{\xi}^{(r)} = \boldsymbol{A}\,\boldsymbol{\theta}^{(r)} - \boldsymbol{b}, \tag{4.33}$$

which can be used as a criterion for terminating the iteration procedure, since the goal of the iteration procedure is to drive the residual to zero. Then one iteration step of the SOR method can be represented by

$$\boldsymbol{\theta}^{(r)} = \boldsymbol{\theta}^{(r-1)} - \omega_{SOR}\,(\boldsymbol{L} + \boldsymbol{D})^{-1}\,\boldsymbol{\xi}^{(r-1)}. \tag{4.34}$$

If $\omega_{SOR} = 1$, the SOR method reduces to the *Gauß-Seidel* method. As mentioned above, in general, it is impossible to choose the optimum value of ω_{SOR}. However, this value lies almost invariably in the range $1 \leq \omega_{SOR} \leq 2$. It can be shown that for a symmetric and positive definite matrix, the SOR iteration is always convergent for any value $0 \leq \omega_{SOR} \leq 2$. In general, the SOR method is divergent for ω_{SOR} outside the interval $[0, 2]$ and convergence is not guaranteed for any value of ω_{SOR} inside $[0, 2]$. A comprehensive treatment and proof of the above results can be found in, e. g., *Varga* [181] and *Axelsson* [9].

In the limit of infinite contrast, i. e., $k^F/k^S \to \infty$, it can occur that $\det \boldsymbol{L} = \det \boldsymbol{D} = 0$ and thus, $\boldsymbol{L}^{-1}$ and $\boldsymbol{D}^{-1}$ do not exist. For example, the discretization equation for the 10-th or 34-th CV in Figure 4.2 is

$$0 = 0 \tag{4.35}$$

in this case, because $k_s = k_w = k_e = k_n = 0$ (the white region). It means that the elements of the 10-th and 34-th rows of the matrix $\boldsymbol{A}$ are equal zero and thus, $\det \boldsymbol{L} = \det \boldsymbol{D} = 0$. There are two ways to fix this problem. The first one is by throwing out the rows and columns, which have only zero elements. This can be done in many ways, the simplest one is just by skipping these rows in the numerical code. Then, the SOR algorithm for the thermal conductivity problem can be summarized as follows

- Initialize by setting: $r = 0$, $\boldsymbol{\theta}^{(0)} = \boldsymbol{\theta}_g$, $\boldsymbol{\xi}^{(0)} = \boldsymbol{A}\,\boldsymbol{\theta}_g - \boldsymbol{b}$
- Advance the counter: $r = r + 1$
- Calculate:
$$\boldsymbol{\theta}^{(r)} = \boldsymbol{\theta}^{(r-1)} - \omega_{SOR}\,\boldsymbol{D}^{-1}\,\boldsymbol{\xi}^{(r-1)}$$
$$\boldsymbol{\xi}^{(r)} = \boldsymbol{A}\,\boldsymbol{\theta}^{(r)} - \boldsymbol{b}$$
- Repeat until convergence.

The second way to treat the problem of infinite contrast is using the *Hoshen-Kopelman* algorithm as described in Section 2.2.2 to extract the *backbone* cluster of the digital image. Every conducting voxel that does not belong to the backbone cluster is changed to a non-conducting voxel. For example, the 2-nd, 4-th, 8-th and 38-th grey voxels (conducting) are switched to be white voxels (non-conducting). Then, the equations according to the *new* digital image are solved with the method described above. The alteration of the isolated conducting voxels to non-conducting ones does not affect the computational result, because the isolated conducting voxels do not contribute any part to the heat flux of the whole system. The rank of the obtained coefficient matrix $\boldsymbol{A}$ will decrease or at least remain the same, since it will contain more rows and columns with zero elements. A bookkeeping program can be used to transform the original coefficient matrix $\boldsymbol{A}$ to the coefficient matrix $\tilde{\boldsymbol{A}}$ which is smaller than $\boldsymbol{A}$. Moreover, the new matrix $\tilde{\boldsymbol{A}}$ is a strict diagonal dominant matrix meanwhile the old matrix $\boldsymbol{A}$ may be a weak diagonal dominant matrix. Therefore, the linear system of equations with the coefficient matrix $\tilde{\boldsymbol{A}}$ can be solved faster and easier than the original one.

Although the optimal value of ω_{SOR} in general can not be determined, however, it can be heuristically estimated as given in e. g., *van Kan & Segal* [179], Section 11.2.6, or *Young* [196]. Moreover, the relaxation parameter ω_{SOR} depends critically on the ordering of equations and unknowns (*Young* [196] and the references therein). Another way is to modify the SOR method using different ω_{SOR} for every half iteration step. As the iteration step goes to infinity, ω_{SOR} should tend to the optimal value $\omega^{\star}_{SOR}$. This method is called SOR with *Chebyshev* acceleration, which can be done using odd-even ordering

and changing ω_{SOR} at each half-step according to the following rule:

$$\left.\begin{aligned} \omega_{SOR}^{(0)} &= 1 \\ \omega_{SOR}^{(1/2)} &= 1/(1-\rho_{\text{jac}}^2/2) \\ \omega_{SOR}^{(r+1/2)} &= 1/(1-\rho_{\text{jac}}^{(r)}/2), \qquad r = 1/2, 1, \ldots, \infty \\ \omega_{SOR}^{(\infty)} &\rightarrow \omega_{SOR}^{\star}. \end{aligned}\right\} \tag{4.36}$$

Here, half-step means that SOR is used to solve only the odd-numbered variables, i. e., θ_1, θ_3, etc. or only the even-numbered ones, i. e., θ_2, θ_4, etc. A compact description and a routine for SOR with *Chebyshev* acceleration can be found in *Press et al.* [145] p. 859-860.

4.4.2 CG method

One of the effective iteration methods to solve a symmetric positive definite linear system of equations is the CG method, which is a nonstationary iterative method. The CG method can be seen as an iterative solution method to solve linear systems of equations (4.12) by minimizing the following quadratic functional

$$f(\boldsymbol{\theta}) = \frac{1}{2}\,\boldsymbol{\xi}\,\boldsymbol{A}^{-1}\,\boldsymbol{\xi}, \tag{4.37}$$

where $\boldsymbol{\xi} = \boldsymbol{A}\boldsymbol{\theta} - \boldsymbol{b}$. Since $\boldsymbol{A}^{-1}$ is positive definite, a minimizer which is $\boldsymbol{\theta} = \boldsymbol{A}^{-1}\boldsymbol{b}$ exists.

To find the minimizer of $f(\boldsymbol{\theta})$, an iterative method is used to construct a new search direction vector $\boldsymbol{d}^r$ at each stage and a local minimizer along this search direction, which is

$$\boldsymbol{\theta}^{(r)} = \boldsymbol{\theta}^{(r-1)} + \tau^{(r)}\,\boldsymbol{d}^{(r)}. \tag{4.38}$$

Correspondingly, the residuals $\boldsymbol{\xi}^{(r)} = \boldsymbol{A}\boldsymbol{\theta}^{(r)} - \boldsymbol{b}$ are updated as

$$\boldsymbol{\xi}^{(r)} = \boldsymbol{\xi}^{(r-1)} + \tau\,\boldsymbol{A}\,\boldsymbol{d}^{(r)}. \tag{4.39}$$

It can be shown that the choice $\tau = \tau^{(r)} = -\boldsymbol{\xi}^{(r-1)^T}\boldsymbol{\xi}^{(r-1)}/\boldsymbol{d}^{(r)^T}\boldsymbol{A}\,\boldsymbol{d}^{(r)}$ minimizes $\boldsymbol{\xi}^{(r)^T}\boldsymbol{A}\,\boldsymbol{\xi}^{(r)}$ over all possible choices for τ in (4.39) (*Axelsson* [9], Section 11.2.1). It can be proven that, if the direction vector $\boldsymbol{d}^r$ is chosen conjugately orthogonal to the previous direction vectors, then it will give the best approximation in the so-called *Krylov* space. Thus,

$$\boldsymbol{d}^{(r+1)} = -\boldsymbol{\xi}^{(r+1)} + \beta^{(r)}\boldsymbol{d}^{(r)}, \tag{4.40}$$

where the choice $\beta^{(r)} = \boldsymbol{\xi}^{(r+1)^T}\boldsymbol{\xi}^{(r+1)}/\boldsymbol{\xi}^{(r)^T}\boldsymbol{\xi}^{(r)}$ guarantees that $\boldsymbol{d}^{(r+1)}$ and $\boldsymbol{A}\,\boldsymbol{d}^{(r)}$ are conjugately orthogonal. The word *conjugate* means that the vectors are orthogonal with respect to $\boldsymbol{A}$, i. e.,

$$\boldsymbol{d}^{(r)^T}\boldsymbol{A}\,\boldsymbol{d}^{(s)} = 0 \qquad \text{for} \quad r \neq s, \tag{4.41}$$

since the product of $\boldsymbol{d}^{(r)^T}\boldsymbol{A}\,\boldsymbol{d}^{(s)} = (\boldsymbol{d}^{(r)}, \boldsymbol{A}\,\boldsymbol{d}^{(s)})$ can be seen as scalar product of two vectors $\boldsymbol{d}^{(r)^T}$ and $\boldsymbol{A}\,\boldsymbol{d}^{(s)}$ in the *Krylov* space. Here, $(\cdot,\cdot)$ indicates a scalar product. The

Krylov space of dimension r associated with $\boldsymbol{A}$ and $\boldsymbol{\xi}^{(0)}$, i. e., $\mathbb{K}^r(\boldsymbol{A}\boldsymbol{\xi}^{(0)})$, is a vector space that is spanned by the vector $\boldsymbol{\xi}^{(0)}$, $\boldsymbol{A}\boldsymbol{\xi}^{(0)}$, ..., $\boldsymbol{A}^{r-1}\boldsymbol{\xi}^{(0)}$. It is worth noting that the minimization of $\frac{1}{2}\boldsymbol{\xi}\,\boldsymbol{A}^{-1}\,\boldsymbol{\xi}$ is equivalent to the minimization of the distance of the approximation $\boldsymbol{\theta}^{(r)}$ and the exact solution $\hat{\boldsymbol{\theta}}$ with respect to norm $\|\cdot\|_{\boldsymbol{A}}$, thus

$$\|\boldsymbol{\theta}^{(r)} - \hat{\boldsymbol{\theta}}\|_{\boldsymbol{A}} = \min_{\boldsymbol{v}\in\mathbb{K}^r(\boldsymbol{A}\boldsymbol{\xi}^{(0)})} \|\boldsymbol{v} - \boldsymbol{x}\|\,. \tag{4.42}$$

The norm $\|\cdot\|_{\boldsymbol{A}}$ can be defined as

$$\|\boldsymbol{v}\| = \boldsymbol{v}^T\boldsymbol{A}\boldsymbol{v}. \tag{4.43}$$

The convergence rate of the CG method can be improved by preconditioning. *Preconditioning* means that the original coefficient matrix $\boldsymbol{A}$ is replaced by another matrix $\hat{\boldsymbol{A}}$ with the same solution as $\boldsymbol{A}$ but smaller condition number. Thus, the convergence rate of $\hat{\boldsymbol{A}}$ is faster than that of $\boldsymbol{A}$. One way to precondition the original coefficient matrix $\boldsymbol{A}$ is to premultiply the matrix $\boldsymbol{A}$ by a preconditioning matrix $\boldsymbol{P}$ such that

$$\hat{\boldsymbol{A}}\boldsymbol{\theta} = \hat{\boldsymbol{b}} \tag{4.44}$$

with $\hat{\boldsymbol{A}} = \boldsymbol{P}\boldsymbol{A}$ and $\hat{\boldsymbol{b}} = \boldsymbol{P}\boldsymbol{b}$. Now the minimization takes place over the *Krylov* space $\mathbb{K}^r(\boldsymbol{P}\,\boldsymbol{A}\,\boldsymbol{\xi}^{(0)})$ instead of the original *Krylov* space $\mathbb{K}^r(\boldsymbol{A}\,\boldsymbol{\xi}^{(0)})$. As posed before, the main restriction in computing the physical quantities of digital images is the storage capacity. This thesis only uses the *Jacobi* preconditioner, because this preconditioner can be applied without using any extra storage. In this case, the preconditioned matrix $\boldsymbol{P}$ is

$$\boldsymbol{P} = \boldsymbol{D}, \tag{4.45}$$

where $\boldsymbol{D}$ is the diagonal part of the coefficient matrix $\boldsymbol{A}$. For a comprehensive treatment and convergence analysis please refer to *Axelsson* [9], Chapter 11. The pseudocode for a

computer implementation takes the following form

$$
\begin{array}{l}
\text{Initialize: } \boldsymbol{\theta}^{(0)} = \boldsymbol{\theta}_g \;;\; \boldsymbol{\xi}^{(0)} = \boldsymbol{A}\boldsymbol{\theta}^{(0)} - b \;;\; \mathbf{h}^{(0)} = \boldsymbol{D}^{-1}\boldsymbol{\xi}^{(0)}; \\
\qquad\qquad \boldsymbol{d}^{(0)} = -\boldsymbol{h}^{(0)} \;;\; \delta_0^{(0)} = {\boldsymbol{\xi}^{(0)}}^T \boldsymbol{h}^{(0)} \\
\qquad\qquad \text{check convergence; continue if necessary} \\
\\
\boldsymbol{f}\text{or } r = 1, 2, \ldots \\
\qquad \boldsymbol{g}^{(r)} = \boldsymbol{A}\boldsymbol{d}^{(r)} \\
\qquad \tau^{(r)} = \delta^{(r-1)} / ({\boldsymbol{d}^{(r)}}^T \boldsymbol{g}^{(r)}) \\
\qquad \boldsymbol{\theta}^{(r)} = \boldsymbol{\theta}^{(r-1)} + \tau^{(r)}\, \boldsymbol{d}^{(r)} \\
\qquad \boldsymbol{\xi}^{(r)} = \boldsymbol{\xi}^{(r-1)} + \tau\, \boldsymbol{A}\, \boldsymbol{d}^{(r)} \\
\qquad \mathbf{h}^{(r)} = \boldsymbol{D}^{-1}\boldsymbol{\xi}^{(r)} \;;\; \delta_1^{(r)} = {\boldsymbol{\xi}^{(r)}}^T \boldsymbol{h}^{(r)} \\
\qquad \text{check convergence; continue if necessary} \\
\qquad \beta^{(r)} = \delta_1^{(r)} / \delta_0^{(r-1)} \;;\; \delta_0^{(r)} = \delta_1^{(r)} \\
\qquad \boldsymbol{d}^{(r+1)} = -\mathbf{h}^{(r)} + \beta^{(r)}\, \boldsymbol{d}^{(r+1)} \\
\\
\boldsymbol{n}\text{ext r}
\end{array}
\tag{4.46}
$$

($\boldsymbol{g}^{(r)}$ and $\boldsymbol{h}^{(r)}$ can be stored in the same vector.)

4.4.3 Complex-valued symmetric coefficient matrix

From the discretization of the *Laplace* equation in the frequency-dependent case, the following linear system is obtained:

$$\boldsymbol{A}\,\boldsymbol{\theta} = \boldsymbol{b}. \tag{4.47}$$

Therein, $\boldsymbol{\theta}$ and $\boldsymbol{b}$ are complex-valued vectors. Here, $\boldsymbol{A}$ is a complex-valued symmetric matrix but not-*Hermite*an, i. e., $\boldsymbol{A} = \boldsymbol{A}^T$ but $\boldsymbol{A} \neq \bar{\boldsymbol{A}}^T$. Since $\boldsymbol{A}$ is not-*Hermite*an, $\boldsymbol{A}$ cannot be a positive definite matrix. This can be proven easily by taking a vector $\boldsymbol{v} \in \mathbb{C}^n$ with the zero elements everywhere except the first element, i. e., $v_1 = 1$ and $v_2 = v_3 = \cdots = v_n = 0$, and then calculating the quadratic form of the matrix which is complex. This result contradicts the definition of a positive definite matrix (*Axelsson* [9], p. 85). Therefore, the methods to solve the positive definite linear systems as discussed previously are not applicable for this case.

Usually in practice, the $n \times n$ complex-valued linear systems (4.47) can be transformed to equivalent $2n \times 2n$ real systems by taking real and imaginary parts of (4.47); hence,

$$\boldsymbol{A}_\star \begin{bmatrix} \Re(\boldsymbol{\theta}) \\ -\Im(\boldsymbol{\theta}) \end{bmatrix} = \begin{bmatrix} \Re(\boldsymbol{b}) \\ \Im(\boldsymbol{b}) \end{bmatrix}, \quad \boldsymbol{A}_\star = \begin{bmatrix} \Re(\boldsymbol{A}) & \Im(\boldsymbol{A}) \\ \Im(\boldsymbol{A}) & -\Re(\boldsymbol{A}) \end{bmatrix}. \tag{4.48}$$

Since $\boldsymbol{A} = \boldsymbol{A}^T$, then $\boldsymbol{A}_\star = \boldsymbol{A}_\star^T$. At a first glance, variants of the CG method which are called MINRES and SYMMLQ are applicable in this problem, because they can be used in

the case of symmetric indefinite linear systems (*Paige & Saunders* [139]). Unfortunately, *Freund* [67] showed that by analyzing the spectral property of the coefficient matrix $\boldsymbol{A}_{\star}$, *Krylov* subspace methods are not applicable to solve the transforming real linear system (4.48). Thus it is implied that the MINRES and SYMMLQ methods are inappropriate to solve (4.48), since the MINRES and SYMMLQ methods as variants of the CG method belong to the family of *Krylov* subspace methods.

The coefficient matrix $\boldsymbol{A}$ can also be rewritten in real linear system as

$$\boldsymbol{A}_{\star\star} \begin{bmatrix} \Re(\boldsymbol{\theta}) \\ \Im(\boldsymbol{\theta}) \end{bmatrix} = \begin{bmatrix} \Re(\boldsymbol{b}) \\ \Im(\boldsymbol{b}) \end{bmatrix}, \quad \boldsymbol{A}_{\star\star} = \begin{bmatrix} \Re(\boldsymbol{A}) & -\Im(\boldsymbol{A}) \\ \Im(\boldsymbol{A}) & \Re(\boldsymbol{A}) \end{bmatrix}. \tag{4.49}$$

The matrix $\boldsymbol{A}_{\star\star}$ is unsymmetric and the resulting system can be solved by GMRES (*Barrett et al.* [11]). Again in this case, the spectra of $\boldsymbol{A}_{\star\star}$ are unsuitable for *Krylov* subspace methods (*Freund* [67]). As in the real case, the convergence rates of these methods depend strongly on the ratio of material parameters k^F/k^S and sometimes, the methods do not converge to proper solutions.

The explanation above and also some numerical and theoretical results produced by *Freund* [67] show that using *Krylov* subspace methods, the equivalent linear real-valued systems are more difficult to solve than the original complex-valued ones. Hence, in this thesis, the modified version of the CG method will be used to solve the complex-valued linear system (4.47) directly. This modified version of the CG method is called conjugate orthogonal conjugate gradients (COCG) (*van der Vorst & Melissen* [177]). Certainly, COCG can be preconditioned to accelerate the convergence as in the classical CG method. Indeed, the pseudocode for CG as displayed in (4.46) is applicable for COCG. The main difference of those two methods is that theoretically, the complex-valued scalar product $(\boldsymbol{x}, \boldsymbol{y}) = \hat{\boldsymbol{x}}^T \boldsymbol{y}$ should be replaced by the bilinear form $(\boldsymbol{x}, \boldsymbol{y}) = \boldsymbol{x}^T \boldsymbol{y}$, where the name *conjugate orthogonal* comes from. However, in the pseudocodes, the difference is invisible, COCG can break down in the case of the complex-valued linear systems, since the *conjugate scalar product* $\boldsymbol{d}^{(r)^T} \boldsymbol{g}^{(r)} = \boldsymbol{d}^{(r)^T} \boldsymbol{A} \boldsymbol{d}^{(r)} = 0$ in (4.46) for $\boldsymbol{d}^{(r)} \neq 0$. In the real linear systems, however, this difficulty does not occur, since if the scalar product $\boldsymbol{d}^{(r)^T} \boldsymbol{A} \boldsymbol{d}^{(r)} = 0$ and then $\boldsymbol{d}^{(r)} = 0$, which implies $\boldsymbol{\xi}^{(r-1)} = 0$ in the corresponding *Krylov* space (*van Kan & Segal* [179], p. 221). The residual $\boldsymbol{\xi}^{(r-1)} = \boldsymbol{A}\boldsymbol{\theta}^{(r-1)} - \boldsymbol{b} = 0$ implies that the exact solution is found.

The pseudocode is the same for the real case (box (4.46), but one has to be aware of the modified scalar product discussed above. The rigorous derivation of the method and the proofs can be found in *van der Vorst & Melissen* [177].

Chapter 5

Effective medium theory

The solutions of the boundary-value problems presented in Chapter 3 depend nonlinearly on the material parameters of the heterogeneous material components and thus depend on the microgeometry of the materials. This dependency implies that the mean values of the solutions of such problems and thus the effective material parameters (cf. 3.7) rely on the detailed microgeometries of the corresponding heterogeneous media. Unfortunately, in general, the complete information of the exact microstructure is not available. Therefore, one has to solve such problems by approximation.

One way to determine the estimated effective material parameters is by proposing the so-called mixing laws. It would be desirable to keep these mixing laws as simple as possible such as only requiring the material properties of phases of heterogeneous media and their volume fractions. However, in general, additional information about the nature of the mixture must be known if the material parameters have to be predicted accurately. This additional information can be particle size and shape, interactions between the phases and the nature of the packing found in the heterogeneous media.

For illustration, consider a biphasic random material composed of the phases φ^F and φ^S with the total volume fractions $\overline{n}^F$ (thermal conductivity k^F) and $\overline{n}^S$ (thermal conductivity k^S), respectively. Note that, for simplicity, the illustration will be given in terms of thermal conductivity. *Wiener* [188] considered a biphasic random material is composed of parallel layers of pure components φ^F and φ^S. If the layers are perpendicular to the direction of the applied temperature gradient (see Figure 5.1.a), then, the system is equivalent to two different thermal conductivities in serial connection and the overall thermal conductivity $\overline{k}$ is given by

$$\overline{k} = \left(\frac{\overline{n}^F}{k^F} + \frac{\overline{n}^S}{k^S} \right)^{-1} . \tag{5.1}$$

This can be proven as follows. Due to the applied temperature gradient $\operatorname{grad}\theta_0$, the obtained heat flux $\mathbf{q}_0$ in the REV is uniform, however, the temperature gradient varies. The volume average of the heat flux and the temperature gradient are given by

$$\overline{\mathbf{q}} = \frac{1}{A\,D} \int_{\mathcal{B}} \mathbf{q}\, \mathrm{d}\mathbf{x} = \frac{1}{A\,D} \int_{\mathcal{B}} \mathbf{q}_0\, \mathrm{d}\mathbf{x} = \mathbf{q}_0 \tag{5.2}$$

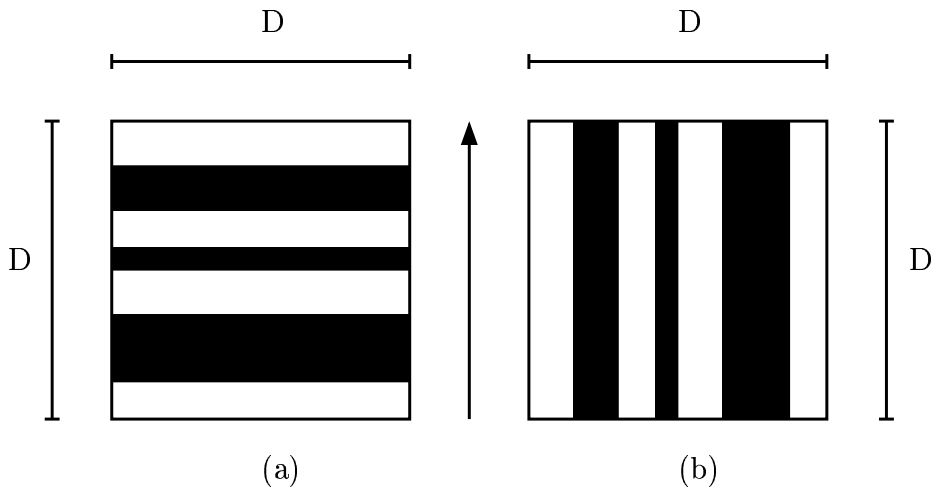

Figure 5.1: The parallel layers associated with the *Wiener* (a) lower bound and (b) upper bound. The arrow points in the direction of the applied temperature gradient $\operatorname{grad}\theta_0$.

and

$$\begin{aligned}\overline{\operatorname{grad}\theta} &= \frac{1}{A\,D}\int_{\mathcal{B}}\operatorname{grad}\theta\,\mathrm{d}\mathbf{x} = \frac{1}{A\,D}\left(\int_{\mathcal{B}^F}\operatorname{grad}\theta\,\mathrm{d}\mathbf{x}+\int_{\mathcal{B}^S}\operatorname{grad}\theta\,\mathrm{d}\mathbf{x}\right)\\ &= -\frac{1}{A\,D}\left(\int_{\mathcal{B}^F}\frac{\mathbf{q}_0}{k^F}\,\mathrm{d}\mathbf{x}+\int_{\mathcal{B}^S}\frac{\mathbf{q}_0}{k^S}\,\mathrm{d}\mathbf{x}\right) = -\mathbf{q}_0\left(\frac{\overline{n}^F}{k^F}+\frac{\overline{n}^S}{k^S}\right). \qquad (5.3)\end{aligned}$$

In (5.2) and (5.3), it is assumed that the cross section A is constant. Substituting (5.2) and (5.3) into (3.160) gives (5.1).

If the layers are parallel to the direction of the applied temperature gradient (see Figure 5.1.b), then the system is equivalent to two different thermal conductivities in parallel connection and the overall thermal conductivity $\overline{k}$ is given by

$$\overline{k} = \overline{n}^F k^F + \overline{n}^S k^S. \qquad (5.4)$$

This can be proven as follows. Due to the applied temperature gradient $\operatorname{grad}\theta_0$, the resulting temperature gradient $\operatorname{grad}\theta$ is uniform in the REV. The volume average of the temperature gradient is given by

$$\overline{\operatorname{grad}\theta} = \int_{\mathcal{B}}\operatorname{grad}\theta\,\mathrm{d}\mathbf{x} = \operatorname{grad}\theta_0. \qquad (5.5)$$

In contrast, the heat flux $\mathbf{q}$ is not uniform in the REV and its volume average can be computed as

$$\begin{aligned}\overline{\mathbf{q}} &= \frac{1}{A\,D}\int_{\mathcal{B}}\mathbf{q}\,\mathrm{d}\mathbf{x} = \frac{1}{A\,D}\left(\int_{\mathcal{B}^F}\mathbf{q}\,\mathrm{d}\mathbf{x}+\int_{\mathcal{B}^S}\mathbf{q}\,\mathrm{d}\mathbf{x}\right)\\ &= -\frac{1}{A\,D}\left(\int_{\mathcal{B}^F}k^F\operatorname{grad}\theta_0\,\mathrm{d}\mathbf{x}+\int_{\mathcal{B}^S}k^S\operatorname{grad}\theta_0\,\mathrm{d}\mathbf{x}\right)\\ &= -\operatorname{grad}\theta_0\,(\overline{n}^F k^F+\overline{n}^S k^S). \qquad (5.6)\end{aligned}$$

Substituting (5.5) and (5.6) into (3.160) yields (5.4). Note that in the elastic case, the corresponding models are the *Reuss* [150] and the *Voigt* models [182].

These empirical mixing laws (5.1) and (5.4) can be collected into one family and can be generalized as

$$(\overline{k})^i = \overline{n}^F (k^F)^i + \overline{n}^S (k^S)^i, \qquad -1 \leq i \leq 1. \tag{5.7}$$

Here, for $i = -1$ and $i = 1$, the previous *Wiener*'s models are recovered. For $i = 1/3$, the famous *Looyenga*'s mixing law [111] is recovered

$$\overline{k}^{1/3} = \overline{n}^F (k^F)^{1/3} + \overline{n}^S (k^S)^{1/3}. \tag{5.8}$$

For $i = 1/2$, one obtains the *Birchak*'s mixing law [29]

$$(\overline{k})^{1/2} = \overline{n}^F (k^F)^{1/2} + \overline{n}^S (k^S)^{1/2}, \tag{5.9}$$

which is used in the microwave remote sensing research. The *Birchak*'s mixing law can be traced back to the last century in the *Beer*'s monograph [12] and was confirmed experimentally by *Gladstone & Dale* [74] in case of liquid properties. By taking the limit $i \to 0$, (5.7) becomes the *Lichtenecker* logarithmic mixture-law [109, 110]

$$\ln(\overline{k}) = \overline{n}^F \ln(k^F) + \overline{n}^S \ln(k^S). \tag{5.10}$$

This can be proven as follows. For $i \to 0$, $(\overline{k})^i$ (as well $(k^F)^i$ and $(k^S)^i$) can be approximated as $1 + i \ln \overline{k}$ (*Arfken & Weber* [6]). Substituting these approximations into (5.7) yields (5.10).

Clearly, the only microgeometrical input in these mixing laws are the volume fractions of the heterogeneous medium. The volume fractions of the components of a heterogeneous medium are the most influential geometrical properties in determining the overall physical properties. However, in general, these simple mixing laws are unable to predict the overall material parameters accurately, because microgeometries are often very complicated and this complexity cannot be captured by a single parameter. To see this intuitively, consider a biphasic medium composed of 50% rubber and 50% steel. Two possible cases arise: (a) Dispersed rubber inclusions are embedded in the connected steel matrix (left side of Figure 5.2); (b) Dispersed steel particles are spread out in the connected rubber matrix (right side of Figure 5.2). Although it is evident that the first medium has very different elastic properties from the second one, a calculation of effective elastic constants which includes only the volume fraction would fail to bring out this distinction. A similar problem will happen in the electric conductivity case, if the rubber and the steel are assumed to be non-conducting and conducting materials, respectively. By employing only the porosity as a geometrical input parameter, one will obtain the same overall electric conductivities, evidently material (a) is conducting and material (b) is non-conducting. Obviously, the nature of the packing found in the heterogeneous media plays an important part in the overall strength and overall conductivity of the above biphasic materials.

An enhanced direct method is an approximation method based on the effective medium theory (EMT). On the other side, the EMT is quite simple to use and will give quite satisfactory results, if used properly. Therefore, in this chapter, the presented approximation

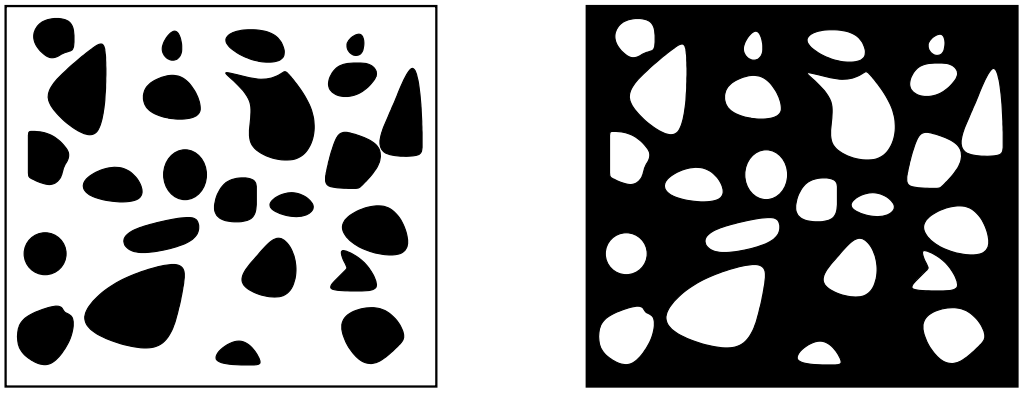

Figure 5.2: 50 − 50 biphasic medium consisting of a disconnected inclusion phase and a connected matrix phase. The black phase is the rubber material and the white phase is the steel.

methods are based on EMT. The main idea of the EMT is that an inclusion is taken out of the original heterogeneous material and inserted into an unknown infinitely extended homogeneous effective medium. Consider that homogeneous boundary conditions are imposed to this medium. Due to the presence of this single inclusion, which has different thermal and/ or elastic properties than those of the surrounding effective medium, the temperature gradient and/ or displacement gradient are disturbed. Therefore, this temperature gradient and/ or displacement gradient inside the inclusion is different to those outside the medium. Because the (averaged) temperature gradient and/ or displacement gradient in the unknown effective medium without the inclusion must be homogeneous, the averaged temperature gradient and/ or displacement gradient within the inclusion must be equal to the averaged temperature gradient and/ or displacement gradient outside the inclusion. In other words, the temperature gradient and/ or displacement gradient actually cannot feel the presence of the inclusion in the averaged sense (*Beran* [17], *Hashin & Shtrikman* [81], *Markov* [115]). This circumstance is defined as *effective medium* as seen by the temperature gradient and/ or displacement gradient (Figure 5.3). The requirement that the disturbance temperature gradient and/ or displacement gradient caused by the inclusion should be zero is called the self-consistent condition and, therefore, the method is called self-consistent method (*Kröner* [103, 104], *Budiansky* [38], *Nemat-Nasser & Hori* [135]). Theoretically, the inclusion can have any form and several inclusions can be inserted into the homogeneous effective medium. If both components of the biphasic material and also the homogeneous effective medium are assumed to behave as isotropic linear materials, one can take an inclusion of spherical shape as the first approximation. The EMT used in this thesis is based on the quasi-static approximation. One can also define an EMT dynamically by requiring that the average forward-scattering amplitudes of the inclusions should be vanish in the low-frequency limit (*Sheng* [162]).

Various classical effective medium approximations such as the *Bruggeman* effective medium approximation (BEMA) [37], the *Maxwell-Garnett* theory (MGT) [122] and the differential effective medium (*Bruggeman* [37]) in the case of the heat conduction are briefly described. The corresponding approaches in the elastic case known as the *Kröner*'s

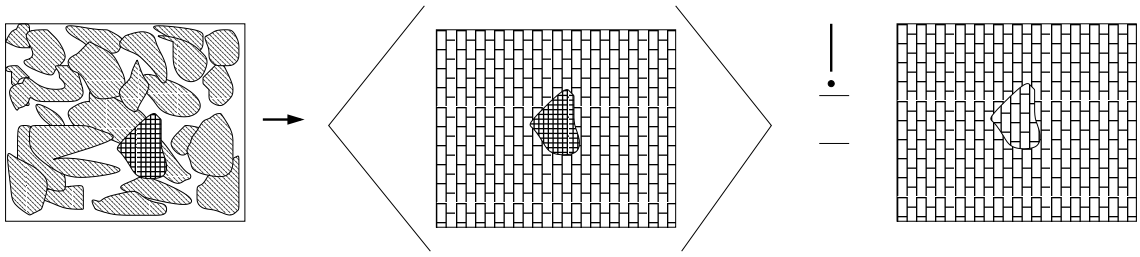

Figure 5.3: The scheme above describes the effective medium theory in finding the effective material parameters of a two-component random medium made up of components φ^F (left-leaning diagonal lines) and φ^S (white). The hatched grain can be φ^F or φ^S and is embedded in the effective medium (bricks), which has the yet unknown effective conductivity and/ or effective elastic moduli as shown in the middle. Upon volume averaging, the disturbance temperature gradient and/ or displacement gradient should vanish, which means that the inclusion is indeed invisible for the temperature gradient and/ or displacement gradient.

self-consistent method [103], as the *Mori-Tanaka* method [133], or as the three-phase model by *Christensen & Lo* [46] are given. All of these mixing laws are established using the solutions of the boundary-value problem of a single inclusion. The solution to this problem has a long history. For an isotropic conducting sphere and ellipsoid in an isotropic matrix the problem was solved by *Poisson*. Later, *Maxwell* treated them in his famous treatise [121]. Much later, *Eshleby* [64] gave the solution to an elastic field of an isotropic ellipsoid in an isotropic matrix. The brief historical remarks can be found in *Markov* [115].

The derivation of these mixing laws will be presented in the framework of the EMT and the volume averaging method. Different mixing laws based on the EMT can be linked to the different microgeometries of the heterogeneous medium. The BEMA treats the random medium with the aggregate microstructure (symmetric microstructure), whereas the MGT treats the random medium with the dispersion microstructure. Another example is the observation conducted by *Berryman & Berge* [25]. They found that different versions of the effective medium are useful for real materials with different classes of microstructures. The differential effective medium theory (*Norris* [137], *Watt* [184]) and the *Hashin* composite spheres assemblage [78] predict good overall elastic properties of a porous foam composed of glass, whereas BEMA is useful in predicting overall elastic behaviour of sintered glass-beads. Therefore, it is important to develop a more general method to incorporate more microstructural information in order to predict the overall material parameters. In order to give a more precise prediction of the transport parameter quantitatively, a more general mixing law based on a local porosity theory will be introduced. This provides more geometric information in terms of local volume fraction distribution and local percolation probabilities.

5.1 Thermal conductivity

5.1.1 Average heat flux through a coated sphere

The mixing laws based on the EMT may be derived using the so-called single inclusion problem. It is a boundary-value problem for an inclusion embedded in an infinite homogeneous medium whose material properties differ from those of the inclusion. The inclusion itself is allowed to be inhomogeneous. Upon solving this boundary-value problem, the temperature field inside the inclusion is known. For an ellipsoidal inclusion, the temperature gradient is constant (*Eshelby* [64], *Markov* [115]). The constant temperature gradient in the inclusion can be connected with the uniform applied field at infinity by the so-called *Wu*'s tensor (concentration factor) [194]. The *Eshelby*'s tensor [64] can be derived from the *Wu*'s tensor and vice versa. It is a second-order tensor for a linear conductive case.

To derive mixing laws for an isotropic heterogeneous material, a spherical inclusion is used. In this case, the *Wu*'s tensor reduces to a scalar quantity. For the sake of completeness, the solution of the single inclusion boundary-value problem is presented here.

Consider an isotropic coated sphere surrounded by an infinite homogeneous medium with the thermal conductivity $k^{(0)}$. The shell (core) of the coated sphere has the radius $R^{(1)}$ ($R^{(2)}$) and the conductivity $k^{(1)}$ ($k^{(2)}$). This ensemble is imposed to an external temperature field with constant gradient at infinity, i. e., $\theta(\mathbf{x} = \infty) = \theta_0\, x_3$ (see Figure 5.4). The temperature distribution is $\theta^{(i)}$ in the region i of the shell (core).

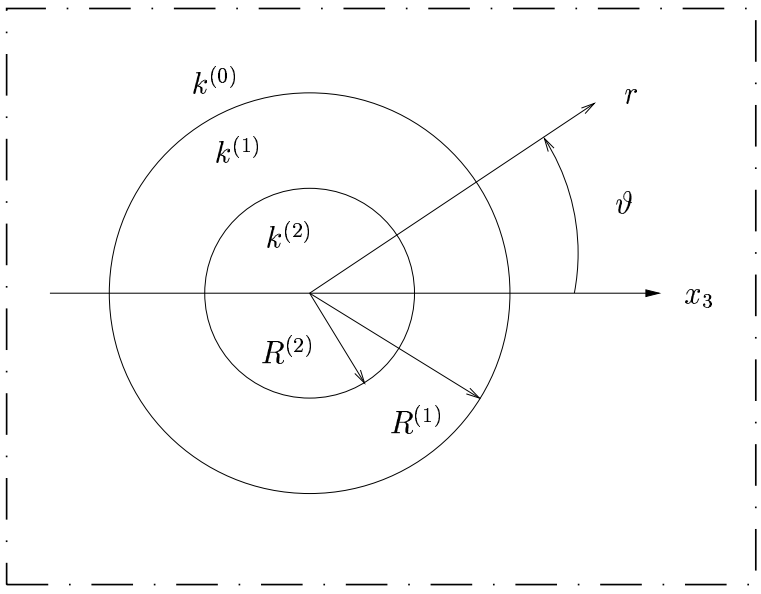

Figure 5.4: Coated spherical inclusion in a homogeneous medium imposed by a temperature field $\theta = \theta_0\, x_3$ at infinity.

Due to the spherical symmetry of the coated sphere, it will be easier to solve this

boundary-value problem in spherical coordinates (r, ϑ, φ). This representation of the spherical coordinates is chosen here to be compatible with the common representation of spherical coordinate system. Then, $(\theta^1, \theta^2, \theta^3)$ in appendix are set to $\theta^1 = r$, $\theta^2 = \vartheta$ and $\theta^3 = \varphi$. By exploiting its azimuthal symmetry $(\frac{\partial}{\partial\varphi}(\cdots) = 0)$ and by considering that $k^{(i)}$ is constant in each layer, the heat conduction equation (B.31) becomes

$$\frac{\partial^2\theta^{(i)}(r,\vartheta)}{\partial r^2} + \frac{1}{r^2}\frac{\partial^2\theta^{(i)}(r,\vartheta)}{\partial\vartheta^2} + \frac{2}{r}\frac{\partial\theta^{(i)}(r,\vartheta)}{\partial r} + \frac{1}{r^2\tan\vartheta}\frac{\partial\theta^{(i)}(r,\vartheta)}{\partial\vartheta} = 0 \tag{5.11}$$

with the boundary conditions at the interfaces $r = R^{(i)}$

$$\begin{aligned} \theta^{(i)}(r,\vartheta)\Big|_{r=R^{(i)}} &= \theta^{(i+1)}(r,\vartheta)\Big|_{r=R^{(i)}}, \\ k^{(i)}\,\frac{\partial\theta^{(i)}(r,\vartheta)}{\partial r}\Bigg|_{r=R^{(i)}} &= k^{(i+1)}\,\frac{\partial\theta^{(i+1)}(r,\vartheta)}{\partial r}\Bigg|_{r=R^{(i)}}. \end{aligned} \tag{5.12}$$

The general solution of (5.11) can be obtained in the form of (*Arfken & Weber* [6], *Jackson* [97])

$$\theta^{(i)}(r,\vartheta) = \sum_{k=0}^{\infty}\left(a_k^{(i)}\,r^k + b_k^{(i)}\,r^{-k-1}\right)P_k(\cos\vartheta), \tag{5.13}$$

where $a_k^{(i)}$ and $b_k^{(i)}$ are constants and $P_k(\cos\vartheta)$ are the *Legendre* polynomials. In spherical coordinates, the imposed external temperature gradient is

$$\operatorname{grad}\theta = \theta_0\,\mathbf{e}_3 = \theta_0\left(\cos\vartheta\,\mathbf{e}_r + \sin\vartheta\,\mathbf{e}_\vartheta\right), \tag{5.14}$$

where the relationships (B.4) and (B.5) are used. By considering the orthogonal property of the *Legendre* polynomials, $P_1(\cos\vartheta) = \cos\vartheta$, and the boundary conditions $(5.12)_2$, (5.13) reduces to

$$\theta^{(i)}(r,\vartheta) = (a^{(i)} + b^{(i)}\,r^{-3})\,r\,\cos\vartheta. \tag{5.15}$$

From the jump conditions (5.12), the boundary condition (θ_0 at $r \to \infty$) and $b^{(2)} = 0$ (to avoid a singularity at $r = 0$), all of the coefficients $a^{(i)}$ and $b^{(i)}$ can be found.

For later purposes, the average heat flux in the coated inclusion, $\overline{\mathbf{q}}^{\text{inc}}$, is given by

$$\begin{aligned} \overline{\mathbf{q}}^{\text{inc}} &= -\frac{1}{V^{\text{inc}}}\int_{\mathcal{B}^{\text{inc}}} k(\mathbf{x})\operatorname{grad}\theta(\mathbf{x})\,\mathrm{d}v \\ &= -\frac{3}{4\pi(R^{(1)})^3}\left(k^{(1)}\int_{\partial\mathcal{B}^1}\theta^{(1)}\,\mathrm{d}\mathbf{a} - k^{(1)}\int_{\partial\mathcal{B}^2}\theta^{(1)}\,\mathrm{d}\mathbf{a} + k^{(2)}\int_{\partial\mathcal{B}^2}\theta^{(2)}\mathrm{d}\mathbf{a}\right) \\ &= -\frac{1}{(R^{(1)})^3}\left[k^{(1)}\,a^{(1)}\left((R^{(1)})^3 - (R^{(2)})^3\right) + k^{(2)}\,a^{(2)}\,(R^{(2)})^3\right]\mathbf{e}_3, \end{aligned} \tag{5.16}$$

where

$$a^{(1)} = \frac{3\,k^{(0)}(2k^{(1)} + k^{(2)})}{(2k^{(0)} + k^{(1)})\,(2k^{(1)} + k^{(2)}) + 2\,(R^{(2)}/R^{(1)})^3\,(k^{(0)} - k^{(1)})\,(k^{(1)} - k^{(2)})}\,\theta_0, \tag{5.17}$$

$$a^{(2)} = \frac{9\,k^{(0)}k^{(1)}}{(2k^{(0)} + k^{(1)})\,(2k^{(1)} + k^{(2)}) + 2\,(R^{(2)}/R^{(1)})^3\,(k^{(0)} - k^{(1)})\,(k^{(1)} - k^{(2)})}\,\theta_0.$$

To obtain the second line of (5.16), (A.13) is used. For a single spherical inclusion, the average heat flux in the inclusion $\overline{\mathbf{q}}^{\text{inc}}$ can be obtained from (5.16) and (5.17) by inserting $k^{(1)} = k^{(2)}$ and $R^{(1)} = R^{(2)}$. Thus, $\overline{\mathbf{q}}^{\text{inc}}$ is

$$\overline{\mathbf{q}}^{\text{inc}} = -k^{(1)} a^{(1)}\, \mathbf{e}_3 = -\frac{3k^{(0)}k^{(1)}}{2k^{(0)} + k^{(1)}}\, \theta_0\, \mathbf{e}_3. \tag{5.18}$$

5.1.2 *Bruggeman* effective medium approximation

In this subsection, the results of the previous section are employed to derive the *Bruggeman* effective medium approximation (BEMA) [37]. Consider a biphasic random material with a volume fraction $\overline{n}^F$ of conductivity k^F and $\overline{n}^S$ of conductivity k^S, respectively, that is imposed under a constant temperature gradient $\theta_0\, \mathbf{e}_3$ across the medium. Evidently, it is $\overline{n}^F + \overline{n}^S = 1$. The BEMA assumes that the phases φ^F and φ^S may be decomposed into m^F and m^S inclusions, respectively. The shape of the inclusions may be arbitrary; however, for a macroscopic isotropic material it can be assumed that the inclusions are roughly spherical. The size of the inclusion is arbitrary, ranging from finite size to infinitesimally small (*Milton* [130], *Hashin* [78]). Then, these inclusion spheres are inserted into an homogeneous effective medium (RVE) of effective conductivity $\overline{k}$. The same boundary conditions are applied to the effective medium.

Applying (3.139) (here, $\mathbf{p}_0 = \theta_0\, \mathbf{e}_3$), the volume average temperature gradient $\overline{\operatorname{grad}\theta}$ can be obtained

$$\overline{\operatorname{grad}\theta} = \frac{1}{V}\int_{\mathcal{B}} \operatorname{grad}\theta(\mathbf{x})\, \mathrm{d}v = \theta_0\, \mathbf{e}_3. \tag{5.19}$$

From (5.18), the volume average heat flux $\overline{\mathbf{q}}$ can be evaluated as

$$\begin{aligned} \overline{\mathbf{q}} &= \frac{1}{V}\int_{\mathcal{B}} \mathbf{q}(\mathbf{x})\, \mathrm{d}v = \frac{m^F}{V}\int_{\mathbb{K}^F} \mathbf{q}(\mathbf{x})\, \mathrm{d}v + \frac{m^S}{V}\int_{\mathbb{K}^S} \mathbf{q}(\mathbf{x})\, \mathrm{d}v \\ &= -\overline{n}^F \frac{3\overline{k}\, k^F}{2\overline{k} + k^F}\, \theta_0\, \mathbf{e}_3 - \overline{n}^S \frac{3\overline{k}\, k^S}{2\overline{k} + k^S}\, \theta_0\, \mathbf{e}_3, \end{aligned} \tag{5.20}$$

where $\mathbb{K}^F$ ($\mathbb{K}^S$) is the inclusion of the phase φ^F (φ^S) and m^F and m^S are the number of the inclusions of φ^F and of the inclusions of φ^S, respectively. In the second step of (5.20), the main assumption of the effective medium approximation is used to convert the integral over the volume V of the RVE into an integral over the volume occupied by the inclusions $\mathbb{K}^F$ and $\mathbb{K}^S$. Recalling that the main assumption of the effective medium approximation is that each inclusion in the effective medium behaves as if it is isolated (cf. Figure 5.5). The average quantities in the last step are found using the results (5.15) and (5.18) of the previous section.

By inserting (5.19) and (5.20) into (3.160), the equation for the effective conductivity $\overline{k}$ can be obtained. Hence,

$$\overline{n}^F \frac{\overline{k} - k^F}{2\overline{k} + k^F} + \overline{n}^S \frac{\overline{k} - k^S}{2\overline{k} + k^S} = 0. \tag{5.21}$$

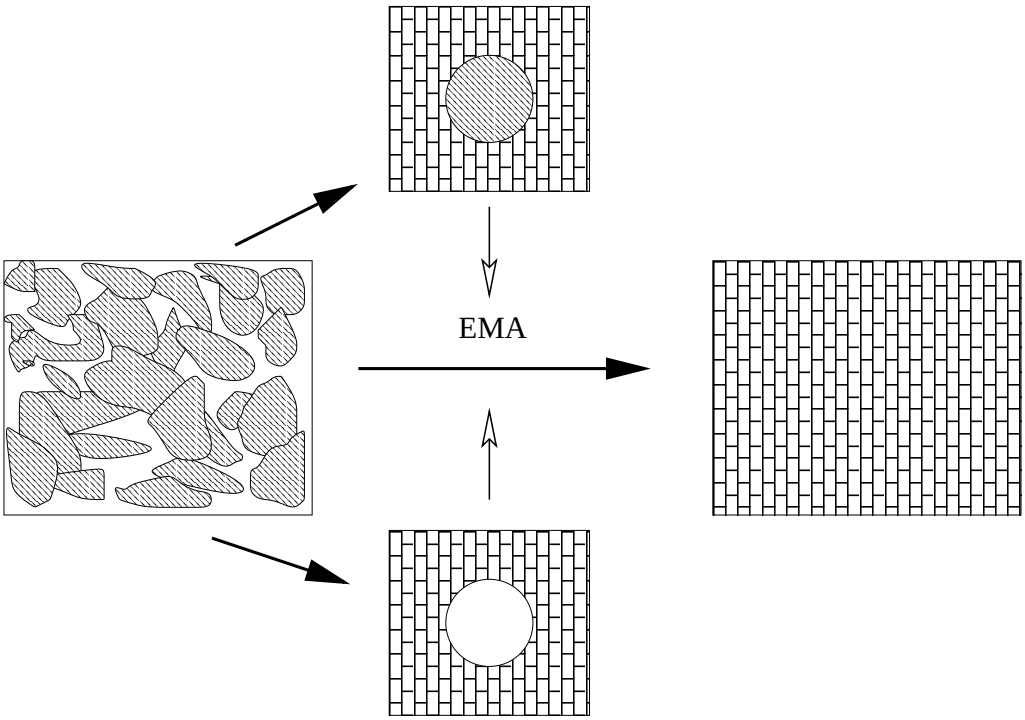

Figure 5.5: Schematic diagram of the *Bruggeman* effective medium approximation to determine the effective material parameters of a random medium, which has two structural units (on the middle): The first one consists of an inclusion with the material properties of material φ^F (left-leaning diagonal lines) embedded in an homogeneous effective medium (bricks region), as shown in the middle upper. The second one consists of an inclusion with the material properties of material φ^S (white region) embedded in an homogeneous effective medium (bricks region), as shown in the middle lower. The right figure is the effective reference medium, which has the effective material parameters obtained upon averaging all structural units. There is no direct interaction between the different inclusions.

Equation (5.21) is known in the physics and electromagnetics literature as the *Bruggeman* effective medium approximation (*Bruggeman* [37], *Sheng* [162], and *Sihvola* [164]) or the *Polder-van Santen* mixing law (*Polder* & *van Santen* [143], *Sihvola* [164], *Ishimaru* [96]). The BEMA is a symmetric mixing law, which means that the simultaneous interchange of k^F and k^S and of $\overline{n}^F$ and $\overline{n}^S$ results in the same overall conductivity.

It can be easily shown in the case of infinite contrast, i. e., $k^F/k^S = \infty$, that the mixing law (5.21) possesses a percolation threshold $\overline{n}_c^F = 1/3$, which means that, if the value of $\overline{n}^F$ is below $1/3$, the effective conductivity equals zero, i. e., $\overline{k} = 0$. This result can be interpreted as follows. Consider that a random material is composed of thermal conducting material $k^F = 1$ and of non-conducting material $k^S = 0$. The heat flux boundary condition (3.73) implies that no heat flux can flow into component φ^S. Therefore, as long as the thermal conducting phase does not form any cluster, which links a boundary side to its opposite side, the heat flux cannot flow through this inhomogeneous material, which implies that $\overline{k} = 0$. But, if the conducting material forms a cluster, which

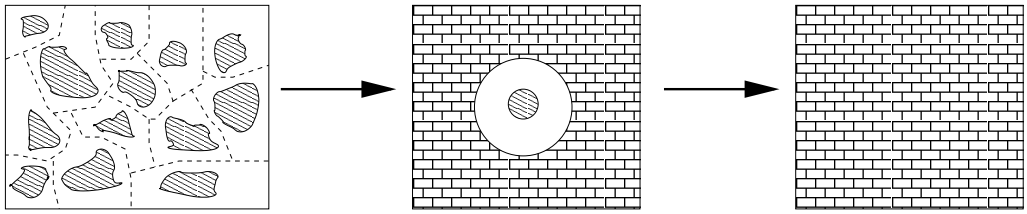

Figure 5.6: Schematic illustration of the *Maxwell-Garnett* approximation to find the effective material parameters of a random medium. The dashed lines show how the random medium is divided into structural units (on the left side). On the middle the structural unit is shown. It consists of a coated sphere, which is composed of a inclusion material as the shell (left-leaning diagonal lines) and matrix material (white region) as the core, embedded in an homogeneous effective medium (bricks region). The right figure is the effective reference medium, which has the unknown effective material parameters.

spans a boundary side to its opposite side, then, a non-vanishing effective conductivity exists ($\overline{k} \neq 0$). It can be proven using statistical analysis that this situation is possible only if the volume fraction $\overline{n}^F$ of the conducting component is greater than $\overline{n}_c^F = 1/3$ (*Landauer* [108]).

On the other hand, the BEMA has its shortcomings. Firstly, it does not allow direct correlations among particles, however, the interactions between particles are taken into account via the effective medium. *Hashin* [80] pointed out that this approximation indeed violates the RVE principle, because the single sphere as a microelement can only see other microelements (spheres) but not directly the minielement (the effective medium). *Hashin* ([80] p. 487) put it figuratively as "the BEMA assumes that a tree sees the forest but a tree sees only other trees". Secondly, the BEMA fails to predict a reasonable effective properties near the percolation threshold (*Davidson & Tinkham* [47]). However, the BEMA predicts very good overall permittivity of snow (*Mätzler* [119]) and for the case of a microstructure consisting of a small concentration of non-overlapping spherical grains embedded in a host. *Milton* [130] has shown that for a certain fractal-type microstructure, the BEMA gives exact overall material parameters.

5.1.3 *Maxwell-Garnett* theory

There are many composite media whose inclusions with the volume fraction $\overline{n}^F$ of conductivity k^F are distributed randomly in the matrix with the volume fraction $\overline{n}^S$ of conductivity k^S (left side of Figure 5.6). For such a medium, it is better to take a coated inclusion consisting of a core φ^F and a shell φ^S (instead of spheres of one constituent as was done in the BEMA) and to insert it into the homogeneous effective medium. Through this coated inclusion, the interaction between the components is taken into account. Consider that a random medium can be partitioned into m non-overlapping windows $\mathbb{K}^j$, which can be

modelized as *Hashin* assemblages [78]. In this case, the average heat flux is given by

$$\overline{\mathbf{q}} = \frac{1}{V}\int_{\mathcal{B}} \mathbf{q}(\mathbf{x})\,\mathrm{d}v = \frac{1}{V}\sum_{j=1}^{m}\int_{\mathbb{K}^j} \mathbf{q}(\mathbf{x})\,\mathrm{d}v = \frac{1}{V}\sum_{j=1}^{m} V_j\,\overline{\mathbf{q}_j(\mathbf{x})}(F_j), \tag{5.22}$$

where V_j is the volume of $\mathbb{K}^j$, and F_j is the microgeometry of the pore space in $\mathbb{K}^j$. In general, it is impossible to determine the average heat flux $\overline{\mathbf{q}_j}(F_j)$ per cell $\mathbb{K}^j$ by solving the boundary-value problem directly. Therefore, one has to find an approximate average heat flux in the cell $\mathbb{K}^j$ under the following assumptions:

- The porous medium is spatially and statistically homogeneous, which means that the average heat flux $\overline{\mathbf{q}}_j(F_j)$ does not depend on the position of the structural unit $\mathbb{K}^j$ in the porous medium.
- The correlation between cells is neglected, and the pore space configurations F_j in each cell are statistically independent. This will be approximately fulfilled for $R_S > L_{co}$, where R_S is the outer radius of the coated sphere and the correlation length L_{co} is defined as the length at which the correlation function decays to $\exp(-1)$.
- The pore space and the matrix space in each cell can be approximated by a coated sphere as first approximation (cf. Figure 5.6 in the middle).

Hence, by (5.16), one has the average heat flux $\overline{\mathbf{q}}(n_j^F)$ in each cell

$$\overline{\mathbf{q}}(n_j^F) = -\frac{1}{V}\sum_{j=1}^{m} \frac{3\,\overline{k}\,k^S[2k^S + k^F + 2\,n_j^F(k^F - k^S)]}{(2\overline{k} + k^S)(2k^S + k^F) + 2n_j^F(k^S - \overline{k})(k^F - k^S)}\,\theta_0\,V_j\,\mathbf{e}_3. \tag{5.23}$$

Contrary to the structural units of the BEMA (cf. Section 5.1.2 and Figure 5.5), in this case, the local volume fraction n_j^F of the dispersed phase can fluctuate from region to region. Therefore, the volume average should be reformulated by introducing the probability distribution $p(n^F, L)$ (2.22) of the local volume fraction n_j^F with the property

$$\overline{n}^F = \frac{1}{V}\sum_{j=1}^{m} n_j^F\,V_j = \int_0^1 n^F\,p(n^F, L)\,\mathrm{d}n^F. \tag{5.24}$$

Then, the average heat flux (5.23) can be expressed as

$$\overline{\mathbf{q}} = -\int_0^1 p(n^F, L)\frac{3\,\overline{k}\,k^S[2k^S + k^F + 2\,n^F(k^F - k^S)]}{(2\overline{k} + k^S)(2k^S + k^F) + 2n^F(k^S - \overline{k})(k^F - k^S)}\,\theta_0\,\mathrm{d}n^F\,\mathbf{e}_3. \tag{5.25}$$

By inserting this expression combined with (5.19) into the definition of the effective conductivity (3.160) and upon simple manipulations, one obtains

$$\int_0^1 p(n^F, L)\frac{(\overline{k} - k^S)(2k^S + k^F) - n^F(k^F - k^S)(2k^S + \overline{k})}{(2\overline{k} + k^F)(2k^F + k^S) + 2n^F(\overline{k} - k^F)(k^F - k^S)}\mathrm{d}n^F = 0. \tag{5.26}$$

When $\mu(p) = \delta(n^F - \overline{n}^F)$, (5.26) reduces to the celebrated MGT [122] which is also called the *Rayleigh* mixing law [149]

$$\frac{\overline{k} - k^S}{\overline{k} + 2k^S} = \overline{n}^F \frac{k^F - k^S}{k^F + 2k^S}. \tag{5.27}$$

(5.27) can be derived in the context of the electromagnetic theory through the *Clausius-Mossotti* relation based on the polarizabilities for determining the effective permittivity (*Sihvola* [164]). The derivation presented here stresses the role of the microstructure. Also, it should be emphasized that the *Maxwell-Garnett* equation (5.27) does not predict a percolation threshold. For the infinite contrast case ($k^F/k^S = \infty$), the effective conductivity is the same as the conductivity of the matrix phase because the inclusions are always prevented by the matrix phase to form an infinite cluster.

The MGT gives good results in predicting the permittivity of composite media (*Sheng* [158, 159], *Sheng & Callegari* [163]).

5.1.4 Differential effective medium

The differential effective medium (DEM) applies the EMT sequentially in determining the effective properties of heterogeneous random media. The DEM method replaces an infinitesimal concentration of the dispersion phase, let's say phase φ^F, into the host phase φ^S. It begins with the homogeneous phase φ^S as an initial host, and is altered in each step as a new concentration $\mathrm{d}n^F$ of the inclusion phase φ^F is inserted. The process is continued until the desired proportion of the constituents is attained. A schematic sketch of the iterative process is displayed in Figure 5.7.

The altered volume fraction $\mathrm{d}n^F$ of the phase φ^F in each step is not equal to $\mathrm{d}n^F$. Since by removing an amount of $\mathrm{d}n^F$ randomly from the effective medium of the previous step, a part of the phase φ^F is also removed. This removed part of φ^F is equal to $n^F\,\mathrm{d}n^F$, where n^F is the volume fraction of the phase in the effective medium of the previous step. Thus, the relationship between the altered volume fraction of the phase φ^F and the new amount of inserted inclusions is given by

$$\mathrm{d}n^F = (1 - n^F)\,\mathrm{d}n^F. \tag{5.28}$$

In each step, the effective material parameters are approximated using the dilute variant of the BEMA that can be obtained by expanding (5.21) around $n^F = 0$. Thus,

$$\overline{k}(n^F + \mathrm{d}n^F) = \overline{k}(n^F) + \frac{3\,\overline{k}(n^F)\,[k^F - \overline{k}(n^F)]}{k^F + 2\overline{k}(n^F)}\,\mathrm{d}n^F. \tag{5.29}$$

In the limit $\mathrm{d}n^F \to 0$, (5.29) becomes to the differential equation

$$(1 - n^F)\frac{\mathrm{d}\overline{k}}{\mathrm{d}n^F} = \frac{3\,\overline{k}\,[k^F - \overline{k}]}{k^F + 2\overline{k}}, \tag{5.30}$$

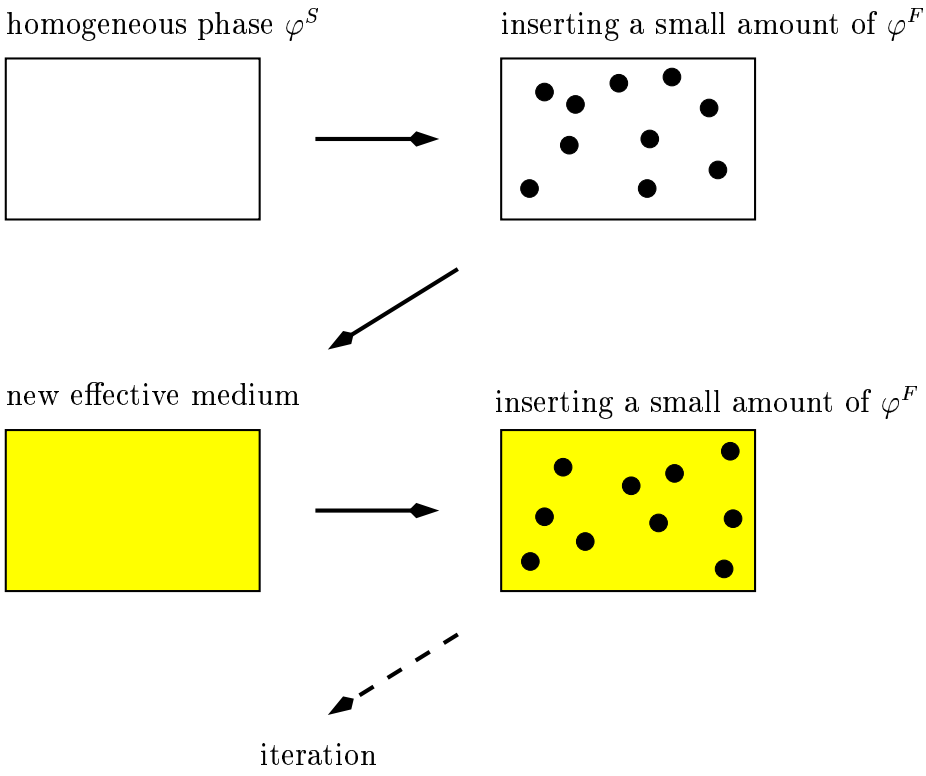

Figure 5.7: A schematic illustration of the iteration steps in the DEM method.

which can be integrated between the limits k^S and $\overline{k}$ and between the limits 0 and $\overline{n}^F$. This yields the following expression:

$$\frac{k^F - \overline{k}}{k^F - k^S} \left(\frac{k^S}{\overline{k}} \right)^{1/3} = 1 - \overline{n}^F. \tag{5.31}$$

Equation (5.31) is valid for the case of the spherical inclusion (for non spherical inclusion see *Norris et al.* [138], *Markov* [115]). Note that (5.29) can be derived rigorously using the theory of *Landau-Lifshitz* [107] which is valid for the dilute case only.

As in the case of the MGT, the DEM method treats the constituents unsymmetrically, which implies that there is a preferred material as a host material. Obviously, the effective material parameters depend crucially on which material is chosen as the host. When the biphasic material is composed of conducting and insulating materials, the difference can be seen immediately.

If the insulating phase is taken as the initial host phase, into which a small amount of the spherical particles of the conducting material is incrementally injected, then, the overall effective conductivity is zero, because in each step, the conducting particles are isolated by the insulating phase. This result is known as *Hanai-Bruggeman* mixing law (*Greffe & Grosse* [76]). If one starts with the conducting phase as the host phase and incrementally adds spherical particles of the insulating phase, then the overall effective conductivity is finite (not equal zero) because a conducting path always exists through

the conducting phase. This result leads to the mixing law of *Sen et al.* [157], which may capture the famous *Archies* law [5]. *Sen et al.* [157] successfully applied their mixing law in explaining the conductivity behaviour of sandstones.

However, this classical biphasic DEM model has a main disadvantage since sometimes it cannot treat different physical phenomena of a *bicontinuous material* in a unified framework. Bicontinuous means that both constituents form infinite paths across the heterogeneous random medium such as rocks, sandstones (*Mavko et al.* [120]) and infiltrated sintered materials (*Allais et al.* [3]). For example, consider a bicontinuous sandstone composed of the brine water (electric conductive material) and rock material (electric non conductive material). Since the overall electric conductivity of the sandstone is not equal to zero, the fluid material should be taken as an initial host phase in order to predict non-zero overall conductivity, but it cannot sustain the shear force since the solid constituent (rock mineral) is disjoint. On the other hand, if the rock mineral is taken as an initial host phase, the DEM model can sustain a shear force but the model is insulating, which is not correct in this case.

5.1.5 Mixing law based on the local porosity theory

It is pointed out in the previous sections that some difficulties occur in treating bicontinuous media. One way to overcome such difficulties is the introduction of a three-component DEM theory in which the solid particles are consolidated through the presence of the so-called cement material (*Sheng* [161]).

Recently, a more general mixing law based on the local porosity theory (MLLPT) was proposed to overcome some of the difficulties outlined above (*Hilfer* [88, 89], *Widjajakusuma et al.* [186]). In the MLLPT, the input of the microstructures is given by local porosity distributions and local percolation probabilities, which describe the porosity fluctuations and connectivity fluctuations, respectively (see also Section 2.2.2).

Similar to Section 5.1.3, the random medium is divided into m cubical non-overlapping windows $\mathbb{K}^1, \cdots, \mathbb{K}^m$ of side length L. In this case, the average heat flux is given by

$$\overline{\mathbf{q}} = \frac{1}{V}\int_S \mathbf{q}(\mathbf{x})\,\mathrm{d}v = \frac{1}{V}\sum_{j=1}^{m}\int_{\mathbb{K}^j} \mathbf{q}(\mathbf{x})\,\mathrm{d}v = \frac{1}{V}\sum_{j=1}^{m} V_j\,\overline{\mathbf{q}_j(\mathbf{x})}(F_j). \tag{5.32}$$

Here, F_j denotes the parameter which describes the geometry of the pore space inside the j-th cell. One has to solve a boundary-value problem to obtain the heat flux $\overline{\mathbf{q}_j(\mathbf{x})}(F_j)$. In practice, it is rarely possible to solve this boundary-value problem straightforwardly, because the complete information of the pore space geometry is generally unknown. However, one can still find an approximate heat flux under the assumptions given in Section 5.1.3 for the derivation of (5.26).

Again, the spherical coated inclusion can be used to approximate the geometry of the pore space and the matrix-space in each cell. Contrary to the dispersion microstructure (Section 5.1.3), there is an unidentifiable inclusion medium in each cell. The indicator function Λ_j can be employed to solve this problem. If a cell is percolating ($\Lambda_j = 1$), then, the structural unit of this cell can be taken as material φ^S coated by material φ^F. For

a non-percolating cell, the core and the shell are made up from materials φ^F and φ^S, respectively. In this case, one can solve the boundary-value problem accurately. This gives the heat flux $\overline{\mathbf{q}}(n_j^F, \Lambda_j, L)$ for each cell. It should be noted that the dependency on the internal surface S_j can be neglected for the thermal conducting problem. By summing over the cells and classifying different cells into different species according to their percolation, (5.32) becomes to

$$\overline{\mathbf{q}} \approx \frac{1}{m}\left[\sum_{j=1}^{m^F} \overline{\mathbf{q}}(n_j^F, \Lambda_j = 1, L) + \sum_{j=1}^{m^S} \overline{\mathbf{q}}(n_j^F, \Lambda_j = 0, L)\right], \tag{5.33}$$

where $m = V(\varphi^S)/V(\mathbb{K})$ is the number of cells in the partitioning of φ^S, m^F is the number of percolating cells, m^S is the number of non-percolating cells and $m = m^F + m^S$. By replacing $k^{(0)}$, $k^{(1)}$, $k^{(2)}$ and $(R^{(2)}/R^{(1)})^3$ with $\overline{k}$, k^F, k^S and $1 - n_j^F$, respectively, in (5.16), the average heat flux $\overline{\mathbf{q}}(n_j^F, \Lambda_j = 1, L)$ for the case of the conducting coated sphere is obtained:

$$\overline{\mathbf{q}}(n_j^F, \Lambda_j = 1, L) = -\frac{3\,\overline{k}\,k^F\,[3k^S + 2n_j^F\,(k^F - k^S)]\,\theta_0}{(k^F + 2\overline{k})\,(k^S + 2k^F) + 2\,(1 - n_j^F)\,(k^F - \overline{k})\,(k^S - k^F)}\,\mathbf{e}_3. \tag{5.34}$$

Similarly, one replaces $k^{(0)}$, $k^{(1)}$, $k^{(2)}$ and $(R^{(2)}/R^{(1)})^3$ with $\overline{k}$, k^S, k^F and n_j^F respectively in (5.16), and obtains the average heat flux of the non-conducting coated sphere

$$\overline{\mathbf{q}}(n_j^F, \Lambda_j = 0, L) = -\frac{3\,\overline{k}\,k^S[k^F + 2k^S + 2\,n_j^F(k^F - k^S)]\,\theta_0}{(k^S + 2\overline{k})\,(k^F + 2k^S) + 2\,n_j^F\,(k^S - \overline{k})\,(k^F - k^S)}\,\mathbf{e}_3. \tag{5.35}$$

In a porous medium, the local volume fraction n_j^F and the indicator function Λ_j for the connectivity can fluctuate from one cell to the next. As discussed in Chapter 2, the fluctuations of n_j^F and Λ_j are captured by $p(n^F, L)$ and $p_{\mathcal{L}}(n^F, L)$, respectively. As a result, the expression for the heat flux in (5.33) has to be reformulated using $p(n^F, L)$ and $p_{\mathcal{L}}(n^F, L)$

$$\begin{aligned}\overline{\mathbf{q}} \;\approx\; & -3\,\theta_0\,\overline{k}\int_0^1 \mu(p, L)\{\,p_{\mathcal{L}}(n^F, L)\,\frac{k^F\,[3k^S + 2n^F\,(k^F - k^S)]}{(k^F + 2\overline{k})\,(k^S + 2k^F) + 2\,(1 - n^F)\,(k^F - \overline{k})\,(k^S - k^F)} \\ & -\; \big[\,1 - p_{\mathcal{L}}(n^F, L)\big]\,\frac{k^S[k^F + 2k^S + 2\,n^F(k^F - k^S)]}{(k^S + 2\overline{k})\,(k^F + 2k^S) + 2\,n^F\,(k^S - \overline{k})\,(k^F - k^S)}\,\}\,\mathrm{d}n^F\,\mathbf{e}_3.\end{aligned} \tag{5.36}$$

By substituting (5.19) and (5.36) into (3.160), and after some algebraic simplifications, the mixing law based on the LPT takes the form of

$$\begin{aligned}&\int_0^1 p(n^F, L)\;p_{\mathcal{L}}(n^F, L)\;\frac{k^{cs}(k^F, k^S, 1 - n^F) - \overline{k}}{k^{cs}(k^F, k^S, 1 - n^F) + 2\,\overline{k}}\,\mathrm{d}n^F + \\ &+\int_0^1 p(n^F, L)[1 - p_{\mathcal{L}}(n^F, L)]\;\frac{k^{cs}(k^S, k^F, n^F) - \overline{k}}{k^{cs}(k^S, k^F, n^F) + 2\,\overline{k}}\,\mathrm{d}n^F = 0,\end{aligned} \tag{5.37}$$

where

$$k^{cs}(k^F, k^S, 1-n^F) = \frac{3k^S + 2n^F(k^F - k^S)}{3k^F - n^F(k^F - k^S)}\, k^F. \tag{5.38}$$

Root finding in the real case

For any given L, the approximate value of the MLLPT of the effective permittivity is the root of $\overline{k}$ of the mixing law (5.37). If μ and λ are known, the value of the MLLPT of the effective permittivity can be obtained by finding the root of the mixing law (5.37) iteratively. To find the root of the mixing law (5.37), firstly, (5.37) has to be evaluated numerically using the *extended midpoint rule* [145]. Thus,

$$F(k) \equiv (n_1^F - n_0^F)\left[\frac{f(n_0^F)}{2} + f(n_1^F) + \cdots + f(n_{n-1}^F) + \frac{f(n_n^F)}{2}\right] = 0, \tag{5.39}$$

where

$$\begin{aligned} f(n^F) &= p(n^F, L)\; p_{\mathcal{L}}(n^F, L)\; \frac{k^{cs}(k^F, k^S, 1-n^F) - k}{k^{cs}(k^F, k^S, 1-n^F) + 2k} + \\ &+ p(n^F, L)\left[1 - p_{\mathcal{L}}(n^F, L)\right]\; \frac{k^{cs}(k^S, k^F, n^F) - k}{k^{cs}(k^S, k^F, n^F) + 2k}, \end{aligned}$$

and n^F is the abscissa. For $k = \overline{k}$, $F(\overline{k})$ is equal to 0.

The next step is applying the *Van Wijngaarden-Dekker-Brent* method (VDB)[145] to find the root. It starts from $a = k^F$, $b = k^S$, which are the end points of the interval in which $\overline{k}$ is searched. The VDB carries out an iteration in which three values a, b and c are present at each step. Here, b is the latest iteration value that is the closest approximation to $\overline{k}$, a is the previous iteration value and c is the previous or an older iteration so that $F(b)$ and $F(c)$ have opposite signs. Clearly, b and c bracket $\overline{k}$ and $|F(b)| \leq |F(c)|$ during each iteration step. The VDB method improves the solution iteratively until the convergence criterion

$$|c - b| \leq \beta + 4.0\,\gamma\,|b| \quad \text{or} \quad F(b) = 0.0 \tag{5.40}$$

is satisfied, where β is the accuracy parameter. In addition to β, the machine accuracy parameter γ is involved to protect against the possibility that β is too small. The value b is returned to be the root of (5.39). Thus, b is the effective permittivity $\overline{k}$.

At each iteration step, the VDB chooses either bisection or inverse quadratic interpolation to find the root. Inverse quadratic interpolation is selected whenever a, b and c are distinctive and the point obtained by interpolation is *accepted*. *Accepted* means that the point is inside the current interval or the bounds decrease rapidly. Otherwise, the *bisection* step is taken. Thus, the VDB method combines the accuracy of bisection with the speed of a higher-order method whenever appropriate. For a detailed explanation, one is referred to *Press et al.* [145], Section 9.3, and references therein.

Length scales and limits of validity of mixing laws based on the LPT

Obviously, the mixing laws based on the LPT (5.37) and (5.50) provide effective material properties, i. e., $\overline{k}$ and $\overline{\overline{\varepsilon}}^c$, which depend on the length of the observable window (measurement cell) $\mathbb{K}$ (see 2.2.2). Therefore, it is important to determine the length, over which (5.37) and (5.50) provide reasonable estimations of $\overline{k}$ and $\overline{\overline{\varepsilon}}^c$.

The mixing laws (5.37) and (5.50), which are generalizations of the effective medium approximation (EMA), are expected to hold in neither the limit $L \to 0$ nor in the limit $L \to \infty$. For $L \to 0$, the observable window becomes a point and the local geometry becomes very simple but strongly correlated, which violates the effective medium assumption. For $L \to \infty$, the local simplicity assumption is not applicable. Therefore, the mixing laws are expected to provide reasonable estimation of the effective permittivity only over an intermediate range of values of L.

Several criteria for determining the length L, which is relevant to the estimation of the transport properties, have been proposed in earlier works on the local porosity theory (*Boger et al.* [34], *Hilfer* [90], *Hilfer et al.* [91] and *Widjajakusuma et al.* [186]). *Boger et al.* [34] gave three methods to determine L. The first method is called the entropy method, which can be described as follows. First, the so-called information function

$$I(L) = \int_1^0 p(n^F, L) \ln p(n^F, L) \, \mathrm{d}n^F \tag{5.41}$$

is introduced and then minimized, i. e.,

$$\left. \frac{\mathrm{d}I}{\mathrm{d}L} \right|_{L=L_{en}} = 0. \tag{5.42}$$

From (5.42), the length L_{en} can be obtained. This length is called entropy length L_{en} (*Boger et al.* [34]). The logical concept of this method is to maximize the geometrical content contained in $p(n^F, L)$. The entropy length of the eight digitized samples of Section 2.4 can be calculated and are depicted in Figure 5.8. These lengths are needed later for estimating the effective material parameters. The minimum points of these entropy functions can be read from these figures and are tabulated in Table 5.1. Note that the local minimum at $L = 2$ exists for some samples due to the bad statistics.

The second method is the correlation method, which is constructed from the fact that the local geometries are assumed to be statistically independent. This assumption is needed to apply an effective medium approximation. This condition is satisfied when the length scale is larger than the correlation length L_{co}. Therefore, the length scale L, at which the transport parameter is calculated, can be considered as the correlation length L_{co}. These correlation lengths have been discussed in Section 2.4 and are summarized in Table 5.1.

The third method is the experimental method. In this method, L is a free parameter determined from the experiments. It will denoted as L_{ex}, which can be implicitly defined as

$$k(L_{ex}) = \overline{k}. \tag{5.43}$$

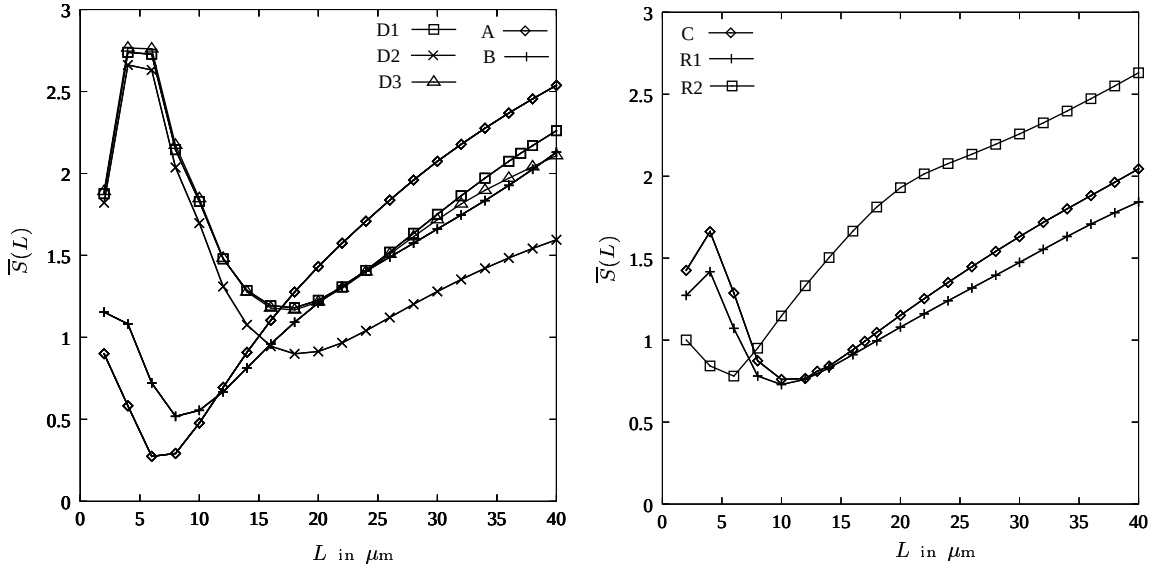

Figure 5.8: The information function $I(L)$ of the eight digitized samples.

Hence, L_{ex} is the length at which the estimated value from the MLLPT equals the experimental (exact) conductivity. Then, L_{ex} will be used as the fix length in estimating the effective material parameters of other physical problems. For example, from the measurement of the effective thermal conductivity, L_{ex} can be found. Now, L_{ex} is used as an input parameter into (5.37) to estimate the effective magnetic permeability.

The fourth method is the *percolation length* method. In this case, the length scale is obtained from $p(L)$ (*Hilfer et al.* [91], *Widjajakusuma et al.* [186]). The idea behind this method is that, since $p(L)$ is often of sigmoidal shape, one can use the inflection point of $p(L)$ at which $p(L)$ changes most rapidly from its trivial value $p(0) = n^F$ at small L to its other trivial value $p(\infty) = 1$ at large L (here, the porous medium is assumed to be globally connected). The length scale related to this method is called *percolation length* L_p, which can be defined as

$$\left.\frac{\mathrm{d}^2 p}{\mathrm{d}L^2}\right|_{L=L_p} = 0. \tag{5.44}$$

The first derivative of $p(L)$ is approximated by central differences. These curves are displayed in Figure 5.9 for different samples. The corresponding maxima are the inflection points of $p(L)$ as given in Table 5.1.

In addition to L_p, there are two other important length scales which contain information of the connectivity of the microstructure. Both of them are also obtained from the function $p(L)$. The first length scale is the threshold length L_c which is defined by

$$p(L_c) = p_c, \tag{5.45}$$

where p_c is the percolation threshold of the underlying lattice. Within the EMA, $p_c = 1/3$. Since $\lim_{L\to 0} p(L) = n^F$, L_c may not exist for samples whose porosity is $n^F > p_c$. Wherever

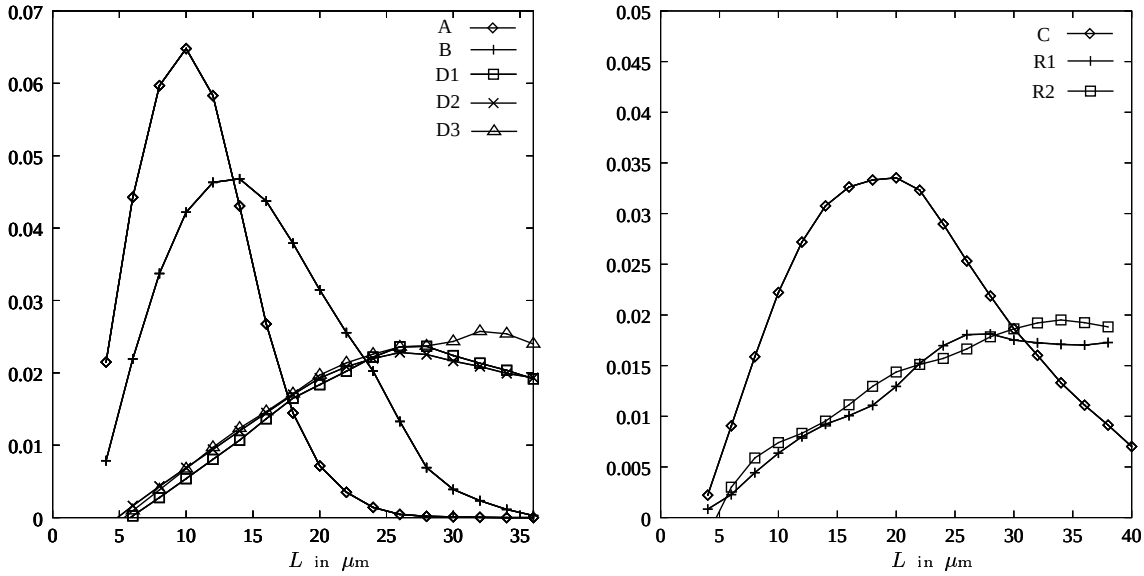

Figure 5.9: First derivative of function $p(L)$ (in unit of pixels) for the samples. The maxima are corresponding to the inflection points.

it exists, we have $\overline{k} = 0$ for $L \leq L_c$. Therefore in the LPT, L_c can be considered as a lower bound of the relevant intermediate range of lengths. The second length scale L_δ is the length at which $p(L)$ approaches its asymptotic value $p(\infty)$ to a given degree of accuracy δ. For a percolating sample, $p(\infty) = 1$ and for a non-percolating sample, $p(\infty) = 0$. Here, L_δ is defined through

$$L_\delta = \sup\{L : |p(\infty) - p(L)| \leq \delta\} \tag{5.46}$$

for small $\delta > 0$. L_δ represents the size of an averaging (smoothing) region that is needed to ensure that the fluctuating microscopic connectivity can be replaced by an averaged connectivity field defined on the continuum. Therefore, L_δ can be used as the size of the RVE with respect to the connectivity. The small parameter δ controls the degree of smoothness. The length L_δ can be considered as an upper bound of the relevant intermediate range of lengths at least if δ is chosen small (e. g., $\delta \leq 0.05$). For small values of δ , L_p always lies between L_c and L_δ, i. e., $L_c \leq L_p \leq L_\delta$. This can easily be verified from Figure 2.8 in Section 2.4 with $\delta = 0.05$ and using (5.46). For the samples A and B, the scales $L_\delta = 17.23$ and $L_\delta = 25.33$ are found, respectively, and for the other samples, $L_\delta > 40$.

5.2 Complex-valued permittivity

This section discusses the scalar transport properties in dissipative or lossy media using a quasi-static approximation. The permittivity problem is taken as representative for the scalar transport properties. The lossy media treated here are of conducting type (for another type of loss mechanism, see *Robert* [151]). In addition to the hitherto requirement

Sample	L_{en}	L_{co}	L_p	L_c
A	6.0	8.0	10.0	4.46
B	8.0	8.4	14.0	8.42
C	10.0	18.4	20.0	13.56
D1	18.0	13.8	28.0	24.72
D2	18.0	21.8	26.0	22.35
D3	18.0	13.9	32.0	23.85
R1	10.0	18.2	28.0	23.49
R2	6.0	6.7	34.0	24.37

Table 5.1: The length scales (in the units of a) which are used by mixing laws based on local porosity theory.

for quasi-static analysis in the lossless media, which requires the inclusions to be small compared to the wavelength in the effective material, one must demand that the penetration depth or the skin depth of the electric field must be much larger than the size of the inclusions. The reason is discussed in Section 3.3.3. One knows that in the conducting medium, the loss decays exponentially, and quick decay is not compatible with the determination of the electric field within the inclusion in the framework of the quasi-static approximation. Under these conditions, the mixing laws derived in the last section for the lossless media can be applied straightforwardly to the lossy media by replacing the corresponding real permittivity and the static fields by the frequency-dependent complex-valued permittivity and the frequency-dependent fields, respectively. Note that in order to emphasize that the permittivity is frequency dependent, the frequency ω will be explicitly written in the following mixing laws.
In this case, the BEMA can be written as

$$\overline{n}^F \frac{\overline{\tilde{\varepsilon}}^c(\omega) - \tilde{\varepsilon}^{cF}(\omega)}{2\overline{\tilde{\varepsilon}}^c(\omega) + \tilde{\varepsilon}^{cF}(\omega)} + \overline{n}^S \frac{\overline{\tilde{\varepsilon}}^c(\omega) - \tilde{\varepsilon}^{cS}(\omega)}{2\overline{\tilde{\varepsilon}}^c(\omega) + \tilde{\varepsilon}^{cS}(\omega)} = 0. \tag{5.47}$$

The MGT takes the form

$$\frac{\overline{\tilde{\varepsilon}}^c(\omega) - \tilde{\varepsilon}^{cF}(\omega)}{\overline{\tilde{\varepsilon}}^c(\omega) + 2\tilde{\varepsilon}^{cF}(\omega)} = \overline{n}^S \frac{\tilde{\varepsilon}^{cS}(\omega) - \tilde{\varepsilon}^{cF}(\omega)}{\tilde{\varepsilon}^{cS}(\omega) + 2\tilde{\varepsilon}^{cF}(\omega)}. \tag{5.48}$$

The two-component DEM method is given by

$$\frac{\tilde{\varepsilon}^{cS}(\omega) - \overline{\tilde{\varepsilon}}^c(\omega)}{\tilde{\varepsilon}^{cS}(\omega) - \tilde{\varepsilon}^{cF}(\omega)} \left(\frac{\tilde{\varepsilon}^{cF}(\omega)}{\overline{\tilde{\varepsilon}}^c(\omega)} \right)^{1/3} = 1 - n^F. \tag{5.49}$$

In the cases of the MGT and the DEM, the phase φ^F is taken as host and the spherical inclusions of the phase φ^S are randomly distributed in φ^F. If the phase φ^F is the fluid phase and φ^S is the solid phase, then, these cases can be seen as suspension problems of perfectly rigid spheres.

The mixing law based on the LPT may be written as

$$\int_0^1 p(n^F, L)\; p_{\mathcal{L}}(n^F, L)\; \frac{\tilde{\varepsilon}^{co}(\tilde{\varepsilon}^{cF}(\omega), \tilde{\varepsilon}^{cS}(\omega); 1-n^F) - \overline{\tilde{\varepsilon}}^c}{\tilde{\varepsilon}^{co}(\tilde{\varepsilon}^{cF}(\omega), \tilde{\varepsilon}^{cS}(\omega); 1-n^F) + 2\,\overline{\tilde{\varepsilon}}^c}\,\mathrm{d}n^F +$$

$$+ \int_0^1 p(n^F, L)\left[1 - p_{\mathcal{L}}(n^F, L)\right]\; \frac{\tilde{\varepsilon}^{co}(\tilde{\varepsilon}^{cS}(\omega), \tilde{\varepsilon}^{cF}(\omega), n^F) - \overline{\tilde{\varepsilon}}^c}{\tilde{\varepsilon}^{co}(\tilde{\varepsilon}^{cS}(\omega), \tilde{\varepsilon}^{cF}(\omega), n^F) + 2\,\overline{\tilde{\varepsilon}}^c}\,\mathrm{d}n^F = 0, \qquad (5.50)$$

where

$$\tilde{\varepsilon}^{co}(\tilde{\varepsilon}^{cF}(\omega), \tilde{\varepsilon}^{cS}, 1-n^F) = \tilde{\varepsilon}^{cF}(\omega)\,\frac{3\tilde{\varepsilon}^{cS}(\omega) + 2n^F[\tilde{\varepsilon}^{cF}(\omega) - \tilde{\varepsilon}^{cS}(\omega)]}{3\tilde{\varepsilon}^{cF}(\omega) - n^F[\tilde{\varepsilon}^{cF}(\omega) - \tilde{\varepsilon}^{cS}(\omega)]}. \qquad (5.51)$$

Root finding in the complex-valued case

As in the real case, the mixing law (5.50) for the complex-valued case (dissipative medium) can only be solved numerically. The downhill method, which was originally proposed by *Ward* [183] and later modified by *Bach* [10], is chosen to find the root of the complex-valued equation (5.50). The downhill method is chosen here because it is robust, does not require the calculations of any derivative and is global which means that it converges to the solution from almost any starting point. The only requirement is that the function must be analytic.

The idea behind the downhill method is to find a local minimum by sliding downhill on a single surface. Consider that the root of the function $f(z)$ has to be found. This local minimum will be the root of the function $f(z)$. In order to construct such a surface function, one can use the following theorem: If $f(z)$ is analytic, then the function $w(z) = |\Re(f(z))| + |\Im(f(z))|$ has no minimum value such that $w \neq 0$. Here, $\Re(z)$ and $\Im(z)$ represent the real and imaginary part of the complex-valued number $z = x + \mathrm{i}y$. The surface $w(z)$ is always above the xy-plane and has zero as the minimum value. It implies that the local minimum is equal to the root of the function $w(z)$. The root z_0 of the function $w(z)$ is also the root of the function $f(z)$, and vice versa. A detailed description can be found in *Bach* [10].

5.3 Linear elastic case

In the previous sections, the computation of the overall thermal conductivity $\overline{k}$ and electric permittivity $\overline{\tilde{\varepsilon}}^c$ in the framework of the EMT has been discussed. In this section, the discussion will be focused on the computation of the effective elasticity moduli. The method remains the same, but somehow, it is more complicated than the conductivity problem, because the elastic case is a tensorial problem, meanwhile the conductivity case is a vectorial problem. For a problem in isotropic linear elasticity, one needs two equations to determine two independent elasticity constants. Other elasticity constant are obtained immediately using the relations (3.109). In this section, it is considered that the constituents φ^F and φ^S are isotropic linear elastic materials which have bulk moduli

K^F and K^S and shear moduli G^F and G^S, respectively. For a linear isotropic elastic composite, one can determine the effective bulk modulus $\overline{K}$ from a uniform dilatation experiment $\boldsymbol{\varepsilon}_0 = (\boldsymbol{\varepsilon} \cdot \mathbf{I})\mathbf{I}$ and the effective shear modulus $\overline{G}$ from a deviatoric applied field $\mathbf{u} = \gamma(X_1\mathbf{e}_1 - X_2\mathbf{e}_2)$.

5.3.1 Average stress in a coated sphere

Many mixing laws based on the EMT are established using the solution of a coated spherical particle or a single spherical particle embedded in an infinite homogeneous effective medium. Therefore, this subsection is devoted to the solution of such boundary-value problems.

From the solution of the single inclusion problem, the displacement fields within the inclusion are known. For an ellipsoidal inclusion, the strain field is constant (*Eshelby* [64], *Markov* [115]). Furthermore, this constant strain field induced in the inclusion can be connected with the uniform applied field at infinity by the so-called *Wu*'s tensor [194]. In the elastic case, the *Wu*'s tensor is a fourth-order tensor and it has a close relationship with the *Eshelby*'s tensor (*Eshelby* [64], *Berryman* [24], *Markov* [115]).

Consider that a core with radius $R^{(2)}$, bulk modulus $K^{(2)}$, and shear modulus $G^{(2)}$ is surrounded by a shell with radius $R^{(1)}$ and elastic moduli $K^{(1)}$ and $G^{(1)}$. This coated sphere is embedded in an infinite homogeneous medium of bulk modulus $K^{(0)}$ and shear modulus $G^{(0)}$. The whole system (coated sphere + homogeneous medium) is imposed by an uniform deformation load at infinity as displayed in Figure 5.10. In the Cartesian coordinates (x_1, x_2, x_3), the load is given by

$$\mathbf{u}(\mathbf{x}) = (\boldsymbol{\varepsilon}_0 \cdot \mathbf{I} + \gamma)\, X_1\, \mathbf{e}_1 + (\boldsymbol{\varepsilon}_0 \cdot \mathbf{I} - \gamma)\, X_2\, \mathbf{e}_2 + (\boldsymbol{\varepsilon}_0 \cdot \mathbf{I})\, X_3\, \mathbf{e}_3, \tag{5.52}$$

where $\mathbf{e}_1$, $\mathbf{e}_2$ and $\mathbf{e}_3$ are unit vectors in x_1-, x_2- and x_3-direction, respectively. In the framework of linear elasticity, this problem can be decomposed into dilatation and deviatoric problems with the corresponding dilatation

$$\mathbf{u}_d(\mathbf{x}) = (\boldsymbol{\varepsilon}_0 \cdot \mathbf{I})\, (X_1\, \mathbf{e}_1 + X_2\, \mathbf{e}_2 + X_3\, \mathbf{e}_3), \tag{5.53}$$

and the corresponding deviatoric field

$$\mathbf{u}_s(\mathbf{x}) = \gamma\, (X_1\, \mathbf{e}_1 - X_2\, \mathbf{e}_2), \tag{5.54}$$

respectively.

Dilatation state

Due to the spherical symmetry, it is convenient to formulate this problem in spherical coordinates (r, ϑ, φ). This representation of the spherical coordinates is chosen here to be compatible with the common representation of a spherical coordinate system. Then, $(\theta^1, \theta^2, \theta^3)$ in the appendix are set to $\theta^1 = r$, $\theta^2 = \vartheta$ and $\theta^3 = \varphi$. At infinity, the outer boundary displacement (5.54) for the dilatation case is given by

$$\mathbf{u}_d = (\boldsymbol{\varepsilon_0} \cdot \mathbf{I}) r\, \mathbf{e}_r, \tag{5.55}$$

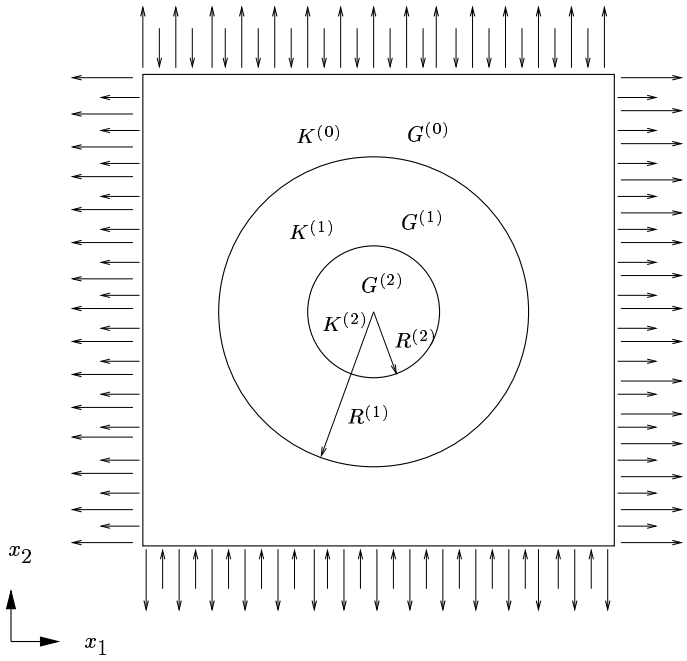

Figure 5.10: Coated spherical inclusion in a homogeneous medium is subject to an uniform displacement load at infinity. Long arrows denote the uniform dilatation and short arrows denote the deviatoric applied field.

where $\mathbf{e}_r$ is the unit vector in r-direction. Since the body and the load are spherically symmetric, the equilibrium equations without body forces (B.39) reduce to a one dimensional equation. Hence,

$$\frac{\partial t_{rr}}{\partial r} + \frac{2}{r}\left(t_{rr} - t_{\vartheta\vartheta}\right) = 0. \tag{5.56}$$

The equilibrium equation (5.56) can be expressed in terms of the radial displacement $u_r^{(i)}$ of each layer. Thus,

$$\frac{\partial^2 u_r^{(i)}}{\partial r^2} + \frac{2}{r}\frac{\partial u_r^{(i)}}{\partial r} - \frac{2}{r^2}u_r^{(i)} = 0. \tag{5.57}$$

At the interface between the i-th and $(i+1)$-th layer, the continuity of the displacement and of the normal stress have to be fulfilled, which can be formulated as

$$\begin{aligned} u_r^{(i)}(R^{(i+1)}) &= u_r^{(i+1)}(R^{(i+1)}), \\ t_{rr}^{(i)}(R^{(i+1)}) &= t_{rr}^{(i+1)}(R^{(i+1)}). \end{aligned} \tag{5.58}$$

The solution of (5.57) is given by *Love* [112] as

$$\mathbf{u}^{(i)}(\mathbf{r}) = (a^{(i)} r + \frac{b^{(i)}}{r^2})\,\mathbf{e}_r, \tag{5.59}$$

with constant coefficients $a^{(i)}$ and $b^{(i)}$. The corresponding stress tensor is given by

$$\mathbf{T}^{(i)}(\mathbf{r}) = (3K^{(i)}\,a^{(i)} - \frac{4G^i\,b^{(i)}}{r^3})\,\mathbf{e}_r \otimes \mathbf{e}_r + (3K^{(i)}\,a^{(i)} + \frac{2G^i\,b^{(i)}}{r^3})\,(\mathbf{e}_\vartheta \otimes \mathbf{e}_\vartheta + \mathbf{e}_\varphi \otimes \mathbf{e}_\varphi) \tag{5.60}$$

Using the internal boundary conditions (5.58), the external boundary condition (5.55) and $b_2 = 0$ to avoid the singularity at $r = 0$, the coefficients $a^{(i)}$ and $b^{(i)}$ can be determined.

By taking the average of (5.60) over the coated inclusion, the average stress $\overline{\mathbf{T}}^{\text{inc}}$ in the inclusion reads

$$\begin{aligned}\overline{\mathbf{T}}^{\text{inc}} &= \frac{1}{V^{\text{inc}}}\int_{\mathcal{B}^{\text{inc}}}\mathbf{T}(\mathbf{r})\,\mathrm{d}v = \frac{3}{4\pi(R^{(1)})^3}\left(\int_{\mathcal{B}1}\mathbf{T}^{(1)}(\mathbf{r})\,dv + \int_{\mathcal{B}^2}\mathbf{T}^{(2)}(\mathbf{r})\,dv\right) = \\ &= \frac{1}{(R^{(1)})^3}\{3K^{(1)}\,a_1[(R^{(1)})^3 - (R^{(2)})^3] + 3K^{(2)}\,a_2\,(R^{(2)})^3\}\,\mathbf{I} \qquad (5.61)\end{aligned}$$

with

$$a_1 = \frac{(3K^{(0)} + 4G^{(0)})(4G^{(1)} + 3K^{(2)})}{(4G^{(0)} + 3K^{(1)})(4G^{(1)} + 3K^{(2)}) + 12(R^{(2)}/R^{(1)})^3(G^{(0)} - G^{(1)})(K^{(1)} - K^{(2)})}\,(\boldsymbol{\varepsilon_0}\cdot\mathbf{I}),$$

$$a_2 = \frac{(3K^{(0)} + 4G^{(0)})(3K^{(1)} + 4G^{(1)})}{(4G^{(0)} + 3K^{(1)})(4G^{(1)} + 3K^{(2)}) + 12(R^{(2)}/R^{(1)})^3(G^{(0)} - G^{(1)})(K^{(1)} - K^{(2)})}\,(\boldsymbol{\varepsilon_0}\cdot\mathbf{I}). \qquad (5.62)$$

In the case of a single sphere, i. e., $K^{(1)} = K^{(2)}$, $G^{(1)} = G^{(2)}$ and $R^{(2)}/R^{(1)} = 1$, (5.61) reduces to

$$\overline{\mathbf{T}}^{\text{inc}} = 3K^{(1)}\,a_1\,\mathbf{I} = 3K^{(1)}\,\frac{3K^{(0)} + 4G^{(0)}}{4G^{(0)} + 3K^{(1)}}\,(\boldsymbol{\varepsilon_0}\cdot\mathbf{I})\,\mathbf{I}. \qquad (5.63)$$

Deviatoric applied field

In spherical coordinates (r, ϑ, φ), the displacement corresponding to the shear deformation (5.54) is given by

$$\mathbf{u}_s(r,\vartheta,\varphi) = \gamma r\sin\vartheta\,(\sin\vartheta\cos2\varphi\,\mathbf{e}_r + \cos\vartheta\cos2\varphi\,\mathbf{e}_\vartheta - \sin2\varphi\,\mathbf{e}_\varphi)\,. \qquad (5.64)$$

Due to the form of the boundary condition (5.64), the displacement in the i-th phase takes the form (*Love* [112])

$$\begin{aligned}\mathbf{u}_s^{(i)}(r,\vartheta,\varphi) &= \tilde{u}_r^{(i)}(r)\sin^2\vartheta\cos2\varphi\,\mathbf{e}_r + \tilde{u}_\vartheta^{(i)}(r)\sin\vartheta\cos\vartheta\cos2\varphi\,\mathbf{e}_\vartheta - \\ &\quad - \tilde{u}_\varphi^{(i)}(r)\sin\vartheta\sin2\varphi\,\mathbf{e}_\varphi. \qquad (5.65)\end{aligned}$$

By substituting the expression (5.65) in the *Lamé-Navier* equations and considering vanishing body forces, the following system of differential equations is obtained :

$$\tilde{u}_\varphi^{(i)}(r) = -\tilde{u}_\vartheta^{(i)}(r),$$

$$2\,(1-\nu)\left[\frac{\partial^2\tilde{u}_r^{(i)}(r)}{\partial r^2} + \frac{2}{r}\frac{\partial\tilde{u}_r^{(i)}(r)}{\partial r} - \frac{2\tilde{u}_r^{(i)}(r)}{r^2} - \frac{3}{r}\frac{\partial\tilde{u}_\vartheta^{(i)}(r)}{\partial r} + \frac{3\tilde{u}_\vartheta^{(i)}(r)}{r^2}\right] +$$

$$+\frac{3\,(1-2\nu)}{r}\left[\frac{\partial\tilde{u}_\vartheta^{(i)}(r)}{\partial r} + \frac{\tilde{u}_\vartheta^{(i)}(r)}{r} - \frac{2\tilde{u}_r^{(i)}(r)}{r}\right] = 0, \qquad (5.66)$$

$$\frac{4\,(1-\nu)}{r}\left[\frac{\partial \tilde{u}_r^{(i)}(r)}{\partial r}+\frac{2\tilde{u}_r^{(i)}(r)}{r}-\frac{3\tilde{u}_\vartheta^{(i)}(r)}{r}\right]+$$

$$+\quad (1-2\nu)\left[\frac{\partial^2 \tilde{u}_\vartheta^{(i)}(r)}{\partial r^2}+\frac{2}{r}\frac{\partial \tilde{u}_\vartheta^{(i)}(r)}{\partial r}-\frac{2}{r}\frac{\partial \tilde{u}_r^{(i)}(r)}{\partial r}\right]=0,$$

where ν is the *Poisson*'s ratio. The condition $(5.66)_1$ yields

$$t_{r\varphi}^{(i)} = -t_{r\vartheta}^{(i)}. \tag{5.67}$$

Then, by $(5.66)_1$ and (5.67), the jump conditions (3.61) and the requirement that the displacement across the interface must be continuous (for a perfect bonding between the phases) reduce to

$$\begin{aligned} u_r^{(i)} &= u_r^{(i+1)}, \\ u_\vartheta^{(i)} &= u_\vartheta^{(i+1)}, \\ t_{rr}^{(i)} &= t_{rr}^{(i+1)}, \\ t_{r\vartheta}^{(i)} &= t_{r\vartheta}^{(i+1)}. \end{aligned} \tag{5.68}$$

The ansatz functions solving (5.66) can be given by

$$\begin{aligned} \tilde{u}_r^{(i)}(r) &= c_1^{(i)}\,r-\frac{6\nu^{(i)}}{1-2\nu^{(i)}}c_2^{(i)}\,r^3+3\frac{c_3^{(i)}}{r^4}+\frac{5-4\nu^{(i)}}{1-2\nu^{(i)}}\,\frac{c_4^{(i)}}{r^2}, \\ \tilde{u}_\vartheta^{(i)}(r) &= c_1^{(i)}\,r-\frac{7-4\nu^{(i)}}{1-2\nu^{(i)}}c_2^{(i)}\,r^3-\frac{2c_3^{(i)}}{r^4}+\frac{2c_4^{(i)}}{r^2}, \\ \tilde{u}_\varphi^{(i)}(r) &= -\tilde{u}_\vartheta^{(i)}(r), \end{aligned} \tag{5.69}$$

where $c_1^{(i)}$, $c_2^{(i)}$, $c_3^{(i)}$ and $c_4^{(i)}$ are constants. Analogously to the dilatation case and to the heat conduction case, $c_1^{(i)}$, $c_2^{(i)}$, $c_3^{(i)}$ and $c_4^{(i)}$ can be evaluated and the average stress $\overline{\mathbf{T}}^{\text{inc}}$ in the whole coated inclusion can be computed. $\overline{\mathbf{T}}^{\text{inc}}$ is given by

$$\begin{aligned} \overline{\mathbf{T}}^{\text{inc}} &= \frac{2}{5(R^{(1)})^3}\left\{\frac{G^{(1)}(R^{(1)})^3}{(2\nu^{(1)}-1)}\left[5c_1^{(1)}(2\nu^{(1)}-1)+21c_2^{(1)}(R^{(1)})^2\right]-\right. \\ &- \frac{G^{(1)}(R^{(2)})^3}{(2\nu^{(1)}-1)}\left[5c_1^{(1)}(2\nu^{(1)}-1)+21c_2^{(1)}(R^{(2)})^2\right]- \\ &- \left.\frac{G^{(2)}(R^{(2)})^3}{(2\nu^{(2)}-1)}\left[5c_1^{(2)}(2\nu^{(2)}-1)+21c_2^{(2)}(R^{(2)})^2\right]\right\}(\mathbf{e}_1\otimes\mathbf{e}_1-\mathbf{e}_2\otimes\mathbf{e}_2). \end{aligned} \tag{5.70}$$

For a single inclusion, the coefficients $c_k^{(i)}$ become

$$\begin{aligned} c_1^{(1)} &= \frac{15\,(\nu^{(0)}-1)G^{(0)}}{5\,\nu^{(0)}\,G^{(0)}-7\,G^{(0)}+10\,G^{(1)}\nu^{(0)}-8\,G^{(1)}}\,\gamma, \\ c_2^{(1)} &= c_1^{(2)}=c_2^{(2)}=0 \end{aligned} \tag{5.71}$$

and the average stress $\overline{\mathbf{T}}^{\text{inc}}$ reduces to

$$\overline{\mathbf{T}}^{\text{inc}} = \frac{30\,(\nu^{(0)}-1)\,G^{(0)}\,G^{(1)}}{5\,\nu^{(0)}\,G^{(0)} - 7\,G^{(0)} + 10\,G^{(1)}\nu^{(0)} - 8\,G^{(1)}}\,\gamma\,(\mathbf{e}_1\otimes\mathbf{e}_1 - \mathbf{e}_2\otimes\mathbf{e}_2). \tag{5.72}$$

5.3.2 *Bruggeman* effective medium approximation

In this subsection, the application of the BEMA to the elastic case is presented. In elastic problems, this approach has been developed by *Budiansky* [38], *Hershey* [86], *Kröner* [103] and *Hill* [93]. This method is known as the self-consistent method in the mechanical community; however, because of historical reasons, in this thesis this method is called the BEMA.

Consider a biphasic random material composed of phases φ^F and φ^S with volume fractions $\overline{n}^F$ and $\overline{n}^S$, respectively. Their bulk and shear moduli are K^F and G^F, and K^S and G^S, respectively. To derive the equations for the effective bulk modulus $\overline{K}$ and the effective shear modulus $\overline{G}$ in the framework of the BEMA, it is assumed that the grains of φ^F and φ^S are roughly spherical. These spherical particles are taken out and embedded into an effective medium, on which uniform boundary conditions are prescribed.

If the uniform boundary condition is a uniform dilatation $\boldsymbol{\varepsilon}_0 = (\boldsymbol{\varepsilon_0}\cdot\mathbf{I})\mathbf{I}$, then, by using (5.63), the average stress field in the inclusion $\mathbb{K}^F$ of phase φ^F and in the inclusion $\mathbb{K}^S$ of phase φ^S can be computed. They are

$$\begin{aligned}
\overline{\mathbf{T}}_{\mathbb{K}^F} &= V_{\mathbb{K}^F}\,3K^F\,\frac{3\overline{K}+4\overline{G}}{4\overline{G}+3K^F}\,(\boldsymbol{\varepsilon_0}\cdot\mathbf{I})\,\mathbf{I},\\
\overline{\mathbf{T}}_{\mathbb{K}^S} &= V_{\mathbb{K}^S}\,3K^S\,\frac{3\overline{K}+4\overline{G}}{4\overline{G}+3K^S}\,(\boldsymbol{\varepsilon_0}\cdot\mathbf{I})\,\mathbf{I},
\end{aligned} \tag{5.73}$$

where $V_{\mathbb{K}^F}$ and $V_{\mathbb{K}^S}$ are the volume of the spheres $\mathbb{K}^F$ and $\mathbb{K}^S$, respectively. Here, it is again assumed that each inclusion behaves as if it is isolated. According to the assumption of the self-consistent condition that the average stress deviation (due to the presence of the inclusions) should be zero (cf. Figure 5.3), i. e.,

$$\frac{m^F}{V}\int_{\mathbb{K}^F}[\mathbf{T}(\mathbf{x}) - 3\overline{K}\boldsymbol{\varepsilon}(\mathbf{x})]\,\mathrm{d}v + \frac{m^S}{V}\int_{\mathbb{K}^S}[\mathbf{T}(\mathbf{x}) - 3\overline{K}\boldsymbol{\varepsilon}(\mathbf{x})]\,\mathrm{d}v = \mathbf{0},$$

which becomes to

$$\left[\overline{n}^F\left(\frac{3K^F}{4\overline{G}+3K^F} - \frac{3\overline{K}}{4\overline{G}+3K^F}\right) + \overline{n}^S\left(\frac{3K^S}{4\overline{G}+3K^S} - \frac{3\overline{K}}{4\overline{G}+3K^S}\right)\right](3\overline{K}+4\overline{G})\,(\boldsymbol{\varepsilon_0}\cdot\mathbf{I})\,\mathbf{I} = \mathbf{0}. \tag{5.74}$$

This leads to the equation for the effective bulk modulus $\overline{K}$:

$$\overline{n}^F\,\frac{K^F-\overline{K}}{3K^F+4\overline{G}} + \overline{n}^S\,\frac{K^S-\overline{K}}{3K^S+4\overline{G}} = 0. \tag{5.75}$$

To determine the effective shear modulus $\overline{G}$, one can prescribe a displacement load $\mathbf{u} = \gamma(X_1\mathbf{e}_1 - X_2\mathbf{e}_2)$ at infinity on a homogeneous effective medium. The deviations of the stresses within the inclusions $\mathbb{K}^F$ and $\mathbb{K}^S$, due to the fact that their elastic moduli differ from those of the surrounding effective material, are

$$\begin{aligned}\Delta\mathbf{T}_{\mathbb{K}^F} &= V_{\mathbb{K}^F}\,\frac{30\,(\overline{\nu}-1)\,\overline{G}\,(G^F-\overline{G})}{5\,\overline{\nu}\,\overline{G}-7\,\overline{G}+10\,\overline{\nu}\,G^F-8\,G^F}\,\gamma\,(\mathbf{e}_1\otimes\mathbf{e}_1-\mathbf{e}_2\otimes\mathbf{e}_2),\\ \Delta\mathbf{T}_{\mathbb{K}^S} &= V_{\mathbb{K}^S}\,\frac{30\,(\overline{\nu}-1)\,\overline{G}\,(G^S-\overline{G})}{5\,\overline{\nu}\,\overline{G}-7\,\overline{G}+10\,\overline{\nu}\,G^S-8\,G^S}\,\gamma\,(\mathbf{e}_1\otimes\mathbf{e}_1-\mathbf{e}_2\otimes\mathbf{e}_2),\end{aligned} \tag{5.76}$$

respectively. Here, $\overline{\nu}$ is the effective *Poisson* ratio. By employing (5.76), the average stress deviation over all spheres in the system can be calculated. Once the average total deviation is calculated, the equation for the effective shear modulus $\overline{G}$ can be obtained by considering that this total deviation should vanish (self-consistent condition). This yields

$$\overline{n}^F\,\frac{G^F-\overline{G}}{G^F+\beta}+\overline{n}^S\,\frac{G^S-\overline{G}}{G^S+\beta}=0. \tag{5.77}$$

with

$$\beta=\frac{\overline{G}(9\,\overline{K}+8\,\overline{G})}{6\,\overline{K}+12\,\overline{G}}. \tag{5.78}$$

The mixing laws (5.75) and (5.77) are also known as *Kröner*'s self-consistent method [103, 104].

5.3.3 *Maxwell-Garnett* theory

In this subsection, another way to derive the MGT will be presented (cf. 5.1.3). Consider that the matrix phase is φ^S and that the spherical inclusions of phase φ^F are randomly distributed in φ^S. The system is subjected to a uniform dilatation $\boldsymbol{\varepsilon}_0 = (\boldsymbol{\varepsilon}_\mathbf{0}\cdot\mathbf{I})\mathbf{I}$. Each inclusion is assumed to be affected by a certain external strain field $\hat{\boldsymbol{\varepsilon}}_0 = \overset{4}{\mathbf{G}}_w\boldsymbol{\varepsilon}_0$, which is equal to the mean strain of the matrix phase φ^S. It should be emphasized that $\hat{\boldsymbol{\varepsilon}}_0 \neq \boldsymbol{\varepsilon}_0$. Here, $\overset{4}{\mathbf{G}}_w$ is a fourth-rank transformation tensor, which is known as *Wu*'s tensor [194]. It connects the mean field strain $\hat{\boldsymbol{\varepsilon}}_0$ with the induced strain $\boldsymbol{\varepsilon}_0$. Then, the average strain can be expressed as

$$\overline{\boldsymbol{\varepsilon}}=\boldsymbol{\varepsilon}_0=\overline{n}^F\,\overline{\boldsymbol{\varepsilon}}^F+\overline{n}^S\,\overline{\boldsymbol{\varepsilon}}^S=\overline{n}^F\overset{4}{\mathbf{G}}_w\,\hat{\boldsymbol{\varepsilon}}_0+\overline{n}^S\hat{\boldsymbol{\varepsilon}}_0. \tag{5.79}$$

The first expression $\overset{4}{\mathbf{G}}_w\hat{\boldsymbol{\varepsilon}}_0$ follows from the assumption that each inclusion is treated as a single inclusion under the strain $\hat{\boldsymbol{\varepsilon}}_0$. By inserting $K^{(0)}=K^S$, $G^{(0)}=G^S$, $K^{(1)}=K^F$ and $\boldsymbol{\varepsilon}_\mathbf{0}\cdot\mathbf{I}=1$ into (5.63), $\overset{4}{\mathbf{G}}_w$ can be obtained:

$$\overset{4}{\mathbf{G}}_w=\frac{3K^S+4G^S}{4G^S+3K^F}\overset{4}{\mathbf{I}}. \tag{5.80}$$

Applying (5.79), (5.80) and considering the definition of $\overline{K}$, i. e., $\overline{\mathbf{T}} = 3\,\overline{K}\,\overline{\boldsymbol{\varepsilon}}$, the MGT for $\overline{K}$ in the case of the spherical inclusions can be written as

$$\frac{K^S - \overline{K}}{3\,\overline{K} + 4\,G^S} = \overline{n}^F \frac{K^S - K^F}{3\,K^F + 4\,G^S}. \tag{5.81}$$

Similarly, under the deviatoric applied field, the MGT for $\overline{G}$ can be found:

$$\frac{G^S - \overline{G}}{\overline{G} + \beta^S} = \overline{n}^F \frac{G^S - G^F}{G^F + \beta^S}. \tag{5.82}$$

Therein,

$$\beta^S = \frac{G^S}{6}\frac{9K^S + 8G^S}{K^S + 2G^S}. \tag{5.83}$$

The system of equations (5.81) and (5.82) is also attributed to the *Mori-Tanaka* method (MTM) [133]; however, due to the historical reason, in this thesis the method called MGT. As in the conductive case, the MGT corresponds to the *Hashin-Shtrikman* bounds, which will be further discussed in Chapter 6.

5.3.4 Differential effective medium

In Section 5.1.4, the basic idea of the differential effective medium (DEM) in the framework of the thermal conductivity has been discussed. This idea can be straightforwardly translated to the elastic case. If the phase φ^F is taken as the inclusion phase and φ^S as the matrix phase, the DEM method for spherical inclusions can be described by the following system of the differential equations

$$\begin{aligned} \frac{\mathrm{d}\overline{K}}{\mathrm{d}\overline{n}^F} &= \frac{(K^F - \overline{K})\,(3\,\overline{K} + 4\,\overline{G})}{(1 - \overline{n}^F)\,(3\,K^F + 4\,\overline{G})}, \\ \frac{\mathrm{d}\overline{G}}{\mathrm{d}\overline{n}^F} &= \frac{5\,\overline{G}\,(G^F - \overline{G})\,(3\overline{K} + 4\overline{G})}{(1 - \overline{n}^F)[6\,G^F\,(\overline{K} + 2\overline{G}) + \overline{G}\,(9\,\overline{K} + 8\,\overline{G})]}, \end{aligned} \tag{5.84}$$

with the initial conditions $\overline{K}(0) = K^S$ and $\overline{G}(0) = G^S$. Integration of the system of the differential equations (5.84) leads to

$$\frac{K^F - \overline{K}}{K^F - K^S}\left(\frac{K^S + 4\overline{G}}{\overline{K} + 4\overline{G}}\right)^3 = 1 - \overline{n}^F, \tag{5.85}$$

$$\left(\frac{G^S}{\overline{G}}\right)^{2/5}\left(\frac{G^F - \overline{G}}{G^F - G^S}\right)\left(\frac{3\,\overline{K} + 4\,G^S}{3\,\overline{K} + 4\,\overline{G}}\right)^c = 1 - \overline{n}^F \tag{5.86}$$

with

$$c = \frac{4\,G^F + 3\,\overline{K}}{20\,G^F + 15\,\overline{K}}.$$

5.3.5 Generalized self-consistent method

As discussed in Subsection 5.1.2, the BEMA has several shortcomings. Firstly, the BEMA actually violates the RVE principle. Secondly, the BEMA does not provide realistic results in the infinite-contrast cases, i. e., in the cases where the inclusions are either voids or rigid particles. However, this shortcomings can be overcome by introducing the so-called generalized self-consistent method (GSSM). In this case, the inclusion inserted in the effective medium is composed of the core material and of the shell material (cf. Figure 5.6). To this end, consider that the matrix phase is φ^S and the inclusion phase is φ^F.

Under a uniform dilatation strain field, the average stress in the particle is given by (5.63). By inserting the average stress and average strain into the average constitutive relation, $\overline{\mathbf{T}} = 3\,\overline{K}\,\overline{\boldsymbol{\varepsilon}}$, and upon algebraic simplification, the equation for $\overline{K}$ takes the form

$$\overline{K} = K^S + \frac{\overline{n}^F (K^F - K^S)(3K^S + 4G^S)}{3\overline{n}^S (K^F - K^S) + (3K^S + 4G^S)}. \tag{5.87}$$

The effective shear modulus can be determined by prescribing a deviatoric field. The average stress in the inclusion can be found. Applying the similar procedure to determine the equations for the effective material parameters, one can obtain the following quadratic equation for $\overline{G}$:

$$A_1 \left(\frac{\overline{G}}{G^S}\right)^2 + A_2 \frac{\overline{G}}{G^S} + A_3 = 0. \tag{5.88}$$

Therein,

$$\begin{aligned}
A_1 &= 8\,c\,c_1(4 - 5\nu^S)(\overline{n}^F)^{10/3} - 2(\,63\,c\,c_2 + 2\,c_1\,c_3\,)(\overline{n}^F)^{7/3} + 252\,c\,c_2\,(\overline{n}^F)^{5/3} - \\
&\quad - 50\,c\,c_2[7 - 12\nu^S + 8(\nu^S)^2]\,\overline{n}^F + 4\,c_2\,c_3\,(7 - 10\,\nu^S), \\
A_2 &= -4\,c\,c_1\,(1 - 5\nu^S)(\overline{n}^F)^{10/3} + 4(63\,c\,c_2 + 2\,c_1\,c_3)(\overline{n}^F)^{7/3} - 504\,c\,c_2(\overline{n}^F)^{5/3} + \\
&\quad + 150\,c\,c_2\,(3 - \nu^S)\,\nu^S\,\overline{n}^F + 3(15\nu^S - 7)\,c_2\,c_3, \\
A_3 &= 4\,c\,c_1\,(5\nu^S - 7)\,(\overline{n}^F)^{10/3} - 2(63\,c\,c_2 + 2\,c_1\,c_3)(\overline{n}^F)^{7/3} + 252\,c\,c_2\,(\overline{n}^F)^{5/3} + \\
&\quad + 25\,c\,c_2[(\nu^S)^2 - 7]\,\overline{n}^F - (7 + 5\nu^S)\,c_2\,c_3
\end{aligned}$$

with

$$\begin{aligned}
c &= \frac{G^F}{G^S} - 1, \\
c_1 &= c\,(7 - 10\nu^S)\,(7 + 5\nu^F) + 105\,(\nu^F - \nu^S), \\
c_2 &= c\,(7 + 5\nu^F) + 35\,(1 - \nu^F), \\
c_3 &= c\,(8 - 10\nu^S) + 15\,(1 - \nu^S).
\end{aligned}$$

Chapter 6

Rigorous bounds and cross properties

The purpose of this chapter is to summarize the bounds methods. Like the effective medium approximation discussed in Chapter 5, the bounds method also uses only partial microstructural information in predicting the effective material properties. Compared to the effective medium approximation that gives a predicted value of the effective material parameter, the bounds method confines the actual value of the effective material parameter using lower and upper bounds. Therefore, these bounds can be used to test the accuracy of an approximation method in estimating the effective material parameters.

The upper and lower bounds can be attained by substituting appropriate trial fields into the principle of the minimization of the potential energy W and the principle of the minimization of the complementary energy W^c, respectively. However, the admissable trial fields that yield tight bounds are hard to find since they must satisfy certain physical conditions and boundary conditions which will be discussed later. Therefore, finding an alternative way to improve the bounds with the same *effort* is necessary. This can be done by introducing a second (reference) homogeneous medium and using the energy potential of this reference medium W_0 to formulate an energy functional difference between the energy of the original heterogeneous medium and that of the reference medium. Note that the capital letter W and the small letter w are used to denote the effective energy potential and the local energy potential. Upon finding this difference, the bounds can be obtained by seeking its minimal and maximal values. In the literature, this method is known as *Hashin-Shtrikman* (HS) variational principle [82]. In the HS principle, the obtained lower or upper bound is determined by the choice of the reference medium. If the energy difference functional is greater than zero ($W - W_0 > 0$), the lower bound is attained; if the energy difference functional is less than zero ($W - W_0 < 0$), the upper bound is attained. Even though the type of the obtained bounds depends on the choice of the trial fields (how much microstructural information is contained in these trial fields). In general, the HS variational principles yield $2n$-point bounds, whereas the classical variational principles yield $2n-1$-point bounds. $2n$-point bounds and $2n-1$-point bounds mean that the $2n$-point correlation functions and the $2n-1$-point correlation functions of the heterogeneous medium are needed in evaluating the corresponding bounds, respectively.

Compared to other approximation methods, this method is more advantageous since it can be improved systematically by incorporating more microstructural information. In the simplest forms, these bounds are only functions of the constituents' volume fractions and the constituents' material parameters. They can be improved in various ways. However, this improvement depends on the geometrical and/or physical quantities that can be given as input parameters.

If the microgeometrical information is known, the simplest bounds can be enhanced by incorporating additional information, which can be given in form of higher point correlation functions of the constituents (*Beran* [17], *Torquato* [170], *Milton* [129]) or phase connectivity information (*Torquato* [171]).

If the effective material parameter can be measured, for example, the effective thermal conductivity, this measured conductivity can be used to improve the bounds on the yet unknown effective material property such as effective magnetic permeability, effective elastic moduli or effective hydraulic conductivity. In the literature, this way of deriving bounds is known as cross-property relationships. The cross-property relationship is important in estimating the effective properties that are more difficult to obtain using the effective properties which are easier to measure (*Markov* [115], *Berryman & Milton* [26], *Torquato* [171], *Gibiansky & Torquato* [73]). The cross-property relationship is valid under the assumption that the same heterogenous material under different physical processes keeps its microgeometry significantly unchanged. Otherwise, one cannot use them because the effective material parameters depend strongly and nonlinearly on the microgeometry of the heterogeneous material.

For dissipative media, for which the fields and material parameters are expressed in terms of the complex-valued variables such as the representation of the frequency dependent permittivity or of the dynamic viscoelastic moduli in the *Fourier* space, there is no direct complex-valued analogy to the variational principles for the real-valued problems. The reason is that one cannot order the complex-valued variables and thus, there exist no minimum or maximum values. To avoid this problem, the bounds on the effective complex-valued permittivity will be derived based on the analytic methods. This method, which was pioneered by *Bergman* [19] and *Milton* [128] independently, is based on the exploitation of analytic properties of the effective material parameter, such as $\overline{k}$, as function of the phase material parameters k^F and k^S. Recently, there are further approaches such as the field equation recursion method, the translation method and the compensated-compactness method to treat such complex-valued problems (*Milton* [131, 132], *Cherkaev* [42]).

Finally, this chapter is organized as follows. Section 6.1 presents some results from the convex analysis (*Ekeland & Teman* [61]), which is needed to derive the bounds on the effective material parameters. Section 6.2 reviews some bounds which are narrower than the elementary bounds on the class of material parameters, in which the material parameter is a proportionality factor between a divergenceless and an irrotational vector. Here, the thermal conductivity is chosen to represent this class. Section 6.3 discusses some bounds on complex-valued material parameters for dissipative systems. These bounds will be derived using the analytic method. Section 6.4 summarizes the bounds on the effective elastic moduli. Finally, Section 6.5 discusses some of the cross-property relations among

various overall material parameters of the heterogeneous materials.

6.1 Duality concept

6.1.1 Classical variational principles

To apply variational principles in deriving the upper and lower bounds, one can use the principle of the potential energy and the principle of the complementary energy, which are dual (conjugate) to each other (*Ponte Castañeda & Suquet* [39], *Willis* [192]). Both principles are related through the *Legendre-Fenchel* transformation (*Ekeland & Teman* [61]).

For a heterogeneous medium, the effective potential energy $W(\overline{\boldsymbol{\rho}})$ is expressed as the average of the local potential energy $w(\boldsymbol{\rho})$:

$$W(\overline{\boldsymbol{\rho}}) = \min_{\boldsymbol{\rho}\in\mathcal{A}} \overline{w(\mathbf{x},\boldsymbol{\rho})} = \min_{\boldsymbol{\rho}\in\mathcal{A}} \frac{1}{V}\int_{\mathcal{B}} w(\mathbf{x},\boldsymbol{\rho})\,\mathrm{d}v. \tag{6.1}$$

Here, $\mathcal{B}$ is the region of the heterogeneous RVE, V its volume and $\overline{\boldsymbol{\rho}}$ the solution for (6.1). The function $\boldsymbol{\rho}$ can be a vector (e. g., temperature gradient) or a tensor quantity (e. g., strain field). The function $\boldsymbol{\rho}$ has to satisfy certain physical and boundary conditions; for example, if the function $\boldsymbol{\rho}$ represents the strain field, then it has to be compatible with the corresponding displacement field and the displacement boundary condition. The set $\mathcal{A}$ is the collection of such admissable functions $\boldsymbol{\rho}$. The minimum condition in (6.1) implies the principle of minimum microscopic potential energy, i. e., among all admissable functions $\boldsymbol{\rho}$, the true field $\hat{\boldsymbol{\rho}}$ should minimize the potential energy. The true local field $\hat{\boldsymbol{\rho}}$ needs not be the same as the macroscopical field $\overline{\boldsymbol{\rho}}$.

Similarly, the effective complementary energy $W^c(\overline{\boldsymbol{\rho}^\star})$ is defined as the average of the local complementary energy $w^c(\mathbf{x},\boldsymbol{\rho}^\star)$; hence,

$$W^c(\overline{\boldsymbol{\rho}^\star}) = \min_{\boldsymbol{\rho}^\star\in\mathcal{A}^\star} \overline{w^c(\mathbf{x},\boldsymbol{\rho}^\star)} = \min_{\boldsymbol{\rho}^\star\in\mathcal{A}^\star} \frac{1}{V}\int_{\mathcal{B}} w^c(\mathbf{x},\boldsymbol{\rho}^\star)\,\mathrm{d}v. \tag{6.2}$$

The solution for (6.2) is denoted by $\overline{\boldsymbol{\rho}^\star}$. The functional $\boldsymbol{\rho}^\star$ is referred to as the dual variable of $\boldsymbol{\rho}$. As in the case of $\boldsymbol{\rho}$, $\boldsymbol{\rho}^\star$ can be a vector field (e. g., heat flux) or a tensor field (e. g., stress tensor) and has to fulfill certain physical and boundary conditions. The minimum condition in (6.2) implies the principle of minimum microscopic complementary energy, i. e., among all admissable functions $\boldsymbol{\rho}^\star$, the true field $\hat{\boldsymbol{\rho}}^\star$ should minimize the complementary energy. The true local field $\hat{\boldsymbol{\rho}}^\star$ needs not be the same as the macroscopical field $\overline{\boldsymbol{\rho}}^\star$.

The effective complementary energy and the effective potential energy are connected via the *Legendre-Fenchel* transformation:

$$W^c(\overline{\boldsymbol{\rho}^\star}) = \max_{\overline{\boldsymbol{\rho}}} \left\{\overline{\boldsymbol{\rho}}\cdot\overline{\boldsymbol{\rho}^\star} - W(\overline{\boldsymbol{\rho}})\right\}. \tag{6.3}$$

Applying the *Legendre-Fenchel* transformation to the effective complementary energy, one obtains the so-called *second conjugate* form of $W(\overline{\boldsymbol{\rho}})$, $W^{cc}(\overline{\boldsymbol{\rho}})$:

$$W^{cc}(\overline{\boldsymbol{\rho}}) = \max_{\overline{\boldsymbol{\rho}^\star}} \left\{ \overline{\boldsymbol{\rho}} \cdot \overline{\boldsymbol{\rho}^\star} - W^c(\overline{\boldsymbol{\rho}^\star}) \right\}. \tag{6.4}$$

Geometrically, the second conjugate functional $W^{cc}(\overline{\boldsymbol{\rho}})$ can be seen as the lower convex envelope of the functional $W(\overline{\boldsymbol{\rho}})$, i. e., the highest function lying under $W(\overline{\boldsymbol{\rho}})$ which is convex. Hence,

$$W^{cc}(\overline{\boldsymbol{\rho}}) \leq W(\overline{\boldsymbol{\rho}}). \tag{6.5}$$

Equality is attained in (6.5) when the functional $W(\overline{\boldsymbol{\rho}})$ is convex. If $W(\overline{\boldsymbol{\rho}})$ is convex, then the maximum conditions in (6.3) and (6.4) lead to the following relations between the dual variables

$$\overline{\boldsymbol{\rho}^\star} = \frac{\partial W(\overline{\boldsymbol{\rho}})}{\partial \overline{\boldsymbol{\rho}}}, \tag{6.6}$$

$$\overline{\boldsymbol{\rho}} = \frac{\partial W^c(\overline{\boldsymbol{\rho}^\star})}{\partial \overline{\boldsymbol{\rho}^\star}}. \tag{6.7}$$

Analogously, for the local forms, the complementary energy $w^c(\mathbf{x}, \boldsymbol{\rho}^\star)$ can be obtained by applying the *Legendre-Fenchel* transformation to the local potential energy $w(\mathbf{x}, \boldsymbol{\rho})$:

$$w^c(\mathbf{x}, \boldsymbol{\rho}^\star) = \max_{\boldsymbol{\rho} \in \mathcal{A}} \left\{ \boldsymbol{\rho} \cdot \boldsymbol{\rho}^\star - w(\mathbf{x}, \boldsymbol{\rho}) \right\}. \tag{6.8}$$

The second conjugate functional of the local potential energy, $w^{cc}(\mathbf{x}, \boldsymbol{\rho})$, can also be obtained:

$$w^{cc}(\mathbf{x}, \boldsymbol{\rho}) = \max_{\boldsymbol{\rho}^\star \in \mathcal{A}^\star} \left\{ \boldsymbol{\rho} \cdot \boldsymbol{\rho}^\star - w^c(\mathbf{x}, \boldsymbol{\rho}^\star) \right\}. \tag{6.9}$$

The functionals $w^{cc}(\mathbf{x}, \boldsymbol{\rho})$ and $w(\mathbf{x}, \boldsymbol{\rho})$ are related by the following inequality equation:

$$w^{cc}(\boldsymbol{\rho}) \leq w(\boldsymbol{\rho}). \tag{6.10}$$

And, if $w(\mathbf{x}, \boldsymbol{\rho})$ is convex in $\boldsymbol{\rho}$, equality is attained. If $w(\mathbf{x}, \boldsymbol{\rho})$ is convex, then similar relations for $\boldsymbol{\rho}$ and $\boldsymbol{\rho}^\star$ as in (6.6) and (6.7) follow from the maximum conditions (6.8) and (6.9):

$$\boldsymbol{\rho}^\star = \frac{\partial w(\mathbf{x}, \boldsymbol{\rho})}{\partial \boldsymbol{\rho}}, \tag{6.11}$$

$$\boldsymbol{\rho} = \frac{\partial w^c(\mathbf{x}, \boldsymbol{\rho}^\star)}{\partial \boldsymbol{\rho}^\star}. \tag{6.12}$$

Note that the above definitions and results can be directly transcribed to a concave function g since in that case $-g$ is a convex function.

Since only the actual solution $\overline{\boldsymbol{\rho}}$ of the energy problem (6.1) gives the minimal potential energy, a one-sided upper bound on the effective energy (and thus the effective material parameters) can be attained by inserting any $\boldsymbol{\rho} \in \mathcal{A}$:

$$W(\overline{\boldsymbol{\rho}}) \leq \overline{w(\mathbf{x}, \boldsymbol{\rho})}. \tag{6.13}$$

Analogously, an upper bound on the effective complementary energy can be obtained for any $\boldsymbol{\rho}^\star \in \mathcal{A}^\star$:

$$W^c(\overline{\boldsymbol{\rho}^\star}) \leq \overline{w^c(\mathbf{x}, \boldsymbol{\rho}^\star)}. \tag{6.14}$$

Especially, by taking $\boldsymbol{\rho} = \overline{\boldsymbol{\rho}}$ and $\boldsymbol{\rho}^\star = \overline{\boldsymbol{\rho}^\star}$ and having regarded the fact that a conjugacy operation is order-reversing ($\overline{\boldsymbol{\rho}}$ and $\overline{\boldsymbol{\rho}^\star}$ are conjugate pair), it leads to

$$(\overline{w^c})^c(\overline{\boldsymbol{\rho}}) \leq W(\overline{\boldsymbol{\rho}}) \leq \overline{w(\overline{\boldsymbol{\rho}})}. \tag{6.15}$$

These simple bounds are analogous to the *Wiener* bounds of a linear conductive material or to the *Reuss* and *Voigt* bounds of a linear elastic material.

6.1.2 *Hashin-Shtrikman* variational principles

In most cases, unfortunately, the simple bounds (6.15) are far apart from each other; meanwhile, to get more restrictive bounds by choosing the admissable fields, which contain more detailed microgeometrical information, is a difficult task. To overcome this problem, the *Hashin-Shtrikman* variational principle, an approach which has been proved to be highly successful, is applied. This principle utilizes a homogeneous reference material (of the same shape and size) with energy density $w_0(\mathbf{x}, \boldsymbol{\rho})$ such that the difference potential $(w - w_0)$ is a convex function. Note that in general $(w - w_0)$ needs not to be convex. As a starting point, the *Legendre-Fenchel* transformation of $(w - w_0)$ can be used:

$$(w - w_0)^c(\mathbf{x}, \boldsymbol{\tau}) = \max_{\boldsymbol{\rho}} \left\{ \boldsymbol{\tau} \cdot \boldsymbol{\rho} - (w - w_0)(\mathbf{x}, \boldsymbol{\rho}) \right\}. \tag{6.16}$$

If $(w - w_0)$ is differentiable, the maximum is attained for

$$\boldsymbol{\tau}(\mathbf{x}) = \frac{\partial[(w - w_0)(\mathbf{x}, \boldsymbol{\rho})]}{\partial \boldsymbol{\rho}}. \tag{6.17}$$

Therein, $\boldsymbol{\tau}$ is a polarization vector or a polarization tensor field. Here, $\boldsymbol{\tau}$ is dual to $\boldsymbol{\rho}$ for the difference of the potential energy $(w - w_0)$, meanwhile $\boldsymbol{\rho}^\star$ is dual to $\boldsymbol{\rho}$ for the potential energy w. As an example in the linear elastic case, if the stress and strain fields of the actual heterogeneous medium are denoted by $\mathbf{T}(\mathbf{x})$ and $\boldsymbol{\varepsilon}(\mathbf{x})$, respectively. The polarization tensor $\boldsymbol{\tau}$ is defined by

$$\boldsymbol{\tau}(\mathbf{x}) = \mathbf{T}(\mathbf{x}) - \overset{4}{\mathbf{C}}_0 \, \boldsymbol{\varepsilon}(\mathbf{x}), \tag{6.18}$$

where $\overset{4}{\mathbf{C}}_0$ is the elastic stiffness of the homogeneous reference medium. The polarization may be interpreted as the necessary condition if it is erroneously assumed that stress and strain in the actual heterogeneous medium are related by the stress-strain-law of the homogeneous reference medium. The term polarization is borrowed from the electromagnetics theory where the polarization is used to compare the magnetic field in vacuum and a matter. Instead of permeability of vacuum, *Hashin* and *Shtrikman* [81] introduced the comparing medium, which allowed them to choose an arbitrary reference medium.

By rewriting (6.16) as

$$w(\mathbf{x}, \boldsymbol{\rho}) \geq \boldsymbol{\tau} \cdot \boldsymbol{\rho} + w_0(\boldsymbol{\rho}) - (w - w_0)^c(\mathbf{x}, \boldsymbol{\tau}) \tag{6.19}$$

and inserting this into the minimum principle of the potential energy (6.1) gives

$$W(\overline{\boldsymbol{\rho}}) \geq \min_{\boldsymbol{\rho} \in \mathcal{A}} \frac{1}{V} \int_{\mathcal{B}} [\boldsymbol{\tau} \cdot \boldsymbol{\rho} + w_0(\boldsymbol{\rho}) - (w - w_0)^c(\mathbf{x}, \boldsymbol{\tau})] \, \mathrm{d}v \tag{6.20}$$

for given $\boldsymbol{\tau}$.

An upper bound on the effective energy density can be obtained by choosing a reference homogeneous medium whose difference potential $(w - w_0)$ is a concave function (for simplicity, the same notation w_0 is used for the energy density of the reference medium) The *Legendre-Fenchel* transform of this difference potential is defined by

$$(w - w_0)_c(\mathbf{x}, \boldsymbol{\tau}) = \min_{\boldsymbol{\rho} \in \mathcal{A}} \{\boldsymbol{\tau} \cdot \boldsymbol{\rho} - (w - w_0)(\mathbf{x}, \boldsymbol{\rho})\}. \tag{6.21}$$

Equation (6.21) can be rewritten as an inequality for $w(\mathbf{x}, \boldsymbol{\rho})$. Substitution of this into (6.1) leads to

$$W(\overline{\boldsymbol{\rho}}) \leq \min_{\boldsymbol{\rho} \in \mathcal{A}} \frac{1}{V} \int_{\mathcal{B}} [\boldsymbol{\tau} \cdot \boldsymbol{\rho} + w_0(\boldsymbol{\rho}) - (w - w_0)_c(\mathbf{x}, \boldsymbol{\tau})] \mathrm{d}v. \tag{6.22}$$

Note that using similar ideas, upper and lower bounds on the effective material parameters can be derived from the complementary energy principle. However, the attained bounds can be proved to be equivalent to those obtained from the potential energy principle as described above.

6.2 Bounds on the thermal conductivity

In this section, the mathematical formalism, which was discussed in the previous section, is applied to derive the bounds on the effective thermal conductivity. In this case, the variable $\boldsymbol{\rho}$ is the temperature gradient $\operatorname{grad} \theta(\mathbf{x})$ and its dual variable is the heat flux vector $-\mathbf{q}(\mathbf{x})$.

In the context of a linear isotropic conductive material, the dissipative potential can be formulated as

$$W(\overline{\operatorname{grad} \theta(\mathbf{x})}) = \min_{\operatorname{grad} \tilde{\theta} \in \mathcal{S}_D} \overline{w(\operatorname{grad} \tilde{\theta}(\mathbf{x}))}. \tag{6.23}$$

The effective energy density $W(\overline{\operatorname{grad} \theta})$ reads

$$W(\overline{\operatorname{grad} \theta}) = \frac{1}{2} \overline{\operatorname{grad} \theta(\mathbf{x})} \cdot (\, \overline{k \operatorname{grad} \theta(\mathbf{x})} \,) \tag{6.24}$$

and the average of the local energy density $\overline{w(\operatorname{grad} \theta(\mathbf{x}))}$ is

$$\overline{w(\operatorname{grad} \theta(\mathbf{x}))} = \frac{1}{2V} \int_{\mathcal{B}} \operatorname{grad} \theta(\mathbf{x}) \cdot [k(\mathbf{x}) \operatorname{grad} \theta(\mathbf{x})] \, \mathrm{d}v. \tag{6.25}$$

Here, $\theta(\mathbf{x})$ is the real temperature field and $\overline{k}$ is the effective thermal conductivity. The thermal conductivity is $k(\mathbf{x}) = \mathcal{I}^F(\mathbf{x})\, k^F + \mathcal{I}^S(\mathbf{x})\, k^S$, where $\mathcal{I}^F(\mathbf{x})$ and $\mathcal{I}^S(\mathbf{x})$ are the indicator functions of phases φ^F and φ^S, respectively, and k^F and k^S the corresponding thermal conductivities. If the *Dirichlet* boundary condition $\theta = \mathbf{p}_0 \cdot \mathbf{x}$ is prescribed, the admissable trial temperature field $\tilde{\theta}$ (hereafter the sign *tilde* is used to denote the trial field) should satisfy this boundary condition and the average of its gradient should be $\mathbf{p}_0$ (cf. Section 3.5.1). Thus, the set $\mathcal{S}_D$ is

$$\mathcal{S}_D = \{\operatorname{grad}\tilde{\theta}(\mathbf{x}) \,|\, \overline{\operatorname{grad}\tilde{\theta}(\mathbf{x})} = \mathbf{p}_0 \quad \text{for } \mathbf{x} \in \mathcal{B},\ \tilde{\theta}(\mathbf{x}) = \mathbf{p}_0 \cdot \mathbf{x} \text{ for } \mathbf{x} \in \partial\mathcal{B}\}. \tag{6.26}$$

The maximum conditions (6.6) and (6.11) can be written as

$$\overline{\mathbf{q}} = -\frac{\partial\, W(\overline{\operatorname{grad}\theta})}{\partial\, \overline{\operatorname{grad}\theta}} = -\overline{k}\,\overline{\operatorname{grad}\theta}, \tag{6.27}$$

$$\mathbf{q}(\mathbf{x}) = -\frac{\partial\, w(\operatorname{grad}\theta(\mathbf{x}))}{\partial \operatorname{grad}\theta(\mathbf{x})} = -k(\mathbf{x}) \operatorname{grad}\theta(\mathbf{x}). \tag{6.28}$$

These maximum conditions imply the global and local constitutive equations (cf. Section 3.7.1). Thereby, $\overline{\mathbf{q}}$ is the true average macroscopic heat flux and $\mathbf{q}(\mathbf{x})$ is the true local heat flux.

The principle of the complementary potential can be formulated as

$$W^c(\overline{\mathbf{q}}) = \min_{\tilde{\mathbf{q}} \in \mathcal{S}_T} \overline{w^c(\tilde{\mathbf{q}}(\mathbf{x}))}. \tag{6.29}$$

The set $\mathcal{S}_T$ of the admissible heat fluxes $\tilde{\mathbf{q}}$ can be given as

$$\mathcal{S}_T = \{\tilde{\mathbf{q}} \,|\, \overline{\tilde{\mathbf{q}}(\mathbf{x})} = -\mathbf{q}_0, \quad \operatorname{div}\tilde{\mathbf{q}}(\mathbf{x}) = 0 \text{ for } \mathbf{x} \in \mathcal{B}, \quad \tilde{\mathbf{q}}(\mathbf{x}) \cdot \mathbf{n} = -\mathbf{q}_0 \cdot \mathbf{n} \text{ for } \mathbf{x} \in \partial\mathcal{B}\} \tag{6.30}$$

with $\mathbf{q}_0$ as the prescribed heat flux and $\mathbf{n}$ as the outward-pointed surface normal.

Using *Legendre-Fenchel* transformation (6.3) and considering the maximum conditions (6.27), the effective complementary energy functional $W^c(\overline{\mathbf{q}})$ can be obtained:

$$W^c(\overline{\mathbf{q}}) = \frac{1}{2}\, \overline{\mathbf{q}} \cdot (\overline{k}^{-1}\, \overline{\mathbf{q}}). \tag{6.31}$$

The local complementary energy $w^c(\mathbf{q}(\mathbf{x}))$ reads

$$w^c(\mathbf{q}(\mathbf{x})) = \frac{1}{2}\mathbf{q}(\mathbf{x}) \cdot (k^{-1}(\mathbf{x})\, \mathbf{q}(\mathbf{x})). \tag{6.32}$$

To get (6.32), the *Legendre-Fenchel* transformation (6.8) and (6.28) are used. The average of the local complementary energy is defined by

$$\overline{w^c(\mathbf{q}(\mathbf{x}))} = \frac{1}{2V} \int_{\mathcal{B}} \mathbf{q}(\mathbf{x}) \cdot [k^{-1}(\mathbf{x})\, \mathbf{q}(\mathbf{x})]\, \mathrm{d}v. \tag{6.33}$$

Considering $\overline{\mathbf{q}(\mathbf{x})} = -\mathbf{q}_0$ and $\overline{\operatorname{grad}\theta(\mathbf{x})} = \mathbf{p}_0$ (cf. Section 3.5.1), both oriented minimum principles can be easily cast in the following inequalities:

$$\frac{\mathbf{q}_0 \cdot \mathbf{q}_0}{\frac{1}{V}\int_{\mathcal{B}} k^{-1}(\mathbf{x})\,\tilde{\mathbf{q}}(\mathbf{x}) \cdot \tilde{\mathbf{q}}(\mathbf{x})\mathrm{d}v} \leq \overline{k} \leq \frac{\frac{1}{V}\int_{\mathcal{B}} k(\mathbf{x})\operatorname{grad}\tilde{\theta}(\mathbf{x}) \cdot \operatorname{grad}\tilde{\theta}(\mathbf{x})\mathrm{d}v}{\mathbf{p}_0 \cdot \mathbf{p}_0}. \tag{6.34}$$

Upon this formulation, the next step is to find appropriate trial fields to solve (6.34). To this end, it is necessary to expand the temperature field θ and the heat flux vector $\mathbf{q}$ in functional series (*Markov* [116]):

$$\theta(\mathbf{x}) = \mathbf{p}_0 \cdot \mathbf{x} + \sum_{n=1}^{\infty} \breve{k}_n(\mathbf{x})\,\breve{\theta}_n(\mathbf{x}), \tag{6.35}$$

$$\mathbf{q}(\mathbf{x}) = -\mathbf{q}_0 + \sum_{n=1}^{\infty} \breve{l}_n(\mathbf{x})\,\breve{\mathbf{q}}_n(\mathbf{x}), \tag{6.36}$$

respectively. Here, the coefficients $\breve{k}_n$ and $\breve{l}_n$ depend on the local geometry and the local material parameters (i. e., thermal conductivity k and thermal resistivity $1/k$, respectively), while $\breve{\theta}_n$ and $\breve{\mathbf{q}}_n$, in addition to the dependence of the geometry and material parameters, depend on the prescribed temperature and prescribed heat flux, respectively.

By truncating the functional series (6.35) and (6.36) after the constant term and taking these uniform fields as trial fields, i. e., $\tilde{\theta}(\mathbf{x}) = \mathbf{p}_0 \cdot \mathbf{x}$ and $\tilde{\mathbf{q}} = -\mathbf{q}_0$, the variational inequalities (6.34) give the lower (harmonic) and upper (arithmetic) bounds:

$$\frac{k^F k^S}{\langle\, k \,\rangle_{inv}} \leq \overline{k} \leq \langle\, k \,\rangle_n\,. \tag{6.37}$$

Therein, the shorthand notation $\langle\, k \,\rangle_n$ and $\langle\, k \,\rangle_{inv}$ are used:

$$\begin{aligned} \langle\, k \,\rangle_n &= \overline{n}^F k^F + \overline{n}^S k^S, \\ \langle\, k \,\rangle_{inv} &= \overline{n}^F k^S + \overline{n}^S k^F. \end{aligned} \tag{6.38}$$

This shorthand notation will be used throughout this chapter. These bounds are referred to as the *Wiener* upper and lower bounds, because they were first noticed by *Wiener* [188]. The *Wiener* bounds are one-point bounds because they only include the one-point correlation functions, i. e., the volume fractions. These bounds are the tightest bounds if only the conductivities and volume fractions of the constituents are known.

To improve the bounds, the trial fields which contain some microgeometrical information of the heterogeneous medium should be chosen. Following *Beran* [15], the simplest class of the trial temperature fields which contain geometrical information is

$$\tilde{\theta} = \mathbf{p}_0 \cdot \mathbf{x} + \frac{\lambda \mathbf{p}_0}{4\pi\,\langle\, k \,\rangle_n} \cdot \int_{\mathcal{B}} \operatorname{grad}_{\mathbf{y}} \frac{\delta k(\mathbf{y})}{|\mathbf{x}-\mathbf{y}|}\,\mathrm{d}\mathbf{y} \tag{6.39}$$

where the operator $\operatorname{grad}_{\mathbf{y}}$ is the gradient with respect to the dummy variable $\mathbf{y}$ and $\delta k = k - \langle k \rangle_n$. The constant parameter λ will be chosen to optimize the obtained bounds. It can be seen that the information about the geometry of the heterogeneous medium is contained in the term $\operatorname{grad}_{\mathbf{y}} \delta k(\mathbf{y})$. Such trial fields are admissible because, for $\lambda = 1$, the trial field coincides with the actual temperature field of a *weak-contrast* heterogeneous medium (*Beran* [15]) and thus matches the series expansion (6.35) till the first order term. A *weak-contrast* heterogeneous medium means that variations of phase properties of the medium are small. Substituting (6.39) into the right-hand side of the inequality (6.34) gives

$$\overline{k} \leq \frac{\mathbf{p}_0 \cdot \mathbf{p}_0 \langle k \rangle_n + 2\lambda \overline{\mathbf{p}_0 \cdot \left[k(\mathbf{x}) \operatorname{grad} \tilde{\theta}\right]} + \lambda^2 \overline{\operatorname{grad} \tilde{\theta} \cdot \left[k(\mathbf{x}) \operatorname{grad} \tilde{\theta}\right]}}{\mathbf{p}_0 \cdot \mathbf{p}_0}. \tag{6.40}$$

The optimal trial field can be gained by minimizing the right-hand side with respect to the parameter λ. This procedure is the same as the *Rayleigh-Ritz* procedure with trial functions based on the solution of the *weak-contrast* case. By substituting the obtained optimal λ-value into (6.40), the *Beran* upper bound on the effective conductivity $\overline{k}$ can be found. Thus,

$$\overline{k} \leq \langle k \rangle_n \left[1 - \frac{\langle (\delta k)^2 \rangle}{3 \langle k \rangle_n^2} \Big/ \left(1 + \frac{\langle (\delta k)^3 \rangle}{\langle k \rangle_n \langle (\delta k)^2 \rangle} I_3^k\right)\right], \tag{6.41}$$

where

$$\begin{aligned}
I_3^k &= \frac{1}{\langle (\delta k)^3 \rangle} \int_{\mathcal{B}} \int_{\mathcal{B}} \langle \delta k(\mathbf{0}) \, \delta k(\mathbf{x}) \, \delta k(\mathbf{y}) \rangle \\
&\quad \operatorname{grad}_{\mathbf{x}} \operatorname{grad}_{\mathbf{x}} \left(\frac{1}{4\pi |\mathbf{x}|}\right) \cdot \operatorname{grad}_{\mathbf{y}} \operatorname{grad}_{\mathbf{y}} \left(\frac{1}{4\pi |\mathbf{y}|}\right) \mathrm{d}v \, \mathrm{d}v, \\
\langle (\delta k)^2 \rangle &= \overline{n}^F \overline{n}^S (k^S - k^F)^2, \\
\langle (\delta k)^3 \rangle &= \overline{n}^F (\overline{n}^S)^2 (\overline{n}^F - \overline{n}^S)(k^S - k^F)^2.
\end{aligned}$$

The three-point correlation function for δk is $\langle \delta k(\mathbf{0}) \, \delta k(\mathbf{x}) \, \delta k(\mathbf{y}) \rangle$, which is a function of the distance between $\mathbf{x}$ and the origin $\mathbf{0}$ and of the distance between $\mathbf{y}$ and the origin $\mathbf{0}$. The integration is taken with respect to $\mathbf{x}$ and $\mathbf{y}$.

This upper bound can be simplified by introducing the so-called *Milton-Torquato* parameters ζ^F and ζ^S (*Milton* [128], *Torquato & Stell* [174]), which is related to I_3^k via

$$\begin{aligned}
I_3^k &= \frac{1}{3(\overline{n}^S - \overline{n}^F)} (2\zeta^F + 3\overline{n}^F - \overline{n}^S), \\
\zeta^S &= 1 - \zeta^F, \\
\zeta^F &= \frac{9}{4\overline{n}^F (1 - \overline{n}^F)} \int_0^\infty \frac{\mathrm{d}r}{r} \int_0^\infty \frac{\mathrm{d}s}{s} \int_{-1}^1 (3\gamma^2 - 1) \, S_3(r, s, \gamma) \, \mathrm{d}\gamma.
\end{aligned} \tag{6.42}$$

The three-point correlation function $S_3(r, s, \gamma)$, which is given in the polar form, is different than the former three-point correlation function $\langle\, \delta k(\mathbf{0})\, \delta k(\mathbf{x})\, \delta k(\mathbf{y})\, \rangle$, because the former one is the correlation function for the random variable $\delta k(\mathbf{x})$ and $S_3(r, s, \gamma)$ is the correlation function for the indicator function $\mathcal{I}^F(\mathbf{x})$. $S_3(r, s, \gamma)$ may be interpreted as the probability that all three vertices of the triangle determined by (r, s, γ) lie in the phase φ^F. Thereby, r and s are the two side-lengths of this triangle and γ is the angle between r and s. The parameters ζ^F and ζ^S lie in the closed interval $[0, 1]$. Note that this representation of ζ^F, as in $(6.42)_3$, is chosen to be suitable for computing ζ^F of digitized heterogeneous media (for other representations of ζ^F see *Helsing* [85]). By means of the parameters ζ^F and ζ^S, (6.41) is simplified to

$$\overline{k} \leq \langle\, k\, \rangle_n - \frac{\overline{n}^F\, \overline{n}^S\, (k^F - k^S)^2}{\langle\, k\, \rangle_{inv} + 2\, \langle\, k\, \rangle_\zeta}, \tag{6.43}$$

in which the shorthand notation

$$\langle\, k\, \rangle_\zeta = \zeta^F k^F + \zeta^S k^S \tag{6.44}$$

is introduced.

In a similar fashion, the *Beran* lower bound can be attained by firstly selecting the trial fields as

$$\tilde{\mathbf{q}}(\mathbf{x}) = -\mathbf{q}_0 - \lambda\, \frac{\delta k}{\langle\, k\, \rangle_n}\, \mathbf{q}_0 + \left\{ \int_{\mathcal{B}} \left[\operatorname{grad}_{\mathbf{y}} \left(k(\mathbf{y}) \operatorname{grad}_{\mathbf{y}} \frac{1}{|\mathbf{x} - \mathbf{y}|} \right) \right] \mathrm{d}\mathbf{y} \right\} \frac{\lambda\, \mathbf{q}_0}{4\pi\, \langle\, k\, \rangle_n}. \tag{6.45}$$

For $\lambda = 1$, this trial field is the solution of the variational principle (6.29) in the case of a weak-contrast heterogeneous medium. Substituting (6.45) into the left-hand side of the inequality (6.34) and minimizing this expression with respect to λ, the *Beran* lower bound can be obtained. In terms of the *Milton-Torquato* parameter ζ^F, the lower *Beran* bound can be expressed as

$$\left\{ \langle\, 1/k\, \rangle_n - \frac{2\, \overline{n}^F\, \overline{n}^S (1/k^F - 1/k^S)^2}{2\, \langle\, 1/k\, \rangle_{inv} + \langle\, 1/k\, \rangle_\zeta} \right\}^{-1} \leq \overline{k}. \tag{6.46}$$

Since the *Beran* bounds use three-point correlation functions in terms of the *Milton-Torquato* parameter ζ^F, the *Beran* bounds belong to the three-point bounds; however, these bounds are not the optimal bounds for a n-component medium with $n \geq 3$ (*Markov* [116]).

The bounds introduced by *Hashin-Shtrikman* [82], which are the optimal two-point bounds, can be obtained directly from the *Beran* bounds. Inserting $\zeta^F = 0$ and $\zeta^F = 1$ into (6.46) yields the *Hashin-Shtrikman* lower and upper bounds

$$\left\{ \langle\, 1/k\, \rangle_n - \frac{2\, \overline{n}^F \overline{n}^S (1/k^F - 1/k^S)^2}{2\, \langle\, 1/k\, \rangle_{inv} + 1/k^S} \right\}^{-1} \leq \overline{k} \leq \langle\, k\, \rangle_n - \frac{\overline{n}^F \overline{n}^S (k^F - k^S)^2}{\langle\, k\, \rangle_{inv} + 2\, k^F}, \tag{6.47}$$

in which it is assumed that $k^S > k^F$. The lower and upper bounds can be reformulated into the forms, which are equal to the *Maxwell-Garnett* mixing rules for isotropic spherical

inclusions. Note that, if the two-point correlation functions are isotropic, the HS bounds involve only the material parameters and the volume fractions of the components (*Markov* [115]).

6.3 Bounds on the complex-valued permittivity

In this section, the bounds on the effective complex-valued permittivity $\overline{\tilde{\varepsilon}}^c$ of a biphasic medium with permittivity $\tilde{\varepsilon}^{cF}$ (phase φ^F) and $\tilde{\varepsilon}^{cS}$ (phase φ^S) will be derived based on the analytical method initiated by *Bergman* [19]. The key step in the analytical method is to express the effective permittivity in its resolvent representation. For this purpose, it is useful to define the following functions:

$$s = \frac{\tilde{\varepsilon}^{cS}}{\tilde{\varepsilon}^{cS} - \tilde{\varepsilon}^{cF}} \tag{6.48}$$

and

$$F(\tilde{\varepsilon}^{cF}, \tilde{\varepsilon}^{cS}) = 1 - \frac{\overline{\tilde{\varepsilon}}^c(\tilde{\varepsilon}^{cF}, \tilde{\varepsilon}^{cS})}{\tilde{\varepsilon}^{cS}} \qquad \text{or} \qquad F(s) = 1 - \frac{\overline{\tilde{\varepsilon}}^c(s)}{\tilde{\varepsilon}^{cS}}. \tag{6.49}$$

In terms of the new variable s, the complex-valued permittivity $\tilde{\varepsilon}^c$ can be expressed as

$$\tilde{\varepsilon}^c(\mathbf{x}) = \mathcal{I}^F(\mathbf{x})\,\tilde{\varepsilon}^{cF} + \mathcal{I}^S(\mathbf{x})\,\tilde{\varepsilon}^{cS} = [1 - \frac{\mathcal{I}^F(\mathbf{x})}{s}]\,\tilde{\varepsilon}^{cS} \tag{6.50}$$

and the boundary-value problem for the calculation of $\overline{\tilde{\varepsilon}}^c$ is

$$\operatorname{div}[\tilde{\varepsilon}^c(\mathbf{x}) \operatorname{grad} U] = 0, \tag{6.51}$$

where U is the electric potential. Using (6.50), (6.51) can be rewritten as

$$\operatorname{div}\operatorname{grad} U = \frac{1}{s}\operatorname{div}[\mathcal{I}^F(\mathbf{x}) \operatorname{grad} U]. \tag{6.52}$$

(6.52) can be solved using the *Green*'s function $G(\mathbf{x}, \mathbf{y})$. For the *Laplace*an, the *Green*'s function $G(\mathbf{x}, \mathbf{y})$ is defined as

$$\operatorname{div}\operatorname{grad} G(\mathbf{x}, \mathbf{y}) = -\delta^3(\mathbf{x}, \mathbf{y}), \tag{6.53}$$

where $\delta^3(\mathbf{x}, \mathbf{y})$ is the three-dimensional *Dirac*-delta function. The *Dirac*-delta function is defined as 1 for $\mathbf{x} = \mathbf{y}$ and zero otherwise. The *Green*'s function can be interpreted as the electrostatic potential, evaluated at the position $\mathbf{x}$ when its charge is located at $\mathbf{y}$ represented by $\delta^3(\mathbf{x}, \mathbf{y})$. It is assumed also that $G(\mathbf{x}, \mathbf{y})$ vanishes at the outer boundaries. By imposing the boundary condition of an external potential $U_0 = x_3$ (unit electric field in the $\mathbf{e}_3$-direction), the solution of the boundary-value problem (6.52) can be expressed as an integral equation:

$$\begin{aligned} U(\mathbf{x}) &= x_3 - \frac{1}{s}\int_{\mathcal{B}} G(\mathbf{x}, \mathbf{y}) \operatorname{div}_{\mathbf{y}}[\mathcal{I}^F(\mathbf{y}) \operatorname{grad}_{\mathbf{y}} U(\mathbf{y})]\, \mathrm{d}v \\ &= x_3 + \frac{1}{s}\int_{\mathcal{B}} \mathcal{I}^F(\mathbf{y}) \operatorname{grad}_{\mathbf{y}} G(\mathbf{x}, \mathbf{y}) \cdot \operatorname{grad}_{\mathbf{y}} U(\mathbf{y})\, \mathrm{d}v. \end{aligned} \tag{6.54}$$

Thereby, the divergence, the gradient and the integration over $\mathcal{B}$ are taken with respect to $\mathbf{y}$. To obtain the last line of (6.54), the integration by parts together with the bondary conditions are used. In the abstract operator language, the last term of (6.54) can be defined as

$$\Gamma U = \int_{\mathcal{B}} \mathcal{I}^F(\mathbf{y}) \operatorname{grad}_{\mathbf{y}} G(\mathbf{x},\mathbf{y}) \cdot \operatorname{grad}_{\mathbf{y}} U(\mathbf{y}) \, \mathrm{d}v. \tag{6.55}$$

(6.54) can be written as

$$U = x_3 + \frac{1}{s}\,\Gamma U \tag{6.56}$$

or equivalently,

$$U = s\,(s-\Gamma)^{-1} x_3. \tag{6.57}$$

If the scalar product (ϕ,ψ) of two functions ϕ and ψ is defined by

$$(\phi,\psi) = \int_{\mathcal{B}} \mathcal{I}^F \operatorname{grad}\phi^\star \cdot \operatorname{grad}\psi \, \mathrm{d}v, \tag{6.58}$$

where $\phi^\star$ is the conjugate complex of ϕ, the linear operator ΓU becomes self-adjoint, i. e., $(\phi,\Gamma\psi) = (\psi,\Gamma\phi)$. This can be easily shown by applying the fact that $G(\mathbf{x},\mathbf{y})$ is real and symmetric, i. e., $G(\mathbf{x},\mathbf{y}) = G(\mathbf{y},\mathbf{x})$.

Consider ϕ_n and f_n be the eigenfunctions and eigenvalues of Γ, i. e., $\Gamma\,\phi_n = f_n\,\phi_n$, then $(s-\Gamma)^{-1}x_3$ and $F(s)$ can be represented as

$$(s-\Gamma)^{-1} x_3 = \sum_n \frac{(x_3,\phi_n)}{s-f_n}\,\phi_n \tag{6.59}$$

and

$$F(s) = \frac{1}{sV}\int_{\mathcal{B}} \mathcal{I}^F \frac{\partial\phi}{\partial x_3}\,\mathrm{d}v = \frac{1}{V}(x_3,(s-\Gamma)^{-1}x_3) = \frac{1}{V}\sum_n \frac{(x_3,\phi_n)^2}{s-f_n} = \sum_n \frac{F_n}{s-f_n}, \tag{6.60}$$

respectively (*Bergman* [21] or *Heuser* [87], p. 208, in the context of the linear operator). It was proven in *Bergman* [21] that F_n and f_n have the following properties:

$$0 \le f_n < 1, \quad 0 < F_n, \quad \sum_n F_n \le 1, \quad F(1) \le 1. \tag{6.61}$$

Furthermore, $F(s)$ can be expanded in powers of $1/s$:

$$F(s) = \frac{\sum_n F_n}{s} + \frac{\sum_n f_n F_n}{s^2} + \cdots + \frac{\sum_n f_n^{r-1} F_n}{s^r} + \cdots . \tag{6.62}$$

The m-th moment of the pole spectrum $\sum_n f_n^m F_n$, can be expressed by the operator Γ; thus

$$\sum_n f_n^m F_n = (x_3,\Gamma^m x_3). \tag{6.63}$$

Here, the m-th moment denotes the power of f_n. Using this relationship the following lower moments can be deduced easily (*Bergman* [21]):

$$\sum_n F_n = \overline{n}^F, \quad \sum_n f_n F_n = \frac{1}{3}\overline{n}^F\overline{n}^S. \tag{6.64}$$

The second equation in (6.64) (the first moment) is valid only for the statistically isotropic material, while the first equation (the zero moment) is applicable for every heterogeneous medium. It can be seen from (6.64) that such m-th moment conveys information about the random variable.

Following *Bergman* [19], by taking the first variation of (6.60) yields

$$\delta F(s) = \sum_n \left(\frac{\delta F_n}{s - s_n} + \frac{F_n \, \delta s_n}{(s - s_n)^2} \right), \tag{6.65}$$

where it was assumed that both the morphological information and the imaginary part $\Im(F(s))$ are given. This implies $\Im(\delta F(s)) = 0$. Then, the bounds can be found by minimizing and maximizing the real part of $F(s)$. For a detailed treatment, one is referred to the work of *Bergman* [19, 21] and *Milton* [127, 128]. All of the bounds obtained using this method will lead to a sequence of narrowing bounds on the effective complex-valued permittivity $\overline{\tilde{\varepsilon}}^c$. The more morphological information is available, the narrower the confined region of the bounds will be.

Geometrically, the bounds can be constructed as follows. At order k the bounds always restrict $\overline{\tilde{\varepsilon}}^c$ to a region of the complex plan enclosed by circular arcs joining two points A^k and B^k. If the arcs are extended to complete circles, then one circle (which through B^k) passes through A^{k-1}, while the other one (which through A^k) passes through B^{k-1}. At order $(k+1)$ the points A^{k+1} and B^{k+1} each lie on one of the arcs joining A^k and B^k (cf. Figure 6.1). Hence, the allowed region Ω^k of bounds of order k is bounded by the pair of arcs $A^k B^k A^{k-1}$ and $A^k B^k B^{k-1}$. The points A^0 and B^0 are defined by

$$A^0 = \tilde{\varepsilon}^{cF}, \qquad B^0 = \tilde{\varepsilon}^{cS} \tag{6.66}$$

and the points A^1 and B^1 by

$$A^1 = \langle \tilde{\varepsilon}^c \rangle_n \,, \qquad B^1 = \langle \tilde{\varepsilon}^c \rangle_{inv}^{-1} \,, \tag{6.67}$$

in which the shorthand notations from the previous section are used. Furthermore, for a statistically isotropic material, the points A^2 and B^2 can be defined to attain tighter bounds. Thus,

$$A^2 = \tilde{\varepsilon}^{cF} + \frac{3\,\overline{n}^S \, \tilde{\varepsilon}^{cF}(\tilde{\varepsilon}^{cS} - \tilde{\varepsilon}^{cF})}{3\,\tilde{\varepsilon}^{cF} + \overline{n}^F(\tilde{\varepsilon}^{cS} - \tilde{\varepsilon}^{cF})}, \qquad B^2 = \tilde{\varepsilon}^{cS} + \frac{3\,\overline{n}^F \, \tilde{\varepsilon}^{cS}(\tilde{\varepsilon}^{cF} - \tilde{\varepsilon}^{cS})}{3\,\tilde{\varepsilon}^{cS} + \overline{n}^S(\tilde{\varepsilon}^{cF} - \tilde{\varepsilon}^{cS})}. \tag{6.68}$$

If the *Milton-Torquato* parameter ζ^F is known, the third-order bounds can be constructed geometrically by defining the points A^3 and B^3:

$$\begin{aligned} A^3 &= \tilde{\varepsilon}^{cF} \frac{1 + \left(2\overline{n}^S + \zeta^F + 1\right)\beta_{SF} + \left(4\overline{n}^S + 2\zeta^F - 2\right)\beta_{SF}^2}{1 - \left(\overline{n}^S - \zeta^F - 1\right)\beta_{SF} + \left[(\overline{n}^S - 2\overline{n}^F)(1 - \zeta^F) - 2\overline{n}^S\right]\beta_{SF}^2}, \\ B^3 &= \tilde{\varepsilon}^{cS} \frac{1 + \left(2\overline{n}^F + 2\zeta^F - 1\right)\beta_{FS} + 2\left[\left(2\overline{n}^F - \overline{n}^S\right)\zeta^F - \overline{n}^F\right]\beta_{FS}^2}{1 - \left(\overline{n}^F - 2\zeta^F + 1\right)\beta_{FS} + \left(\overline{n}^F - 2\,\zeta^F\right)\beta_{FS}^2}. \end{aligned} \tag{6.69}$$

Therein,

$$\beta_{ij} = \frac{\tilde{\varepsilon}^{ci} - \tilde{\varepsilon}^{cj}}{\tilde{\varepsilon}^{ci} + 2\tilde{\varepsilon}^{cj}}, \qquad i, j = F, S.$$

In Figure 6.1, $\tilde{\varepsilon}^{cF} = 87.74 + \mathrm{i}\,87.74$ and $\tilde{\varepsilon}^{cF} = 4.7$ are used; the real part (permittivity) is in unit of vacuum dielectric constant ε_0 and the imaginary part in unit Siemens/meter [S/m].

Note that for the real-valued permittivity, these lens-shaped bounds reduce to the well-known bounds on the real-valued thermal conductivity in Section 6.2. The points A^1 and B^1 correspond to the *Wiener* bounds, A^2 and B^2 are equivalent to the HS bounds and A^3 and B^3 are *Beran* bounds.

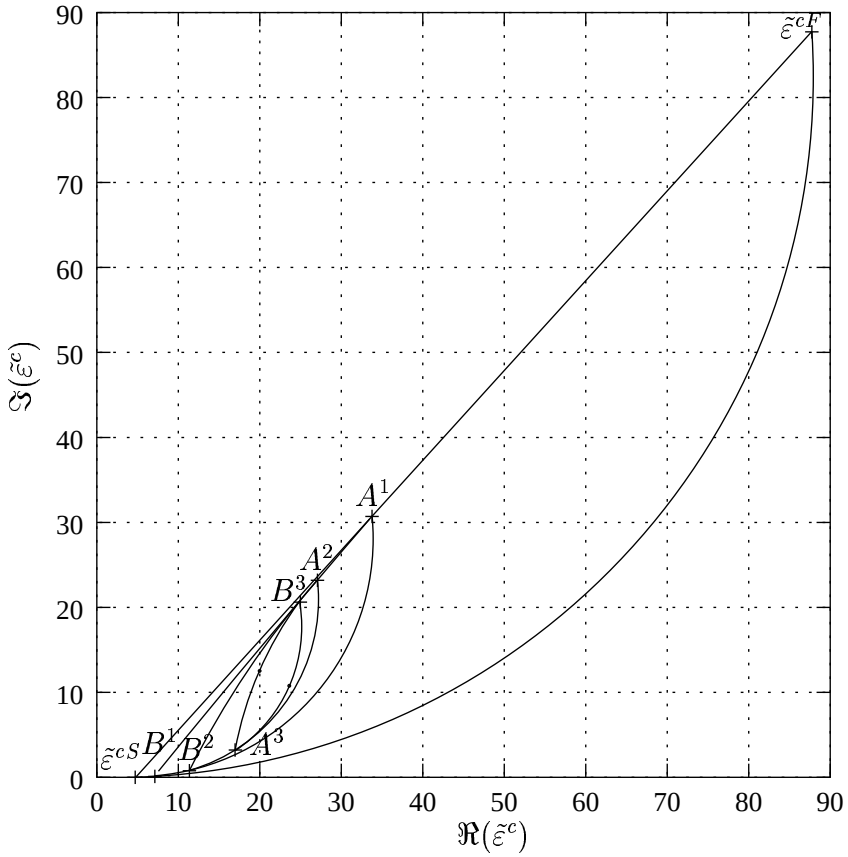

Figure 6.1: Geometrical construction of the complex-valued bounds.

6.4 Bounds on the elastic constants

As in the thermal conductivity problem, the bounds on the overall elastic moduli will be deduced using variational principles; hence, the corresponding variational principles will be formulated firstly. For an elastic composite, the principle of the potential energy can be formulated as

$$W(\overline{\boldsymbol{\varepsilon}}) = \min_{\tilde{\boldsymbol{\varepsilon}} \in \mathcal{S}_D} \overline{w(\tilde{\boldsymbol{\varepsilon}}(\mathbf{x}))}, \tag{6.70}$$

where $W(\overline{\boldsymbol{\varepsilon}})$, $w(\tilde{\boldsymbol{\varepsilon}}(\mathbf{x}))$, $\overline{\boldsymbol{\varepsilon}}$ and $\tilde{\boldsymbol{\varepsilon}}(\mathbf{x})$ denote the effective elastic potential density, the local elastic potential density, the average strain field and the admissable trial strain field,

respectively. For the prescribed strain at the boundary, $\boldsymbol{\varepsilon}(\mathbf{x}) = \boldsymbol{\varepsilon}_0$, according to (3.147) the average strain reads $\overline{\boldsymbol{\varepsilon}} = \boldsymbol{\varepsilon}_0$. In this case, the set of the admissable trial strain fields $\mathcal{S}_D$ is given by

$$\mathcal{S}_D = \left\{ \tilde{\boldsymbol{\varepsilon}} \,|\, \overline{\tilde{\boldsymbol{\varepsilon}}(\mathbf{x})} = \boldsymbol{\varepsilon}_0, \quad \tilde{\boldsymbol{\varepsilon}}(\mathbf{x}) = \boldsymbol{\varepsilon}_0 \text{ for } \mathbf{x} \in \partial\mathcal{B} \right\}. \tag{6.71}$$

In the case of the linear isotropic composite, the minimization of the potential energy (6.70) can be cast into the form:

$$\tfrac{1}{2}\,[\overline{K}\,(\overline{\boldsymbol{\varepsilon}} \cdot \mathbf{I})^2 + 2\,\overline{G}\;\overline{\boldsymbol{\varepsilon}}^D \cdot \overline{\boldsymbol{\varepsilon}}^D] \leq \frac{1}{2V}\int_{\mathcal{B}} K(\tilde{\boldsymbol{\varepsilon}} \cdot \mathbf{I})^2 \,\mathrm{d}v + \frac{1}{2V}\int_{\mathcal{B}} 2\,G\,\tilde{\boldsymbol{\varepsilon}}^D \cdot \tilde{\boldsymbol{\varepsilon}}^D \,\mathrm{d}v. \tag{6.72}$$

The principle of the complementary energy, which relates the effective complementary energy $W^c(\overline{\mathbf{T}})$ and the local complementary energy $w^c(\tilde{\mathbf{T}}(\mathbf{x}))$, is defined by

$$W^c(\overline{\mathbf{T}}) = \min_{\tilde{\mathbf{T}} \in \mathcal{S}_T} \overline{w^c(\tilde{\mathbf{T}}(\mathbf{x}))}, \tag{6.73}$$

where $\overline{\mathbf{T}}$ and $\tilde{\mathbf{T}}(\mathbf{x})$ are the average stress tensor and the admissable trial stress field, respectively. If the surface traction $\mathbf{t}_0 = \mathbf{T}_0\,\mathbf{n}$ is prescribed, according to (3.149) the average stress field is given by $\overline{\mathbf{T}} = \mathbf{T}_0$. The admissable stress fields can be collected in the set $\mathcal{S}_T$, which has the following properties

$$\mathcal{S}_T = \left\{ \tilde{\mathbf{T}} \,|\, \overline{\tilde{\mathbf{T}}(\mathbf{x})} = \mathbf{T}_0, \quad \operatorname{div} \tilde{\mathbf{T}}(\mathbf{x}) = 0 \text{ for } \mathbf{x} \in \mathcal{B}, \quad \tilde{\mathbf{T}}(\mathbf{x})\mathbf{n} = \mathbf{T}_0\,\mathbf{n} \text{ for } \mathbf{x} \in \partial\mathcal{B} \right\}. \tag{6.74}$$

For a linear isotropic heterogeneous material, the minimization of the complementary energy (6.73) can be formulated as

$$\frac{1}{2}\left[\frac{\overline{K}^{-1}\,(\overline{\mathbf{T}} \cdot \mathbf{I})^2}{9} + \frac{\overline{G}^{-1}\,\overline{\mathbf{T}}^D \cdot \overline{\mathbf{T}}^D}{2}\right] \leq \frac{1}{2V}\int_{\mathcal{B}} \frac{K^{-1}\,(\tilde{\mathbf{T}} \cdot \mathbf{I})^2}{9}\,\mathrm{d}v + \frac{1}{2V}\int_{\mathcal{B}} \frac{G^{-1}\,\tilde{\mathbf{T}}^D \cdot \tilde{\mathbf{T}}^D}{2}\mathrm{d}v. \tag{6.75}$$

Using a uniform trial strain function $\tilde{\boldsymbol{\varepsilon}}(\mathbf{x}) = \alpha\,\mathbf{I}$ and a uniform trial stress function $\tilde{\mathbf{T}}(\mathbf{x}) = -p\mathbf{I}$, which describe dilatation states, the lower and upper bounds on the effective bulk modulus $\overline{K}$ can be obtained directly from (6.72) and (6.75) as

$$\frac{K^F K^S}{\langle\, K\,\rangle_{inv}} \leq \overline{K} \leq \langle\, K\,\rangle_n\,, \tag{6.76}$$

in which the shorthand notation (6.38) is used. The bounds on the effective shear modulus can be attained upon substituting constant trial fields, $\tilde{\boldsymbol{\varepsilon}}(\mathbf{x}) = \boldsymbol{\varepsilon}_0$ and stress fields $\tilde{\mathbf{T}}(\mathbf{x}) = \mathbf{T}_0$, with the properties $\boldsymbol{\varepsilon}_0 \cdot \mathbf{I} = 0$ and $\mathbf{T}_0 \cdot \mathbf{I} = 0$ (shear state), into the variational inequalities (6.72) and (6.75). Thus, $\overline{G}$ is bounded by

$$\frac{G^F G^S}{\langle\, G\,\rangle_{inv}} \leq \overline{G} \leq \langle\, G\,\rangle_n\,. \tag{6.77}$$

These lower and upper bounds are also known as *Reuss* [150] and *Voigt* [182] bounds, respectively. *Reuss* [150] and *Voigt* [182] gave the bounds on the effective elastic tensor $\overset{4}{\overline{\mathbf{C}}}$ for an anisotropic material:

$$(\overline{n}^F \overset{4}{\mathbf{C}}^{F-1} + \overline{n}^S \overset{4}{\mathbf{C}}^{S-1})^{-1} \leq \overset{4}{\overline{\mathbf{C}}} \leq (\overline{n}^F \overset{4}{\mathbf{C}}^F + \overline{n}^S \overset{4}{\mathbf{C}}^S). \tag{6.78}$$

These bounds reduce to (6.76) and (6.77) for an isotropic material. In this work, these bounds will not be explicitly used because they are far apart from each other.

As in the thermal conductivity case, the real strain and stress fields can be represented in some functional series and the uniform trial stress and strain fields can be seen as the first truncated term of these functional series. Using trial fields based on the expansion of the actual solutions of a weak-contrast heterogeneous medium, *Beran* and *Molyneux* [16] developed three-point bounds, which are an elastic counterpart of the three-point *Beran* bounds (6.43) and (6.46). *Milton* [129] later simplified these bounds and gave them in the form

$$\left[\langle 1/K \rangle_n - \frac{4\overline{n}^F \overline{n}^S (1/K^S - 1/K^F)^2}{4\langle 1/K \rangle_{inv} + 3\langle 1/G \rangle_\zeta}\right]^{-1} \leq \overline{K} \leq \langle K \rangle_n - \frac{3\overline{n}^F \overline{n}^S (K^S - K^F)^2}{3\langle K \rangle_{inv} + 4\langle G \rangle_\zeta}. \tag{6.79}$$

Analogously, the three-point bounds on the effective shear modulus, which are called *McCoy* bounds [62], can be developed and simplified (*Milton* [129]). Thus,

$$\left[\langle 1/G \rangle_n - \frac{\overline{n}^F \overline{n}^S (1/G^S - 1/G^F)^2}{\langle 1/G \rangle_{inv} + 6\,\Xi}\right]^{-1} \leq \overline{G} \leq \langle G \rangle_n - \frac{6\overline{n}^F \overline{n}^S (G^S - G^F)^2}{6\langle G \rangle_{inv} + \Theta}, \tag{6.80}$$

in which

$$\begin{aligned}
\Xi &= \frac{10\langle K \rangle_n^2 \langle 1/K \rangle_\zeta + 5\langle G \rangle_n \langle 3G + 2K \rangle_n \langle 1/G \rangle_\zeta + \langle 3K + G \rangle_n^2 \langle 1/G \rangle_\eta}{\langle 9K + 8G \rangle_n^2}, \\
\Theta &= \frac{10\langle G \rangle_n^2 \langle K \rangle_\zeta + 5\langle G \rangle_n \langle 3G + 2K \rangle_n \langle G \rangle_\zeta + \langle 3K + G \rangle_n^2 \langle G \rangle_\eta}{\langle K + 2G \rangle_n^2}, \\
\langle G \rangle_\eta &= \eta^F G^F + \eta^S G^S.
\end{aligned}$$

Here, the parameter η^F and η^S (not to be confused with the entropy quantity η) are defined as

$$\begin{aligned}
\eta^F &= \frac{5\zeta^F}{21} + \frac{75}{28\overline{n}^F \overline{n}^S} \int_0^\infty \int_0^\infty \int_{-1}^1 (35\gamma^4 - 30\gamma^2 + 3)\, S_3(r, s, \gamma)\, \mathrm{d}\gamma \frac{\mathrm{d}s}{s} \frac{\mathrm{d}r}{r}, \\
\eta^S &= 1 - \eta^F.
\end{aligned} \tag{6.81}$$

The family of HS bounds can be derived similarly to bounds derived using classical variational principles. It is considered that the strain field $\boldsymbol{\varepsilon}(\mathbf{x})$ can be expanded into a

series (the counterpart of the series (6.35) and (6.36)). By inserting this series into the polarization tensor $\boldsymbol{\tau}^{\star}$, one has a series expansion for $\boldsymbol{\tau}$:

$$\boldsymbol{\tau}(\mathbf{x}) = (\overset{4}{\mathbf{C}} - \overset{4}{\mathbf{C}}_0)\,[\boldsymbol{\varepsilon}_0 + \sum_{n=1}^{\infty} \mathbf{C}_n(\mathbf{x})\,\breve{\boldsymbol{\varepsilon}}_n(\mathbf{x})], \tag{6.82}$$

where $\mathbf{C}_n$ is the function of the local geometry and the elastic constants and $\breve{\boldsymbol{\varepsilon}}_n(\mathbf{x})$ depends on the geometry, elastic constants and the prescribed boundary conditions. Since there is no restriction on $\boldsymbol{\tau}$, one can take $\boldsymbol{\tau} = \lambda(\overset{4}{\mathbf{C}} - \overset{4}{\mathbf{C}}_0)\,\boldsymbol{\varepsilon}_0$, as in the case of deriving *Beran* bounds on the conductivity. By taking the extreme value of λ and by choosing the elastic constants so that the difference of the energy potentials $w - w_0 < 0$ ($w - w_0 > 0$), one obtains a lower (upper) bound. Usually, the energy potential of one of the composed phases of the heterogeneous medium is chosen as w_0. Hence, for the effective bulk modulus $\overline{K}$, the HS bounds are given by

$$\left[\sum_{i=1}^{2} \frac{\overline{n}^i}{K^{(i)} + K_{min}}\right]^{-1} - K_{min} \leq \overline{K} \leq \left[\sum_{i=1}^{2} \frac{\overline{n}^i}{K^{(i)} + K_{max}}\right]^{-1} - K_{max}, \tag{6.83}$$

where $K_{min} = \frac{4}{3}\min\{G^F, G^S\}$, $K_{max} = \frac{4}{3}\max\{G^F, G^S\}$, and $i = F, S$. For the effective shear modulus $\overline{G}$, the HS bounds can be written as

$$\left[\sum_{i=1}^{2} \frac{\overline{n}^i}{G^i + G_{min}}\right]^{-1} - G_{min} \leq \overline{G} \leq \left[\sum_{i=1}^{2} \frac{\overline{n}^i}{G^i + G_{max}}\right]^{-1} - G_{max}, \tag{6.84}$$

where

$$\begin{aligned} G_{min} &= \frac{3}{2}\left(\frac{1}{\min\{G^F, G^S\}} + \frac{10}{9\,\min\{K^F, K^S\} + 8\,\min\{G^F, G^S\}}\right)^{-1}, \\ G_{max} &= \frac{3}{2}\left(\frac{1}{\max\{G^F, G^S\}} + \frac{10}{9\,\max\{K^F, K^S\} + 8\,\max\{G^F, G^S\}}\right)^{-1}. \end{aligned}$$

For a detailed discussion, one is referred to *Markov* & *Zvyatkov* [118] or *Nemat-Nasser* & *Hori* [135].

Note that for the so-called *Hill* medium [92], i. e., $G^F = G^S = G$, $\overline{K}$ can be calculated exactly. By inserting $G^F = G^S = G$ into *Beran-Molyneux* bounds (6.79) yields

$$\overline{K} = \langle\, k \,\rangle_n - \frac{3\overline{n}^S\overline{n}^F(K^S - K^F)^2}{3\,\langle\, K \,\rangle_{inv} + 4G}. \tag{6.85}$$

6.5 Cross-properties relationship

As discussed before, from cost and time considerations, performing experimental measurements on each material sample of various microstructures, phase properties and different

physical boundary-value problems is barely a feasible task. Therefore, it is important in practice to predict the unknown effective physical properties and geometrical quantities using some other known properties (both geometrical and physical), which is known as the cross-property relationship.

A typical example is the occurrence of a cross-property relationship due to the mathematical similarity among the potential equations which govern different physical phenomena such as electromagneticsm, diffusion, fluid flow, heat conduction and so on. For this case, the bounds can be written as

$$\overline{k} < \langle k \rangle_n - (\langle k_+ \rangle_n - \overline{k}_+) \left[\frac{\overline{n}^S k_+^F (k^F - k^S)^2}{\overline{n}^S k_+^F (k^F - k^S)(k_+^F - k_+^S) + (\overline{k}_+ - k_+^F)(k_+^S k^F - k_+^F k^S)} \right], \tag{6.86}$$

$$\begin{aligned} \overline{k} \quad & > \langle 1/k \rangle_n \\ - \quad & \left[\frac{(\langle 1/k_+ \rangle_n - 1/\overline{k}_+)(1/k^F - 1/k^S)^2 (\overline{n}^F/k_+^S)}{(\overline{n}^F/k_+^S)(1/k^F - 1/k^S)(1/k_+^F - 1/k_+^S) + (1/\overline{k}_+ - 1/k_+^S)(1/(k_+^F k^S) - 1/(k_+^S k^F))} \right]^{-1}, \end{aligned}$$

where the following condition has to be fulfilled:

$$\frac{k^F}{k_+^F} \geq \frac{k^S}{k_+^S}. \tag{6.87}$$

The sign + indicates that the material parameters of the phases k_+^S and k_+^F and its effective material parameter $\overline{k}_+$ are known. The detailed derivation of the bounds (6.86) can be found in *Prager* [144]. Note that the above results can be straightforwardly transcribed to the other phenomena by only changing the corresponding physical interpretation. Obviously, the tighter bounds can be attained by putting in more information of this type.

The simplest form of the cross-property relationship between the thermal conductivity $\overline{k}$ and elastic moduli $\overline{K}$, $\overline{G}$ and $\overline{E}$ can be given as

$$\frac{\overline{K}}{K^S} \leq \frac{\overline{k}}{k^S}, \tag{6.88}$$

$$\frac{\overline{G}}{K^S} \leq \frac{3\overline{k}}{2k^S}, \tag{6.89}$$

$$\frac{\overline{E}}{K^S} \leq \frac{3\overline{k}}{k^S}, \tag{6.90}$$

where $\overline{E}$ is the effective *Young*'s modulus. Here, it is assumed that the *Poisson* ratios ν_i are positive and $K^F/K^S \leq k^F/k^S$. Using these assumptions, the above relationship can

be extended to obtain the tighter bounds, if the effective *Poisson* ratio $\overline{\nu}$ is known:

$$\frac{\overline{G}}{K^S} \leq \frac{3\,\overline{k}\,(1-2\overline{\nu})}{2\,k^S\,(1+\overline{\nu})}, \tag{6.91}$$

$$\frac{\overline{E}}{K^S} \leq \frac{3\,\overline{k}\,(1-2\overline{\nu})}{k^S}. \tag{6.92}$$

The three-points bounds (6.43), (6.46) and (6.79) are related by the geometrical parameter ζ^F. By exploiting this fact, one can attain a general cross-property relationship among thermal conductivity and elastic moduli. Note that in this case, there is no need to assume that $K^F/K^S \leq k^F/k^S$ and $\nu_i > 0$. These cross-property bounds are tighter than the well-known HS bounds (*Berryman* & *Milton* [26]).

Consider that the effective thermal conductivity can be measured and $(k^F - k^S) > 0$. Then, the *Beran* upper (6.43) and lower bounds (6.46) can be reformulated to derive lower and upper bounds on the geometrical parameter ζ^F, respectively:

$$\frac{\frac{1}{2}\,\overline{n}^F\overline{n}^S(k^F-k^S)}{\langle\, k\,\rangle_n - \overline{k}} - \frac{\frac{1}{2}\,\langle\, k\,\rangle_{inv} + k^S}{(k^F-k^S)} \leq \zeta^F \leq \frac{2\,\overline{n}^F\overline{n}^S(1/k^F-1/k^S)}{\langle\, 1/k\,\rangle_n - 1/\overline{k}} - \frac{2\,\langle\, 1/k\,\rangle_{inv} + 1/k^S}{1/k^F-1/k^S}. \tag{6.93}$$

For $(k^F - k^S) \leq 0$, the inequalities in (6.93) are reversed. If the effective bulk modulus $\overline{K}$ can be measured and $(G^F - G^S) < 0$, the bounds on ζ^F can be obtained from the *Beran-Molyneux* bounds (6.79):

$$\zeta^F \geq \frac{1}{1/G^F - 1/G^S}\left[\frac{\frac{4}{3}\,\overline{n}^F\overline{n}^S(1/K^S-1/K^F)^2}{\langle\, 1/K\,\rangle_n - 1/\overline{K}} - \left(\frac{4}{3}\,\langle\, 1/K\,\rangle_{inv} + 1/G^S\right),\right] \tag{6.94}$$

$$\zeta^F \leq \frac{1}{G^F - G^S}\left[\frac{\frac{3}{4}\,\overline{n}^F\overline{n}^S(K^S-K^F)^2}{\langle\, K\,\rangle_n - \overline{K}} - \left(\frac{3}{4}\,\langle\, K\,\rangle_{inv} + G^S\right)\right].$$

In the case of $(G^F - G^S) > 0$, the inequalities in (6.94) should be reversed. Using the fact that $5\zeta^F/21 \leq \eta^F$ and $5\zeta^S/21 \leq \eta^S$ (*Milton* and *Phan-Thien* [125]), which can be rewritten as

$$\frac{5\zeta^F}{21} \leq \eta^F \leq \frac{16+5\zeta^F}{21}, \tag{6.95}$$

relates the *McCoy* three-point bounds on the shear modulus (6.80) to the other three-point bounds.

Chapter 7

Examples

Various methods which are applied to estimate the effective material parameters of heterogeneous media have been thoroughly discussed in the previous chapters. The aim of this chapter is to quantitatively verify these various methods and to compare the methods with each other by using real material data. Through this comparison, one can conclude the reliability of the approximation method in predicting the effective material parameters. The real materials discussed here are digitized spatial images of real natural sandstones, which have been discussed in Section 2.4. The samples are two different kinds of weakly consolidated sandstones *Sst06d* and *Sst20d* which are denoted as A and B, respectively, *Berea* sandstone (C) and three slices of the *Fontainebleau* sandstone that are indicated as D1, D2 and D3, and two reconstructions of the Berea sandstone (R1 and R2). The data sets of these samples are tabulated in Table 2.1. Section 7.1 is devoted to the case of linear conductive materials. Section 7.2 focuses on the effective electromagnetical property of dissipative solids. Section 7.3 discusses the effective response of linear elastic solids.

7.1 Thermal conductivity

Since detailed information of the geometries of the samples were known within the limits of the experimental resolution, the heat conduction equation (4.1) was solved using a finite volume method (FVM) as described in Section 4.1. The outer boundary conditions were chosen as follows: Two opposite boundaries were maintained at $\theta = \theta_1$ and $\theta = \theta_2$ such that a temperature gradient existed across the sample. The potential gradient was applied in x_1-, x_2- and x_3-direction. The other four faces were assumed to be insulated, i. e., $\mathbf{q} \cdot \mathbf{n} = 0$. In each direction, the corresponding volume average of the temperature gradient and of the heat flux were taken. The corresponding effective conductivity $\overline{k}$ was determined from these average quantities. For all samples, the obtained effective conductivity is anisotropic. The effective isotropic conductivity was constructed by taking the arithmetic average of this anisotropic conductivity, which is complied with the result of *Schulgasser* [156]. Table 7.1 displays the (normalized) effective conductivities of these samples for six different conductivity contrasts, ranging from $k^F/k^S = 2.0$ to $k^F/k^S = \infty$. Because the effective conductivity function satisfies the *homogeneity property*, i. e.,

$\overline{k}(\lambda\, k^F, \lambda\, k^S) = \lambda \overline{k}(k^F, k^S)$ (*Milton* [132]), the thermal conductivity of phase φ^F can be taken as $k^F = 1.0\,\mathrm{W/m\,K}$. Table 7.2 presents the deviation of the arithmetical average effective conductivity from that in x_1-, x_2- and x_3-direction. It is interesting to observe that at lower contrast ratio the connectivity information can be ignored. This can be verified from the samples C, R1 and R2, which have almost the same porosities but very different connectivity properties (cf. Section 2.4). As the contrast ratio increases, the discrepancy between the effective conductivities of these three samples (C, R1 and R2) becomes significant. At $k^F/k^S = 10^4$ and $k^F/k^S = \infty$, the effective conductivity of sample C is approximately three to four times larger than the effective conductivities of samples R1 and R2, respectively. This implies that the connectivity plays an important role in determining the effective conductivity if the contrast ratio is high. Note that at the infinite contrast, one might think of the material parameter k as the electric conductivity instead of the thermal conductivity.

Samples	k^F/k^S					
	2.0	10.0	18.6681	100.0	10000.0	∞
A	0.631896	0.252684	0.193043	0.124521	0.104032	0.103796
B	0.599673	0.207937	0.148954	0.081470	0.060319	0.060059
C	0.570113	0.169611	0.112065	0.046674	0.024353	0.024021
D1	0.547499	0.147621	0.093615	0.034355	0.013924	0.013584
D2	0.558877	0.160331	0.104717	0.042741	0.022830	0.022563
D3	0.545953	0.145685	0.091920	0.033401	0.013774	0.013448
R1	0.569115	0.162087	0.102498	0.033760	0.007441	0.006836
R2	0.566999	0.156613	0.097128	0.029526	0.003793	0.003084

Table 7.1: Numerically exact values of $\overline{k}$ [W/m K] at different contrast ratio k^F/k^S for the eight samples.

Samples	k^F/k^S					
	2.0	10.0	18.6681	100.0	10000.0	∞
A	$\pm$0.001230	$\pm$0.004642	$\pm$0.004996	$\pm$0.004704	$\pm$0.004189	$\pm$0.004178
B	$\pm$0.003502	$\pm$0.012303	$\pm$0.013253	$\pm$0.013128	$\pm$0.012326	$\pm$0.012307
C	$\pm$0.000296	$\pm$0.001339	$\pm$0.001527	$\pm$0.001903	$\pm$0.002550	$\pm$0.002597
D1	$\pm$0.000487	$\pm$0.001707	$\pm$0.002083	$\pm$0.002952	$\pm$0.004198	$\pm$0.004247
D2	$\pm$0.000543	$\pm$0.002288	$\pm$0.002659	$\pm$0.002965	$\pm$0.003278	$\pm$0.003292
D3	$\pm$0.000230	$\pm$0.000587	$\pm$0.000606	$\pm$0.000858	$\pm$0.001570	$\pm$0.001600
R1	$\pm$0.000055	$\pm$0.000202	$\pm$0.000238	$\pm$0.000211	$\pm$0.000136	$\pm$0.000109
R2	$\pm$0.000021	$\pm$0.000096	$\pm$0.000115	$\pm$0.000116	$\pm$0.000530	$\pm$0.000604

Table 7.2: The standard deviation of $\overline{k}$ [W/m K] for the eight samples.

The accuracy of an approximation method or a micromechanical model in predicting the effective conductivity can be justified by checking if the predicted effective conductivity

is within the HS bounds. Therefore, as the first step the HS bounds should be evaluated. In the case of a statistically isotropic material, the HS bounds and the approximation from the *Maxwell-Garnett* theory (MGT) for spherical inclusions are the same. Therefore, the HS bounds (6.47) can be calculated using the MGT. The lower bound can be found by considering that the inclusion phase is φ^F and the host phase is φ^S, the results for these eight samples are presented in the Table 7.3. The upper bound can be attained by taking φ^S as the inclusion phase and φ^F as the host phase. This case can be seen as the solid particles that are embedded in the fluid such as in the suspension problem. The upper bounds for different contrast ratios are tabulated in Table 7.4. As discussed in Section 5.1.3, the MGT is an unsymmetrical mixing law and therefore, it is difficult to choose which phase is the continuous phase and which phase is the dispersed phase for such bicontinuous heterogeneous samples. Nevertheless, the MGT can be used as the bounds on the effective conductivity.

Samples	k^F/k^S					
	2.0	10.0	18.6681	100.0	10000.0	∞
A	0.630435	0.194737	0.114081	0.023515	0.000241	0.0
B	0.598721	0.168211	0.096582	0.019460	0.000198	0.0
C	0.569653	0.146071	0.082313	0.016244	0.000165	0.0
D1	0.546711	0.129888	0.072073	0.013985	0.000141	0.0
D2	0.557471	0.137344	0.076772	0.015016	0.000152	0.0
D3	0.545237	0.128884	0.071444	0.013847	0.000140	0.0
R1	0.569982	0.146310	0.082466	0.016278	0.000165	0.0
R2	0.569694	0.146101	0.082332	0.016248	0.000165	0.0

Table 7.3: The predicted effective conductivity using the MGT with the phase φ^S as the host phase.

Samples	k^F/k^S					
	2.0	10.0	18.6681	100.0	10000.0	∞
A	0.640845	0.323009	0.284160	0.247317	0.238891	0.238806
B	0.607335	0.268064	0.227110	0.188374	0.179530	0.179441
C	0.576213	0.218115	0.175383	0.135061	0.125868	0.125775
D1	0.551368	0.178966	0.134929	0.093453	0.084008	0.083912
D2	0.563051	0.197296	0.153861	0.112916	0.103586	0.103492
D3	0.549763	0.176459	0.132341	0.090795	0.081333	0.081238
R1	0.576567	0.218677	0.175965	0.135660	0.126471	0.126378
R2	0.576257	0.218185	0.175456	0.135136	0.125943	0.125850

Table 7.4: The predicted effective conductivity using the MGT with the phase φ^F as the host phase.

The next step is to apply a symmetrical mixing law such as the BEMA (5.21) in predicting the effective conductivity of the bicontinuous medium. Table 7.5 presents the

predicted effective conductivity using the BEMA. For the case of the lower contrast, the BEMA provides good prediction results, but as the contrast ratio increases, the prediction of the BEMA becomes less accurate. In the limit of infinite contrast, the effective conductivities calculated from the BEMA for all samples vanished although the samples are fully connected. The reason is that the BEMA has a percolation threshold at 1/3, while all of the samples have the porosities below this percolation threshold ($\overline{n}^F < 1/3$).

Samples	k^F/k^S					
	2.0	10.0	18.6681	100.0	10000.0	∞
A	0.634198	0.240179	0.167632	0.063697	0.002252	0.0
B	0.601132	0.192794	0.122630	0.032178	0.000385	0.0
C	0.570974	0.157363	0.093135	0.020269	0.000214	0.0
D1	0.547348	0.134587	0.076263	0.015340	0.000157	0.0
D2	0.558404	0.144730	0.083577	0.017351	0.000179	0.0
D3	0.545837	0.133268	0.075335	0.015096	0.000154	0.0
R1	0.571313	0.157721	0.093413	0.020360	0.000215	0.0
R2	0.571016	0.157407	0.093170	0.020280	0.000214	0.0

Table 7.5: The predicted effective conductivity using the BEMA.

To overcome a percolation threshold problem, it is very common to use the DEM method (5.31). Here, the phase φ^F is taken as the initial host phase. Table 7.6 displayed the estimated effective conductivity for all the samples using the DEM. As in the case of the mixing law which uses only the average porosity as the geometrical input parameter, the predicted effective conductivities for the samples C and its reconstruction R1 and R2 remain the same. It can be taken from Tables 7.3-7.6 that predicted results using the BEMA and the DEM are always located within the HS bounds, cf. Tables 7.3 and 7.4 and *Markov* [115].

Samples	k^F/k^S					
	2.0	10.0	18.6681	100.0	10000.0	∞
A	0.637720	0.290807	0.242404	0.193115	0.181142	0.181019
B	0.604419	0.237706	0.187325	0.135640	0.122888	0.122757
C	0.573747	0.192190	0.141005	0.088230	0.074921	0.074782
D1	0.549471	0.158885	0.108016	0.055662	0.042129	0.041986
D2	0.560861	0.174188	0.123049	0.070311	0.056847	0.056706
D3	0.547910	0.156835	0.106021	0.053751	0.040215	0.040071
R1	0.574094	0.192685	0.141502	0.088731	0.075427	0.075288
R2	0.573790	0.192252	0.141067	0.088292	0.074984	0.074845

Table 7.6: The predicted effective conductivity using the DEM.

The *Looyenga*'s formula (5.8) [111], which has been widely used and has been observed to match well with the experiments, was applied to calculate the effective conductivity.

The results are presented in Table 7.7. As can be seen, this formula gives good predictions for a wide range of the contrast ratio and also gives a non-zero effective conductivity in the limit of the infinite contrast. In general, the estimation of the effective conductivity using this formula is better than that of the DEM method. In the case of the reconstructed samples, the *Looyenga*'s formula gives the best estimation compared to all mixing formulae.

Samples	k^F/k^S					
	2.0	10.0	18.6681	100.0	10000.0	∞
A	0.635427	0.256808	0.191437	0.101522	0.043452	0.032768
B	0.602616	0.212254	0.149598	0.068533	0.022414	0.015069
C	0.572446	0.174931	0.115895	0.044626	0.010033	0.005592
D1	0.548592	0.147942	0.092485	0.029854	0.004221	0.001763
D2	0.559782	0.160323	0.103112	0.036345	0.006557	0.003216
D3	0.547059	0.146285	0.091077	0.029024	0.003950	0.001606
R1	0.572787	0.175333	0.116251	0.044864	0.010139	0.005668
R2	0.572489	0.174981	0.115940	0.044656	0.010046	0.005602

Table 7.7: The predicted effective conductivity using the *Looyenga*'s mixing law.

The effective conductivities which were predicted by the MLLPT could be obtained by solving (5.37). These predicted effective conductivities are still depending on the length scale L, which can be seen in Figure 7.1 (for contrast ratio $k^F/k^S = 2$) and Figure 7.2 (for the contrast ratio $k^F/k^S = \infty$).

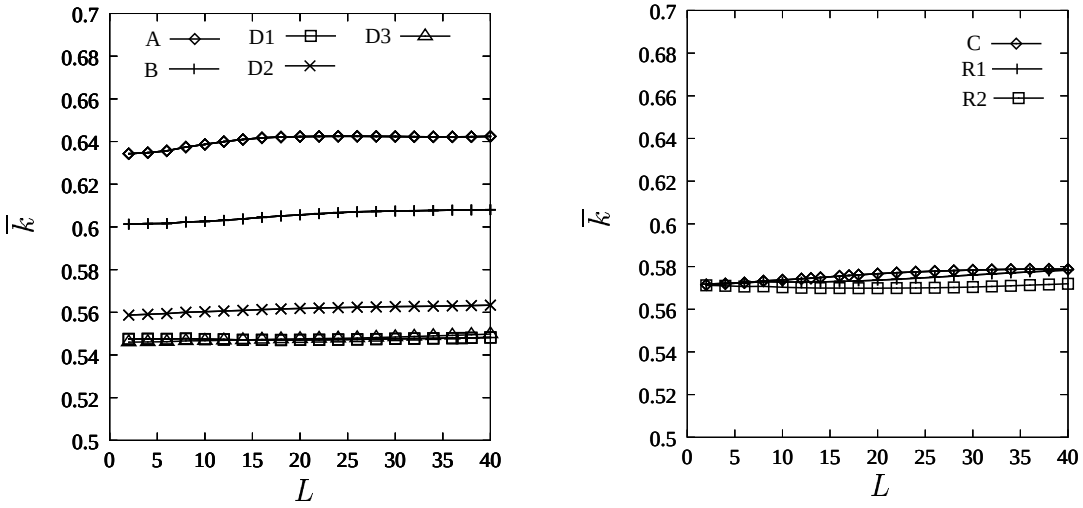

Figure 7.1: The prediction of the MLLPT for the eight digitized samples at contrast ratio $k^F/k^S = 2.0$.

As discussed in Subsection 5.1.5, there are several criteria to determine the length scale L. The first three length scales, i. e., the entropy length scale L_{en}, the correlation length

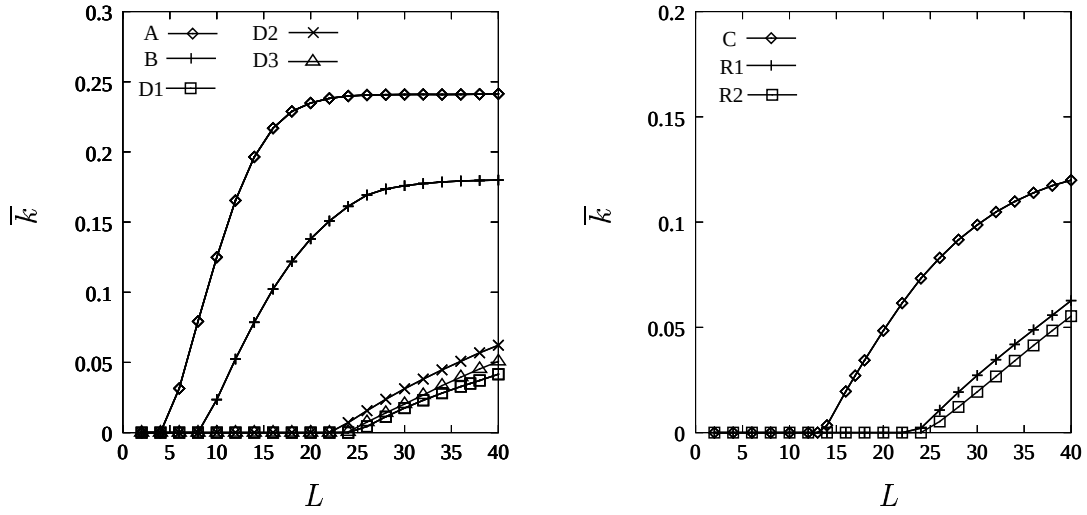

Figure 7.2: The prediction of the MLLPT for the eight digitized samples in the limit of the infinite contrast ratio $k^F/k^S = \infty$.

scale L_c and the percolation length scale L_p, are given in Table 5.1. The estimated effective conductivities at these length scales are tabulated in Table 7.8 (at L_{en}), in Table 7.9 (at L_c), and in Table 7.10 (at L_p).

Samples	k^F/k^S					
	2.0	10.0	18.6681	100.0	10000.0	∞
A	0.635676	0.250020	0.180348	0.083206	0.032650	0.031459
B	0.602311	0.204875	0.138522	0.050682	0.002502	0.0
C	0.573724	0.169446	0.107229	0.031046	0.000493	0.0
D1	0.547035	0.142215	0.085862	0.022529	0.000325	0.0
D2	0.561543	0.158207	0.099027	0.028867	0.000522	0.0
D3	0.547442	0.143419	0.087168	0.023510	0.000360	0.0
R1	0.572762	0.164719	0.101638	0.026158	0.000326	0.0
R2	0.570610	0.158761	0.095563	0.022582	0.000257	0.0

Table 7.8: The predicted effective conductivity using the MLLPT at the entropy length L_{en} for different contrast k^F/k^S.

It is obvious that for the lower contrast ratio, the estimated effective conductivity at the smallest length scales are in better agreement with the exact values. Because L_{en} is the smallest length scale of the three length scales (L_{en}, L_{co} and L_p) for almost all of the samples, the effective conductivity $\overline{k}$ at L_{en} gave the best predicted results. As the contrast ratio increases, the length scale at which the best predicted effective value is obtained will also increase (cf. Figure 7.3). Therefore, for the limit of the infinite contrast ratio, the effective conductivities of all of the samples at L_p are the best estimation of the MLLPT. Moreover, the MLLPT at L_p gave the non-vanishing effective conductivity

Samples	k^F/k^S					
	2.0	10.0	18.6681	100.0	10000.0	∞
A	0.637416	0.263302	0.198706	0.113316	0.079674	0.079217
B	0.602367	0.206219	0.140411	0.053555	0.006904	0.004712
C	0.576230	0.187307	0.130782	0.037571	0.037570	0.037181
D1	0.547101	0.140531	0.083470	0.019936	0.000238	0.0
D2	0.561983	0.162262	0.104377	0.028296	0.002290	0.0
D3	0.547005	0.140590	0.083543	0.019999	0.000239	0.0
R1	0.573300	0.169213	0.107772	0.033105	0.000676	0.0
R2	0.570645	0.158802	0.095715	0.022844	0.000263	0.0

Table 7.9: The predicted effective conductivity using the MLLPT at the correlation length L_{co} for different contrast k^F/k^S.

Samples	k^F/k^S					
	2.0	10.0	18.6681	100.0	10000.0	∞
A	0.638687	0.278290	0.219968	0.148374	0.125254	0.124988
B	0.603744	0.227919	0.170846	0.102120	0.078864	0.078580
C	0.576644	0.191039	0.135842	0.071349	0.048700	0.048402
D1	0.547447	0.150578	0.097085	0.036990	0.011926	0.011319
D2	0.562381	0.167030	0.110820	0.044727	0.016235	0.015601
D3	0.548663	0.156191	0.104190	0.046997	0.027069	0.026782
R1	0.575525	0.180634	0.122208	0.051539	0.019957	0.019263
R2	0.570981	0.179435	0.123621	0.058747	0.034459	0.034099

Table 7.10: The predicted effective conductivity using the MLLPT at the percolation length L_p for different contrasts k^F/k^S.

and the MLLPT at L_{en} and L_{co} gave the zero effective conductivity (except for sample A). The reason for these results is that, as long as the used length scale is larger than the threshold length L_{co}, the effective conductivity at that length scale is not equal to zero. From Figure 7.2 and Table 7.10, it can be seen that the MLLPT at L_p can differentiate the effective conductivities of samples C, R1 and R2. However, the predicted effective conductivities of R1 is three times and that of R2 is eleven times larger than their corresponding exact values, respectively.

Figure 7.3 plots the experimental length L_{ex} against the ratio k^F/k^S for all the eight samples. For the samples R1 and R2, the ranges of the experimental length L_{ex} are quite wide. Therefore, it is difficult to choose a length scale using the experimental method and then applying this chosen length scale to estimate the effective material parameter. Moreover, this implies that there is no good criterion to determine an appropriate length scale L, at which the MLLPT gives good predicted effective values for the whole range of the contrast ratio.

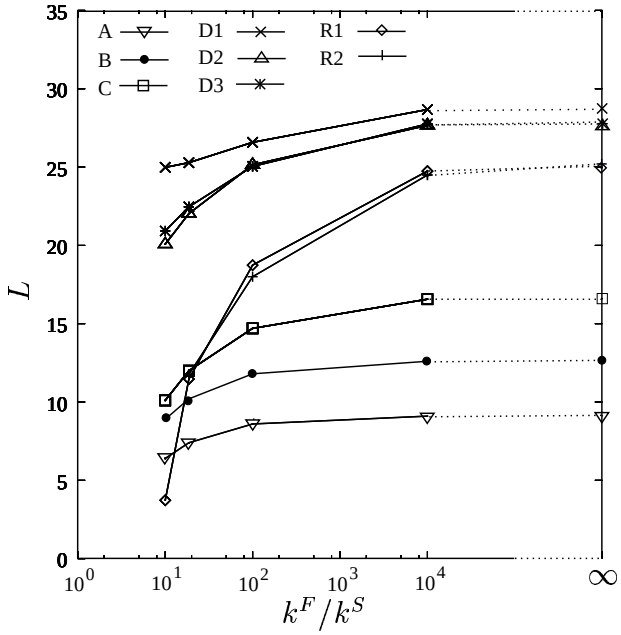

Figure 7.3: The experimental length L_{ex} of the eight digitized samples.

It is interesting to note that at lower contrast the MLLPT does not give any improvement if compared to the traditional mixing laws. This can be traced back to the fact that for the lower contrast the morphology such as the porosity distribution and the connectivity information plays a less important role than one might think. For the high contrast, the prediction of the LPT at L_p gives reasonable results.

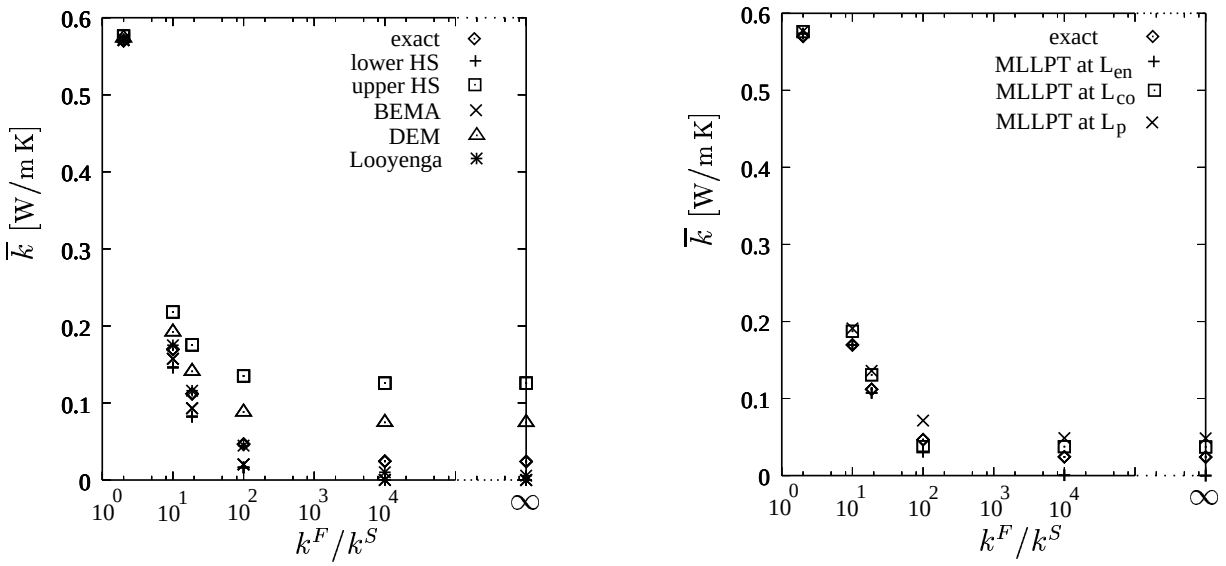

Figure 7.4: The estimated effective conductivity $\overline{k}$ for different contrasts for sample C (Berea sandstone) from various mixing laws and from simulated data (*exact*).

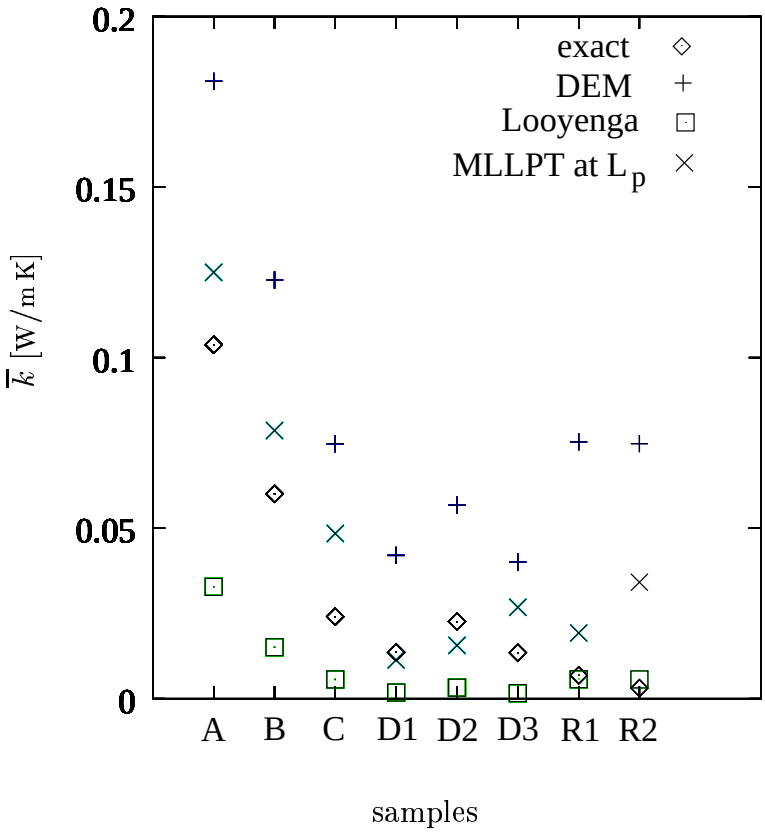

Figure 7.5: The effective conductivity predicted by the DEM, the *Looyenga*, the LPT (at L_p) and by the simulated effective conductivity (exact) for the eight samples in the case of the infinite contrast.

For elucidatory purposes, Figure 7.4 displays the results from different mixing laws and from the simulation (exact calculation) for the particular case of sample C (*Berea* sandstone). These effective permittivities are plotted as a function of the contrast for the Berea sandstone. All of the prediction results are within the HS bounds. For all of the contrast ratio, the predictions of the DEM are overestimated, while the predictions of the *Looyenga*'s formula and of the BEMA are underestimated. In the case of low contrast, all the approximation methods provided similarly good results. As the contrast ratio increases, the results of the approximation methods begin to differ. For the low contrast, the MLLPT gives almost the same results at any length scales. However, at the infinite contrast the MLLPT at L_{en} gives a zero effective conductivity.

Figure 7.5 shows the results from different mixing laws which give the non-zero effective conductivities for the infinite contrast and from the simulation. This includes the DEM, the *Looyenga* and the MLLPT at L_p. For all the samples, the DEM gives overestimated results, while the *Looyenga*'s formula gives underestimated results. The MLLPT gives the best results for many samples. However, for samples D3, R1, and R2, the *Looyenga*'s formula gives the best results.

Finally, the improved bounds on the effective conductivity are discussed, if a measured

effective conductivity at a different temperature is known. If the effective conductivity for the contrast ratio $k^F/k^S = 2.0$ is known, then, using (6.86), the stricter bounds for another contrast ratio can be found. This is demonstratively done using the samples C, R1 and R2 for the contrast ratios $k^F/k^S = 10.0$, 18.66681, 100.0 and ∞. The results are tabulated in the Table 7.11.

		Samples		
k^F/k^S	bounds	C	R1	R2
10.0	lb	0.147092	0.144465	0.140687
	ub	0.197095	0.192921	0.186076
18.6681	lb	0.083058	0.081133	0.078472
	ub	0.151968	0.147264	0.139661
100.0	lb	0.016433	0.015944	0.015294
	ub	0.109265	0.104030	0.095671
10000.0	lb	0.000167	0.000161	0.000155
	ub	0.099512	0.094152	0.085615

Table 7.11: The lower and upper bounds on $\overline{k}$ at different contrasts k^F/k^S using the known $\overline{k}$ of the contrast ratio $k^F/k^S = 2.0$.

Compared to the HS bounds of Tables 7.3 and 7.4, the attained bounds are slightly tighter for all of these three samples. Figure 7.6 displays the upper bound on $\overline{k}$ in the limit of the infinite contrast by using the information of the measured $\overline{k}$ at other contrast ratios. The solid lines without symbols represent the simulated exact results of the samples. The lower bound is always equal to zero; however, the upper bound can be used as an approximation of the effective conductivity. The attained upper bounds are improved by using the measured $\overline{k}$ of the increased contrast ratio k^F/k^S. Obviously, the upper bound which is attained using the $\overline{k}$ of the contrast ratio $k^F/k^S = 10000$ gives very good predicted values of $\overline{k}$. It should be emphasized that, contrary to the HS bounds, the *Prager* method gives different bounds for samples C, R1 and R2.

7.2 Complex-Valued permittivity

For a dissipative medium and a low frequency case, the electric field is governed by the *Laplace* equation. As in the case of the real-valued conductivity, the effective complex-valued permittivity were obtained by solving the *Laplace* equation with the complex-valued permittivity on the digitized samples. The boundary conditions were chosen such that a potential gradient was applied across the sample and the fluxes were set to zero on the other faces of the sample, i. e., $\partial U/\partial \mathbf{n} = \mathbf{0}$. The complex-valued permittivity of phases φ^F and φ^S are $\tilde{\varepsilon}^{cF} = 87.74 + \mathrm{i}\, 87.74/\omega$ (brine water) and $\tilde{\varepsilon}^{cS} = 4.7$ (rock matrix), respectively. The permittivities are given in the units of the dielectric permittivity of the vacuum $\varepsilon_0 = 8.854 \times 10^{-12}\,\mathrm{F/m}$. The effective frequency-dependent permittivities (the real parts

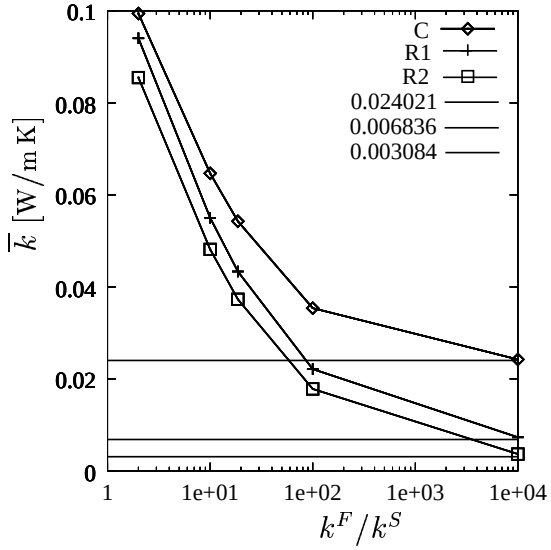

Figure 7.6: The improved upper bound on the effective conductivity for the infinite contrast using the knowledge of the measured effective conductivity from five different contrast ratio.

of the effective complex-valued permittivities), which were normalized by dividing by the factor 87.74, of the four samples (A,B,C and D1) for six different frequencies, ranging from $\omega = 10^2$/s to $\omega = 10^{-4}$/s, are presented in Table 7.12. The corresponding effective frequency-dependent conductivities, which were obtained by multiplying the imaginary parts of the effective complex-valued permittivities with their corresponding ω and normalized by 87.74, are given in Table 7.13. For a large ω, the complex-valued permittivity is approximately equal to its real part. In this case, the effective permittivity can be obtained from the quasi-static case with the contrast ratio $\tilde{\varepsilon}^{cF}/\tilde{\varepsilon}^{cS} \approx 87.74/4.7 = 18.6681$. This could be verified by comparing the real effective permittivity of the second column ($\omega = 100$) of Table 7.12 with the real valued effective conductivity of contrast ratio 18.6681 (cf. Table 7.1). Similarly, the case of a very small ω (in the limit of $\omega \to 0$) corresponds to the case of the infinite contrast ratio, because the complex-valued permittivity is dominated by its imaginary part. It can be easily seen by comparing the last column of Table 7.13 with the effective conductivity of the infinite contrast for the quasi-static case in Table 7.1.

Figure 7.7 shows the estimated frequency-dependent effective complex-valued permittivity using the MLLPT at different length scales for the sample A. The left hand side of this figure plots the effective electric permittivity (the real part of the complex-valued permittivity) and the right-hand side gives the effective electric conductivity (the imaginary part of the complex-valued permittivity). For the lower frequency ($\omega \leq 0.1$), the estimation by the MLLPT are the best at the length scale $L > 12\,a$; however, for higher frequencies, the estimations at $L = 8\,a$ are in good agreement with the exact numerical results (symbol $\diamond$) in the Figure 7.7. Here, a is the resolution. The predicted electric conductivity of the MLLPT at the length scale $L = 9\,a$ are in good agreement with

Samples	ω					
	10^2	1	10^{-1}	10^{-2}	10^{-3}	10^{-4}
A	0.193044	0.198781	0.224930	0.230480	0.230604	0.230605
B	0.148955	0.154478	0.187802	0.199264	0.199580	0.199583
C	0.112065	0.117166	0.162189	0.195960	0.206099	0.206726
D1	0.093616	0.097424	0.138156	0.194101	0.198950	0.199005

Table 7.12: The frequency-dependent electric permittivities for different frequencies obtained by direct numerical simulation.

Samples	ω					
	10^2	1	10^{-1}	10^{-2}	10^{-3}	10^{-4}
A	0.118806	0.115367	0.104841	0.103812	0.103796	0.103796
B	0.075951	0.072877	0.061707	0.060089	0.060060	0.060059
C	0.041362	0.038774	0.027175	0.024144	0.024025	0.024021
D1	0.028205	0.026379	0.017290	0.013759	0.013586	0.013584

Table 7.13: The frequency-dependent electric conductivities for different frequencies obtained by direct numerical simulation.

the numerical exact result (denoted by cross in the Figure 7.7) for the lower frequency ($\omega \leq 0.1$). However, for the higher frequency, the MLLPT at $L = 8\,a$ gives the best result as in the electric permittivity (the real part). As in the quasi-static case, it is difficult to determine the appropriate length scale at which the MLLPT gives good estimations for the both material parameters and for the whole range. The same behaviour is also observed for the sample B.

In Figure 7.8, the estimated frequency-dependent effective complex-valued permittivity for the sample C using the MLLPT is plotted. As in the case of the sample A, the best predicted values of the effective permittivity and the effective conductivity were obtained at different length scales.

Figure 7.9 displays the prediction of the MLLPT for the frequency-dependent effective complex-valued permittivity for the sample D1. For the higher frequencies ($\omega = 1$ and $\omega = 100$), the same length scale $L = 26$ gives the best predicted effective permittivity and the effective conductivity. In the case of the low frequencies, the length scale $L = 32$ gives the best predicted effective permittivity, while the length scale $L = 28$ yields a quite good estimation of the effective conductivity.

To testify the validity of the MGT and the BEMA approximation, the sample D1 was used. Figure 7.10 gives the *Cole-Cole* plot, which represents the relation between the real part (permittivity) and the imaginary part (conductivity) of the simulated effective complex-valued permittivity, the predicted effective complex-valued permittivity using the MGT and the BEMA. Here, MGF and MGS indicate the MGT using φ^F and φ^S as the host phases, respectively. It also plots the predicted $\overline{\tilde{\varepsilon}}^c$ using the MLLPT at the length scale $L = 26\,a$ and $L = 32\,a$. The estimations of the BEMA and the MLLPT yield

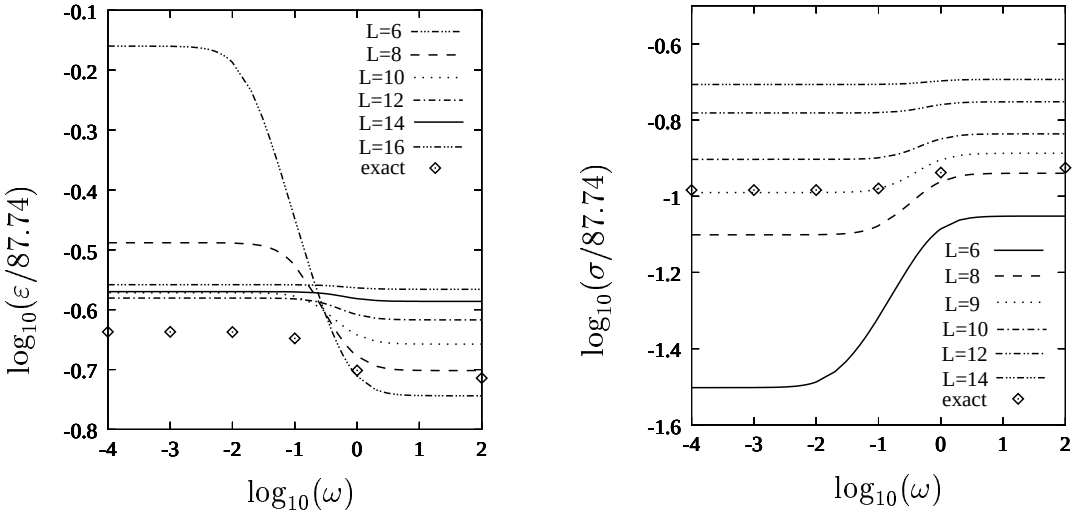

(a) effective permittivity (b) effective conductivity

Figure 7.7: The effective complex-valued permittivity predicted using the MLLPT for the sample A.

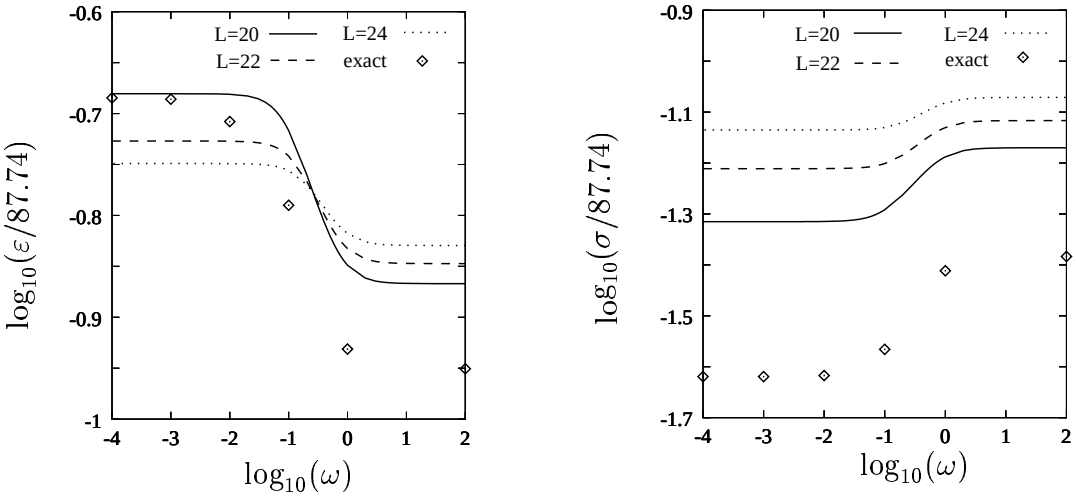

(a) effective permittivity (b) effective conductivity

Figure 7.8: The effective complex-valued permittivity predicted using the MLLPT for the sample C.

more or less the same predicted values for all frequencies.

Now, attention is paid to the bounds method. Again the sample D1 was used. For $\omega = 1.0$ ($\tilde{\varepsilon}^{cF} = 87.74 + \mathrm{i}\,87.74$ and $\tilde{\varepsilon}^{cS} = 4.7$), (6.66)-(6.68) give the required points for

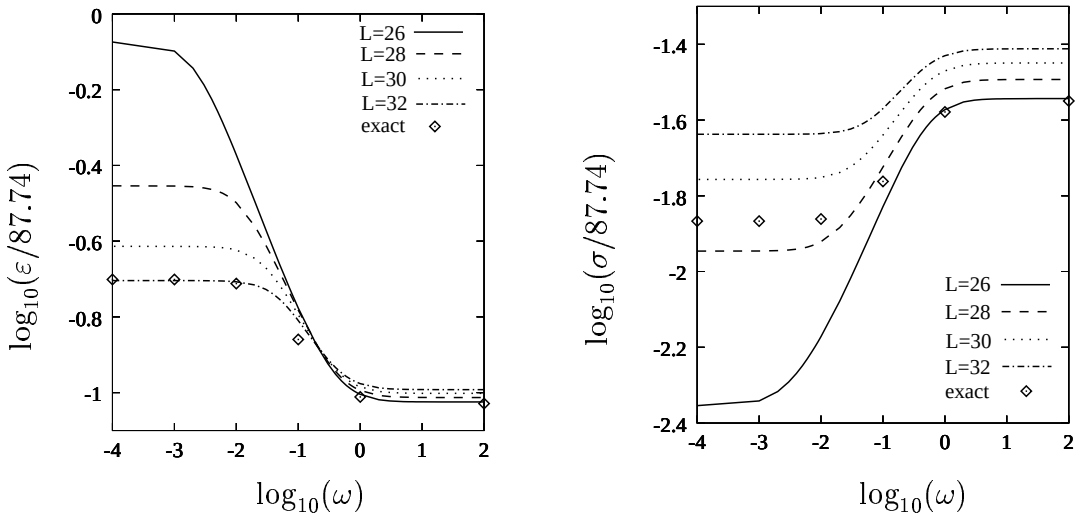

(a) effective permittivity (b) effective conductivity

Figure 7.9: The effective complex-valued permittivity predicted using the MLLPT for the sample D1.

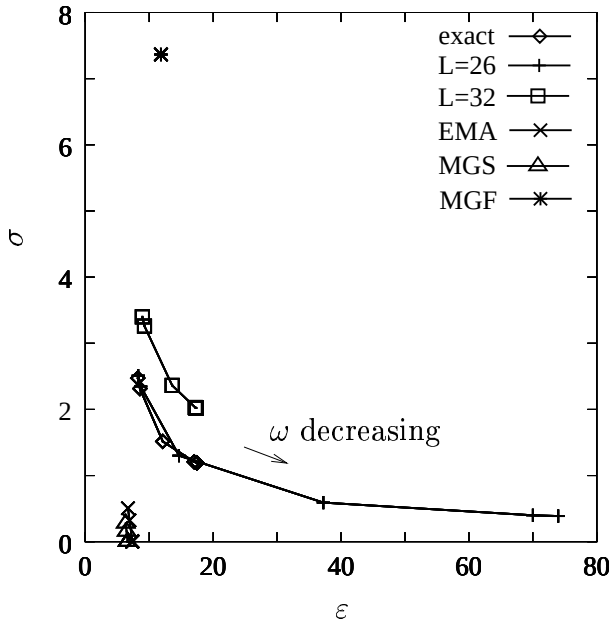

Figure 7.10: The *Cole-Cole* representation of the effective complex-valued permittivity predicted using various mixing laws for the sample D1.

attaining the bounds:

$$
\begin{aligned}
A^0 &= 87.74 + \mathrm{i}\,87.74, & B^0 &= 4.7,\\
A^1 &= 14.731232 + \mathrm{i}\,10.598992, & B^1 &= -0.006481 - \mathrm{i}\,0.006434,\\
A^2 &= 11.843674 + \mathrm{i}\,7.367486, & B^2 &= 6.461553 + \mathrm{i}\,0.155642.
\end{aligned}
$$

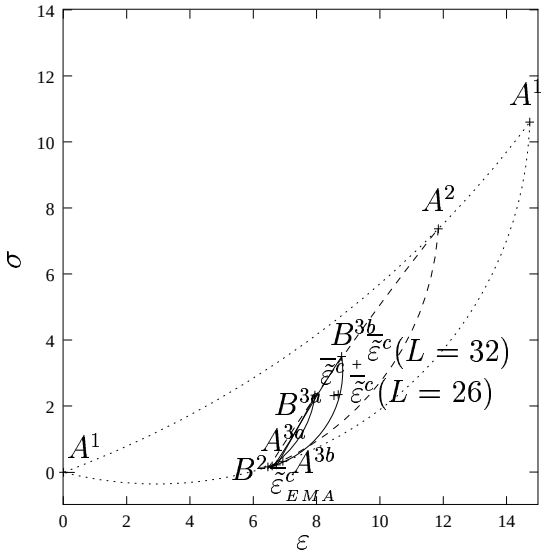

Figure 7.11: The effective complex-valued permittivity predicted using different mixing laws and the bounds method.

To obtain points A^3 and B^3, one needs the *Milton-Torquato* parameter of sample D1, which can be estimated applying (6.93) and (6.94), and the measured effective thermal conductivity. The case of the contrast ratio $k^F/k^S = 2.0$ ($k^F = 1.0$ and $k^S = 0.5$) was chosen, because it gives the tightest bounds on ζ^F. Hence,

$$0.118523 \leq \zeta^F \leq 0.211927.$$

By substituting $\zeta^F = 0.118523$ and $\zeta^F = 0.211927$ into (6.69), the corresponding points A^{3a} and B^{3a}, and A^{3b} and B^{3b} were found. Thus,

$$\begin{aligned} A^{3a} &= 6.597617 + \mathrm{i}\,0.185218, & B^{3a} &= 7.945902 + \mathrm{i}\,2.329847, \\ A^{3b} &= 6.729925 + \mathrm{i}\,0.216804, & B^{3b} &= 8.790632 + \mathrm{i}\,3.498335. \end{aligned}$$

Due to the uncertainty of ζ^F, the region Ω^3 of the third order bounds is a union of the lens-shaped region confined by arcs $A^{3a}B^{3a}A^2$ and $A^{3a}B^{3a}B^2$, and of the region confined by arcs $A^{3b}B^{3b}A^2$ and $A^{3b}B^{3b}B^2$. The bounds are shown in Figure 7.11. The points A^2 and B^2 are the same as the prediction using the MGT with φ^F and φ^S as the host phases, respectively. The simulated ($\overline{\tilde{\varepsilon}}^c$) and estimated results using the BEMA ($\overline{\tilde{\varepsilon}}^c_{EMA}$) and the MLLPT ($\overline{\tilde{\varepsilon}}^c(L=26)$ and $\overline{\tilde{\varepsilon}}^c(L=32)$ at the length scales $L = 26$ and $L = 32$, respectively) are also depicted in Figure 7.11. The point $\overline{\tilde{\varepsilon}}^c(L=26)$ lies within the region Ω^3, which implies that in this case the prediction of the MLLPT at the length scale $L = 26$ gives a very good result (cf. also 7.9).

7.3 Elastic moduli

The last numerical example is concerned with the prediction of the elastic moduli using various methods. For the direct numerical estimation, the FEM is applied. The effective

bulk modulus $\overline{K}$ and the effective shear modulus are estimated by employing different micro-mechanical models. These include the BEMA (5.75) and (5.77), the MGT (5.81) and (5.82), the DEM (5.85) and (5.86), and the GSCM (5.87) and (5.88). The bounds on $\overline{K}$ and on $\overline{G}$ are also discussed. This includes the *Reuss* and *Voigt* (RV) bounds (6.76) and (6.77), the *Hashin-Shtrikman* (HS) bounds (6.83) and (6.84) and the *Beran-Molyneux* (BM) and the *McCoy* (M) bounds (6.79) and (6.80).

As the sample, the digitized biphasic medium with the dimension $64 \times 64 \times 64$ voxels and the resolution $7.5\,\mu$m was used. The volume fractions of phases φ^F and φ^S are $\overline{n}^F = 0.10642$ and $\overline{n}^S = 0.89358$, respectively. Two different contrast ratios of the bulk moduli and of the shear moduli were investigated. The first case is that $K^F = 1.0$ and $G^F = 2.0$ for phase φ^F and $K^S = 20.0\,K^F$ and $G^S = 25.0\,G^F$ for phase φ^S were chosen. The second case is that $K^F = 17.5$ and $G^F = 8.0$, $K^S = 100\,K^F$ and $G^S = 100\,G^F$ for the phases φ^F and φ^S, respectively, were selected. All of them are given in units of $10^5\,\mathrm{N/mm^2}$.

For the simulation purpose, the periodic boundary conditions were chosen. Here, the periodic boundary conditions mean that the displacement vectors $\mathbf{u}^\star$ can be decomposed into its average $\overline{\mathbf{u}}$ and a fluctuation term $\mathbf{u}^\star(\mathbf{x})$ which is periodic on $\partial\mathcal{B}$. In order to satisfy the equilibrium state, the tractions $\mathbf{t} = \mathbf{T}\mathbf{n}$ are opposite on opposite sides of $\partial\mathcal{B}$ (anti periodic). Note that the external normal vectors $\mathbf{n}$ also have the opposite signs. This kind

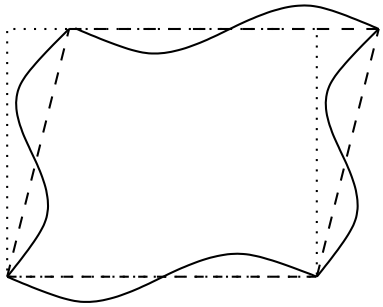

Figure 7.12: Periodic boundary conditions applied to an REV under simple shear strain.

of boundary conditions is pointed out to give a more accurate estimation of the effective moduli than those using uniform displacements or uniform traction boundary conditions (*Terada et al.* [169], *Miehe et al.* [124]). The estimation of the effective elastic moduli using FEM are tabulated in Table 7.16.

To estimate the *Milton-Torquato* parameter ζ^F, the inverse relationship of the *Beran* bounds (6.93) was applied. If the thermal conductivities of phases φ^F and φ^S were taken as $k^F = 2.0\,\mathrm{W/m\,K}$ and $k^S = 1.0\,\mathrm{W/m\,K}$, then, by applying the FVM, the corresponding effective conductivity was found. Using $\overline{k} = 1.082998\,\mathrm{W/m\,K}$, the bounds on ζ^F were attained. Thus,

$$0.083262 \leq \zeta^F \leq 0.153725. \tag{7.1}$$

From the relationship (6.95), the bounds on η were obtained:

$$0.019824 \leq \eta^F \leq 0.798506. \tag{7.2}$$

From this microgeometrical information ($\overline{n}^F$, ζ^F and η^F) and from the elastic moduli of the components, the lower and upper bounds up to the third-order bounds were attained. They are tabulated in Table 7.14 (on $\overline{K}$) and in Table 7.15 (on $\overline{G}$). Obviously, the upper

	(i)			(ii)		
bounds	RV	HS	BM	RV	HS	BM
lower	6.618177	11.943330	15.986586	151.704552	222.664803	499.148975
upper	17.978020	17.485412	17.444625	1565.627350	1340.618682	1323.861420

Table 7.14: The upper and lower bounds on the effective bulk modulus $\overline{K}$.

	(i)			(ii)		
bounds	RV	HS	M	RV	HS	M
lower	14.068338	19.922870	27.569061	69.350653	125.713345	177.188080
upper	44.891840	40.268140	39.979112	715.715360	654.465783	651.473758

Table 7.15: The upper and lower bounds on the effective shear modulus $\overline{G}$.

and lower bounds on the elastic moduli are quite far apart from each other. However, the upper *Beran-Molyneux* and *McCoy* bounds give good approximations of the effective bulk modulus $\overline{K}$ and the effective shear modulus $\overline{G}$, respectively.

The prediction using various models are presented in Table 7.16. All of the predicted results are within the HS bounds, but only the estimation results using the BEMA and the DEM lie within the third order bounds. However, in case (ii) the predicted effective bulk modulus ($\overline{K} = 662.960275$) using the DEM is very underestimated. Compared to the results obtained by other methods, the BEMA produces results in best accordance with the simulated data. The reason can be that the BEMA treats both components symmetrically which is compatible with the symmetric microstructure (aggregate microstructure) of the sample. Meanwhile, all other methods treat the components unsymmetrically (assuming that one phase is a host phase and another phase is an inclusion phase).

Method	(i)		(ii)	
	$\overline{K}$	$\overline{G}$	$\overline{K}$	$\overline{G}$
FEM	16.749559	36.500698	1136.912262	593.339692
BEMA	17.358724	39.308028	1295.105534	639.933747
MGT	17.485412	40.268139	1340.618681	654.465783
DEM	17.191944	39.777817	662.960275	636.895921
GSCM	17.485412	40.222095	1340.618681	652.808635

Table 7.16: The effective elastic moduli obtained by direct numerical simulation (FEM) and using various models.

Chapter 8

Summary and conclusions

8.1 Summary

In this thesis, the effective material parameters of a heterogeneous medium, whose local properties may be considered as random function of the position, have been determined. The material parameters studied in this thesis can be divided into three different classes. The first class is the material parameter that relates a divergenceless vector to an irrotational vector. This includes the dielectric constant, the electric conductivity, the thermal conductivity, the magnetic permeability, and the diffusion constant. The second class is the complex-valued material parameter which also relates a solenoidal vector to a irrotational vector. The complex-valued material parameter is used to describe the time-harmonic (dynamic) behaviour, but it is limited only to the low-frequency situations. The third class are the moduli of an elastic material.

These effective material parameters have been predicted using three different methods. The first one was by directly solving the balance equations together with the constitutive equation. In order to solve these equations, the information of the microgeometry of the heterogeneous medium has to be known. The detailed information of the microgeometry was obtained using either computer assisted tomography or micromechanical models. The computation has been carried out by applying the finite volume method and the finite element method. Upon solving these equations, the average field quantities were obtained. By assuming that these macroscopical average fields follow certain constitutive equations, the effective material parameters can be determined.

The second method is the self-consistent approximation. In this case, various mixing laws based on the effective medium approximation were applied. Except for the mixing law based on the local porosity theory which uses the information of the porosity and connectivity distribution, all of the mixing laws use porosity as the only structural input parameter. In the case of the thermal conductive material, the following models were used: *Bruggeman* effective medium approximation (BEMA), *Maxwell-Garnett* theory (MGT), the differential effective medium (DEM) and the mixing law based on the local porosity theory (MLLPT). The same models were applied to estimate the effective complex-valued permittivity. The effective elastic moduli were obtained by the *Kröner*'s self-consistent

method, the *Maxwell-Garnett* theory (*Mori-Tanaka* method) and the three-phase model (*Christensen & Lo* [46]).

The third applied method was the bounds method which was used to confine the effective material parameters. These methods need only partial information of the geometry of the heterogeneous medium. The advantage of these methods over the mixing laws is that they can be improved successively by adding more microstructural information. Furthermore, the bounds can also be improved by utilizing the effective physical properties of another class of material properties. This kind of improvement is called the cross-property relationship. For the effective thermal conductivity, the bounds given here are the *Hashin-Shtrikman*, the *Beran* and the improved *Prager* bounds. For the effective elastic moduli, the *Reuss* and the *Voigt*, the *Hashin-Shtrikman*, the *Beran-Molyneux*, the *McCoy*, and the cross-property bounds are presented. The last three of them are tighter than the *Hashin-Shtrikman* bounds. In the case of the effective complex-valued permittivity, the bounds based on the *Bergman* representation were applied. These bounds have lens-shaped forms in the complex plane, which reduce to the well-known bounds on the thermal conductivity in the case of the real-valued permittivity (the imaginary part is vanished).

To verify the difference of the presented methods, eight digitized samples of sandstone were employed. Six samples (A, B, C, D1, D2, D3) are obtained from the computer assisted tomography. The remaining two samples (R1 and R2) are generated from the same given medium C, but with different length scales. The generated samples R1 and R2 have the same two-point correlation functions and porosities as the original sample C.

In the case of the prediction of the effective thermal conductivity, all of the eight digitized samples were employed. Each sample was investigated with six different contrast ratios which ranges from $k^F/k^S = 2$ to $k^F/k^S = \infty$. In the case of the low contrast, all of the approximation methods provided similarly good results for the effective conductivity. It is worth emphasizing, that although the mixing law based on the local porosity theory contains more microstructural information, it did not give a better estimation than other mixing laws. Therefore, it can be concluded that for the lower contrast ratio, the morphology (connectivity) of the heterogeneous medium does not play such an important role as one might think. With increasing contrast ratio the results of the approximation methods began to differ. Therefore, for the higher contrast ratio, the morphology has an extremely important role. The upper *Prager* bound using the effective moduli of the lower contrast ratio ($k^F/k^S = 100$ or $k^F/k^S = 10000$) yielded a very good estimation of the effective conductivity for the contrast ratio $k^F/k^S = \infty$. Since the numerical methods in the case of the infinite contrast ratio converged very slow, the upper *Prager* bound could be combined with the numerical method to estimate the effective thermal conductivity. For the samples with similar porosities, the classical mixing laws provided more or less the same effective thermal conductivity, even though the measured effective conductivities were very different (cf. samples C, R1 and R2), while MLLPT gave different predictions for these three samples. However, MLLPT yields overestimated predictions.

In the case of estimating the effective complex-valued permittivity, this thesis used only four samples which were denoted as A, B, C and D1. All of the mixing laws based

on the effective medium approximation did not give satisfactory predictions for the whole frequency range from $\omega = 10^{-4}$ to $\omega = 10^{2}$. The mixing law based on the local porosity theory predicted reasonable results depending on the chosen length scales. In other words, the accuracy of the results depended on the length scale. It should be emphasized that the main problem arising in MLLPT is the determination of the length scale L, because it depends on the frequency and also on the physical process. It has been seen that two different length scales had to be chosen in order to achieve the best real part of the effective complex-valued permittivity (the real-valued effective permittivity) and the best imaginary part of the effective complex-valued permittivity (the real-valued effective conductivity), respectively. This dependence was also clearly seen in the case of the determination of the effective thermal conductivity. It has been shown that other commonly used mixing laws which are based on the effective medium approximation failed to accurately predict the effective complex-valued permittivity (see also *Ma et al.* [114]). Contrarily, in this case, the bounds methods gave reasonable good results.

For the estimation of the elastic moduli, the predictions of the self-consistent method were in good agreement with the computational results. Contrary to *Christensen*'s results [45], the generalized self-consistent method did not provide better results than the self-consistent method. The reason can be traced back to the different microstructures of the heterogeneous systems. The systems investigated by *Christensen* [45] are suspensions of particles, which have the dispersion microstructures. Therefore, the unsymmterical mixing law such as the generalized self-consistent method gives better results than those based on the self-consistent method. Meanwhile, the sample investigated here has an aggregate microstructure, where the symmetrical mixing law such as the self-consistent method is more compatible with the microstructure. It has also been verified that the self-consistent method provides good predicted effective moduli of polycrystals (*Zaoui* [197]). For the bounds methods, the attained third-order lower and upper bounds on the effective moduli were still apart from each other; however, the upper bounds could be used to predict the effective moduli.

8.2 Directions for future work

In this section, there are some proposals for improving and extending the present work.

To compute a larger three-dimensional sample, a straightforward extension has to be introduced. A straightforward extension means that the numerical algorithms are implemented on a parallel or vector computer. Through parallelization or vectorization, one can use the faster solvers which need large storage capacity. This can be multi-grid solvers or wavelet based preconditioning solvers. Since wavelet functions can capture local properties very well (*Van Den Berg*) [18]), it will be useful to exploit this properties directly by developing wavelet-*Galerkin* methods (*Amaratunga & Williams* [4], *Williams & Amaratunga* [189]) for solving the balance equations of the heterogeneous medium.

The approaches used in this thesis are based on the quasi-static treatment of the fields. For high frequency problems or wave phenomena in heterogeneous media, the approaches have to be extended, in order to take into account the dynamical effects. To solve the

wave equations in heterogeneous media, the corresponding numerical algorithms have to be implemented. Some approximation methods for the dynamic problem based on the effective medium exist (*Sheng* [162], *Kanaun* [99]), however, a detailed study which compares the results of these approximation methods with those obtained by the simulation or by experiments should be done, since this is the only way to justify the approximation method based on the effective medium approximation. Contrary to the effective medium approach, bounds cannot be attained in the general time-dependent case (*Willis* [190]). Note that due to the inhomogeneity, the waves might be scattered and localized, which makes the study of the waves phenomena in inhomogeneous media more difficult. The studies of such phenomena are an active research field (*Rossum & Nieuwenhuizen* [180], *Sheng* [160]).

Another extension of this work is the treatment of anisotropy and of the nonlinear case. If only the material nonlinearity is taken into account and the medium is assumed to be isotropic and rigid such as the nonlinear heat conductivity or nonlinear electromagnetical heterogeneous media, the geometrical parameter such as the *Milton-Torquato* parameter ζ^F and ζ^S which can be obtained from the linear case, can still be used. Therefore, it is useful to establish the third-order bounds for such materials. Note that for the power-law materials, the third-order bounds and some self-consistent approximation exist. However, some comparisons with the experimental and simulation results are still needed. In general, further work on the bounds methods for the nonlinear case are expected to be done. Furthermore, the energy functionals in the nonlinear cases are not always convex, which makes the establishment of the bounds for the nonlinear material more complicated. In addition to the material nonlinearity, the geometrical nonlinearity can be taken into account. Obviously, in this case, the microstructure of the heterogeneous medium will always change at every stage of the deformation process. This makes the analysis of such problems very tedious and complicated. Further study is needed in this field.

Many heterogeneous materials show coupled effects such as thermomechanical, piezoelectric or magnetoelectric effects. Therefore, the mixing laws or the bounds methods which take into account such effects should be developed. The corresponding existing mixing laws (*Nemat-Nasser & Hori* [135], *Sihvola* [164]) which are heuristically obtained need to be further examined in order to specify the range of the application of these mixing laws. It is also useful to develop cross-property relationships which link the values of different overall properties for such coupled material parameters.

Another interesting extension is to use the results of the homogenization process in designing advanced materials. Through the bounds on the effective materials, one can gain some insight into the microstructure of the design material and also learn the limits of the improvement in the material properties of such heterogeneous materials due to the variation of the microstructures. Therefore, the bounds on the the effective material parameters are important to design an optimal material or structure.

Appendix A

Some useful formulae of vector and tensor calculus

This appendix summarizes some basic results of vector and tensor calculus, which are used in this thesis. The notation used here and in the next section is based on *de Boer*'s notation [48, 49] and the detailed treatment will be found there. The capital bold and the small bold letters designate tensor and vector fields, respectively. The vector $\mathbf{n}$ indicates the unit normal vector of the surface, meanwhile the symbols $\mathrm{d}v$, $\mathrm{d}\mathbf{a}$ and $\mathrm{d}\mathbf{x}$ denote the volume element, the surface element and the line element, respectively.

Double cross tensor product of tensors

The cross tensor product of two second-rank tensors $\mathbf{T}$ and $\mathbf{S}$ is given by

$$(\mathbf{T} \# \mathbf{S})(\mathbf{u}_1 \times \mathbf{u}_2) = \mathbf{T}\mathbf{u}_1 \times \mathbf{S}\mathbf{u}_2 - \mathbf{T}\mathbf{u}_2 \times \mathbf{S}\mathbf{u}_1. \tag{A.1}$$

The adjunct tensor and determinants

The adjunct tensor $\overset{+}{\mathbf{T}}$ is defined through the cross tensor product:

$$\overset{+}{\mathbf{T}} = \tfrac{1}{2}(\mathbf{T} \# \mathbf{T}). \tag{A.2}$$

The determinant of a tensor $\mathbf{T}$ can be written as

$$\det \mathbf{T} = \tfrac{1}{6}(\mathbf{T} \# \mathbf{T}) \cdot \mathbf{T}. \tag{A.3}$$

Through (A.2) and (A.3) the inversion of tensor $\mathbf{T}$ can be given by (*de Boer* [49], p. 537)

$$\overset{+}{\mathbf{T}} = (\det \mathbf{T})\,(\mathbf{T}^T)^{-1}. \tag{A.4}$$

Some useful identities

$$\mathbf{u}\cdot(\mathbf{v}\times\mathbf{w}) = \mathbf{v}\cdot(\mathbf{w}\times\mathbf{u}) = \mathbf{w}\cdot(\mathbf{u}\times\mathbf{v}), \tag{A.5}$$

$$\operatorname{div}(\phi\,\mathbf{v}) = \mathbf{v}\cdot\operatorname{grad}\phi + \phi\operatorname{div}\mathbf{v}, \tag{A.6}$$

$$\operatorname{div}(\mathbf{u}\otimes\mathbf{v}) = (\operatorname{grad}\,\mathbf{u})\mathbf{v} + (\operatorname{div}\mathbf{v})\mathbf{u}, \tag{A.7}$$

$$\operatorname{rot}(\mathbf{u}\times\mathbf{v}) = \mathbf{u}\operatorname{div}\mathbf{v} - \operatorname{grad}\mathbf{v}\,\mathbf{u} - \mathbf{v}\operatorname{div}\mathbf{u} + \operatorname{grad}\mathbf{u}\,\mathbf{v}, \tag{A.8}$$

$$\int_{\mathcal{B}}\operatorname{div}\mathbf{T}\,\mathrm{d}v = \int_{\partial\mathcal{B}}\mathbf{T}\,\mathrm{d}\mathbf{a}, \tag{A.9}$$

$$\int_{\mathcal{B}}\operatorname{div}\mathbf{u}\,\mathrm{d}v = \int_{\partial\mathcal{B}}\mathbf{u}\cdot\mathrm{d}\mathbf{a}, \tag{A.10}$$

$$\int_{\mathcal{S}}\operatorname{rot}\mathbf{u}\cdot\mathrm{d}\mathbf{a} = \oint_{\partial\mathcal{S}}\mathbf{u}\cdot\mathrm{d}\mathbf{x}, \tag{A.11}$$

$$\int_{\mathcal{B}}\operatorname{grad}\mathbf{u}\,\mathrm{d}v = \int_{\partial\mathcal{S}}\mathbf{u}\otimes\mathrm{d}\mathbf{a}, \tag{A.12}$$

$$\int_{\mathcal{B}}\operatorname{grad}\theta\,\mathrm{d}v = \int_{\partial\mathcal{S}}\theta\,\mathrm{d}\mathbf{a}. \tag{A.13}$$

Appendix B

Spherical basis system

This appendix discusses the spherical coordinate system, i. e., the system which is suitable to analyze the n-layered spherical inclusion problem. A brief summary of transformation laws between the Cartesian and the spherical coordinate systems and of tensor analysis in spherical coordinate systems is given. A comprehensive treatment of vector and tensor analysis can be found elsewhere (*Betten* [28], *de Boer* [48, 49]). This appendix also provides some equations of physics in a spherical coordinate system, which are extensively used in this thesis.

B.1 Transformation laws

In spherical coordinates, a point P is represented by coordinates θ^1, θ^2, and θ^3 (Fig. B.1). Thereby, θ^1 is the distance from P to the origin $\mathcal{O}$, θ^2 is the angle between the radial line $\mathcal{OP}$ and the positive x_3-axis, and θ^3 is the angle between the plane containing P and the x_3-axis and the x_1x_3-plane. The notation $(\theta^1, \theta^2, \theta^3)$ is chosen here because it allows for a compact representation of doing the tensor analysis. However, in the rest of this work, $\theta^1 = r$, $\theta^2 = \vartheta$ and $\theta^3 = \varphi$ are set to be compatible with the common representation of spherical coordinate system in engineering and science.

The transformation relations between Cartesian (x_1, x_2, x_3) and spherical $(\theta^1, \theta^2, \theta^3)$ coordinate systems according to Fig. B.1 take the form

$$\begin{aligned} x_1 &= \theta^1 \sin\theta^2 \cos\theta^3, \\ x_2 &= \theta^1 \sin\theta^2 \sin\theta^3, \\ x_3 &= \theta^1 \cos\theta^2. \end{aligned} \tag{B.1}$$

Hence, the position vector $\mathbf{x}$ and the corresponding line element $\mathrm{d}\mathbf{x}$ are given by

$$\begin{aligned} \mathbf{x} &= \theta^1 \sin\theta^2 \cos\theta^3\, \mathbf{e}_1 + \theta^1 \sin\theta^2 \sin\theta^3\, \mathbf{e}_2 + \theta^1 \cos\theta^2\, \mathbf{e}_3, \\ \mathrm{d}\mathbf{x} &= \frac{\partial \mathbf{x}}{\partial \theta^1}\,\mathrm{d}\theta^1 + \frac{\partial \mathbf{x}}{\partial \theta^2}\,\mathrm{d}\theta^2 + \frac{\partial \mathbf{x}}{\partial \theta^3}\,\mathrm{d}\theta^3 = \mathbf{h}_1\,\mathrm{d}\theta^1 + \mathbf{h}_2\,\mathrm{d}\theta^2 + \mathbf{h}_3\,\mathrm{d}\theta^3, \end{aligned} \tag{B.2}$$

respectively.

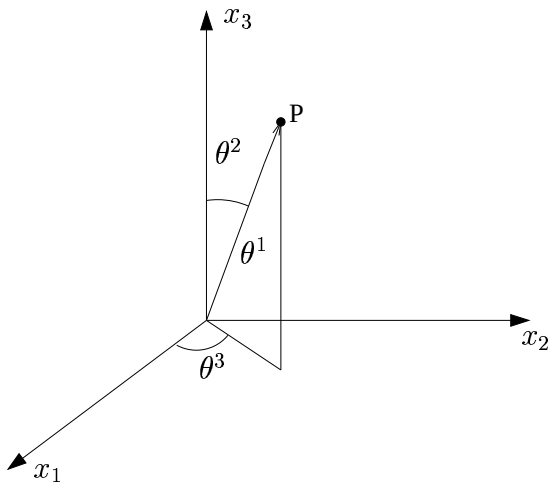

Figure B.1: Spherical polar coordinates

The covariant basis vectors (natural tangential basis) of spherical coordinates are defined by the differentiation of the position vector with respect to the coordinates θ^1, θ^2 and θ^3:

$$\begin{aligned}
\mathbf{h}_1 &= \frac{\partial \mathbf{x}}{\partial \theta^1} = \sin\theta^2 \left(\cos\theta^3\, \mathbf{e}_1 + \sin\theta^3\, \mathbf{e}_2\right) + \cos\theta^2\, \mathbf{e}_3, \\
\mathbf{h}_2 &= \frac{\partial \mathbf{x}}{\partial \theta^2} = \theta^1\, \cos\theta^2 \left(\cos\theta^3\, \mathbf{e}_1 + \sin\theta^3\, \mathbf{e}_2\right) - \theta^1\, \sin\theta^2\, \mathbf{e}_3, \\
\mathbf{h}_3 &= \frac{\partial \mathbf{x}}{\partial \theta^3} = \theta^1\, \sin\theta^2 \left(-\sin\theta^3\, \mathbf{e}_1 + \cos\theta^3\, \mathbf{e}_2\right).
\end{aligned} \tag{B.3}$$

The unit basis vectors are obtained by dividing the basis vectors by their lengths

$$\begin{aligned}
\overset{*}{\mathbf{h}}_1 &= \sin\theta^2 \cos\theta^3\, \mathbf{e}_1 + \sin\theta^2 \sin\theta^3\, \mathbf{e}_2 + \cos\theta^2\, \mathbf{e}_3, \\
\overset{*}{\mathbf{h}}_2 &= \cos\theta^2 \cos\theta^3\, \mathbf{e}_1 + \cos\theta^2 \sin\theta^3\, \mathbf{e}_2 - \sin\theta^2\, \mathbf{e}_3, \\
\overset{*}{\mathbf{h}}_3 &= -\sin\theta^3\, \mathbf{e}_1 + \cos\theta^3\, \mathbf{e}_2.
\end{aligned} \tag{B.4}$$

Note that the usual representation of the unit basis vectors of the spherical coordinates $\mathbf{e}_r$, $\mathbf{e}_\vartheta$ and $\mathbf{e}_\varphi$, which respectively, define the radial, the meridional and the circumferential directions, are related as

$$\mathbf{e}_r = \overset{*}{\mathbf{h}}_1, \qquad \mathbf{e}_\vartheta = \overset{*}{\mathbf{h}}_2, \qquad \mathbf{e}_\varphi = \overset{*}{\mathbf{h}}_3. \tag{B.5}$$

By solving (B.4), one has the orthonormal Cartesian basis vectors in terms of the unit

basis vectors of the spherical coordinate system

$$\begin{aligned} \mathbf{e}_1 &= \sin\theta^2 \cos\theta^3 \overset{*}{\mathbf{h}}_1 + \cos\theta^2 \cos\theta^3 \overset{*}{\mathbf{h}}_2 - \sin\theta^3 \overset{*}{\mathbf{h}}_3, \\ \mathbf{e}_2 &= \sin\theta^2 \sin\theta^3 \overset{*}{\mathbf{h}}_1 + \cos\theta^2 \sin\theta^3 \overset{*}{\mathbf{h}}_2 + \cos\theta^3 \overset{*}{\mathbf{h}}_3, \\ \mathbf{e}_3 &= \cos\theta^2 \overset{*}{\mathbf{h}}_1 - \sin\theta^2 \overset{*}{\mathbf{h}}_2. \end{aligned} \tag{B.6}$$

Note that these basis vectors $\mathbf{e}_i$ and $\overset{*}{\mathbf{h}}_i$ coincide with their corresponding reciprocal basis vectors, i. e.,

$$\mathbf{e}_i = \mathbf{e}^i \quad \text{and} \quad \overset{*}{\mathbf{h}}_i = \overset{*}{\mathbf{h}}{}^i. \tag{B.7}$$

From the relations (B.4) and (B.6), one can determine the tensors $\mathbf{A}$ and $\mathbf{B}$, which give the relationships between every vector or tensor in the Cartesian system and those in the spherical coordinate system and vice versa, respectively. These tensors $\mathbf{A}$ and $\mathbf{B}$ are given by

$$\mathbf{A} = a^{ij} \, (\overset{*}{\mathbf{h}}_i \otimes \overset{*}{\mathbf{h}}_j) \quad \text{with} \quad a^{ij} = \begin{bmatrix} \sin\theta^2 \cos\theta^3 & \sin\theta^2 \sin\theta^3 & \cos\theta^2 \\ \cos\theta^2 \cos\theta^3 & \cos\theta^2 \sin\theta^3 & -\sin\theta^2 \\ -\sin\theta^3 & \cos\theta^3 & 0 \end{bmatrix} \tag{B.8}$$

and

$$\mathbf{B} = b_{ij} \, (\mathbf{e}_i \otimes \mathbf{e}_j) \quad \text{with} \quad b_{ij} = \begin{bmatrix} \sin\theta^2 \cos\theta^3 & \cos\theta^2 \cos\theta^3 & -\sin\theta^3 \\ \sin\theta^2 \sin\theta^3 & \cos\theta^2 \sin\theta^3 & \cos\theta^3 \\ \cos\theta^2 & -\sin\theta^2 & 0 \end{bmatrix}. \tag{B.9}$$

In component form, an arbitrary vector $\mathbf{u}$ and an arbitrary second-rank tensor $\mathbf{T}$ may be expressed in the Cartesian basis system by

$$\begin{aligned} \mathbf{u} &= \bar{u}_i \, \mathbf{e}_i, \\ \mathbf{T} &= \bar{t}_{ij} \, \mathbf{e}_i \otimes \mathbf{e}_j \end{aligned} \tag{B.10}$$

and in spherical coordinate unit basis by

$$\begin{aligned} \mathbf{u} &= \overset{*}{u}{}^i \, \overset{*}{\mathbf{h}}_i, \\ \mathbf{T} &= \overset{*}{t}{}^{ij} \, \overset{*}{\mathbf{h}}_i \otimes \overset{*}{\mathbf{h}}_j, \end{aligned} \tag{B.11}$$

where *Einstein*'s summation convention is used. Note that $\overset{*}{u}{}^i$ and $\overset{*}{t}{}^{ij}$ are physical coefficients of $\mathbf{u}$ and $\mathbf{T}$. Since for the orthonormal basis system the covariant and the contravariant basis vectors are equivalent ($\mathbf{e}_i \equiv \mathbf{e}^i$), the vector coefficients can be written in covariant form. The coefficients transform according to the equation

$$\begin{aligned} \overset{*}{u}{}^i &= a^{ij} \, \bar{u}_j, \\ \bar{u}_i &= b_{ij} \, \overset{*}{u}{}^j \end{aligned} \tag{B.12}$$

and the tensor coefficients are subject to the transformation law

$$\begin{aligned} \overset{*}{t}{}^{ij} &= a^{ik}\, a^{jl}\, \bar{t}_{kl}, \\ \bar{t}_{ij} &= b_{ik}\, b_{jl}\, \overset{*}{t}{}^{kl}. \end{aligned} \tag{B.13}$$

The contravariant basis vectors are defined by

$$\mathbf{h}_i \cdot \mathbf{h}^j = \delta_i^j, \tag{B.14}$$

where δ_i^j is the *Kronecker* symbol. By employing (B.3) and (B.14), the contravariant basis vectors of the spherical coordinate system can be calculated as

$$\begin{aligned} \mathbf{h}^1 &= \sin\theta^2 \left(\cos\theta^3\, \mathbf{e}_1 + \sin\theta^3\, \mathbf{e}_2\right) + \cos\theta^2\, \mathbf{e}_3, \\ \mathbf{h}^2 &= \frac{1}{\theta^1} \cos\theta^2 \left(\cos\theta^3\, \mathbf{e}_1 + \sin\theta^3\, \mathbf{e}_2\right) - \frac{1}{\theta^1} \sin\theta^2\, \mathbf{e}_3, \\ \mathbf{h}^3 &= \frac{1}{\theta^1 \sin\theta^2} \left(-\sin\theta^3\, \mathbf{e}_1 + \cos\theta^3\, \mathbf{e}_2\right). \end{aligned} \tag{B.15}$$

The covariant metric coefficients can be computed via

$$h_{ij} = \mathbf{h}_i \cdot \mathbf{h}_j = \begin{bmatrix} 1 & 0 & 0 \\ 0 & (\theta^1)^2 & 0 \\ 0 & 0 & (\theta^1)^2 \sin^2\theta^2 \end{bmatrix}. \tag{B.16}$$

Similarly, the contravariant metric coefficients yields

$$h^{ij} = \mathbf{h}^i \cdot \mathbf{h}^j = \begin{bmatrix} 1 & 0 & 0 \\ 0 & (\theta^1)^{-2} & 0 \\ 0 & 0 & (\theta^1)^{-2} \sin^{-2}\theta^2 \end{bmatrix}. \tag{B.17}$$

The covariant and contravariant metric coefficients are inverse to each other, which can be proved easily by multiplying (B.16) with (B.17).

B.2 Tensor analysis in spherical coordinates

For a tensor analysis in convective coordinates, a suitable differentiation procedure, which is known as covariant derivative, is required. Covariant derivatives play the role of regular partial derivatives in convective coordinate system and reduce to the regular partial differentiation in a Cartesian coordinate system. Hence, the coefficients produced by the covariant derivative have to fulfill the transformation laws for tensor quantities. The covariant derivative can be done conveniently by introducing *Christoffel* symbols of the second kind, which can be defined as the vector coefficients of the derivative of the covariant basis vectors $\mathbf{h}_i$ given in the covariant basis vectors $\mathbf{h}_k$. Thus,

$$\mathbf{h}_{i,j} = \Gamma_{ij}^{\cdot\cdot k}\, \mathbf{h}_k\,, \tag{B.18}$$

where $(\cdot)_{,j}$ indicates partial differentiation with respect to the coordinate θ^j. For example, the *Christoffel* symbols $\Gamma_{ij}^{\cdot\cdot k}$ can be computed via

$$\Gamma_{ij}^{\cdot\cdot k} = \tfrac{1}{2}\, h^{kl}\, (h_{il,j} + h_{jl,i} - h_{ij,l}). \tag{B.19}$$

By substituting the covariant and contravariant metric coefficients (B.16) and (B.17) into the defining equations (B.19) for the *Christoffel* symbols, one obtains that all of $\Gamma_{ij}^{\cdot\cdot k} = 0$ except

$$\begin{aligned}
\Gamma_{22}^{\cdot\cdot 1} &= -\theta^1, \\
\Gamma_{33}^{\cdot\cdot 1} &= -\theta^1 \sin^2\theta^2, \\
\Gamma_{12}^{\cdot\cdot 2} &= \Gamma_{21}^{\cdot\cdot 2} = \frac{1}{\theta^1}, \\
\Gamma_{33}^{\cdot\cdot 2} &= -\sin\theta^2\, \cos\theta^2, \\
\Gamma_{13}^{\cdot\cdot 3} &= \Gamma_{31}^{\cdot\cdot 3} = \frac{1}{\theta^1}, \\
\Gamma_{23}^{\cdot\cdot 3} &= \Gamma_{32}^{\cdot\cdot 3} = \frac{\cos\theta^2}{\sin\theta^2}.
\end{aligned} \tag{B.20}$$

From now on, the fields are assumed to be functions of the coordinates θ^i. The gradient of a scalar field θ is given by

$$\operatorname{grad}\theta = \frac{\mathrm{d}\theta}{\mathrm{d}\mathbf{x}} = \theta_{,k}\, \mathbf{h}^k = \theta_{,1}\, \overset{*}{\mathbf{h}}_1 + \frac{1}{\theta^1}\, \theta_{,2}\, \overset{*}{\mathbf{h}}_2 + \frac{1}{\theta^1 \sin\theta^2}\, \theta_{,3}\, \overset{*}{\mathbf{h}}_3. \tag{B.21}$$

The gradient of a vector field $\mathbf{u} = u^i\, \mathbf{h}_i$ can be found as

$$\operatorname{grad}\mathbf{u} = \frac{\mathrm{d}\mathbf{u}}{\mathrm{d}\mathbf{x}} = (u^i{}_{,k} + u^l\, \Gamma_{lk}^{\cdot\cdot i})\, \mathbf{h}_i \otimes \mathbf{h}^k. \tag{B.22}$$

In a contravariant basis system, the gradient of a vector field $\mathbf{u} = u_i\, \mathbf{h}^i$ yields

$$\operatorname{grad}\mathbf{u} = \frac{\mathrm{d}\mathbf{u}}{\mathrm{d}\mathbf{x}} = (u_{i,k} - u_l\, \Gamma_{ik}^{\cdot\cdot l})\, \mathbf{h}^i \otimes \mathbf{h}^k. \tag{B.23}$$

The gradient of a tensor field $\mathbf{T} = t^{ij}\, \mathbf{h}_i \otimes \mathbf{h}_j$ is given by

$$\operatorname{grad}\mathbf{T} = \frac{\mathrm{d}\mathbf{T}}{\mathrm{d}\mathbf{x}} = \left(t^{ij}{}_{,k} + t^{lj}\, \Gamma_{kl}^{\cdot\cdot i} + t^{il}\, \Gamma_{kl}^{\cdot\cdot j}\right) \mathbf{h}_i \otimes \mathbf{h}_j \otimes \mathbf{h}^k. \tag{B.24}$$

The divergence of a vector field $\mathbf{u}$ is defined by

$$\operatorname{div}\mathbf{u} = \operatorname{grad}\mathbf{u} \cdot \mathbf{I}, \tag{B.25}$$

where $\mathbf{I}$ is the second-rank fundamental unit tensor. Thus, if the vector $\mathbf{u}$ is expressed in terms of covariant basis vectors ($\mathbf{u} = u^i\, \mathbf{h}_i$), its divergence is given by

$$\operatorname{div}\mathbf{u} = \operatorname{div}(u^i\, \mathbf{h}_i) = u^i{}_{,i} + u^l\, \Gamma_{li}^{\cdot\cdot i}, \tag{B.26}$$

and if $\mathbf{u} = u_i\,\mathbf{h}^i$ the divergence of $\mathbf{u}$ takes the form

$$\operatorname{div}\mathbf{u} = \operatorname{div}(u_i\,\mathbf{h}^i) = (u_{i,k} - u_l\,\Gamma_{ik}^{\cdot\cdot l})\,h^{ik}. \tag{B.27}$$

The divergence of a tensor field $\mathbf{T} = t^{ij}\,\mathbf{h}_i \otimes \mathbf{h}_j$ can be evaluated via

$$\operatorname{div}\mathbf{T} = \operatorname{div}(t^{ij}\,\mathbf{h}_i \otimes \mathbf{h}_j) = (t^{ij}_{\cdot\cdot,j} + t^{lj}\,\Gamma_{lj}^{\cdot\cdot i} + t^{il}\,\Gamma_{lj}^{\cdot\cdot j})\,\mathbf{h}_i. \tag{B.28}$$

In general, the values of covariant and contravariant basis vectors are no unit vectors, therefore, they should be normalized in physical and engineering applications. The relations between the covariant or contravariant coefficients and the coefficients of unit vectors (physical components) can be expressed as

$$\begin{aligned} \overset{*}{u}{}^i &= u^i\sqrt{h_{(ii)}} &&= u_i\sqrt{h^{(ii)}}, \\ \overset{*}{t}{}^{ij} &= t^{ij}\sqrt{h_{(ii)}\,h_{(jj)}} &&= t_{ij}\sqrt{h^{(ii)}h^{(jj)}}, \end{aligned} \tag{B.29}$$

where the brackets (ii) and (jj) indicate that there is no sum over i and j, respectively.

B.3 Some applications

B.3.1 *Laplace* equation

For the case of an inhomogeneous but isotropic thermal conductivity $k(\mathbf{x})$, the governing partial differential equation is

$$\operatorname{div}[k(\mathbf{x})\operatorname{grad}\theta(\mathbf{x})] = 0, \tag{B.30}$$

where $\theta(\mathbf{x})$ is the temperature field. In spherical coordinates, (B.30) takes the form

$$(k\,\theta_{,1})_{,1} + \frac{1}{(\theta^1)^2}(k\,\theta_{,2})_{,2} + \frac{1}{(\theta^1)^2(\sin\theta^2)^2}(k\,\theta_{,3})_{,3} + \frac{2k}{\theta^1}\,\theta_{,1} + \frac{k}{(\theta^1)^2\tan\theta^2}\,\theta_{,2} = 0. \tag{B.31}$$

(B.31) is obtained by substituting $\mathbf{u} = k\operatorname{grad}\theta$ in (B.27), where $\operatorname{grad}\theta$ is given by (B.21).

B.3.2 Linear isotropic elasticity

In spherical coordinates, the displacement vector $\mathbf{u}$ can be expressed as

$$\mathbf{u} = \overset{*}{u}{}^i\ \overset{*}{\mathbf{h}}_i\,. \tag{B.32}$$

Plugging (B.32) into the kinematical relation between displacement and strain,

$$\boldsymbol{\varepsilon} = \tfrac{1}{2}[\operatorname{grad}\mathbf{u} + (\operatorname{grad}\mathbf{u})^T], \tag{B.33}$$

and by combining using (B.29), (B.22), (B.20) and (B.7), the linear strain tensor $\boldsymbol{\varepsilon}$ can be computed and written as

$$\boldsymbol{\varepsilon} = \overset{*}{\varepsilon}{}^{ij}\ \overset{*}{\mathbf{h}}_i \otimes \overset{*}{\mathbf{h}}_j \tag{B.34}$$

with

$$
\begin{aligned}
\overset{*}{\varepsilon}{}^{11} &= \overset{*}{u}{}^{1}_{,1}, \\
\overset{*}{\varepsilon}{}^{22} &= \frac{1}{\theta^1}\,(\overset{*}{u}{}^{2}_{,2} + \overset{*}{u}{}^{1}), \\
\overset{*}{\varepsilon}{}^{33} &= \frac{1}{\theta^1 \sin\theta^2}\,\overset{*}{u}{}^{3}_{,3} + \frac{1}{\theta^1}\,\overset{*}{u}{}^{1} + \frac{1}{\theta^1 \tan\theta^2}\,\overset{*}{u}{}^{2}, \\
\overset{*}{\varepsilon}{}^{12} &= \overset{*}{\varepsilon}{}^{21} = \frac{1}{2}\left(\frac{1}{\theta^1}\,\overset{*}{u}{}^{1}_{,2} + \overset{*}{u}{}^{2}_{,1} - \frac{1}{\theta^1}\,\overset{*}{u}{}^{2}\right), \\
\overset{*}{\varepsilon}{}^{13} &= \overset{*}{\varepsilon}{}^{31} = \frac{1}{2}\left(\frac{1}{\theta^1 \sin\theta^2}\,\overset{*}{u}{}^{1}_{,3} + \overset{*}{u}{}^{3}_{,1} - \frac{1}{\theta^1}\,\overset{*}{u}{}^{3}\right), \\
\overset{*}{\varepsilon}{}^{23} &= \overset{*}{\varepsilon}{}^{32} = \frac{1}{2}\left(\frac{1}{\theta^1 \sin\theta^2}\,\overset{*}{u}{}^{2}_{,3} + \frac{1}{\theta^1}\,\overset{*}{u}{}^{3}_{,2} - \frac{1}{\theta^1 \tan\theta^2}\,\overset{*}{u}{}^{3}\right).
\end{aligned}
\tag{B.35}
$$

For an isotropic body, the fourth-rank elasticity tensor $\overset{4}{\mathbf{C}}$ is given by

$$
\begin{aligned}
\overset{4}{\mathbf{C}} &= 2G\left[(\mathbf{I}\otimes\mathbf{I})^{\overset{23}{T}} + \frac{\nu}{1-2\nu}(\mathbf{I}\otimes\mathbf{I})\right] \\
&= 2G\left[\delta^{ik}\,\delta^{jl} + \frac{\nu}{1-2\nu}\,\delta^{ij}\,\delta^{kl}\right]\overset{*}{\mathbf{h}}_i \otimes \overset{*}{\mathbf{h}}_j \otimes \overset{*}{\mathbf{h}}_k \otimes \overset{*}{\mathbf{h}}_l\,.
\end{aligned}
\tag{B.36}
$$

Using the *Hooke*'s law $\mathbf{T} = \overset{4}{\mathbf{C}}\,\boldsymbol{\varepsilon}$, the stress tensor $\mathbf{T}$ can be calculated as

$$
\mathbf{T} = 2G\left(\overset{*}{\varepsilon}{}^{ij} + \frac{\nu}{1-2\nu}\,\overset{*}{\varepsilon}{}^{mm}\,\delta^{ij}\right)\overset{*}{\mathbf{h}}_i \otimes \overset{*}{\mathbf{h}}_j\,. \tag{B.37}
$$

The equilibrium equation reads

$$
\operatorname{div}\mathbf{T} + \rho\,\mathbf{f} = \mathbf{0}, \tag{B.38}
$$

where $\rho\,\mathbf{f} = \rho\,\overset{*}{f}{}^{i}\,\overset{*}{\mathbf{h}}_i$ is the body force. Using (B.28) and $(B.29)_2$, (B.38) can be formulated in component notation as

$$
\begin{aligned}
\overset{*}{t}{}^{11}_{,1} + \frac{1}{\theta^1}\,\overset{*}{t}{}^{12}_{,2} + \frac{1}{\theta^1 \sin\theta^2}\,\overset{*}{t}{}^{13}_{,3} + \frac{1}{\theta^1}(2\,\overset{*}{t}{}^{11} - \overset{*}{t}{}^{22} - \overset{*}{t}{}^{33}) + \frac{1}{\theta^1 \tan\theta^2}\,\overset{*}{t}{}^{12} + \rho\,\overset{*}{f}{}^{1} &= 0, \\
\overset{*}{t}{}^{12}_{,1} + \frac{1}{\theta^1}\,\overset{*}{t}{}^{22}_{,2} + \frac{1}{\theta^1 \sin\theta^2}\,\overset{*}{t}{}^{23}_{,3} + \frac{3}{\theta^1}\,\overset{*}{t}{}^{12} + \frac{1}{\theta^1 \tan\theta^2}(\overset{*}{t}{}^{22} - \overset{*}{t}{}^{33}) + \rho\,\overset{*}{f}{}^{2} &= 0, \\
\overset{*}{t}{}^{13}_{,1} + \frac{1}{\theta^1}\,\overset{*}{t}{}^{23}_{,2} + \frac{1}{\theta^1 \sin\theta^2}\,\overset{*}{t}{}^{33}_{,3} + \frac{3}{\theta^1}\,\overset{*}{t}{}^{13} + \frac{2}{\theta^1 \tan\theta^2}\,\overset{*}{t}{}^{23} + \rho\,\overset{*}{f}{}^{3} &= 0.
\end{aligned}
\tag{B.39}
$$

Substituting the relations (B.35) into (B.37) and plugging this in (B.39), the equilibrium equations can be expressed in terms of the displacement components.

Bibliography

[1] J. Aboudi. *Mechanics of Composite Materials.* Elsevier, Amsterdam, 1991.

[2] P. M. Adler. *Porous media.* Butterworth-Heinemann, Boston, 1992.

[3] L. Allais, T. Bretheau, and A. Zaoui. Experimental and theoretical approach of the influence of morphology on a two-phase material mechanical behavior. In S. Torquato and D. Krajcinovic, editors, *Macroscopic behavior of heterogeneous materials from the microstructure*, volume AMD-Vol. 147, pages 13–25. ASME, New York, 1992.

[4] K. Amaratunga and J. R. Williams. Wavelet-*galerkin* solutions for one-dimensional partial differential equations. *Int. J. Numer. Meth. Eng.*, 37:2703–2716, 1994.

[5] G. E. Archie. The electrical resistivity log as an aid in determining some reservoir characteristics. *Trans. AIME*, 146:54, 1942.

[6] G. B. Arfken and H. J. Weber. *Mathematical Methods for Physicists.* Academic Press, San Diego, 1995.

[7] J. I. Auñón and V. Chandrasekar. *Introduction to probability and random processes.* McGraw-Hill, New York, 1996.

[8] J. Axell and J. Helsing. Conductance fluctuations in weakly inhomogeneous finite-size random media. *Phys. Rev. B*, 42:4471–4476, 1990.

[9] O. Axelsson. *Iterative solution methods.* Cambridge University Press, Cambridge, 1994.

[10] H. Bach. On the downhill method. *Comm. ACM*, 12:675–677, 684, 1969.

[11] R. Barrett, M. Berry, T. F. Chan, J. Demmel, J. Donato, J. Dongarra, V. Eijkhout, R. Pozo, C. Romine, and H. Van der Vorst. *Templates for the Solution of Linear Systems: Building Blocks for Iterative Methods.* SIAM, Philadelphia, PA, 1994.

[12] A. Beer. *Einleitung in die höhere Optik.* Friedrich Vieweg and Sohn, Braunschweig, 1853.

[13] A. Bensoussan, J. L. Lions, and G. Papanicolaou. *Asymptotic analysis of periodic structures.* North-Holland, Amsterdam, 1978.

[14] M. Beran. Statistical continuum theories. *Trans. Soc. Rheol.*, 9:339–355, 1965.

[15] M. Beran. Use of a variational approach to determine bounds for the effective permittivity of a random medium. *Nuovo Cimento*, 38:771–782, 1965.

[16] M. Beran and J. Molyneux. Use of classical variational principles to determine bounds for the effective bulk modulus in heterogeneous media. *Q. Apll. Math.*, 24:107–118, 1966.

[17] M. J. Beran. *Statistical Continuum Theories*. Wiley, New York, 1968.

[18] J. C. Van Den Berg, editor. *Wavelets in Physics*. Cambridge University Press, Cambridge, 1999.

[19] D. Bergman. The dielectric constant of a composite material – a problem in classical physics. *Phys. Rep.*, 43:377–407, 1978.

[20] D. J. Bergman. Exactly solvable microscopic geometries and rigorous bounds for the complex dielectric constant of a two-component composite materials. *PRL*, 44:1285–1287, 1980.

[21] D. J. Bergman. Rigorous bounds for the complex dielectric constant of a two-component composite. *Ann. Phys.*, 138:78–114, 1982.

[22] D. J. Bergman and D. Stroud. Physical properties of macroscopically inhomogeneous media. *Solid State Physics eds. H. Ehrenreich and D. Turnbull*, 46:147–269, 1992.

[23] J. G. Berryman. Relationship between specific surface area and spatial correlation functions for anisotropic porous media. *J. Math. Phys.*, 28:244–245, 1987.

[24] J. G. Berryman. Generalization of Eshelby's formula for a single ellipsoidal elastic inclusion to poroelasticity and thermoelasticity. *Phys. Rev. Lett.*, 79:1142–1145, 1997.

[25] J. G. Berryman and P. A. Berge. Rock elastic properties: Dependence on microstructure. In C. S. Chang and J. W. Ju, editors, *Homogenization and constitutive modeling for heterogeneous materials*, volume 166 of *AMD*. ASME, New York, 1993.

[26] J. G. Berryman and G. W. Milton. Microgeometry of random composites and porous media. *J. Phys. D: Appl. Phys.*, 21:87–94, 1988.

[27] J.G. Berryman. Measurement of spatial correlation functions using image processing techniques. *J. Appl. Phys.*, 57:2374–2384, 1985.

[28] J. Betten. *Elementare Tensorrechnung für Ingenieure*. Vieweg, Braunschweig, 1977.

[29] J. R. Birchak, L. G. Gardner, J. W. Hipp, and J. M. Victor. High dielectric constant microwave probes for sensing soil moisture. *Proc. of the IEEE*, 62:93–98, 1974.

[30] B. Biswal and R. Hilfer. Microstructure analysis of reconstructed porous media. *Physica A*, 266:307–311, 1999).

[31] B. Biswal, C. Manwart, and R. Hilfer. Three-dimensional local porosity analysis of porous media. *Physica A*, 225:221, 1998.

[32] B. Biswal, C. Manwart, R. Hilfer, S. Bakke, and P.E. Øren. Quantitative analysis of experimental and synthetic microstructures for sedimentary rock. *Physica A*, 273:452–475, 1999.

[33] M. Bobeth and G. Diener. Field fluctuations in multicomponent mixtures. *J. Mech. Phys. Solids*, 34:1–17, 1986.

[34] F. Boger, J. Feder, T. Jøssang, and R. Hilfer. Microstructural sensitivity of local porosity distributions. *Physica A*, 187:55, 1992.

[35] J. Botsis and C. Beldica. Strength characteristics and fatigue crack growth in a composite with long aligned fibers. *Int. J. Fracture*, 69:27–50, 1995.

[36] S. R. Broadbent and J. M. Hammersley. Percolation processes I. Crystals and mazes. *Proc. Cambridge Phil. Soc.*, 53:629–641, 1957.

[37] D. A. G. Bruggeman. Berechnung verschiedener physikalischer Konstanten von heterogenen Substanzen. I. Dielektrizitätskonstanten und Leitfähigkeiten der Mischkörper aus isotropen Substanzen. *Ann. Phys.*, 24:636, 1935.

[38] B. Budiansky. On the elastic moduli of some heterogeneous materials. *J. Mech. Phys. Solids*, 13:223–227, 1965.

[39] P. P. Castañeda and P. Suquet. Nonlinear composites. *Adv. Appl. Mech.*, 34:171–302, 1998.

[40] K. R. Castleman. *Digital image processing.* Pretince Hall, Upper Saddle River, New Jersey, 1996.

[41] H. Cheng and S. Torquato. Electric field fluctuations in random dielectric composites. *Phys. Rev. B*, 56:8060–8068, 1997.

[42] A. Cherkaev. *Variational methods for structural optimization.* Springer-Verlag, New York, 2000.

[43] T. C. Choy. *Effective medium theory.* Oxford university press, Oxford, 1999.

[44] R. M. Christensen. *Mechanics of Composite Materials.* J. Wiley & Sons, New York, 1979.

[45] R. M. Christensen. A critical evaluation for a class of micromechanics models. *J. Mech. Phys. Solids*, 38:379–404, 1990.

[46] R. M. Christensen and K. H. Lo. Solutions for effective shear properties in three phase sphere and cylinder models. *J. Mech. Phys. Solids*, 27:315–330, 1979.

[47] A. Davidson and M. Tinkham. Phenomenological equations for the electrical conductivity of microscopically inhomogeneous materials. *Phys. Rev. B*, 13:3261–3267, 1976.

[48] R. de Boer. *Vektor- und Tensorrechnung für Ingenieure.* Springer, Berlin, 1982.

[49] R. de Boer. *Theory of Porous Media.* Springer, Berlin, 2000.

[50] R. de Boer and W. Ehlers. *Theorie der Mehrkomponentenkontinua mit Anwendung auf bodenmechanische Probleme, Teil I.*, volume 40. Forschungsberichte aus dem Fachbereich Bauwesen der Universität G.H. Essen, Essen, 1986.

[51] P. Debye, H. R. Anderson, and H. Brumberger. Scattering by an inhomogeneous solid II: The correlation function and its application. *J. Appl. Phys.*, 28:679, 1957.

[52] W. J. Drugan and J. R. Willis. A micromechanics-based nonlocal constitutive equation and estimates of representative volume element size for elastic composites. *J. Mech. Phys. Solids*, 44:497–524, 1996.

[53] F. A. L. Dullien. Characterization of porous media - pore level. *Transport in Porous Media*, 6:581, 1991.

[54] D. R. Durran. *Numerical methods for wave equations in geophysical fluid dynamics.* Springer-Verlag, New York, 1999.

[55] W. Ehlers. On thermodynamics of elasto-plastic porous media. *Archives of Mechanics*, 41:73–93, 1989.

[56] W. Ehlers. *Poröse Medien -ein kontinuummechanisches Modell auf der Basis der Mischungstheorie-. Habilitationsschrift*, volume 47. Forschungsberichte aus dem Fachbereich Bauwesen der Universität G.H. Essen, Essen, 1989.

[57] W. Ehlers. Toward finite theories of liquid-saturated elasto-plastic porous media. *Int. J. Plasticity*, 7:433–475, 1991.

[58] W. Ehlers. *Continuum Mechanics I (in German).* Lectures Notes at T. U. Darmstadt, Darmstadt, 1993.

[59] W. Ehlers. *Continuum Mechanics II (in German).* Lectures Notes at T. U. Darmstadt, Darmstadt, 1993.

[60] W. Ehlers. Grundlegende Konzepte in der Theorie poröser Medien. *Technische Mechanik*, 16:63–76, 1996.

[61] I. Ekeland and R. Teman. *Convex analysis and variational problems.* North-Holland, Amsterdam, 1976.

[62] A. C. Eringen, editor. *Recent advances in engineering sciences*, volume 5, New York, 1970. Gordon and Breach.

[63] A. C. Eringen and G. A. Maugin. *Electrodynamics of Continua* **I**. Springer-Verlag, Berlin, 1989.

[64] J. D. Eshelby. The determination of the elastic field of an ellipsoidal inclusion and related problems. *Proc. Roy. Soc. London A*, 241:376–396, 1957.

[65] J. H. Ferziger and M. Perić. *Computational methods for fluid dynamics*. Springer-Verlag, Berlin, 1996.

[66] P. J. Flory. Molecular size distribution in three dimensional polymers i & ii. *J. Am. Chem. Soc.*, 63:3083–3100, 1941.

[67] R. W. Freund. Conjugate gradient-type methods for linear systems with complex symmetric coefficient matrices. *SIAM J. Sci. Stat. Comput.*, 13:425–448, 1992.

[68] E. J. Garboczi and D. P. Bentz. Fundamental computer simulation models for cement-based materials. In J. Skalny, editor, *Materials science of concrete*, volume 2. American Ceramic Society, Westerville, Ohio, 1991.

[69] E. J. Garboczi and D. P. Bentz. Computational materials science of cement-based materials. *Mater. Res. Soc. Bulettin*, 18:50–54, 1993.

[70] E. J. Garboczi, D. P. Bentz, and N. S. Martys. Digital images and computer modelling. In P.-Z. Wong, editor, *Experimental Methods for Porous Media*. Academic Press, New York, 1999).

[71] E. J. Garboczi, M. F. Thorpe, M. S. DeVries, and A. R. Day. Universal conductivity curve for a plane containing random holes. *Phys. Rev. A*, 43:6473–6482, 1991.

[72] C. W. Gardiner. *Handbook of Stochastic Methods*. Springer Verlag, Berlin, 1997.

[73] L. V. Gibiansky and S. Torquato. Link between the conductivity and elastic moduli of composite materials. *PRL*, 71:2927–2930, 1993.

[74] J. H. Gladstone and T. P. Dale. Researches on the refraction, dispersion, and sensitiveness of liquids. *Phil. Trans. Roy. Soc. London*, 153:317–343, 1863.

[75] G. H. Golub and C. F. van Loan. *Matrix computations*. John Hopkins University Press, Baltimore, 1989.

[76] J. L. Greffe and C. Grosse. Static permittivity of emulsions. In A. Priou, editor, *Dielectric properties of heterogeneous materials*, chapter 2. Elsevier, Amsterdam, 1992.

[77] P. M. Gresho and R. L. Sani. *Incompressible flow and the finite element method. Volume 1: Advection-Diffusion*. John Wiley & Sons, New York, 2000.

[78] Z. Hashin. The elastic moduli of heterogeneous materials. *ASME J. Appl. Mech.*, 29:143–150, 765–766, 1962.

[79] Z. Hashin. *Theory of fiber reinforced materials.* NASA CR-1974, 1972.

[80] Z. Hashin. Analysis of composite materials. *J. Appl. Mech.*, 50:481–505, 1983.

[81] Z. Hashin and S. Shtrikman. A variational approach to the theory of the effective magnetic permeability of multiphase materials. *J. Appl. Phys.*, 33:3125–3131, 1962.

[82] Z. Hashin and S. Shtrikman. A variational approach to the theory of the elastic behaviour of polycrystals. *J. Mech. Phys. Solids*, 10:343–352, 1962.

[83] Z. Hashin and S. Shtrikman. A variational approach to the theory of the elastic behaviour of multiphase materials. *J. Mech. Phys. Solids*, 11:127–140, 1963.

[84] P. Haupt. *Continuum Mechanics and Theory of Materials.* Springer Verlag, Berlin, 2000.

[85] J. Helsing. Bounds to the conductivity of some two-component composites. *J. Appl. Phys.*, 73:1240–1245, 1993.

[86] A. V. Hershey. The elasticity of an isotropic aggregate of anisotropic cubic crystals. *J. Appl. Mech.*, 21:236–241, 1954.

[87] H. Heuser. *Funktionalanalysis.* B. G. Teubner, Stuttgart, 1992.

[88] R. Hilfer. Geometric and dielectric characterization of porous media. *Phys. Rev. B*, 44:60, 1991.

[89] R. Hilfer. Local porosity theory for electrical and hydrodynamical transport through porous media. *Physica A*, 194:406, 1993.

[90] R. Hilfer. Transport and relaxation phenomena in porous media. *Adv. in Chem. Phys.*, XCII:299, 1996.

[91] R. Hilfer, J. Widjajakusuma, and B. Biswal. Dielectric relaxation in water saturated sedimentary rocks. *Granular Matter*, pages 137–141, 2000.

[92] R. Hill. Elastic properties of reinforced solids: some theoretical principles. *J. Mech. Phys. Solids*, 11:357–372, 1963.

[93] R. Hill. A self-consistent mechanics of composite materials. *J. Mech. Phys. Solids*, 13:213–222, 1965.

[94] G. Holzapfel. *Nonlinear solid mechanics: A continuum approach for engineering.* J. Wiley & Sons, New York, 2000.

[95] T. J. R. Hughes. *The finite element method.* Prentice-Hall, Englewood Cliffs, N. J., 1987.

[96] A. Ishimaru. *Electromagnetic wave propagation, radiation and scattering.* Prentice Hall, Englewood Cliffs, N.J., 1991.

[97] J. D. Jackson. *Klassische Elektrodynamik*. de Gruyter, Berlin, 1983.

[98] D. Jeulin and M. Ostoja-Starzewski, editors. *Mechanics of random and multiscale microstructures*. CISM courses and lectures. Springer, Wien, in preparation.

[99] S. Kanaun. Self-consistent methods in the problem of wave propagation through heterogeneous media. In K. Markov and L. Preziosi, editors, *Heterogeenous Media*. Birkhäuser, Basel, 2000.

[100] I. C. Kim and S. Torquato. Determination of the effective conductivity of heterogeneous media by Brownian motion simulation. *J. Appl. Phys.*, 68:3892–3903, 1990.

[101] J. A. Kong. *Electromagnetic Wave Theory*. J. Wiley & Sons, New York, 1986.

[102] D. Krajcinovic. *Damage Mechanics*. North-Holland, Amsterdam, 1996.

[103] E. Kröner. Berechnung der elastischen Konstanten des Vielkristalls aus den Konstanten des Einkristalls. *Z. Phys.*, 151:504–518, 1958.

[104] E. Kröner. Elastic moduli of perfectly disordered composite materials. *J. Mech. Phys. Solids*, 15:319–, 1958.

[105] E. Kröner. *Statistical Continuum Mechanics*. CISM Courses and Lectures N0. 92, Udine, Italy. Springer-Verlag, Wien, 1972.

[106] E. Kröner. Bounds for effective elastic moduli of disordered materials. *J. Mech. Phys. Solids*, 25:137–155, 1977.

[107] L. D. Landau, E. M. Lifsic, and L. P. Pitaevskij. *Electrodynamics of continuous media*. Elsevier, Amsterdam, 1984.

[108] R. Landauer. Electrical conductivity in inhomogeneous media. In J.G. Garland and D.B. Tanner, editors, *Electrical Transport and Optical Properties of Inhomogeneous Materials*, page 2, New York, 1978. American Institute of Physics.

[109] K. Lichtenecker. Die Dieletrizitäskonstante natürlicher und kunstlicher Mischkörper. *Phys. Zeitschrift*, 27:115–158, 1926.

[110] K. Lichtenecker and K. Rother. Die Herleitung des logarithmischen Mischunggesetzes aus allgemeinen Prinzipien der stationären Strömung. *Phys. Zeitschrift*, 32:255–260, 1931.

[111] H. Looyenga. Dielectric constants of heterogeneous mixtures. *Physica*, 31:401–406, 1965.

[112] A. E. H. Love. *A Treatise on the Mathematical Theory of Elasticity*. Dover, New York, 1944.

[113] B. Lu and S. Torquato. Local volume fraction fluctuations in heterogeneous media. *J. Chem. Phys.*, 93:3452–3459, 1990.

[114] H. Ma, B. Zhang, W. Y. Tam, and P. Sheng. Dielectric-constant evaluation from microstructures. *Phys. Rev. B*, 61:962–966, 2000.

[115] K. Markov. Elementary micromechanics of heterogeneous media. In K. Markov and L. Preziosi, editors, *Heterogeenous Media*. Birkhäuser, Basel, 2000.

[116] K. Z. Markov. Application of Volterra-Wiener series for bounding the overall conductivity of heterogeneous media. I. General procedure. *SIAM J. Appl. Math.*, 47:831–849, 1987.

[117] K. Z. Markov. Application of Volterra-Wiener series for bounding the overall conductivity of heterogeneous media. II. Suspensions of equi-sized spheres. *SIAM J. Appl. Math.*, 47:850–870, 1987.

[118] K. Z. Markov and Kr. D. Zvyatkov. Functional series and Hashin-Shtrikman type bounds on the effective properties of random media. In K. Z. Markov, editor, *Advances in mathematical modelling of composite materials*, volume 15 of *Series on advances in mathematics for applied sciences*, pages 59–140. World Scientific, Singapore, 1994.

[119] C. Mätzler. Microwave permittivity of dry snow. *IEEE Trans. on Geoscience and Remote Sensing*, 34:573–581, 1996.

[120] G. Mavko, T. Mukerji, and J. Dvorkin. *The rock physics handbook*. Cambridge University Press, Cambridge, UK, 1998.

[121] J. C. Maxwell. *A Treatise on Electricity and Magnetism* **1,2** *3rd ed. 1891*. Dover publication Inc., New York, 1954.

[122] J. C. Maxwell-Garnett. Colours in metal glasses and in metal films. *Trans. Royal Soc.*, CCIII:385, 1904.

[123] J-C. Michel, H. Moulinec, and P. Suquet. A computational method based on augmented Lagrangians and Fast Fourier Transforms for composites with high contrast. *Comp. Model. Engng. Sc.*, 1:79–88, 2000.

[124] C. Miehe, A. Koch, and C. Bayreuther. Strain-driven homogenization of nonlinear composites for different constraints on the displacement fluctuations. *Report/Preprint No. 00-I-02. Institut für Mechanik (Bauwesen). Lehrstuhl I. Universität Stuttgart*, 2000.

[125] G. Milton and N. Phan-Thien. New bounds on the effective moduli of two-component materials. *Proc. Roy. Soc. Lond. A*, 380:305–331, 1982.

[126] G. W. Milton. Bounds on the complex dielectric constant of a composite materials. *Appl. Phys. Lett.*, 37:300–302, 1980.

[127] G. W. Milton. Bounds on the complex permittivity of a two-component composite materials. *J. Appl. Phys.*, 52:5286–5293, 1981.

[128] G. W. Milton. Bounds on the electromagnetic, elastic, and other properties of two-component composites. *Phys. Rev. Lett.*, 46:542–545, 1981.

[129] G. W. Milton. Bounds on the elastic and transport properties of two-component composites. *J. Mech. Phy. Solids*, 30:177–191, 1982.

[130] G. W. Milton. The coherent potential approximation is arealizable effective medium scheme. *Comm. Math. Phys.*, 99:463–500, 1985.

[131] G. W. Milton. A brief review of the translation method for bounding effective elastic tensors of composites. In G. A. Maugin, editor, *Proceedings of the 6-th Symposium on Continuum Models and Discrete Systems*, pages 60–74. Longman, Harlow, 1990.

[132] G. W. Milton. The field equation recursion method. In G. Dal Maso and G. Dell'Antonio, editors, *Composite media and homogenization theory*, pages 223–245. Birkhäuser, Boston, MA, 1991.

[133] T. Mori and K. Tanaka. Average stress in matrix and average elastic energy of materials with misfitting inclusions. *Acta Metallica*, 21:571–573, 1973.

[134] H. Moulinec, J-C. Michel, and P. Suquet. Effective properties of composite materials with periodic microstructure: A computational approach. *Comput. Methods Appl. Mech. Engrg*, 172:109–143, 1999.

[135] S. Nemat-Nasser and M. Hori. *Micromechanics : Overall Properties of Heterogeneous Materials*. Elsevier, Amsterdam, 2000.

[136] A. M. Neville. *Properties of concrete*. Longman, Essex, 4 edition, 1995.

[137] A. N. Norris. A differential scheme for the effective moduli of composites. *Mech. Mater.*, 4:1–16, 1985.

[138] A. N. Norris, P. Sheng, and A. J. Callegari. Effective-medium theories for two-phase dielectric media. *J. Appl. Phys.*, 57:1990–1996, 1985.

[139] C. C. Paige and M. A. Saunders. Solution of sparse indefinite systems of linear equations. *SIAM J. Numer. Anal.*, 12:617–629, 1975.

[140] A. Papoulis. *Probability, random variables, and stochastic processes*. McGraw-Hill, New York, 1965.

[141] S. Patankar. *Numerical heat transfer and fluid flow*. Hemisphere Publishing Corporation, New York, 1980.

[142] Wong Po-zen, editor. *Methods in the physics of porous media*, volume 35 of *Experimental methods in the physical sciences*. Academic Press, San Diego, 1999.

[143] D. Polder and J. H. Van Santen. The effective permeability of mixtures of solids. *Physica*, 12:257–271, 1946.

[144] S. Prager. Improved variational bounds on some bulk properties of a two-phase random medium. *J. Chem. Phys.*, 50:4305–4312, 1969.

[145] W. H. Press, S. A. Teukolsky, W. T. Vetterling, and B.P. Flannery. *Numerical Recipes in Fortran. The art of scientific computing. Second Edition.* Cambridge University Press, Cambridge, 1992.

[146] A. Priou, editor. *Dielectric properties of heterogeneous materials.* Elsevier, Amsterdam, 1992.

[147] J. Quintanilla. Microstructure and properties of random heterogeneous materials: a review of theoretical results. *Polymer Engineering and Science*, 39:559–585, 1999.

[148] J. Quintanilla and S. Torquato. Local volume fraction fluctuations in periodic heterogeneous media. *J. Chem. Phys.*, 110:3215–3219, 1999.

[149] Lord Rayleigh. On the influence of obstacles arranged in rectangular order upon the properties of a medium. *Phil. Mag.*, 32:481–502, 1892.

[150] A. Reuss. Berechnung der Fließgrenze von Mischkristallen aufgrund der Plastizitäsbedingung für Einkristalle. *ZAMM*, 9:49–58, 1929.

[151] P. Robert. *Electrical and magnetic properties of materials.* Artech House, Norwood, Massachusetts, 1988.

[152] F. J. Sabina and J. R. Willis. A simple self-consistent analysis of wave propagation in particulate composites. *Wave Motion*, 10:127–142, 1988.

[153] M. Sahimi. *Applications of percolation theory.* Taylor & Francis Publ., London, 1994.

[154] M. Sahimi. *Flow and transport in porous media and fractured rocks.* VCH, New York, 1996.

[155] A. E. Scheidegger. *The physics of flow through porous media.* University of Toronto Press, Toronto, 1957.

[156] K. Schulgasser. Relationship between single-crystal and polycrystal electrical conductivity. *J. Appl. Phys.*, 47:1880–1886, 1976.

[157] P. N. Sen, C. Scala, and M. H. Cohen. A self-similar model for sedimentary rocks with application to the dielectric constant of fused glass beads. *Geophysics*, 46:781–796, 1981.

[158] P. Sheng. Pair-cluster theory for the dielectric constant of composite media. *Phys. Rev. B*, 22:6364–6368, 1980.

[159] P. Sheng. Theory for the dielectric function of granular composite media. *Phys. Rev. Lett.*, 45:60–63, 1980.

[160] P. Sheng, editor. *Scattering and localization of classsical waves in random media.* World Scientific, Singapore, 1990.

[161] P. Sheng. Consistent modeling of the electrical and elastic properties of sedimentary rocks. *Geophysics*, 56:1236–1243, 1991.

[162] P. Sheng. *Introduction to Wave Scattering, Localization, and Mesoscopic Phenomena.* Academic Press, San Diego, 1995.

[163] P. Sheng and A.J. Callegari. Consistent theoretical description for electrical and acoustic properties of sedimentary rocks. In D.L. Johnson and P.N. Sen, editors, *Physics and chemistry in porous media*, New York, 1984. AIP.

[164] A. Sihvola. *Electromagnetic mixing formulas and applications.* The Institution of Electrical Engineers, London, 1999.

[165] D. Stauffer and A. Aharony. *Perkolationstheorie.* Wiley/VCH, Weinheim, 1995.

[166] W. H. Stockmayer. Theory of molecular size distribution and gel formation in branched chain polymers. *J. Chem. Phys.*, 11:45–55, 1943.

[167] D. Stroud and F. P. Pan. Self-consistent approach to electromagnetic propagation in composite media: Application to model granular metals. *Phys. Rev. B*, 17:1602, 1978.

[168] P. Suquet, editor. *Continuum micromechanics*, volume 377 of *CISM courses and lectures.* Springer, Wien, 1997.

[169] K. Terada, M. Hori, T. Kyoya, and N. Kikuchi. Simulation of the multi-scale convergence in computational homogenization approach. *Int. J. Solids Structures*, 37:2285–2311, 2000.

[170] S. Torquato. Random heterogeneous media: Microstructure and improved bounds on effective properties. *Appl. Mech. Rev.*, 44:37–76, 1991.

[171] S. Torquato. Connection between morphology and effective properties of heterogeneous materials. In S. Torquato and D. Krajcinovic, editors, *Macroscopic behavior of heterogeneous materials from the microstructure*, volume AMD-Vol. 147, pages 53–65. ASME, New York, 1992.

[172] S. Torquato and G. Stell. Microstructure of two-phase random media. I. The n-point probability functions. *J. Chem. Phys.*, 77:2071–2077, 1982.

[173] S. Torquato and G. Stell. Microstructure of two-phase random media. III. The n-point matrix probability functions for fully penetrable spheres. *J. Chem. Phys.*, 79:1505–1510, 1983.

[174] S. Torquato and G. Stell. Microstructure of two-phase random media. V. The n-point matrix probability functions for impenetrable spheres. *J. Chem. Phys.*, 82:980–987, 1985.

[175] C. Truesdell, editor. *Rational thermodynamics*. Springer, Berlin, 1984.

[176] C. Truesdell and R. A. Toupin. *The classical field theories*, volume III/1 of *Handbuch der Physik*. Springer-Verlag, Berlin, 1960.

[177] H. A. van der Vorst and J. B. M. Melissen. A *petrov-galerkin* type method for solving $ax = b$, where a is symmetric complex. *IEEE Trans. Magn.*, 26:706–708, 1990.

[178] O. van Genabeek and D. H. Rothman. Macroscopic manifestations of microscopic flows through porous media: Phenomenology from simulation. *Annual Reviews of Earth Sciences*, 24:63–87, 1996.

[179] J. J. I. M. van Kan and A. Segal. *Numerik partieller Differentialgleichungen für Ingenieure*. B.G. Teubner, Stuttgart, 1995.

[180] M. C. W. van Rossum and Th. M. Nieuwenhuizen. Multiple scattering of classical waves: microscopy, mesoscopy, and diffusion. *Rev. Mod. Phys.*, 71:313–371, 1999.

[181] R. S. Varga. *Matrix iterative analysis*. Springer, Berlin, 2000.

[182] W. Voigt. Über die Beziehung zwischen den beiden Elastizitätskonstanten isotroper Körper. *Ann. Phys.*, 38:573–587, 1887.

[183] J. A. Ward. The downhill method of solving $f(z) = 0$. *J. ACM*, 4:148–150, 1957.

[184] J. P. Watt, G. F. Davies, and R. J. O'Connell. The elastic properties of composite materials. *Rev. Geophys. Space Phys.*, 14:541–563, 1976.

[185] J. Widjajakusuma, B. Biswal, and R. Hilfer. Quantitative prediction of effective material properties of heterogeneous media. *Computational Materials Science*, 16:70, 1999.

[186] J. Widjajakusuma, B. Biswal, and R. Hilfer. Predicting transport parameters of heterogeneous media. *Preprint*, 2000.

[187] J. Widjajakusuma, C. Manwart, B. Biswal, and R. Hilfer. Exact and approximate calculations for the conductivity of sandstones. *Physica A*, 270:325, 1999.

[188] O. Wiener. Die Theorie des Mischkörpers für das Feld der stationären Strömung. *Abh. Math. Phys. Sachs. Akad. Wiss.*, 32:509, 1912.

[189] J. R. Williams and K. Amaratunga. Introduction to wavelets in engineering. *Int. J. Numer. Meth. Eng.*, 37:2365–2388, 1994.

[190] J. Willis. Lectures on mechanics on random media. prelimanary notes. In D. Jeulin and M. Ostoja-Starzewski, editors, *Mechanics of random and multiscale microstructures*. CISM, Udine, Italy, Springer, To be appear.

[191] J. R. Willis. Variational and related methods for the overall properties of composites. *Adv. Appl. Mech.*, 21:1–78, 1981.

[192] J. R. Willis. The overall response of nonlinear composite media. *Eur. J. Mech. A/Solids*, 19:S165–S184, 2000.

[193] W. S. Wladimirow. *Gleichungen der mathematischen Physik*. VEB Deutscher Verlag der Wissenschaften, Berlin, 1972.

[194] T. T. Wu. The effect of inclusion shape on the elastic moduli of a two-phase material. *Int. J. Sol. Struct.*, 2:2–8, 1966.

[195] C. Yeong and S. Torquato. Reconstructing random media. *Phys. Rev. E*, 57:495, 1998.

[196] D. M. Young. *Iterative solution of large linear systems*. Academic Press, New York, 1971.

[197] A. Zaoui. Structural morphology and constitutive behaviour of microheterogeneous materials. In P. Suquet, editor, *Continuum Micromechanics*, volume 377 of *CISM courses and lectures*, pages 291–347. Springer, Wien, 1997.